A DIFFERENTIAL LIDAR SYSTEM BASED ON A XENON CHLORIDE LASER

Roger Bradley Millington

A Thesis Submitted for the Degree of PhD
at the
University of St Andrews

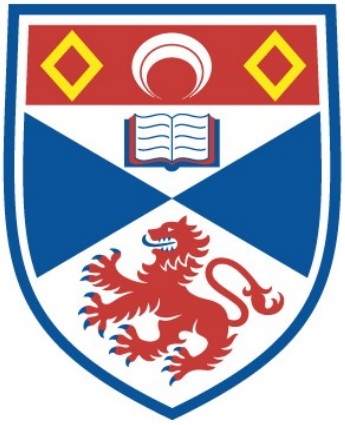

1985

A DIFFERENTIAL LIDAR SYSTEM BASED ON A XENON CHLORIDE LASER

A thesis presented by

R B Millington, BSc

to the

University of St Andrews

in application for the degree of

Doctor of Philosophy

April 1985

ProQuest LLC.
789 East Eisenhower Parkway
P.O. Box 1346
Ann Arbor, MI 48106 – 1346

DECLARATION

I hereby certify that this thesis has been composed by me, and is a record of work done by me, and has not previously been presented for a higher degree.

This research was carried out in the Physical Sciences Laboratory of St Salvator's College, in the University of St Andrews, under the supervision of Dr A Maitland.

R B Millington

CERTIFICATE

I certify that R B Millington has spent nine terms at research work in the Physical Sciences Laboratory of St Salvator's College, in the University of St Andrews, under my direction, that he has fulfilled the conditions of Ordinance No 16 (St Andrews) and that he is qualified to submit the following thesis in application for the Degree of Doctor of Philosophy.

A Maitland

Research Supervisor

AUTHOR'S CAREER

The author was born in Lancashire in 1958. Primary education was in Oldham and Leyland, Lancashire. Secondary education was at Balshaw's Grammar School, Leyland and at Runshaw Sixth Form College, Leyland. A BSc in Physics was obtained in the University of St Andrews (1976-1980). From June 1980, the author has been employed as a Research Assistant in the Department of Physics, University of St Andrews, working on laser and optical projects, supported by the South of Scotland Electricity Board, for the detection of environmental pollutants.

ACKNOWLEDGEMENT

I give my thanks and appreciation to Arthur Maitland for all the help, encouragement and advice that I have received from him. Thanks also, to my colleagues, past and present, in the Laser 1 Group; Ben, Unny, Colin, Tim, David, Ian, Graeme, Robert and Janet for valuable discussions. I am grateful for the advice and the skills of the technical personnel of the Physics department's mechanical and electronics workshops, the teaching laboratories and the stores. Thanks to the administrative and janitorial staff of the department for essential services and humour.

I am very grateful to Jim Smith and Jim Grant and the South of Scotland Electricity Board for their support, without which this work would not have been possible. Thanks to SSEB staff of Technical Services, the transport department and of Methil power station.

Finally, "thank-you" to my family for their enduring support in the course of preparation of this thesis.

Abstract

A differential absorption lidar (DIAL) system, based on a xenon chloride excimer laser, has been developed and applied to measurements of atmospheric sulphur dioxide. This thesis describes the basis of the technique, the construction and operation of the prototype system, and its theoretical and practical sensitivity to sulphur dioxide concentration.

The system, comprising the laser, telescope, detector and data handling equipment was developed for robustness in the field, and novel features have been included for this purpose. The Newtonian type telescope was chosen for its small image size and adequate field-of-view. It uses a "Cassegrain" type primary mirror and a visible reflector at the focus, allowing direct viewing of the scattering target. This feature is used in conjunction with direct viewing through the laser cavity, through a dielectric coated mirror, to permit laser/telescope alignment on the target.

The laser itself is pumped by transverse discharge after corona/U.V preionization. Laser characteristics have been measured. Those of primary importance to lidar are the energy per pulse, at 5 to 8mJ, the pulse duration of 32ns, the maximum pulse repetition rate, at 20pps, and the number of pulses to half energy, at 18000 per gas fill. The emission spectrum of the laser, with wavelengths at 307.92nm and 308.17nm, has been compared with the absorption spectrum of sulphur dioxide, showing a difference between the respective absorption coefficients. This indicated the suitability of this particular laser to the differential absorption technique.

Unique selection between these wavelengths, per pulse, is desirable for

optimum sensitivity in DIAL. However, a novel method has been devised for modifying the relative wavelength content of one of the pulses, by inserting an absorption cell of sulphur dioxide into the laser optical cavity. The advantages of this over "distinct" wavelength selection are cheapness and robustness. However, theoretical work has shown a subsequent loss of sensitivity to atmospheric sulphur dioxide concentration, by a factor of about 5. A 3-element birefringent filter has been designed in case a more conventional tuning method is required.

Specification of the detector and its operating conditions have been closely defined in order to optimise sensitivity to very low levels of backscattered light, whilst reducing the effects of unwanted background and noise. To this end, a solar-blind photomultiplier has been employed in conjunction with a narrow-band interference filter, centred around the laser emission wavelength.

A relatively simple signal handling circuit was built to perform the minimum requirement of measuring the intensity of backscattered radiation. A micro-computer is used to control the circuitry in test and data acquisition modes, and to store data, allowing signal averaging and subsequent data analysis. Program algorithms for data analysis were developed from lidar and DIAL theory.

A theoretical investigation of atmospheric scattering properties was carried-out to provide scatter coefficients for application in the lidar equation. The validity of the lidar equation was proved when computer-modelled oscilloscope traces of lidar return signals were found to match, closely, experimental traces of return signals from the smoke plume at Methil power station. A theoretical treatment, using the lidar equation,

gave expressions for target gas concentrations as a function of return signal intensities. This was done for the case where unique wavelength pulses are transmitted into the atmosphere and was repeated for the case of "mixed wavelength" pulses, applying to the DIAL experiment.

Prediction of sensitivity of the system in measuring sulphur dioxide concentration is based on the noise content of the return signals. The analysis has given a detection limit range of about 10ppm.m to 800ppm.m, for the "mixed wavelength" application and an expected range of 2ppm.m to 160ppm.m if the laser is tuned conventionally, depending on signal strength and number of averaged pulse pairs. Errors expected in measurements of finite sulphur dioxide concentrations are given.

The system was applied to measuring sulphur dioxide, emitted under control, into the path of the laser pulse. Measured peaks of about 120ppm were expected and measurements taken successively are in agreement with expected dispersal rates. Fluctuations of measured sulphur dioxide levels, about a mean, are shown to be within the theoretically-evaluated error limits. This close agreement between theory and experiment allows the theoretical detection limits to be treated as realistic.

To my grandfather, James Bradley.

Contents

Chapter 8 Derivation and Application of the Single Wavelength Lidar Equation

8.1 Introduction to Rayleigh and Mie Scattering in the Lower Atmosphere

8.1.1 Rayleigh Scattering

8.1.2 Mie Scattering

8.2 The Lidar Equation for Atmospheric Transmission of a Laser Pulse

8.2.1 Attenuation by Scatter and Absorption

8.2.2 Collection Efficiency and Backscatter to the Receiver

8.2.3 Optical Efficiencies of the System

8.2.4 The Lidar Equation

8.3 The Lidar Transfer Function

8.3.1 Transfer of an Infinitesimal Rectangular Laser Pulse

8.3.2 The Impulsive Transfer Equation Compared with the Lidar Equation

8.3.3 How to Apply the Transfer Function

8.4 A Model of the Lidar Return from a Scattering Atmosphere

8.4.1 Background to the Model

8.4.2 Program Operation

8.4.3 Modelled Returns

8.5 Single Pulse Experiments at Methil Power Station

8.6 Comparison Between Experimental and Modelled Single Pulse Lidar Returns

8.7 Sample Time and Range Resolution

Appendices for Chapter 8

A8.1 Rayleigh Scattering Coefficients

A8.1(a) Rayleigh Scattering

A8.1(b) Rayleigh Backscatter

Chapter 1 Introduction and Review

The first chapter of this thesis is an introduction to the $XeCl^*$ excimer laser differential absorption lidar (DIAL) system for monitoring SO_2 in power station smoke plumes. The meaning of the acronyms lidar and DIAL are explained later in full. The system was developed at St.Andrews on behalf of the South of Scotland Electricity Board.

Background information on SO_2 emissions and transport and effects on the environment provide an indication as to the relevance of such a monitoring technique. Other forms of SO_2 measuring systems are reviewed as a preliminary to introducing laser optical methods as atmospheric probes and ultimately in detecting SO_2. A good summary of pollution monitoring methods is given in table 1, after a report by R.S Adrain and S.Sutton (1979) of the Central Electricity Generating Board. Finally, the DIAL laser system specific to this project is introduced, its features are described briefly and it is compared with previous types of SO_2 DIAL systems.

1.1 Sulphur Dioxide Emission and its Environmental Effects

This section is a brief review of sulphur dioxide (SO_2) and its occurrence as an environmental pollutant.

1.1.1 Sulphur Dioxide

The sulphur content of the fossil fuels, oil or coal, is oxidised upon combustion to form sulphur dioxide, a colourless, toxic gas. From the point of view of this thesis, its principle property is that it readily dissolves in water to form sulphurous acid which then slowly oxidises to sulphuric acid (Brady and Clauser, Materials Handbook, 1977).

1.1.2 Anthropogenic SO_2 Emissions

Sulphur dioxide has always been emitted naturally into the atmosphere from volcanic activity but man has added significantly to this by burning fossil fuels. The modern global sulphur cycle is given in figure 1.1.1. The most significant increase in European SO_2 emission has been in the post 1950 period, shown in the trend of figure 1.1.2.

A large proportion of atmospheric SO_2 is contributed by the burning of oil and coal. Much of the SO_2 is emitted from fossil fuelled electric power stations. The residence time of the gas in the atmosphere is about 4 days, nearly 75% being washed out by rain, nearly 25% absorbed by plants, soils and the ocean; the rest is oxidised chemically.

The effects of SO_2 on the environment have become cause for concern, especially so since the 1950's, following a correlation between the 1952 rise in the ambient London level and otherwise unattributable deaths (figure 1.1.3). Perhaps more serious than these isolated cases is the long-

term damage to lakes, vegetation and wildlife which has been observed during the past 10 years or so and partially attributed to SO_2 as a contributory factor in acid rain production.

1.1.3 Distribution and Effects of SO_2 Emissions in Europe

Before the end of the 1960's the SO_2 problem appeared to be on a local scale. That is, the gases and smoke emitted from factories and power stations were trapped beneath any inversion layer, at a height of usually less than 40m, to form a smog, creating a health risk in the vicinity of the emitters. The policy for remedial action was simply to make chimneys taller so that emission occurred above the inversion layer thus allowing dispersion and dilution of the smoke and gases away from the locality. However, the continued presence of atmospheric SO_2, according to the trend of figure 1.1.2, has led to pollution effects in places remote from areas of industrialization. Dispersion of sulphur and nitrogen oxides and their respective effects are summarized in figures 1.1.4 and 1.1.5.

The emmision of SO_2 results in the washing out of the sulphate ion in acid rain, the effects of which are the subject of present day controversy (Mellanby, 1977; Harriman and Morrison, 1980; Schreiber, 1980; Hinrichsen, 1982; Hoyle, 1982; Pearce, 1982). The acidity of the rain affects buildings, soil and water chemistry, vegetation, water supplies and ,ultimately, human health. The effects on different localities vary according to the existing resilience or buffering against the deluge of acidity. Most of Britain is able to resist much of the acidity and has therefore escaped the worst effects, these being confined to some parts of Northern Scotland (Harriman and Morrison, 1980). In Europe, parts of Scandinavia and West Germany are badly affected (Mellanby, 1977; Pearce, 1982).

Sulphur dioxide gas is poisonous to vegetation, if exposed for one hour or more to levels of just less than 1ppm (Heicklen, p.128, 1976; N.Irving Sax, 1963). At higher concentrations, human health suffers, as summarised in table 1.1.1.

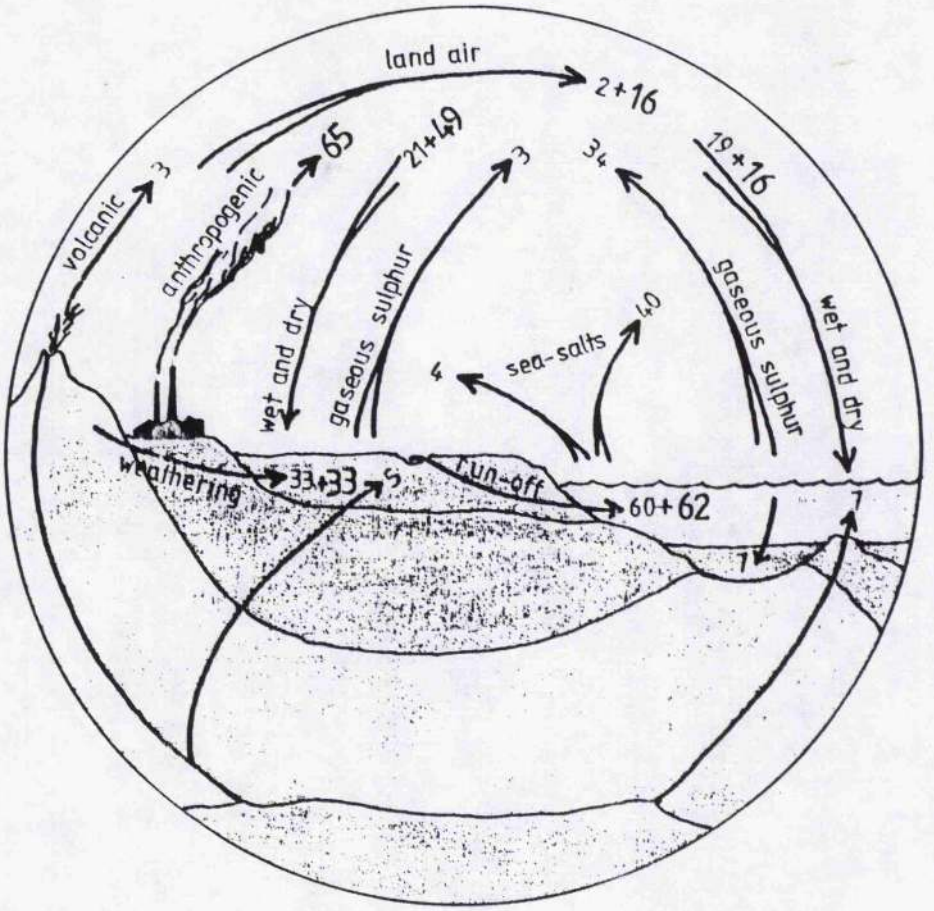

Figure 1.1.1 The global sulphur cycle. Natural flows, millions tonnes per year, are in small figures and anthropogenic flows are in large figures.

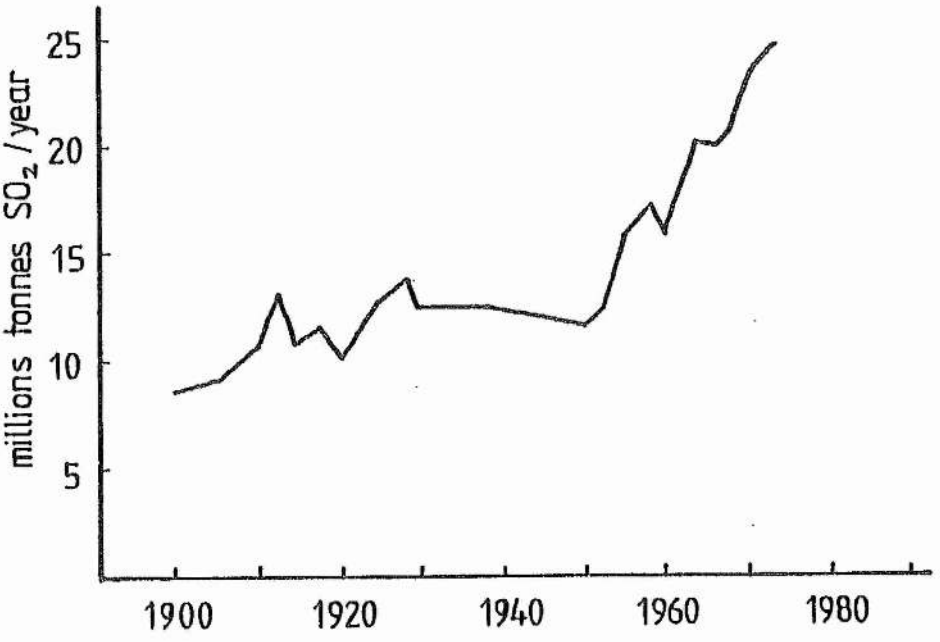

Figure 1.1.2 European anthropogenic emissions of SO_2 (as sulphur).

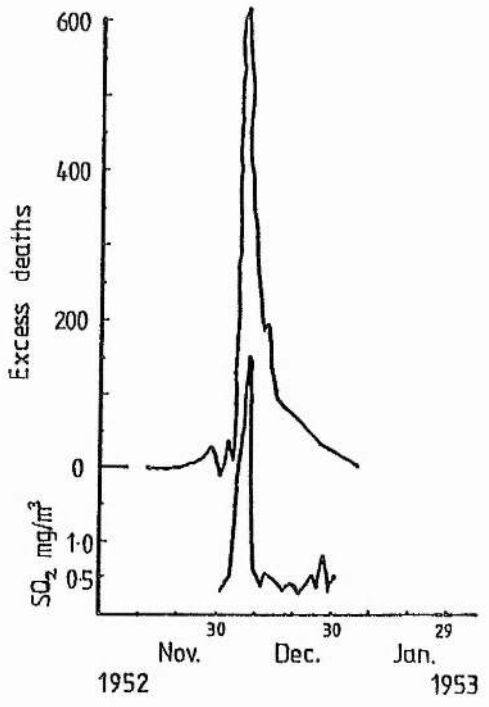

Figure 1.1.3 Deaths in London attributable to the 1952 smog. (Lowther, 1970)

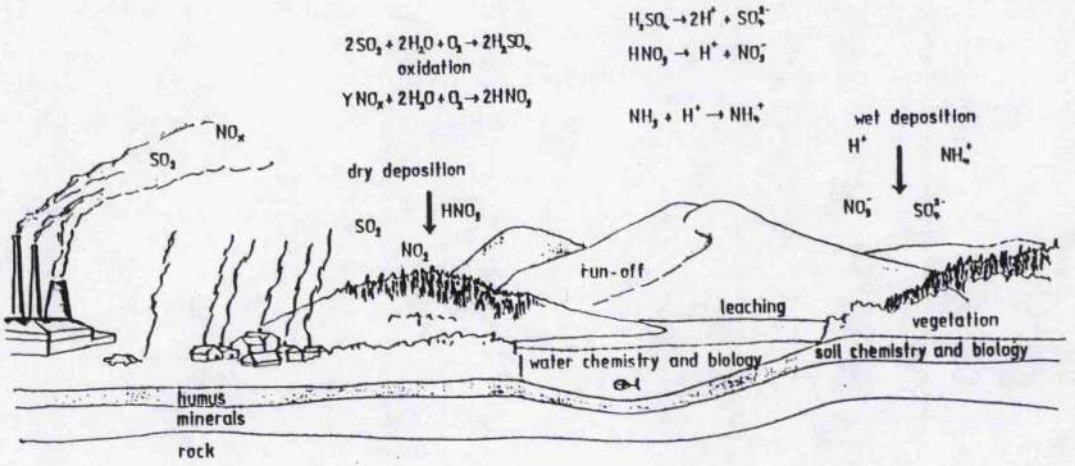

Figure 1.1.4 Transport of sulphur and nitrogen oxides.

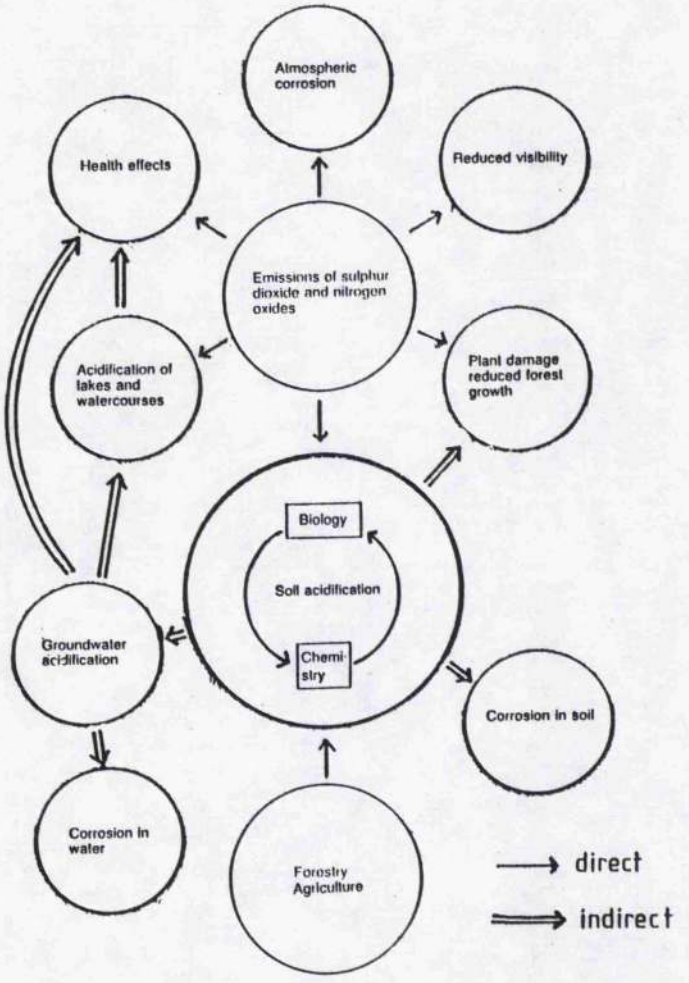

Figure 1.1.5 Environmental effects of SO_2 and NO_x emissions.

Table 1 Instruments for Pollution Monitoring
(After Adrain and Sutton, 1979)

Category	Technique	Application
Sampling	Mass spectrometry Gas chromatography Absorption spectroscopy Fluorescence spectroscopy	Samples collected by aircraft or balloons. High sensitivity (ppb) Poor spatial resolution
Long path (range integrated)	Absorption spectroscopy	High sensitivity (ppb)
	Correlation spectroscopy	ppm sensitivity but background interference
Remote detection (range resolved)	Sodar	Wind, turbulence, meteorological
	Lidar	Visibility and plume structure
	Fluorescence lidar	Low altitude
	Raman lidar	Low range sensitivity; individual pollutants identified
	Differential lidar	High (ppb) sensitivity

Table 1.1.1 Fast Effects of SO_2 on Health

Minimum effective concentration (ppm)	Effect
0.3 - 1	taste detection threshold
0.5 - 3	odour detection threshold
6 - 12	irritation of nose and throat
20	irritation of eyes
400 - 500	dangerous to life
10,000	irritation of moist skin

1.2 Methods for Measuring Sulphur Dioxide Concentration

This section refers to methods for measuring the concentration of SO_2 in air. Consideration is made of methods based on single point sampling followed by analysis and those remote sensing methods which do not employ laser radiation. The techniques may be categorised into chemical and electro-chemical and optical and radiation methods, although exceptions have been noted.

1.2.1 Chemical and Electro-chemical Techniques

Sulphur dioxide in a sample of the air is re-acted with a liquid, solid or gas re-agent which is appropriate to the method being used to analyse and determine the concentration. The resulting change in a property, attributable to SO_2, is measured and interpreted as the original SO_2 concentration in the air sample. Interfering effects from other gases are removed by filtration.

1.2.1(a) Colourimetry (De Vos et al, 1974)

The sample is bubbled through a liquid re-agent. The change in colour intensity is compared with a standard and the extent of the change is interpreted as the SO_2 concentration.

1.2.1(b) Electrical Conductivity (De Vos et al, 1974)

The sample is bubbled through diluted hydrogen peroxide to oxidise any SO_2 to sulphuric acid, creating sulphate ions. Since the level of ions dictates the electrical conductivity the resulting change in conductivity is measured to give the concentration of SO_2 in the sample.

1.2.1(c) Electrode Reaction (A Verdin,1974)

A sensor which is an electrolytic cell is introduced into a known volume of SO_2 laden air. The electrolytic cell, with its electrodes, electrolyte and potential chosen so that they are appropriate to SO_2 measurement, is used to allow reaction between SO_2 and the electrode. Measurement of the current is related to SO_2 concentration. The sensors are supplied as sealed cells with low cost and sensitivity to 1 ppm of SO_2. A particular detector for the potentiometric determination of gaseous concentrations used a solid sulphate electrolyte and platinum electrodes (Gauthier and Chamberland, 1977). Another solid state detector for hot gas analysis of SO_2-SO_3 mixtures is the electrolytic technique of Gauthier et al (1981).

1.2.1(d) Coulometric Titration

The sample is passed through a cell of a halogen electrolyte (Br_2 or I_2). The reduction/oxidation potential across the cell is dependent on the free halogen concentration which is reduced during reaction with SO_2. The difference between a fixed potential and the resulting redox potential is amplified and passed to a halogen re-generator to maintain halogen levels. At the same time the current flow is measured and interpreted to give the SO_2 concentration. The procedure is applied in flue gas measurements.

1.2.2 Optical and Radiation Techniques

Most of the monitoring instruments classified under this heading employ a technique based on absorption spectrometry or, in more developed form, in correlation spectrometry. This type of instrument is more suitable for accurate automatic sensing than the chemical and electrochemical counterparts. The technique is suitable for short path lengths over which the absorption effects can be integrated.

1.2.2(a) Absorption Spectrometry

In absorption spectrometry measurement is made of the level of radiation after it has passed through a sample of the gas with known absorption cross-section. By comparing the measurement with respect to an unattenuated reference source of the radiation the difference can be interpreted as concentration using an algorithm of the form of the Beer-Lambert exponential. The reference allows compensation for variations in pressure, temperature or volume and any for gases which may otherwise interfere with the result.

A recently reported UV absorption instrument is capable of automatic continuous measurement of SO_2, NO and NO_2 air pollutants (Izumi and Nakamura, 1981; Izumi et al, 1981). A more unusual device uses X-ray absorption spectrometry to analyse a sample in which the SO_2 content has been isolated by gas chromatography (Rudichenko and Dobrochiver, 1976).

1.2.2(b) Correlation Spectrometry

Correlation spectrometry is a development from the basic absorption spectrometry. The detected radiation, having passed through the target gas laden atmosphere, is dispersed by a grating spectrometer. The dispersed radiation is passed through a mask with slits corresponding to the spectral location of target gas absorption peaks. Measurements of the radiation intensity at the absorption features, in relation to a standard, provides the target gas concentration result. The radiation source can be skylight, earth's surface reflected sunlight or an artificial source. The technique can be used to measure ambient levels over a long integrated path or flue gas concentrations. The radiation source can be remote from the detector and correlation instrument in a closed path situation or they may be housed together for open path remote monitoring. Correlation instruments and the

differential laser lidar system described in later sections are the only methods used generally for measuring trace levels of SO_2 in the atmosphere, away from the earth's surface (Hamilton et al, 1978).

Cross-stack flue gas monitoring has been carried out using an IR correlation spectrometer, capable of measuring 100 ppm with 20% accuracy (Herget et al, 1976; Tanabe and Herget, 1976). An interesting feature of this is the gas flow used to purge the receiver and transmitter windows to ensure minimal losses in the hostile environment of the chimney. Sensing of air pollutants over a long integrated path can be done using skylight as the light source (Onderlinden and Stackeo, 1977). However, most SO_2 monitors of this type appear to use artificial radiation sources with the possibility of obtaining range information or of higher power signals (Evangelisti et al, 1977). Long path measurements averaged over 24 hours have been taken at Drax power station, Yorkshire, using an artificial light source (Sandroni and Cerutti, 1977). The detection limits achieved were 50ppb. Sources of UV radiation have been employed for trace SO_2 measurement of the atmosphere (Hamilton at al, 1978) with the UV correlation spectrometer being used to investigate SO_2 transport from power stations in conjunction with UV laser lidar, described in the sections below (Houlgate et al, 1977).

1.2.3 Mass Spectrometry

Although not generally employed as a ground based method for measuring trace SO_2 in air samples, a mass spectrometer has been used in a balloon flight to measure SO_2 levels of 30 ppm (Sagawa and Itoh, 1977).

1.3 Lidar and Laser Methods for Sensing

This section introduces the history and development of the laser as a tool for atmospheric probing with laser radar devices. The basic theory of lidar and general structure of lidar systems are described. A brief description of the methods by which atmospheric species may be detected and their concentrations measured is completed by an introduction to differential absorption lidar (DIAL), including basic DIAL theory.

1.3.1 Introduction

Previous to the advent of the laser, optical methods for detection of atmospheric gases had proved successful. Within a few years of the first laser development this intense and highly directional form of radiation was being applied even more effectively as an atmospheric probe. Laser systems developed for remote monitoring carry several advantages over single point sampling methods (Hinkley (Ed.), Melfi, Laser Monitoring of the Atmosphere, p.9).

The acronym LIDAR is derived from LIght Detection and Ranging (Middleton and Spilhaus, 1953), describing the basis of an optical remote sensing system. The ranging feature is obtained by measuring the time of flight of the light pulse to the target and back to the origin. Since the early part of the 60's lidar has been applied in ranging devices in civilian and military use, in meteorological investigation of aerosol layers, clouds, smog and temperature inversions and in wind velocimeters. The first system in lidar operation was reported in 1962 by Smullin and Fiocco who obtained return echoes from the moon, having transmitted a 550 Joule ruby laser pulse. They then applied the technique to the detection of scattering layers in the atmosphere (Fiocco and Smullin, 1963) as did Collis et al,

also using a pulsed ruby laser (Collis et al, 1964). These first experiments obtained signals which were intensity modulated by the extent of backscatter at the range of interest. Some of the lidar applications are described in a little more detail in the sub-sections below. The most significant development of lidar has been in the investigation of specific atmospheric species by virtue of the modification to the laser radiation on its interaction with those species. Such techniques are also described below, leading up to the method of DIfferential Absorption Lidar (DIAL) upon which the excimer laser DIAL system of this project is based. The single-ended lidar signal is obtained through the mechanism of backscattering by the target and atmospheric molecules or by return by a retro-reflector.

1.3.2 Lidar Equation

Propagation of a laser pulse to the atmospheric target and back to a detector, shown schematically in figure 1.3.1, is described by the lidar equation. The form of this equation applied in chapters 8 and 9 is developed in the first parts of chapter 8. However the following is a brief introduction to the accepted form of the equation, similar to that originally used in radar applications.

The lidar equation takes into account the attenuation of the laser beam by the scattering and the absorption by the solid and liquid aerosol particles and molecular constituents of the atmosphere. A correction for a preferential 180^{o} scattering is a function of the scattering coefficient. The geometric collection efficiency and optical transmission efficiencies are included. The equation has been expressed in various ways, including those forms given by Northend et al (1966), Hamilton (1969), Ahmed (1973), Byer and Garbuny (1973), Adrain et al (1979), Uchino et al (1979) and Megie

and Menzies (1980). It can be expressed as a photon current received from an element of length Δr at range r in the single wavelength, single scattering equation given by

$$n'(r) = (n_o/\tau)\,\Delta r\,\beta'(A/4\pi r^2)t_T t_R \exp[-2\int_o^r \alpha\,dr - 2\int_o^r \sigma N(r)dr] \quad s^{-1} \quad (1.3.1)$$

where n_o is the total number of transmitted photons in time τ, t_T and t_R are the transmission and reception efficiencies respectively, β' is the linear backscatter coefficient, A is the receiver area, α is the combination of the Rayleigh and Mie linear scatter coefficients, N is the number density of one absorbing species and σ is the absorption cross-section of that species. Sometimes the photon terms are replaced by power terms as in the form used in chapter 2 (Northend et al, 1966) to investigate telescope collection efficiency. The lidar equation is applied to suit different lidar purposes.

1.3.3 Lidar Equipment

The basic components of a lidar system are a pulsed laser transmitter, a telescope to collect the scattered light, a detector to convert the optical to an electrical signal and a signal processing unit which terminates in some form of output which can be related to SO_2 concentration and range.

The laser type and wavelength is selected for the particular job. The single wavelength lidar systems have used high power pulsed ruby or CO_2 lasers. Systems requiring a variation in wavelength employ tunable dye lasers pumped, for example, by a frequency-doubled Nd-YAG source. Lately, as in this work, the use of the excimer laser has proved to be promising for UV applications. Telescope design does not have such a broad range of possibilities, especially for operation in the UV where reflecting

telescopes are a necessity. In the visible and near infra-red, a lens based instrument is desirable, especially for compactness in some of the range finding systems. Detectors vary from the simple p-i-n diode and amplifier to the expensive, fast response, high gain photomultiplier tube. The detector itself may be arranged with a narrow band interference filter, polarizer or spectrometer in a detector head. All three major components are often mounted together in a transceiver head with full alt-azimuth movement. The electrical signal from the detector is passed (in the simplest case) to an oscilloscope to display voltage against time (range), or intensity modulated against range and angle of elevation (Allen and Evans, 1972). Usually the signal is passed to a storage system for later averaging and computer analysis. This type of system, including the laser triggering and sometimes the detector gain, is often operated from a central switching control. An example of a lidar system, that of Adrain et al (1979), is given in the block schematic of figure 1.5.3(b).

1.3.4 Ranging Systems

Most lidar systems possess a ranging facility based on a measurement of the flight of the pulse to and from a scattering target. However, certain items of equipment have been constructed primarily as ranging devices for surveying and for military use. The waveguide CO_2 laser has lent itself to the compact transmit/receive optics head of a rangefinder with a maximum range of several kilometres and a range accuracy of 10m. (Hulme et al, 1981).

1.3.5 Meteorological Probes for Investigation of Particulate Matter

The experiments of Fiocco and Smullin (1963) and Collis et al (1964) gave returns from atmospheric aerosol scattering layers, proving the potential for detection of smog and cloud layers (Northend et al, 1966) and the

location of temperature inversions.

Information on aerosol concentrations has been obtained by, amongst others, Northam et al (1974) and Reiter et al (1978) by taking aerosol returns in comparison to the "clear air" molecular return. The difference in the signals is uniquely attributable to the aerosol backscatter. Analytically, the lidar equation of the form of (1.3.1) is repeated for the aerosol scatter and "clear air" cases and the two equations are ratioed to relate power ratios to the aerosol coefficient, which is interpreted as a product of the cross-section and the concentration. Northam et al compared the lidar method with conventional dustsonde measurements and obtained close correlation. Reiter et al investigated the tropospheric and stratospheric aerosol with a computer controlled ruby laser lidar, using the same technique. The purpose of the experiments was to monitor aerosols in support of studies of their effects on the earth's albedo and stratospheric chemistry and the effects of natural and artificial pollutants on climate.

A more particular application of lidar in the study of aerosols is the investigation of smoke plume returns in air pollution mapping. Two systems applied in this way were reported by Allen and Evans (1972) and Cook et al (1972), both using ruby lasers and fully mobile, van mounted equipment. Allen and Evans obtained intensity modulated displays from a disk playback of recorded returns, showing a spatial representation of smoke plume dispersal and cloud formation. The work of Cook et al measured smoke plume transmittance by comparing returns from before and after the plume.

1.3.6 Detection of Atmospheric Species by Lidar Methods

A further refinement to the lidar method of atmospheric sounding is the adaption of the technique to detect and measure certain trace gases in the atmosphere and in smoke plume emissions. Three techniques exist for isolation of an individual species in remote single-ended lidar. In a single-ended system the mechanism for signal return is by a retro-reflector or suitable topographic target (eg. wall, tree), giving a result which is averaged over the entire path length. Alternatively, range resolvable returns can be obtained by distributed backscatter from molecules but especially from aerosols, specifically, water vapour and smoke, along the optical path. The distinct advantages of such a system applied to SO_2 measurements, over a gas monitor of the type described in section 1.2, is the availability of results with little delay and over a range of several kilometres. The three methods, Raman lidar, fluorescence lidar and differential absorption lidar (DIAL) are outlined below, the former two with some examples. DIAL is explained and developed more fully in the next section.

1.3.6(a) Raman Lidar

In Raman lidar, a wavelength is transmitted to excite the target molecules contained, say, within a smoke plume. Most of the radiation scattered and collected from the plume is at the original laser wavlength. However, a small proportion is shifted spectrally to another wavelength which is peculiar to the target molecule, enabling its identification. This Raman shift is dependent on the internal molecular vibration and rotation levels. The level of the wavelength shifted component is analysed and interpreted as the concentration of the target molecule. Raman scattering cross-sections are very small so the process is usually limited to measurements of high concentration at low range (Derr and Little, 1970).

Some of the first Raman lidar experiments were carried out by Kobayasi and Inaba (1970) to measure concentrations of some atmospheric gases and constituents of an oil plume. Pulses from a ruby laser at 694.3 nm were transmitted and returns received by a reflecting telescope from ranges within 200 m. A grating monochromator was used to select the Raman shifted wavelengths corresponding to the particular species. The atmospheric constituents O_2, N_2 and CO_2 were detected. In an artificially produced oil plume SO_2 and CO were detected. The Raman spectra of these gases is given (Kobayasi and Inaba, 1970) in figure 1.3.2. The theoretical detection limit of SO_2 in this case was given as 1.2 ppm at 20 m range.

In 1974 Zakharov and Torgovichev developed a mobile lidar system, using a UV dye laser source, with which they obtained stimulated Raman spectra of N_2, H_2O and CO_2 from free atmospheric returns at 100 m range. The resonant Raman spectrum of O_2 was noted from the same experiment. An artificially contaminated atmosphere gave stimulated Raman spectra of CO_2 and C_2H_4. Zakharov and Torgichev then applied the system to measurement of NO_2, H_2CO and H_2S from vehicle exhausts, including CO, CO_2, C_2H_4 and NO from a traffic environment, thus proving the value of such a remote sensing technique. Both of these latter projects detected atmospheric nitrogen amongst the other gases. Melfi (1972), using a ruby laser source, used the measurement of Raman scattering by nitrogen as a way of measuring atmospheric transmission.

It has been usual for a ruby laser or conventionally pumped dye laser to be applied as the source in Raman lidar. However, it would appear possible that the $XeCl^*$ excimer laser, the source used in this work, may be applied as a Raman lidar source if Raman scattering cross-sections of interesting

species were great enough to provide useful Raman spectra. Work on the Raman shifting of excimer wavelengths is being carried out within the laser group at St.Andrews (I.Park and A.Maitland, St.Andrews) though not with direct application to remote Raman scattering by atmospheric species.

1.3.6(b) Fluorescence Lidar

Fluorescence lidar uses a laser pulse of a wavelength which is specifically situated at the absorption peak of the target gas. The target gas molecules fluoresce over a broad band from near the laser wavelength up to the infra-red, with a spectral characteristic which is peculiar to the gas. This has similarity to the Raman method where transmission and detection equipment operate at different wavelength (Derr and Little, 1970). Measurement of the fluorescence backscatter gives a measure of gas abundance. However, the method is not easy to apply to give absolute values unless a reference molecule is used to give a relative result. The low level of fluorescence returns, in comparison with background levels, makes the method more suitable to night time operation.

The possibility of using fluorescence lidar for measuring atmospheric NO_2 concentrations has been discussed and analysed by Gelbwachs (1973) with specific regard to comparison of the method with DIAL. The conclusion was that, although DIAL overcomes the problem of acheiving greater sensitivity in the presence of daytime background, fluorescence lidar may have a role to play in clear sky night time detection of NO_2. Zakharov and Torgichev (1974) reported the strong fluorescence spectra of vapours and aerosols of diesel fuel, benzene, soil dust and industrial smoke, allowing them to be identified in an analysis of the fluorescence spectra obtained from a vehicular traffic environment at 300 to 500 m range, supplementary to a Raman study (described above) which gave signals which were weaker by 100

(stimulated Raman scattering) to 10^5 (resonant Raman scattering) times. More recently a report by Schuster and Kyle (1980) has indicated the feasibility of studying plume transport and diffusion by observing fluorescence lidar returns from a fluorescent tracer injected into the plume.

Fluorescence lidar seems to have its main application potential in observing high levels of low altitude vapours, aerosols and dusts and not in the isolation and measurement of molecular trace elements, although the latter can be achieved at low range, using a high power pulse and sensitive detection.

1.3.6(c) Differential Absorption Lidar: Introduction

Differential absorption lidar, DIAL, in contrast with previously described lidar techniques, uses two wavelengths transmitted from two lasers, from a dual line laser or from a tunable laser. The two DIAL wavelengths have different corresponding absorption cross-sections on the absorption spectrum of the target gas to be detected. Thus, in measuring the return powers from each of the two wavelengths, any difference is ascribed to the presence of the gas of interest. A distinct advantage over Raman or fluorescence lidar is that consideration of the return power ratios effectively normalises the results in eliminating effects of scatter or non-differential absorption. These are factors which cannot, by their complex nature, be predicted with sufficient accuracy.

The detailed analysis, giving the DIAL equations, including a further development in this work, is given in chapter 9 with evaluations with regard to the $XeCl^*$ laser system used in SO_2 detection. An introduction to this work is given in section 1.6. Generally, however, the DIAL analysis

starts with the lidar equation (1.3.1), applied to give return photon currents from range r as n'(r) at wavelength λ_1. The equation is repeated for wavelength λ_2 to give a return photon current n". The respective total number of output photons and the absorption cross-section is n_1 and σ_1 at λ_1 and n_2 and σ_2 at λ_2. The return pulse at λ_1 is given by

$$n'(r) = (n_1/\tau)\Delta r\beta'(A/4\pi r^2)t_T t_R . \exp[-2\int_o^r \alpha\, dr - 2\int_o^r \sigma_1 N(r)dr] \quad s^{-1} \quad (1.3.2)$$

Similarly, the pulse at λ_2 is given by

$$n''(r) = (n_2/\tau)\Delta r\beta'(A/4\pi r^2)t_T t_R . \exp[-2\int_o^r \alpha\, dr - 2\int_o^r \sigma_2 N(r)dr] \quad s^{-1} \quad (1.3.3)$$

In equations (1.3.2) and (1.3.3) the scattering terms are assumed to be equivalent where λ_1 and λ_2 are close, say within 10 nm. The absorbing gas is assumed to be unique or other absorbers are assumed to have the same absorption at λ_1 and λ_2. Equations (1.3.2) and (1.3.3) are ratioed, cancelling scatter and efficiency terms, to give

$$n'(r)/n''(r) = (n_1/n_2).\exp[-2\int_o^r (\sigma_1 - \sigma_2)N(r)dr] \quad (1.3.4)$$

The return at the range r is obtained through the sample length 2r. This allows the integral in equation (1.3.4) to be approximated to express the molecular number concentration as an average, N, over the range in the equation

$$\int_o^r N(r)dr \simeq N.r \quad (1.3.5)$$

Equation (1.3.4) is then re-arranged to give the concentration as an interpretation of the return signal power ratio, n'/n" in the DIAL

relation, given as

$$N = (-1/2r(\sigma_1 - \sigma_2)).\ln[(n'(r)/n''(r)).(n_2/n_1)] \quad m^{-3}. \qquad (1.3.6)$$

Equation (1.3.6) is a simple form of the DIAL equation for pulses, each of unique wavelength. It can be modified by a conversion, involving temperature and pressure, to give concentration in ppm (chapter 9). The quantities n_1 and n_2 provide normalization of the returns for variation between the intensities of the two pulses.

The historical development of DIAL is described in section 1.4, below. Specific cases of DIAL SO_2 detection are discussed in section 1.5.

Lidar Equation :

$$n_i(r) = \frac{n_o}{\tau} \Delta r \quad \beta'(r) \quad \frac{t_T \, t_R \, A}{4\pi r^2} \exp\left[-2\int_o^r \alpha \, dr - 2\int_r^{r+\Delta r} \sigma N \, dr\right] \quad \text{sec}^{-1}$$

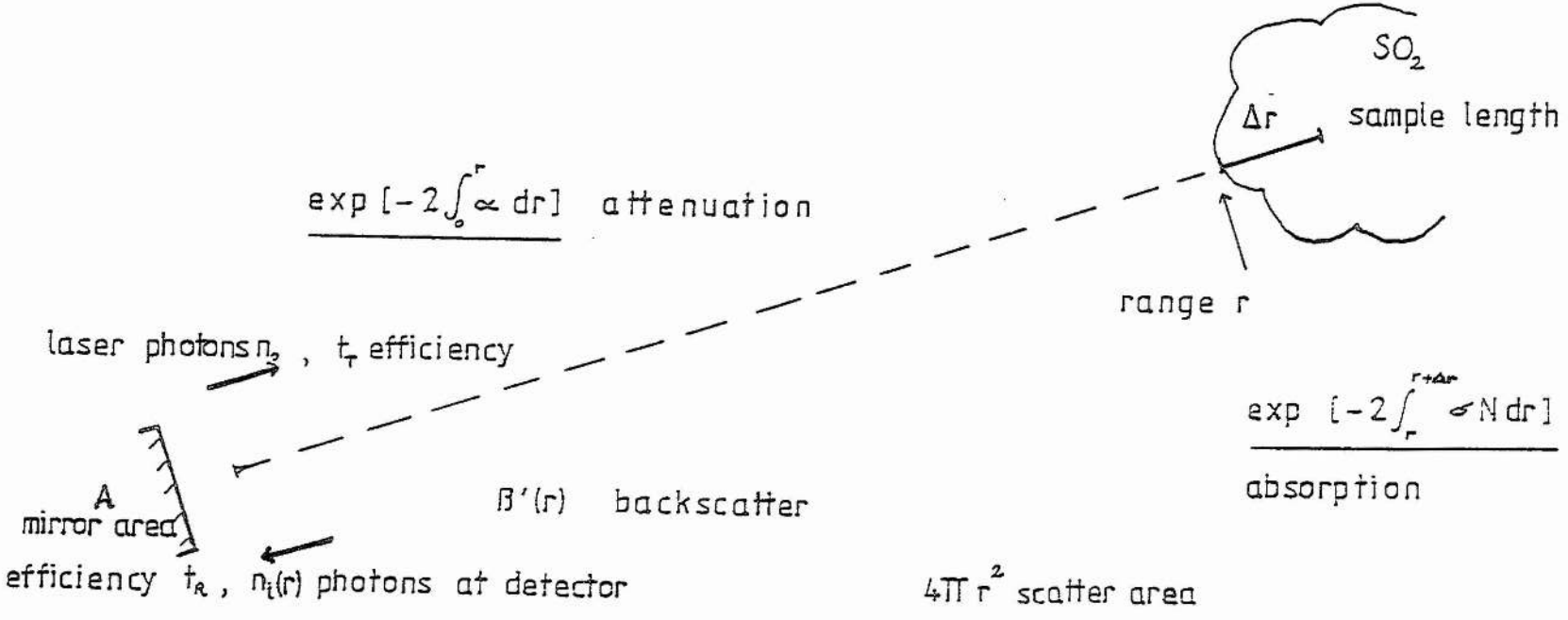

Figure 1.3.1 Representation of the lidar return from an SO_2 laden smoke target and the basic components of the lidar equation.

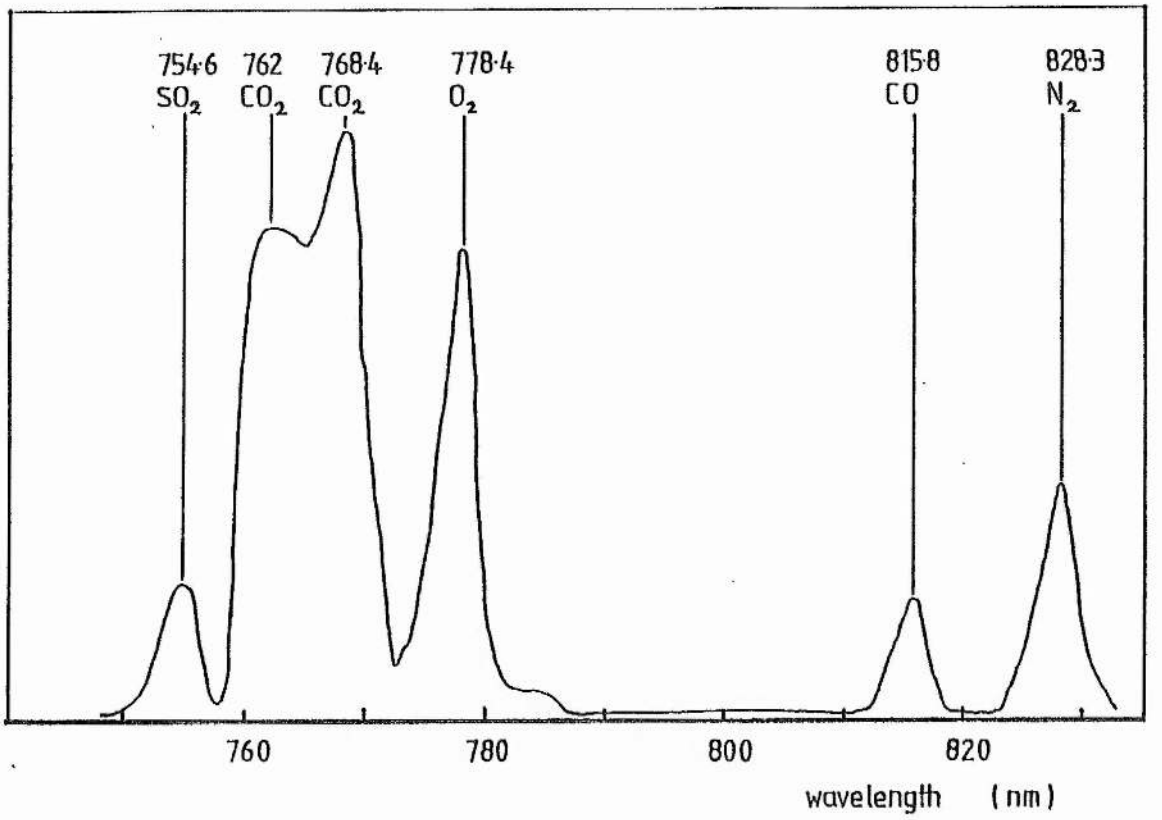

Figure 1.3.2 Raman spectra of SO_2, O_2, N_2, CO_2 and CO, detected with a ruby laser Raman lidar at 694.3 nm.
(Kobayasi and Inaba, 1970)

1.4 DIAL Development

1.4.1 Feasibility Studies and Predicted Success of DIAL (Referred)

The feasibility of DIAL has been the subject of analysis ever since the idea was hinted at by Reagan (1968). At first the analyses considered the return signal from over the entire detected range in a long path monitoring system. For instance, Hanst and Morreal (1968) referred to a method of air pollutant measurement using absorption of IR radiation from an artificial source. Kildal and Byer (1971) reviewed and compared lidar methods and, after a feasibility study of long path sampling, concluded that DIAL offers the best detection sensitivity. Such long path methods were applied later to measurements of SO_2 by Kuhl and Spitschan (1975) and Gibson and Thomas (1975) who used a UV laser in the region 297-308 nm. However, spatial resolution of target gas concentration, useful for pollution mapping, has been the usual application for DIAL systems.

In comparing lidar methods for monitoring free atmospheric gases, a major feasibility investigation of DIAL, by Measures and Pilon (1972), considered the possible application of a tunable dye laser, offering the selection of a wavelength which is most suitable to the technique used and to the particular target gas. The DIAL, Raman scattering and fluorescence scattering techniques were compared for SO_2 detection and spatial mapping. The conclusion was that DIAL is more suitable, as regards range and sensitivity, than Raman scattering; the fluorescence method may be useful at night time if a high laser power is used for low range (<500m) operation. DIAL sensitivity to SO_2 was predicted to be less than 0.1 ppm for a 6m range element (0.6 ppm.m) at ranges up to a few kilometres. However, the reduction in long range sensitivity to higher concentrations, due to increased signal absorption, was shown to reduce the range of, say,

a measurement of 10 ppm (6 ppm.m) to within about 1 km. DIAL studies for NO_2 and CO_2 have been made by Byer and Garbuny (1973), Gelbwachs (1973) and Vanin et al (1976). Expected sensitivities to NO_2 of 1ppm.m have been reported.

1.4.2 DIAL Experiments in Application to Gas Studies

Concentrations of trace gases such as NO, NO_2, N_2O, H_2O, CH_4, CO_2, SO_2 and O_3 have been measured in DIAL experiments, summarised in table 1.4.1. One of the earliest applications of DIAL to studies of smoke or steam plumes is that of Granatstein et al (1973) who simulated a steam plume containing CH_4 and CO_2, which they measured by the DIAL technique using backscatter of HeNe radiation from the water droplets. The HeNe laser was tuned between 3.391 μm, an absorption line of CH_4, and 4.217 μm, an absorption line of CO_2, by using a rotating prism as one of the cavity ends. The experiments supported the idea of DIAL for remote sensing of smoke plume pollutants.

An advantage of DIAL is that it allows sensing of pollutants which are located at a situation which is remote from the transmission/detection equipment. This aspect was the basis of experiments from 1974, starting with tunable dye laser systems applied at wavelengths between 440 nm and 470 nm to NO_2 (Grant et al, 1974; Rothe et al, 1974) and a UV source applied to SO_2 and to O_3 (Grant and Hake, 1975). The experiments of Grant et al and Grant and Hake were calibrated remote measurements in that the monitored gas was contained within a sample chamber situated a few hundred metres away. The mechanism for the return signal was backscatter obtained from aerosols and molecules behind the chamber. Such experiments demonstrated the feasibility of measuring free atmospheric SO_2.

The first report of remote sampling of a truly free gas was given by Rothe

et al (1974), who operated a tunable dye laser source to detect NO_2 concentrations down to 0.2 ppm over Cologne, at ranges within 4 km.

The first infra-red DIAL system, using a grating tuned CO_2 TEA laser source, was applied to measurements of atmospheric water vapour (Murray et al, 1976) at ranges up to 12 km. Murray et al suggested the application of CO_2 laser wavelengths to DIAL monitoring of O_3, SO_2, NH_3, freon 11, freon 12, freon 113, vinyl chloride, ethylene and methanol, although UV is more suitable for SO_2 and O_3 measurements. Another system applied to water vapour measurements, using a dye laser, utilised the water vapour absorption band at 590 nm (Vanin et al, 1976). Although only the water vapour experiments were reported this particular system was designed as a universal lidar for operation in DIAL, Raman scatter lidar, fluorescence lidar and other modes.

Of relevance to this work is the application of DIAL to the measurement of SO_2 emitted in power station smoke plumes. Tunable, frequency doubled dye laser systems have been applied to measure SO_2 levels near to power station chimneys and to investigate the long range dispersion (Hoell et al, 1975; Adrain et al, 1979; Hawley, 1981). More detail of SO_2 studies is given in section 1.5.

Although the dye laser has been the principal source for DIAL techniques other lasers have been used in the detection of different gases. For example, the HeNe laser was applied to measurement of CH_4 and CO_2 (Granatstein, 1973), the CO_2 laser was applied to water vapour studies (Murray et al, 1976) and to NO measurements (Menyuk et al, 1980) and a DF laser DIAL has measured atmospheric N_2O (Altmann et al, 1980). Recent development of the family of excimer lasers (see chapter 4), producing high

powered UV pulses, has provided another source for lidar. The $XeCl^*$ excimer laser has already been used (Uchino et al, 1979) to observe stratospheric ozone by a method based on DIAL, although atmospheric scattering properties were quantified by other means. Uchino et al reviewed the possibilities for applying excimer lasers to lidar monitoring of the upper atmosphere. The $XeCl^*$ excimer laser is relevant in this thesis as the source for the SO_2 DIAL system under consideration.

Table 1.4.1 DIAL Experiments in Application to Gas Studies

Investigator	Radiation	Gas and Situation
Kreuzer and Patel 1971	I.R	NO; lab. sample cell
Granatstein et al 1973	HeNe laser 3.391 m and 4.217 m	CH_4, CO_2; lab. steam plume
Rothe et al 1974	Tunable dye laser 455nm and 470nm	NO_2; free, remote
Grant et al 1974	Tunable dye laser 440nm and 450nm	NO_2; remote sample cell
Grant and Hake 1975	Tunable dye laser 292.3nm and 293.3nm 292.3nm and 294.0nm	SO_2; remote sample cell O_3; remote sample cell
Murray et al 1976	I.R CO_2 laser around 10.3 m	H_2O; free, remote
Vanin et al 1976	Tunable dye laser about 590nm	H_2O; free, remote
Adrain et al 1979	Tunable dye laser 300.1nm and 299.5nm	SO_2; free, remote
Uchino et al 1979	$XeCl^*$ excimer laser 307.9nm and 308.2nm	O_3; free, remote
Menyuk et al 1980	I.R CO_2 laser around 5.3 m	NO; free, remote
Altmann et al 1980	DF laser 3.85 m and 3.89 m	N_2O; free, remote
Hawley 1981	Tunable dye laser 299.32nm and 300.04nm	SO_2; free, remote

1.5 Differential Absorption Lidar (DIAL) for SO_2 Monitoring

This section concentrates on some previous applications of DIAL to SO_2 monitoring. It describes laser sources and wavelengths and their relation to SO_2 absorption spectra. It indicates the form of presentation of information on SO_2 concentration and dispersal and the measurement sensitivity. Particular reference is made to the remote sample chamber DIAL experiments of Grant and Hake (1975) and the mobile remote DIAL systems reported by Adrain et al (1979) and Hawley (1981)(SRI International), all using tunable dye lasers as the probe source. Details of these works are summarised in table 1.5.1.

1.5.1 SO_2 DIAL Systems

The dual wavelength DIAL method explained in sub-section 1.3.6(c) is applied to SO_2 detection by selecting two wavelengths so that a difference exists between the corresponding absorption cross-sections. This is illustrated in the vibrational absorption spectrum of SO_2 in figure 1.5.1 where the two wavelengths are shown at 299.5 nm at an absorption trough and at 300.1 nm at an absorption peak. The wavelength variation used by Adrain et al in a flashlamp pumped rhodamine dye laser was by an intra-cavity birefringent filter (birefringent filters are described in chapter 5) before frequency doubling to around 300 nm with an intra-cavity ADP (ammonium dihydrogen phosphate) crystal.

The system reported by Hawley (1981), used two tunable dye lasers, each pumped by the 2nd harmonic of a Nd-YAG laser. The wavelengths, stated as 299.32 nm at the trough and 300.04 nm at the peak, are indicated on the SO_2 absorption spectrum in figure 1.5.1.

Grant and Hake (1975) suggested the use of two dye lasers for near simultaneous (within 1 ms) pulse transmission, as an improvement on the single tunable laser system operated at 292.3 nm and 293.3 nm.

Differential lidar return signals are obtained at the detector as a function of range, appearing as a function of time on an oscilloscope trace. The typical form of differential pulse pair returns are shown in the two traces of figure 1.5.2 (Adrain and Sutton, 1979). The low range higher intensity returns are attributed to near field scatter from the atmosphere. The later, lower level pulses are obtained via backscatter from a smoke plume. In places where the plume contains SO_2 the difference in the extent of the absorption between the two wavelengths creates a return signal level differential, the weaker signal being at a wavelength corresponding to the absorption peak on the SO_2 spectrum (figure 1.5.1). The difference, expressed as a signal intensity ratio, is interpreted according to an algorithm of the form of equation (1.3.6) as SO_2 concentration averaged over the range r. An elaboration on equation (1.3.6), described in chapter 9, shows how consideration of another pulse pair but from range $r + \Delta r$ allows range resolved measurements of the target gas. The element Δr is determined by the spatial length of the laser pulse and the bandwidth of the signal measuring system.

Signal handling and control equipment in the three examples of SO_2 DIAL systems have been described by Grant and Hake (1975), Adrain et al (1979) and Hawley (1981),(1979). Two of these systems are illustrated in the system schematics reproduced in figures 1.5.3(a) and (b). All the systems use photomultiplier detection of return pulses followed by analogue to digital conversion and storage on magnetic tape/disc or in computer memory. The level of sophistication of the analytical devices varies from the basic

real-time oscilloscope trace and storage in the Grant and Hake system to the computer based signal retrieval, averaging and data presentation described by Adrain et al and Hawley (1979). Additional features include monitoring and recording of laser output energy for pulse normalization and computer control of laser and detector switching.

Once obtained, the concentration value from any particular sample element can be taken as a result on its own. However, the ranging aspect of lidar, given time of flight measurements, allows SO_2 concentration distribution to be mapped along the propagation direction of the laser pulse. By varying the laser/receiver in altitude and azimuth it is possible to map the spatial distribution of SO_2 in all dimensions. It has been more useful, however, to consider sections (2 dimensions) through the atmosphere, each in a vertical or a horizontal plane. A report by Hawley (1981) shows a horizontal ground level scan taken at five azimuth angles, giving SO_2 concentrations around a power station chimney; this is reproduced in figure 1.5.4.

1.5.2 SO_2 DIAL Sensitivity

Measurement sensitivity in DIAL depends on many factors including the accuracy of cross-section data, tuning accuracy, laser output energy variations etc..

Differentiation of equation (1.3.6) gives the concentration uncertainty ΔN as a function of signal ratio uncertainty $\Delta(n'/n'')$ in the expression

$$\Delta N / \Delta(n'/n'') = -1/2r(\sigma_1 - \sigma_2)(n'/n'') \qquad (1.5.1)$$

which shows how the integrated range, r, is likely to affect the

concentration error. In range resolved DIAL measurements, analysed in sections 9.4 and 9.7, the range element Δr appears in the denominator of the concentration error expression of the form of (1.5.1). The sensitivity of a range resolved DIAL system to SO_2 concentration is best described by the lowest useful value product of the SO_2 concentration and range element, expressed in units of ppm.m. DIAL system (Grant and Hake, 1975; Adrain et al, 1979; Hawley, 1981) sensitivites are listed in table 1.5.1. In any DIAL system a strong signal from a short range target gives a greater sensitivity by virtue of the greater S/N ratio. Thus, the maximum range from which measurements can be made is dependent on the requirement of lower detection limit.

The detection limits of the SO_2 DIAL systems are of the order of magnitude which would allow detection of ambient atmospheric SO_2 concentrations, at about 0.01 ppm in the rural environment and 0.01 to 0.3 ppm in the urban environment (Collis and Russell, 1976).

The references to previous SO_2 DIAL systems show the factors (absorption cross-section, range return element and number of pulses averaged) which influence sensitivity to SO_2 concentration. The variation in some of these factors is considered and evaluated in the theoretical treatment of the $XeCl^*$ excimer laser DIAL system, given in chapter 9. The detection sensitivities given in the examples in table 1.5.1 are listed in table 11.2.1 in comparison with the theoretical sensitivity of the $XeCl^*$ laser DIAL system.

1.5.3 Latest SO_2 DIAL Systems

Recent SO_2 DIAL systems are listed in table 1.5.2, where all the entries are referred to in the proceedings of the 12th International Laser Radar Conference, 1984. Further development is being undertaken on SO_2 DIAL by, mainly, European users. Most of the systems are mobile and some are reported to be sensitive to 0.015ppm at a few kilometres range. The sensitivities and reported performance of these systems are comparable with the examples given in table 1.5.1. Thus, no significant improvements appear to have been made to SO_2 DIAL systems over the last four or five years.

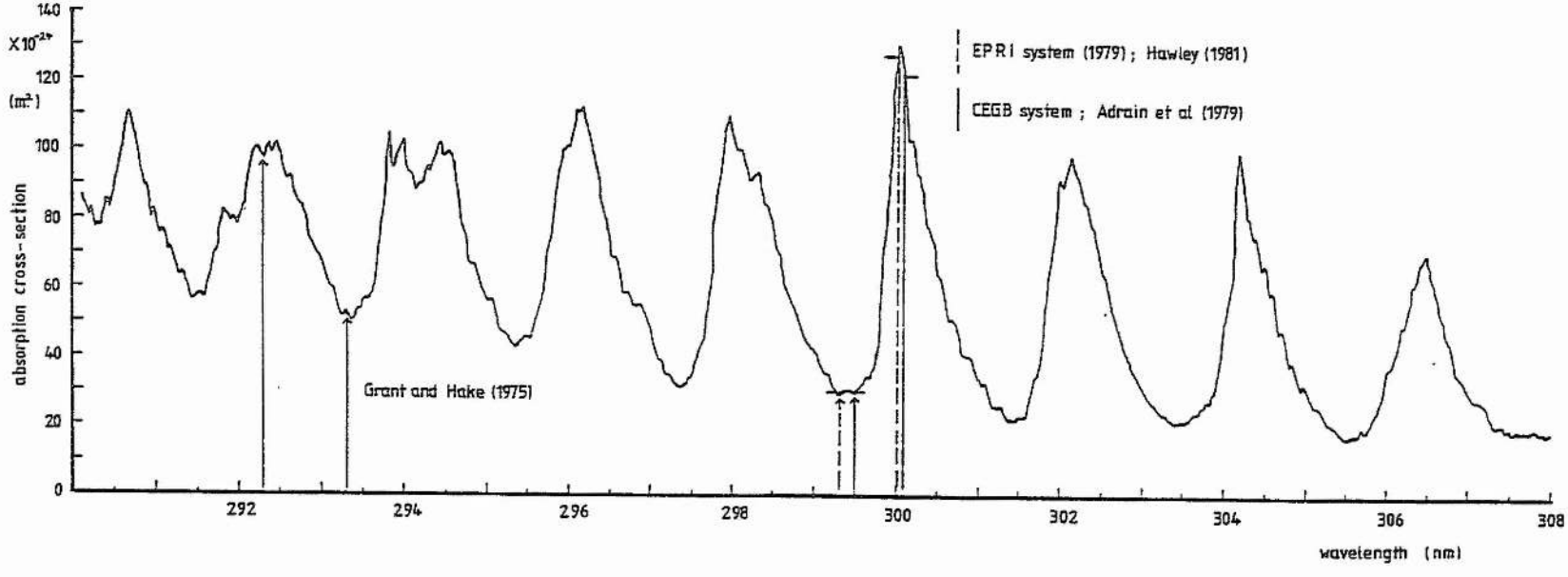

Figure 1.5.1 Absorption spectrum of SO_2 (Brassington, 1981) showing the DIAL wavelengths employed in three systems.

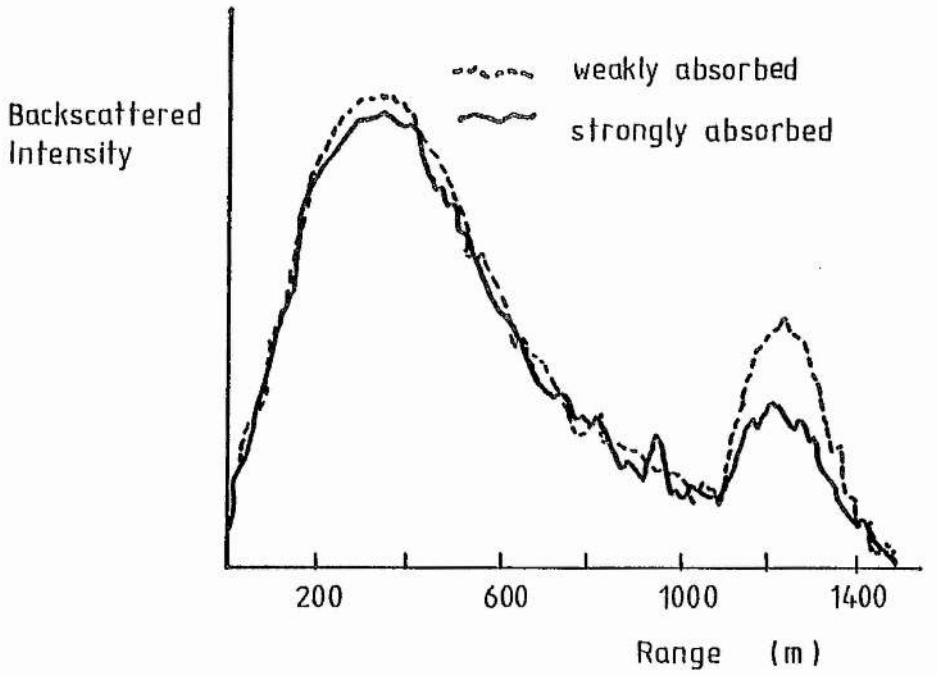

Figure 1.5.2 Differential pulse pair returns, after Adrain and Sutton (1979).

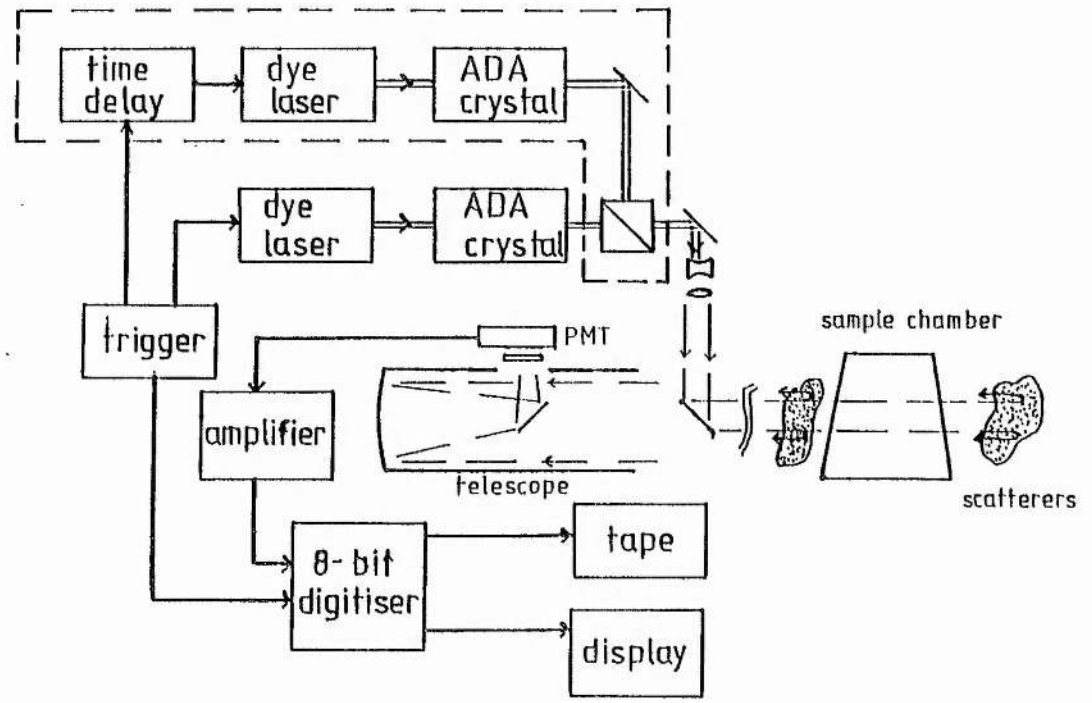

(a)

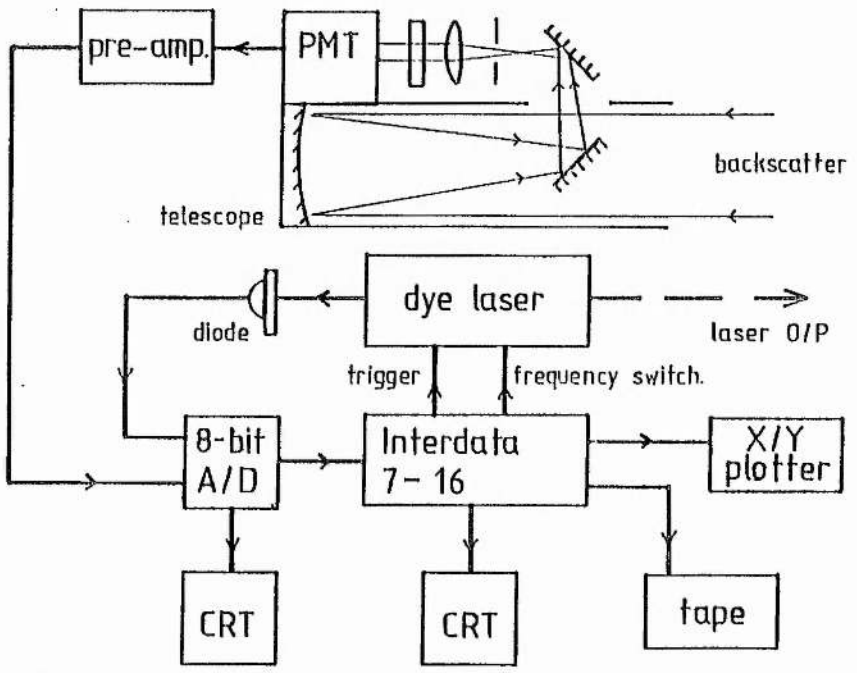

(b)

Figure 1.5.3 SO_2 DIAL system block diagrams from
(a) Grant and Hake (1975)
(b) Adrain et al (1979)

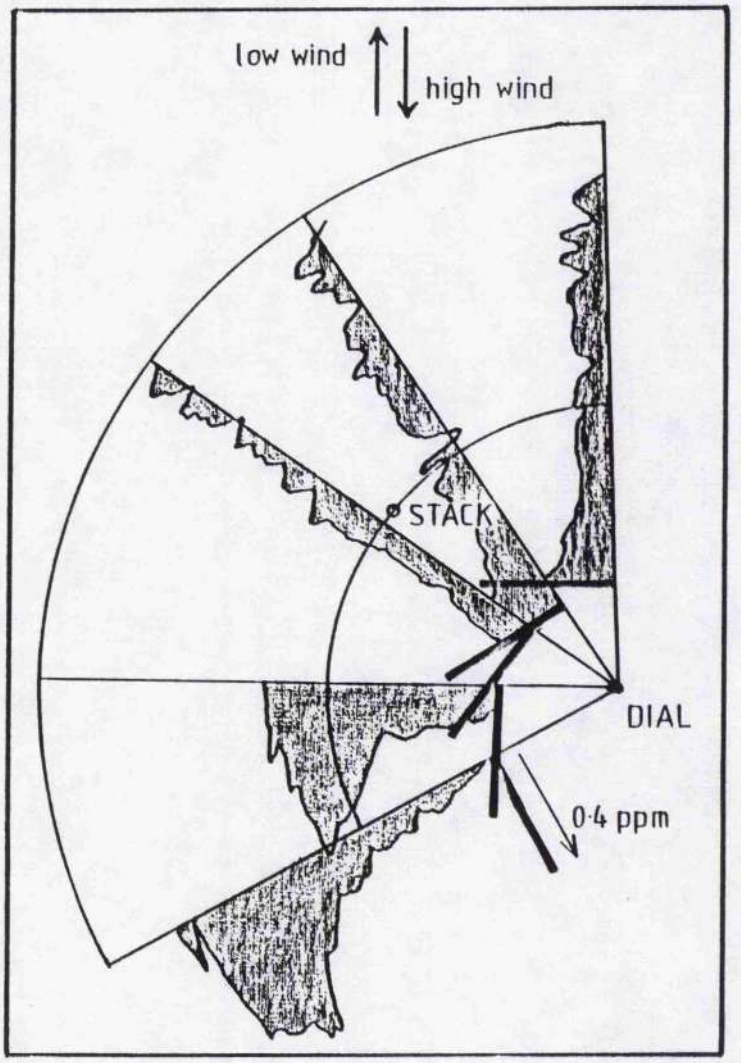

Figure 1.5.4 Ground level scan of SO_2 dispersal, measured by the EPRI system. After Hawley (1981).

Table 1.5.1 DIAL Experiments for SO_2 Monitoring (3 references)

Investigator	Laser	Receiver/Detector	SO_2 Absorption X-section ($X10^{-24}$) (Brassington, 1981) $_1(m^2)$	$_2(m^2)$	Pulse Pairs Averaged	Detection Sensitivity Theoretical	Experimental
Grant and Hake 1975	Rhodamine 6G dye laser, frequency doubled by non-linear crystal and tuned between 292.3nm and 293.3nm 0.75mJ, 200ns pulse @ 0.017 pps	0.056m^2 collection area Filter @ 293nm, 13nm fwhm, 17% peak transmission RCA 7200 PMT	53 @ 293.3nm	99.5 @ 292.3nm	8	10 ppm.m 0.1ppm in 100m sample @ 300m range from remote SO_2 chamber	60 ppm.m 0.6ppm in 100m sample @ 300m range from remote SO_2 chamber
Adrain et al 1979	Flashlamp pumped rhodamine 6G dye laser tuned by intra-cavity birefringent filter to 600nm and frequency doubled by non-linear ADP crystal. Tuned between 300.1nm and 299.5nm 0.1mJ, 1μs pulse @ 25 pps	0.03m^2 collection area Filter @ 300nm, 10nm fwhm, 20% peak transmission EMI 9789 QB PMT	30 @ 299.5nm	121 @ 300.1nm	200	3 ppm.m 0.02ppm in 150m sample @ 2km range free remote gas	10.5 ppm.m 0.07ppm in 150m sample @ 1km range free remote gas
Hawley 1981	2 Nd-YAG lasers, each frequency doubled by ADA crystal, pumping rhodamine 6G and coumarin 2 dye laser, respectively, followed by ADA crystal frequency doubling to 299.32nm and 300.04nm. 10mJ, 10ns pulse @ 10 pps	0.175m^2 collection area	30 @ 299.32nm	127 @ 300.04nm	100	10 ppm.m 0.05ppm in 200m sample @ 1.5km range free remote gas	

Table 1.5.2 Latest SO_2 DIAL Systems (1984)

Users	Laser	Sensitivity	System
C Cahen Electricite de France	Tunable dye laser		Mobile
R Capatini et al France	Quantel (500mJ) pumping Quantel Rh.8 dye laser 300.01nm and 299.65nm 12mJ, 10Hz		Semi- mobile
H G Edner et al Sweden	Nd-YAG pumping dye laser		Mobile
R M Hoff Canada	Ruby laser (used with COSPEC)		Mobile
A Marzorati Italy	Nd-YAG (2nd harmonic) pumping dye laser Grating/prism tuned 300nm, 10mJ	0.05ppm $\leq$3km range Δr= 15-200m	Mobile
B W Joliffe et al Britain	2X Nd-YAG dye lasers Near simultaneous emission of DIAL pulses 10-20mJ, 10Hz		Mobile
W Staehr et al W.Germany	2X flashlamp-pumped Candela SSL 500 dye lasers (Rh.6G) 10-60mJ 296.17 and 297.35nm	0.015ppm $\leq$3km range Δr=300m m=120	Fixed

1.6 Excimer Laser DIAL for SO_2 Monitoring

The final target for this work was to provide the South of Scotland Electricity Board with a mobile system for remote detection of SO_2 contained within fossil fuelled power station smoke plumes, using a Differential Absorption Laser Lidar technique based on that described in sections 1.3.6(c), 1.4 and 1.5. SO_2 DIAL systems constructed by previous workers (see section 1.5, table 1.5.1) have been succesful in measuring SO_2 levels down to urban trace quantities (0.02 ppm, Adrain et al, 1979). These systems, developed by CEGB (Adrain et al, 1979) and by EPRI (Hawley, 1979, 1981) have "clean air" sensitivity but are bulky. In each, the laser source has been one or two tunable dye lasers, involving pumping of a dye then tuning followed by frequency doubling by non-linear crystal to give the two desired UV wavelengths. The system described here is based on a transverse electric discharge $XeCl^*$ excimer laser giving direct, single stage high power pulse generation of two UV wavelengths. The $XeCl^*$ lasing spectrum and the corresponding region of the SO_2 absorption spectrum are shown in figures 1.6.1(a) and (b).

In theory, the sensitivity of this $XeCl^*$ laser system is down by a factor of 10 (cf. Table 1.5.1) on a tunable dye laser system, the price expected for the simplicity and its attendant advantages.

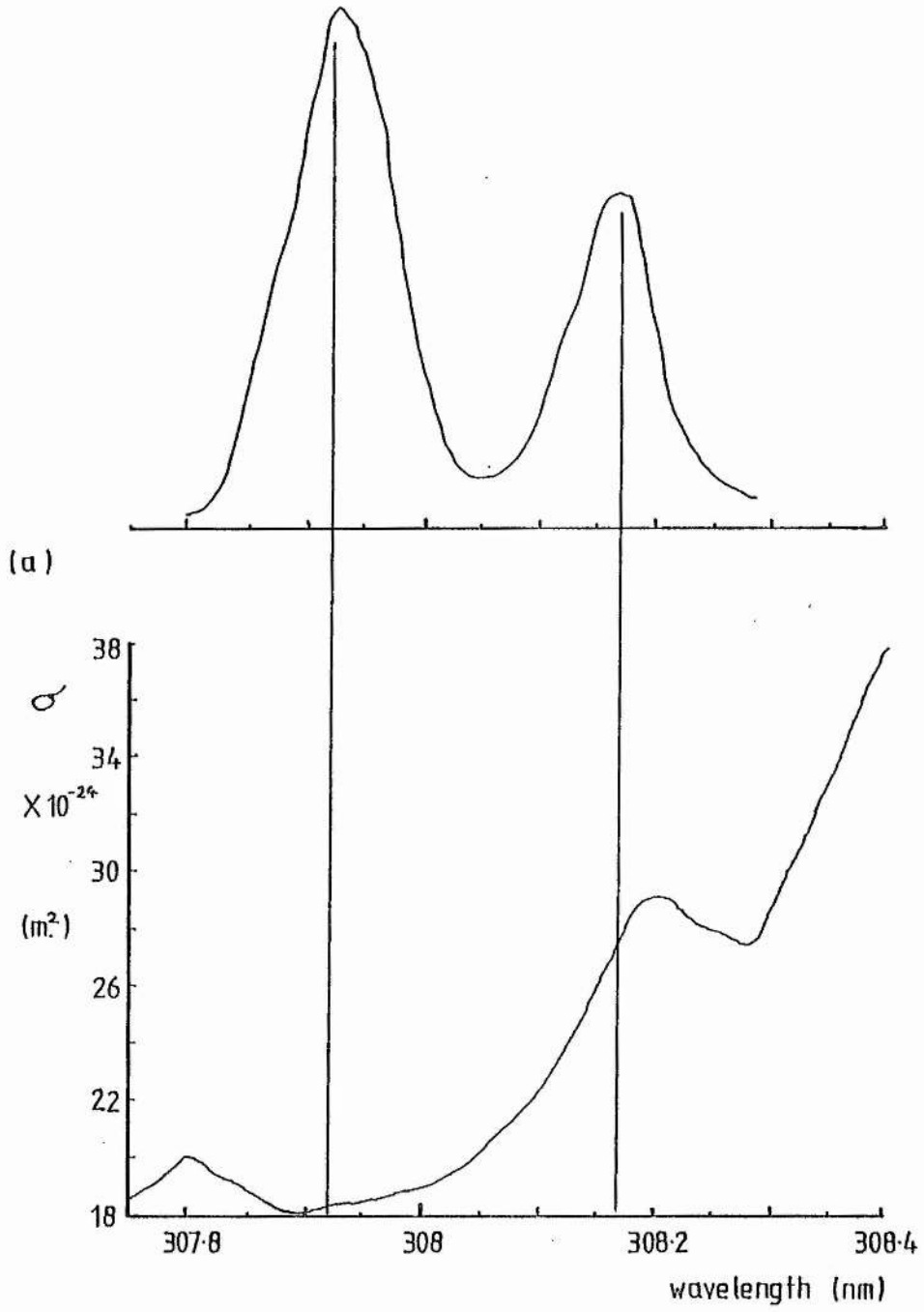

Figure 1.6.1 Relation between (a) the $XeCl^*$ lasing spectrum (chapter 4) and (b) the SO_2 absorption spectrum around 308 nm, after Brassington (1981).

1.7 State-of-the-art Excimer Laser Lidar

This section summarises the present (1984) application of excimer lasers to lidar systems for atmospheric measurements. All references apply to the proceedings of the 12th International Laser Radar Conference, 1984. Table 1.7.1 lists the applications. Their main use is in ozone measurements by the DIAL technique, where the reference wavelength is usually supplied by another type of laser. However, Werner at al have reported the use of a $XeCl^*$ laser as the single source for ozone measurements, using Raman shifting in CH_4 and H_2 cells to provide the DIAL reference wavelength. McDermid et al have designed a fluorescence lidar system for tropospheric hydroxyl measurements, based upon a $XeCl^*$ laser which is tuned by three air-spaced etalons contained in a pressure vessel. A single excimer laser source is more widely used in Raman or fluorescence lidar systems. No report has been made of a $XeCl^*$ laser as the single source in DIAL SO_2 concentration measurements.

Table 1.7.1 Application of Excimer Lasers to Lidar

Users	Laser	Application and Features
I I Ippolitov et al	KrF^* 248.5nm 30mJ, $\leq$5Hz	Raman scattered detection of C_6H_6, C_2H_4, CH_3OH (268 - 270 nm) Possible interference from broad-band fluorescence
I S McDermid et al	$XeCl^*$ oscillator-amplifier, tuned over 307.6 - 308.4 nm by three air-spaced etalons in a pressure vessel 100mJ, 25Hz	Tropospheric hydroxyl measurement by fluorescence
J Pelon and G Megie	$XeCl^*$ Treated as single line Reference wavelength from 3rd harmonic of Nd-YAG at 355nm	Tropospheric and stratospheric ozone measurements above 25km
L Pokora and S Kalisti	$XeCl^*$ Home-built with Blumlein circuit	Laser design stage only Possible O_3 DIAL application
J Werner et al	$XeCl^*$ (Lambda Physik EMG 102E, 150mJ, $\leq$100Hz) Treated as single line Reference wavelength from Raman shifting in CH_4 and H_2 cells	Stratospheric ozone layer Simultaneous emission of DIAL pulses
V E Zuev et al	$XeCl^*$ Reference wavelength from N_2 at 337nm or from $XeBr^*$ at 281.8nm	Stratospheric ozone DIAL (10 - 40 km)

References for Chapter 1

Adrain R.S and Sutton S; Differential lidar - a new technique for atmospheric pollution measurement, CEGB Research, November (1979)

Adrain R.S, Brassington D.J, Sutton S, Varey R.H; The measurement of SO_2 in power station plumes with differential lidar, Opt. and Quantum Electron. 11, 253-264, (1979)

Ahmed S.A; Molecular air pollution monitoring by dye laser measurement of differential absorption of atmospheric elastic backscatterers, Appl.Opt., 12, 4, April (1973)

Allen R.J and Evans W.E; Laser radar (LIDAR) for mapping aerosol structure, Rev.Sci.Instrum., 43, 10, October (1972)

Altmann J, Lahmann W, Weitkamp C; Remote measurement of atmospheric N_2O with DF laser lidar, Appl.Opt., 19, 20, 3453, 15 October (1980)

Bowen H.J.M; Natural Cycles of the Elements and the Perturbations by Man; Environment and Man, vol.6; The Chemical Environment, Ed.Lenihan and Fletcher

Brady and Clauser; Materials Handbook, M^{c}Graw Hill, (1977)

Brassington D.J; Tunable dye laser measurement of the SO_2 absorption spectrum between 290 and 317nm, RD/L/2055N81, Job.No. VC299, CERL, June (1981)

Brassington D.J; Sulphur dioxide absorption cross-section measurements from 290nm to 317nm, Appl.Opt., 20, **21**, 1 November (1981)

Byer R.L and Garbuny M; Pollutant detection by absorption using Mie scattering and topographic targets as retroreflectors, Appl.Opt., 12, 7, 1496, July (1973)

Cahen C; Lidar Measurements of Atmospheric Pollution, Proc. 12th International Laser Radar Conference, Aix-en-Provence, France, 13-17 August (1984)

Capatini R, Ancellet G, Megie G, Pelon J and Renaut D; DIAL Lidar Measurements of Atmospheric Pollutants (SO_2,O_3) During the Fos-Berre '83 Experiment, p.269, Proc. 12th International Laser Radar Conference, Aix-en-Provence, France, 13-17 August (1984)

Collis R.T.H and Russell P.B; Lidar measurements of particles and gases; Laser Monitoring of the Atmosphere, Ed. E.D Hinkley; Topics in Applied Physics vol.14, Springer-Verlag

Collis R.T.H et al; Laser radar echoes from the clear atmosphere, Nature, 203, 508, 1 August (1964)

Collis R.T.H et al; Laser radar echoes from a stratified atmosphere, Nature, 203, 1274-1275, September (1964)

Cook C.S, Bethke G.W, Conner W.D; Remote measurement of smoke plume transmittance using lidar, Appl.Opt., 11, 8, 1742, August (1972)

Derr V.E and Little C.G; A comparison of remote sensing of the clear atmosphere by optical, radio and acoustic radar techniques, Appl.Opt., 9, 9, 1976, September (1970)

De Vos et al, The Pollution Reader, (1974)

Edner H G, Egeback A-L, Hertz H M, Fredriksson K A, Sunesson J A, Svanberg S R, Uneus L P, Wendt E W; Development and Applications of DIAL Systems, p.257, Proc. 12th International Laser Radar Conference, Aix-en-Provence, France, 13-17 August (1984)

Evangelisti F, Giovanelli G, Orsi G, Tirabassi T, Vittori O; A mask correlation remote sensor for in situ measurement of SO_2 optical depths on long light source-instrument distances, 24th Congresso Internazionale per l'Elettronica, Rome, Italy, 28-30 March (1977), p.123-30

Fiocco G and Smullin L.D; Detection of scattering layers in the upper atmosphere (60-140km) by optical radar, Nature, 199, 1275-1276, September (1963)

Gauthier M and Chamberland A; Solid state detectors for the potentiometric determination of gaseous oxide concentrations, J.Electrochem. Soc.(USA), 124, **10**, 1579-83, October (1977)

Gauthier et al; Hot gas analysis of SO_2-SO_3 mixtures, J.Electrochem.Soc. (USA), 128, 2, 371-8, February (1981)

Gelbwachs J; NO_2 lidar comparison: fluorescence vs. backscattered differential absorption, Appl.Opt. 12, 12, 2812, December (1973)

Gibson and Thomas; Nature, 256, 561, (1975)

Granatstein V.L, Rhinewine M, Fitch A.H; Remote sensing of gas concentrations in smoke stack emissions, Appl.Opt., 12, 7, 1511, July (1973)

Grant W.B, Hake R.D Jr., Robbins R.C, Liston E.M, Proctor E.K Jr.; Calibrated remote measurement of NO_2 using the differential absorption backscatter technique, Appl.Phys.Lett. 24, 11, 550, 1 June (1974)

Grant W.B and Hake R.D; Calibrated remote measurement of SO_2 and O_3 using atmospheric backscatter, J.Appl.Phys., 46, 7, 3019, July (1975)

Hamilton P.M, Varey R.H, Millan M.M; Remote sensing of SO_2, Atmos.Environ. (GB), 12, 1-3, 127-33, (1978)

Hamilton P.M; The application of a pulsed light rangefinder (lidar) to the study of chimney plumes, Philos.Trans.R.Soc.London A, 265, 153-172, (1969)

Hanst P.L and Morreal J.A; Detection and measurement of air pollutants by absorption of I.R radiation, J.Air.Pollut.Control Assoc., 18, 754, (1968)

Harriman R and Morrison B; Ecology of acid streams draining forested and non-forested catchments in Scotland, Proc.Int.Conf.Ecol.Impact. Acid.Precip., Norway, 1980, SNSF project, p.312.

Hawley J.G; Dual wavelength laser radar probes for air pollutants, Laser Focus, p.60, March (1981); Characterization of the EPRI differential absorption lidar (DIAL) system, Final Report, EA-1267, Project 862-14, December (1979)

Heicklen J; Atmospheric Chemistry, Academic Press, 1976

Herget W.F, Jahnke J.A, Burch D.E, Gryvnak O.A; Infra-red correlation instrument for in situ measurement of gaseous pollutant concentrations, Appl.Opt., 15, 5, 1222-8, (1976)

Hinrichsen D; Acid Rain: A problem for the Eighties, IUCN Bulletin, April/May/June 1982, p.40

Hoell J.M, Wade W.R, Thompson R.T; International Conference on Environmental Sensing and Assessment, Las Vegas, Nevada, (1975)

Hoff R M; Simultaneous Lidar and Correlation Spectroscopy Measurements of Sea, Land and Pond Breeze Dispersion During the Sixth Remote Sensing Campaign of the CEC, June 1983, p.263, Proc. 12th International Laser Radar Conference, Aix-en-Provence, France, 13-17 August (1984)

Houlgate R, Fisher B.E.A, Gotaas Y, Hamilton P.M, Maul P, Moore D.J; Observations and calculations of airborne sulphur from multiple sources out to 100km, Atmos.Environ.(GB), 11, 12, 1163-70, (1977)

Hoyle P; The silent scourge, Time, p.38, 8 November, (1982)

Hulme K.F, Collins B.S, Constant G.D, Pinson J.T; A CO_2 laser rangefinder using heterodyne detection and chirp pulse compression, Opt. and Quantum Electron., 13, 35-45, (1981)

Ippolitov I I, Klimkin V M, Mitchenov V M, Sokovikov V G, Shelevoi V D; Raman Lidar Based on Excimer Laser, p.331, Proc. 12th International Laser Radar Conference, Aix-en-Provence, France, 13-17 August (1984)

Izumi T and Nakamura K; Wavelength modulated derivative spectrometer capable of an automatic analysis of environmental air pollutants, J.Phys.E (GB), 14, 1, 105-12, January (1981)

Izumi T, Sekino S, Shimizu A, Uno N, Takeda N, Maeda T; Continuous analyzer for air pollutants, Anritsu Tech.Bull.(Japan), 41, 99-115, April (1981)

Joliffe B W, Felton R C, Swann N R, Woods P T; Field Measurement Studies Using a Differential Absorption Lidar System, p.267, Proc. 12th International Laser Radar Conference, Aix-en-Provence, France, 13-17 August (1984)

Kildal H and Byer R.L; Comparison of laser methods for the remote detection of atmospheric pollutants, Proc.IEEE, 59, 1644-1663, December (1971)

Kobayasi T and Inaba H; Laser-Raman radar for air pollution probe, Proc.IEEE, 58, 10, October (1970)

Kreuzer L.B and Patel C.K.N; Science, 173, 45, (1971)

Kuhl J and Spitschan H; Opt.Commun., 13, 6, (1975)

Lawther P.J; Air pollution and its effects on man; Aspects of Environmental Protection, Ed. Dr.S.H Jenkins, (1970)

Marzorati A, Corio W, Zanzottera E; Remote Sensing of SO_2 During Field Tests at Fos-Berre in June 1983, p.259, Proc. 12th International Laser Radar Conference, Aix-en-Provence, France, 13-17 August (1984)

McDermid I S, Laudenslager J B, Pacala T J; Design of a Narrow-bandwidth Lidar System for Tropospheric Hydroxyl Measurements, p.313, Proc. 12th International Laser Radar Conference, Aix-en-Provence, France, 13-17 August (1984)

Measures R.A and Pilon G; A study of tunable laser techniques for remote mapping of specific gaseous constituents of the atmosphere, Opto-electron., 4, 141-153, (1972)

Mellanby K; Acid rain, Nature, 268, 99, 14 July, (1977)

Megie G and Menzies R.T; Complementarity of U.V and I.R differential absorption lidar for global measurement of atmospheric species, Appl.Opt., 19, 7, 1173, 1 April (1980)

Melfi S.H; Laser monitoring of the atmosphere, Topics in Applied Physics, Vol.14, Ed. E.D Hinkley, 1976

Menyuk N, Killinger D.K, DeFeo W.E; Remote sensing of NO using a differential absorption lidar, Appl.Opt., 19, 19, 3282, 1 October (1980)

Michels F, Zetzsch I, Stuhl F; Z.Naturforsch.a (Germany), 33A, 7, 782-5, July (1978)

Middleton and Spilhaus; Meteorological Instruments, (1953)

Murray E.R, Hake R.D Jr., van der Laan J.E, Hawley J.G; Atmospheric water vapour measurements with an infra-red (10 m) differential absorption lidar system, Appl.Phys.Lett., 28, 9, 542, 1 May (1976)

Northam G.B, Rosen J.M, Melfi S.H, Pepin T.J, McCormick M.P, Hofmann D.J, Fuller W.H Jr.; Dustsonde and lidar measurement of stratospheric aerosols: a comparison, Appl.Opt., 13, 10, 2416, October (1974)

Northend C.A, Honey R.C, Evans W.E; Laser radar (lidar) for meteorological observations, Rev.Sci.Instrum., 37, 4, April (1966)

Onderlinden D and Strackeo L; Computer assisted correlation spectrometer for the remote sensing of air pollutants, Rev.Sci.Instrum., 48, 7, 752-6, July (1977)

Pearce F; Science and politics don't mix at acid rain debate, New Sci., 1 July, (1982)

Pelon J, Megie G; Lidar Monitoring of the Ozone Vertical Distribution in the Troposphere and Stratosphere, p.247, Proc. 12th International Laser Radar Conference, Aix-en-Provence, France, 13-17 August (1984)

Pokora L, Kalisti S; N_2 and XeCl Ultraviolet Lasers Worked Out in IPPLM as Emitters in the Lidar Technique, p.337, Proc. 12th International Laser Radar Conference, Aix-en-Provence, France, 13-17 August (1984)

Reagan J.A; Applying lidar as an atmospheric probe, Laser Focus, pp.26-39, June 1968

Reiter R, Jaeger H, Carnuth W, Littfass M; Stratospheric aerosol layers monitored by lidar, Remote Sensing of the Atmosphere; Inversion Methods and Applications, p.277-286, (1978)

Rothe K.W, Brinkmann U, Walther H; Applications of tunable dye lasers to air pollution detection: Measurement of the atmospheric NO_2 concentrations by differential absorption, Appl.Phys. B, 3, 115-119, (1974)

Rudichenko V.E and Dobrochiver I.G; The use of an X-ray absorption detector in gas chromatography (air pollution detection), Ind.Lab.(USA), 42, 3, 371-2, March (1976)

Sandroni S and Cerutti C; Long path measurement of atmospheric SO_2 by a Barringer Cospec II, Atmos.Environ., 11, 12, 1225-32, (1977)

Sagawa E, and Itoh T; Mass spectrometric observation of SO_2 in the atmosphere, Geophys.Res.Lett., 4, 1, 29-32, January (1977)

Sax N.I; Dangerous Properties of Industrial Materials, Reinhold, (1963)

Schreiber R.K; Acid rain: Industrial fallout in the north woods, Fish and Wildlife News, p.8, August/September, (1980)

Schuster B.G and Kyle T.G; Pollution plume transport and diffusion studies using fluorescence lidar, Appl.Opt., 19, 15, 2524, 1 August (1980)

Smullin L.D and Fiocco G; Optical echoes from the moon, Nature, 194, 1267, (1962): Proc.Inst.Radio Engineers, 50, 1703, (1962)

Staehr W, Lahmann W, Weitkamp C, Michaelis W; Differential-Absorption Lidar System for NO_2 and SO_2 Monitoring, p.281, Proc. 12th International Laser Radar Conference, Aix-en-Provence, France, 13-17 August (1984)

Tanabe L.H and Herget W.F; Determination of SO_2 concentrations from a coal burning power plant stack by Fourier spectrometry, Proc.Soc. Photo-optical Instrumentation Engineers, vol.95, Modern Utilization of I.R Technology, Civilian and Military II, San Diego, Calif., 26-27 August (1976), p.66-73

Uchino O, Maeda M, Hirono M; Applications of excimer laser to laser-radar observations of the upper atmosphere, IEEE J.Quantum Electron., QE-15, 10, October (1979)

Vanin N.V, Migulin A.V, Rybakov S.Yu; Lidar for atmospheric investigations by various methods, Sov.J.Quantum Electron., 6, 9, September (1976)

Verdin A; Monitoring of Gaseous Effluent; Aspects of Environmental Protection, Ed. Dr.S.H Jenkins

Werner J, Rothe K W, Walther H; Lidar Measurements of the Stratospheric Ozone Layer, p.225, Proc. 12th International Laser Radar Conference, Aix-en-Provence, France, 13-17 August (1984)

Zakharov V.M and Torgovichev V.A; Lidar detection of atmospheric contaminants by raman scattering and fluorescence spectra; Remote Sensing of the Atmosphere: Inversion methods and Applications, p.287-294, 1974

Zuev V E, Ippolitov I I, Marichev V N; A Lidar Facility for Investigating the Middle Atmosphere, p.251, Proc. 12th International Laser Radar Conference, Aix-en-Provence, France, 13-17 August (1984)

Chapter 2 The Lidar Telescope

This chapter is a description of the theoretical and practical investigation which was required in evolving a telescope for the excimer laser DIAL system. The instrument was constructed after careful consideration of light gathering capability (section 2.1), field of view (section 2.3), image size (section 2.4) and compatibility with the laser and detector in the lidar transceiver. Results of the analysis of field of view and image size with respect to the mirror separation and detector size and position provided the basis for choice of telescope type.

2.1 Size of the Telescope Collecting Mirror

In order to extend lidar range, the collecting mirror area should be as large as possible. However, in view of the disproportionate rise in cost as the mirror size increases, an investigation based on atmospheric scatter was made to define the relation between maximum range and mirror area, given an arbitrary measurement threshold.

The lidar equation (described in chapter 8) is applied under the conditions of two model atmospheres with respective visibilities of 5 km.(hazy) and 23 km.(clear). Maximum range is defined by the range from which the minimum detectable signal is obtained, given a certain laser pulse energy. The expression for instantaneous received power from range r is given by

Northend et al (1966) to be

$$P_r = P_o(c\tau/2)\beta'(A/4\pi r^2).t_T t_R.\exp(-2\int_b^r \alpha dr).\exp(-2\int_b^r \sigma N dr), \qquad (2.1.1)$$

where α (m^{-1}) is the atmospheric linear scatter coefficient, β'(m^{-1}) is the backscatter coefficient and σ (m^2) is the absorption cross-section of a gas with number density N (m^{-3}). Backscattering is described (Hamilton, 1969) by the expression

$$\beta' = 1.5\alpha_R + 0.5\alpha_M \quad m^{-1}, \qquad (2.1.2)$$

where α_R is the Rayleigh scatter coefficient, given (Kruse et al, Elements of Infra-red Technology) by

$$\alpha_R = 1.1 \times 10^{-6} \lambda^{-4} \quad m^{-1} \qquad (2.1.3)$$

and α_M is the Mie scatter coefficient, given by

$$\alpha_M = (3.91 \times 10^{-3}/V)(0.55/\lambda)^{0.585V} \quad m^{-1}, \qquad (2.1.4)$$

for λ in μm. and visibility, V in km. The gas absorption term in equation (2.1.1) is deliberately neglected and the exponential scatter absorption term is approximated, assuming a uniform atmosphere, to $\exp[-2(\alpha_R + \alpha_M)r]$.

Received power is measured at a photomultiplier output as the voltage developed across a load resistor, R_L, by the amplified signal current. Thus the minimum detectable optical power is given by the minimum detectable, or useable, voltage, V_{min}, in the expression

$$P_{r\ min} = hcV_{min}/\lambda\eta GeR_L, \qquad (2.1.5)$$

where η is the photomultiplier cathode quantum efficiency and G is the photomultiplier gain.

Laser output power is expressed as the output energy, E_o, and the laser pulse fwhm, τ, in the expression

$$P_o\tau = E_o, \qquad (2.1.6)$$

which is combined with equations (2.1.1) and (2.1.5) to give

$$hV_{min}/\lambda\eta GeR_L = (E_o\beta' At_T t_R/8\pi r^2_{max}).\exp[-2(\alpha_M + \alpha_R)r_{max}]. \qquad (2.1.7)$$

The values given in table 2.1.1 are inserted into equation (2.1.7) to give

$$1.913 \times 10^{-12} = (E_o A/r^2_{max}).\exp(-0.00304r_{max}) \qquad (2.1.8)$$

for a hazy atmosphere and

$$4.105 \times 10^{-12} = (E_o A/r^2_{max}).\exp(-0.00114r_{max}) \qquad (2.1.9)$$

for a clear atmosphere. Laser energy was expected to be in the range 1mJ to 50mJ. Figure 2.1.1 shows mirror diameter vs. maximum range for pulse energies of 1mJ and 50mJ, over a range of mirror diameter up to 50 cm., although such a large size would be far too expensive for this job.

The detection limit is set for single pulse operation without any expressions to show the effect of averaging for low level detection. With

these conditions the maximum range may seem rather low, especially since such a large load resistance is used. It must be borne in mind, however, that the enhanced backscatter from a smoke plume target would improve the signal level at greater range. Even so, the range vs. mirror size relation does serve to show the flattening off where maximum range is not increased much for the substantial extra cost of a mirror larger than about 30 cm in diameter. This analysis indicated the suitability of a 10 or 12 inch mirror and, consequently, a 10 inch Newtonian and 10 inch Cassegrain type (Dall-Kirkham is possibly a more accurate description) set were purchased.

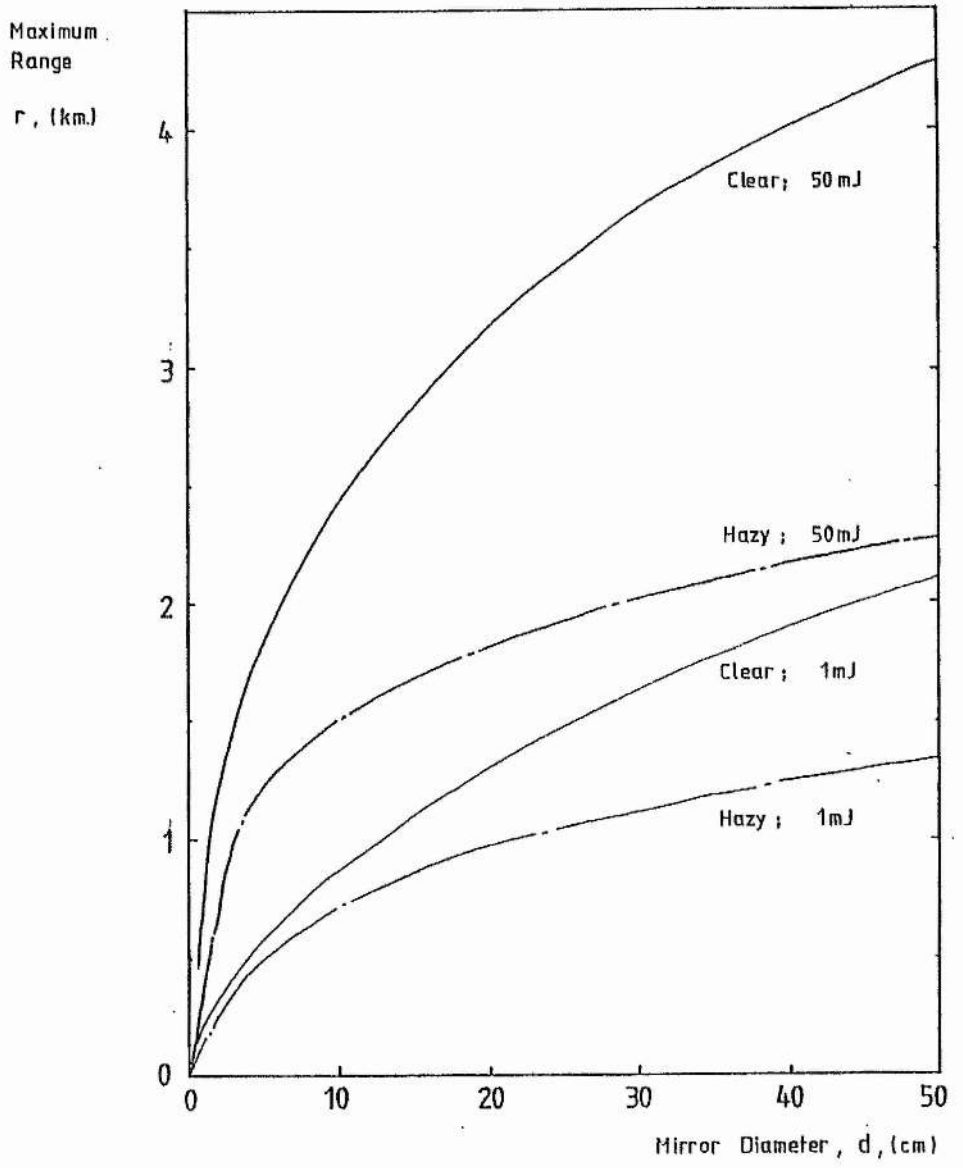

Figure 2.1.1 Relation between the maximum lidar range and the mirror area at two laser energies and under two conditions of visibility.

Table 2.1.1 Specification for the Application of a Simple Lidar Equation to Define the Relation between Maximum Lidar Range, r_{max}, and Telescope Mirror Area, A.

Quantity	Symbol	Value
Cathode quantum efficiency	η	0.01
Photomultiplier gain	G	10^6
O/P load resistance	R_L	100 kΩ
Minimum useful voltage	V_{min}	10mV
Transmission efficiency	t_T	1
Reception efficiency	t_R	0.2
Rayleigh scatter coefficient	α_R	$1.22X10^{-4}$ m^{-1} @ 308 nm, V=5km
Mie scatter coefficient (hazy)	α_M	$1.4X10^{-3}$ m^{-1} @ 308 nm, V=5km
Mie scatter coefficient (clear)	α_M	$4.5X10^{-4}$ m^{-1} @ 308 nm, V=23km
Backscatter coefficient (hazy)	β'	$8.8X10^{-4}$ m^{-1} @ 308 nm, V=5km
Backscatter coefficient (clear)	β'	$4.1X10^{-4}$ m^{-1} @ 308 nm, V=23km

2.2 A Paraxial Analysis of the Cassegrain Telescope

The specification supplied with the Cassegrain mirror set was not to be trusted, according to the supplier. It was necessary therefore, to define the focal lengths by experiment. This analysis takes the well known lens equation and applies it to the primary and secondary mirrors of the Cassegrain set. In sub-section 2.2.1 the equations are applied to an optical bench experiment to give primary and secondary focal lengths from measurements of object and image plane distances. In sub-section 2.2.2 an expression is derived to relate mirror separation to focal plane position in the complete instrument, allowing the mirror-to-mirror distance to be set for a convenient detector location.

2.2.1 Measurement of Primary and Secondary Mirror Focal Lengths

In the Cassegrain telescope a hyperbolic convex secondary mirror is used with a spherical primary so that their optical axes coincide. A central hole in the primary allows the focal plane to fall behind it. The grade B mirror set obtained for the lidar consists of a spherical primary and a spherical convex secondary for cheapness (for Cassegrain, read "Cassegrain type"). The focal length values supplied by the manufacturer were not reliable as they applied to a grade A set so it was decided to measure them as a precaution. Figure 2.2.1 shows the optical layout of the instrument and the locations of the respective object and image planes. The primary image and object planes are real, as is the secondary object plane, but the secondary image plane is virtual. This has consequence in applying the sign convention to the lens equation. Figure 2.2.2 is drawn to illustrate the necessity of placing the primary focal plane within that of the secondary

if a real final image is to be formed. This becomes apparent in section 2.2.2 after a theoretical treatment. The ray diagram of 2.2.1 shows the

parameters applied in the lens equation for the two mirrors. The equation describing the paraxial dimensions of the primary mirror is

$$1/f = 1/s_o + 1/s_i, \qquad (2.2.1)$$

where f is the primary focal length (positive), s_o is the mirror to object plane distance (positive) and s_i is the mirror to image plane distance. An optical bench experiment gave the Cassegrain primary focal length as $f = 128 \pm 0.5$ cm.

The secondary mirror is treated in the same way with the equation

$$1/f' = 1/s_o' + 1/s_i', \qquad (2.2.2)$$

where f' is the secondary focal length (positive), s_o' is the mirror to virtual object distance (positive) and s_i' is the mirror to image distance (negative). The sign convention is defined by a positive direction to the right of the optical element. Measurements using the secondary mirror were made in conjunction with the primary, permitting the substitution for virtual object distance s_o' so that it is defined in terms of the observables s_i and d. The secondary was placed at a distance d from the primary. After making the substitution $s_o' = s_i - d$ then equation (2.2.2) becomes

$$1/f' = 1/(s_i - d) + 1/s_i'. \qquad (2.2.3)$$

The quantities s_i, d and s_i' were measured directly to give the secondary focal length as $f' = 29.5 \pm 0.9$ cm.

2.2.2 Mirror Separation and Focal Plane Position

Equations (2.2.1) and (2.2.2) are used to derive a relation between the final focal plane position with respect to the primary, and the mirror separation, for an object at infinity. Figure 2.2.3 shows the parameters involved and explains any substitutions made. Taking equation (2.2.1) for an object at infinity then the image distance is the primary focal length ($f = s_i$). In equation (2.2.2), s'_o and s'_i can be replaced by $(s_i - d)$ and $-(b + d)$ respectively, giving the expression

$$1/f' = 1/(s_i - d) - 1/(b + d). \qquad (2.2.4)$$

Thus the mirror to focal plane distance, b, in terms of the mirror separation, d, is given by

$$b = (2df' + d^2 - fd - ff')/(f - d - f'). \qquad (2.2.5)$$

The quadratic in d can be solved to give

$$d = (f - b - 2f')/2 + (1/2)[(2f' + b - f)^2 - 4(f'b - ff' - fb)]^{1/2}. \qquad (2.2.6)$$

For convergence to a real focal point the inequalities (2.2.7) apply to b, demanding that the mirror separation, d, is restrained within the limits of (2.2.8). Thus the inequality

$$f - f' < d < f \qquad (2.2.7)$$

leads to

$$+\infty > b > -d. \qquad (2.2.8)$$

Inequality (2.2.8) gives the absolute maximum limit on d for a finite focal length. However, a convenient focal plane position requires much narrower bounds on the mirror separation. The lower limit $f - f' < d$ ensures that the primary focal plane falls within that of the secondary, though the latter is virtual. In the equality $f = d + f'$ the system is afocal as a result of the secondary image plane being at the position of the primary focal plane, illustrated in figure 2.2.4.

Application of the focal length values (from sub-section 2.2.1) to inequality (2.2.8) gives the absolute limits on d of

$$98.5 < d < 128 \text{ cm.} \qquad (2.2.9)$$

The more realistic range of d values is plotted for focal plane position in figure 2.2.5, using equation (2.2.6). Figure 2.2.5 shows the precision necessary in setting the mirror separation if the location of the focal plane is to be reasonably well defined. When the Cassegrain telescope was constructed the mirror separation was set at 104 cm. with an accuracy of 0.5 cm. This was adequate for knowing where to place the detector as the converging cone of the telescope was narrow at an overall focal ratio of f:20.

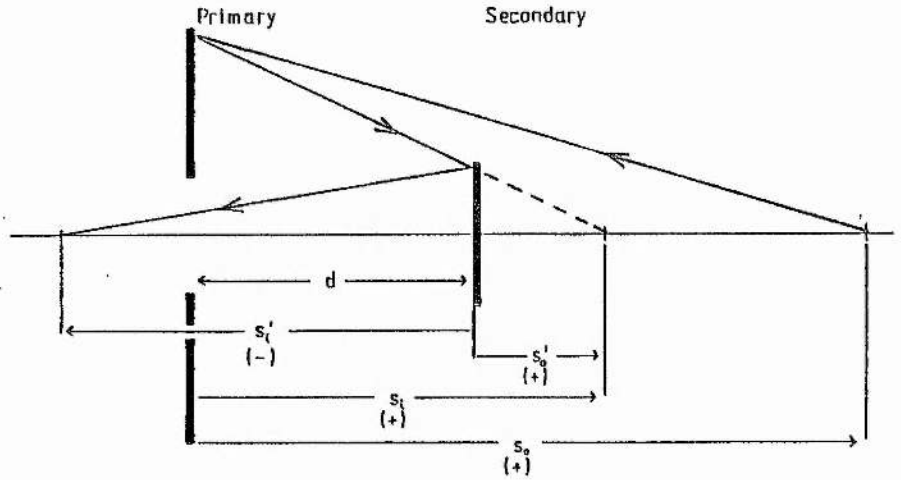

Figure 2.2.1 Lens equation parameters in the 'Cassegrain' telescope

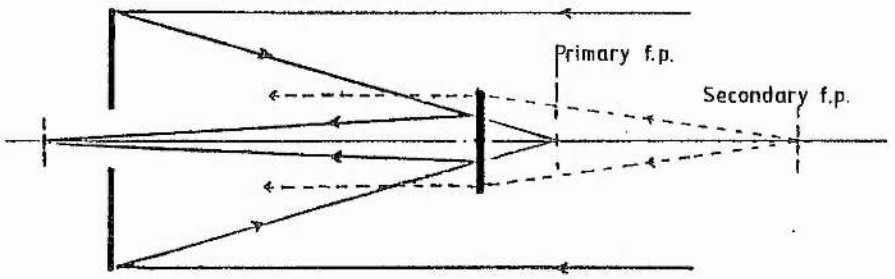

Figure 2.2.2 Relative position of the primary and secondary focal planes

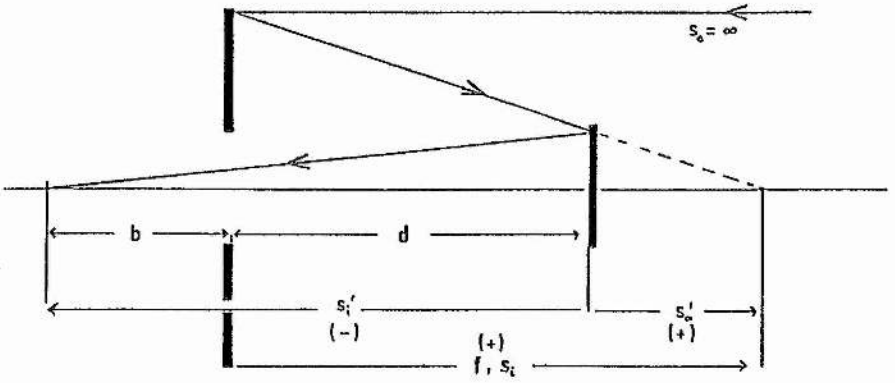

Figure 2.2.3 Mirror separation and focal plane position in the 'Cassegrain' telescope

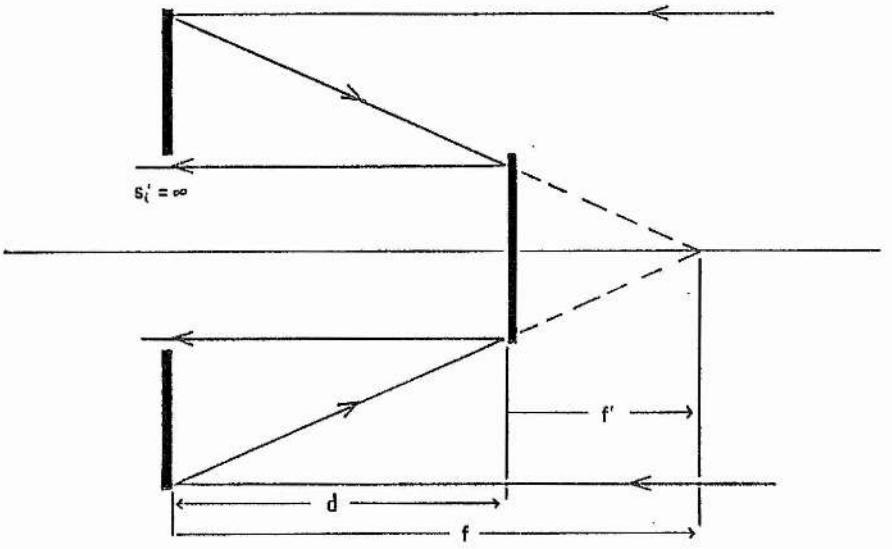

Figure 2.2.4 Infinite focal plane in the 'Cassegrain' telescope

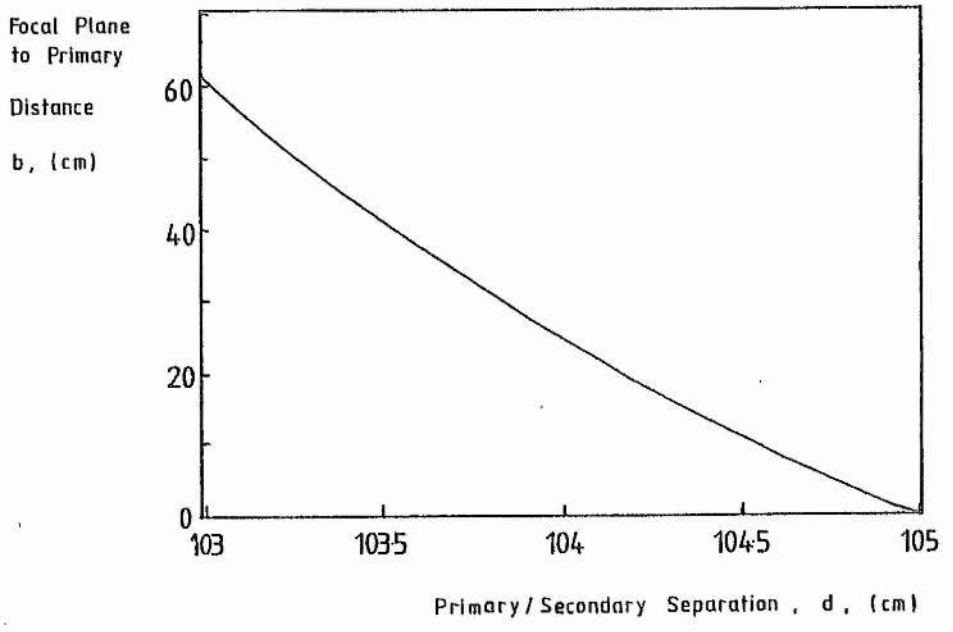

Figure 2.2.5 Focal plane position vs. mirror separation in the 'Cassegrain' telescope

2.3 Telescope Fields of View

This section compares the maximum fields of view of the Newtonian, Cassegrain and combination Newtonian focus/Cassegrain primary telescopes in order to provide the lidar receiving instrument with a field of view greater than the laser field of transmission so that radiation is collected efficiently from the entire illuminated target. As a guide to requirement, the full planar angle of divergence of the laser was expected to be in the range 8 mrads to 15 mrads, the value being confirmed in laser measurements (chapter 4).

The ray analysis is carried out with respect to the components of the Newtonian and Cassegrain mirror sets, consisting of two spherical primary mirrors, a 45° elliptical flat secondary and a spherical concave secondary. The detector is assumed to be centred on the optical axis. An expression is set up to describe the field as a function of mirror separation, applying to any combination of mirrors after substitution of the appropriate dimensions.

There are three ways in which the effective field may be restricted:-

(i) The telescope tube itself can vignette the field of view of the optics. However, a tube which contains the primary mirror is usually diametrically large enough. The converted PVC drainpipe used in the lidar instruments was large enough to contain a field with a full angle of about 50 mrads, about four times greater than necessary. Figure 2.3.1 introduces the full field, θ, with this limit described by a half angle of view α_t.

(ii) A more critical problem is to set a great enough primary/secondary

mirror separation so that all the boundary rays at the field extremity reach the focal plane, bearing in mind that the separation should not be so great as to place the focal plane inaccessibly within the telescope. In this section the equation describing field of view, limited in this way, connects half angle of view to mirror-to-mirror distance with the separation in terms of the primary and secondary diameters and primary focal length. The results serve to compare the fields obtained with the Newtonian set, the Cassegrain set and the Newtonian/Cassegrain combination with regard to any other dimensional bounds imposed by focal plane location. The Cassegrain result is a check that the critical mirror separation, set by the paraxial analysis in sub-section 2.2.2, allows adequate field.

(iii) The effective full field may be lost if the detector is smaller than the image formed at the focal plane. Section 2.4 compares the theoretical image sizes in the Cassegrain and Cassegrain/Newtonian systems so that, further to the discussion of field in this section, the final choice of lidar telescope was made.

2.3.1 Derivation of the General Field Equation

Figure 2.3.2 illustrates, in a ray diagram, the field set by the secondary mirror size and the mirror separation d. The diagram applies generally to all the telescope configurations under discussion. The Cassegrain secondary mirror diameter, D_s, corresponds to the minor axis length of the Newtonian elliptical flat at 45^o. Since the edge of the 45^o flat nearest to the primary restricts the field size (see figure 2.3.2) the distance between this edge and the primary is considered for the Newtonian and the Newtonian/Cassegrain and is called, d', equivalent to d for the Cassegrain. The actual centre-to-centre separation in a telescope with the

45^{o} flat is given by $d' + D_s/2$.

The field is defined by the maximum half angle of view, α_t, made between a direction parallel to the optical axis and the edge ray just accommodated by the optics, where no light loss is incurred in taking parallel rays from the extreme edges of the field. In figure 2.3.2 the edge rays are incident upon the primary mirror at an angle of ϕ with the radius of curvature. Through corresponding and alternate angles the link with focal length, f, and primary diameter, D_p, is given by equation (2.3.2). Another relation, equation (2.3.1), introduces the separation, d, and the secondary diameter, D_s.

$$\alpha_t + 2\theta = \tan^{-1}(D_p - D_s)/2d \quad {}^{o} \qquad (2.3.1)$$

$$\alpha_t + \theta = \tan^{-1}(D_p/4f) \quad {}^{o} \qquad (2.3.2)$$

The angle θ is replaced in the simultaneous equations (2.3.1) and (2.3.2) to give

$$\alpha_t = 2\tan^{-1}(D_p/4f) - \tan^{-1}(D_p - D_s)/2d \quad {}^{o}. \qquad (2.3.3)$$

Equation (2.3.3) is applied in sub-sections 2.3.1(a), (b) and (c) to each combination of the mirror sets resulting in figure 2.3.3 which indicates the field of view of each type.

2.3.1(a)Field of view of the Newtonian Set: Application of Equation(2.3.3)
The parameters for the Newtonian set are given in table 2.3.1. These are applied to the field of view equation (2.3.3) to plot field of view for mirror separation in figure 2.3.3. Although a large separation is desirable for larger field the distance is restrained to a maximum to allow

convenient siting of the focal plane position, preferably outside and a little away from the telescope tube. The centre-to-centre mirror separation is given by $d+D_s/2$ (figure 2.3.2) so that the maximum separation is given by

$$d_{max} = f - D_s/2 - p, \qquad (2.3.4)$$

where p is the focal plane to secondary distance along the optical axis. The tube employed here has an outside diameter of 32.5 cm., giving p = 16.25 cm. and a permitted maximum of d_{max} = 110.4 cm. By this restriction, the maximum useable half angle of view is 9 mrad, a full field of 18 mrad, which is adequate for the the lidar where the maximum expected laser divergence is 15 mrad. However, the photomultiplier cathode cannot conveniently be placed so close to the telescope tube so it is useful to consider focal plane positions further out from the side of the tube. Distances of the focal plane from the tube O.D are indicated in figure 2.3.3, determining that the detector should be within 2 cm. of the tube if a laser divergence of say 15 mrad is to be covered. This is subject to the results of the discussion on image size at the focal plane given in section 2.4.

2.3.1(b)Field of View of the Cassegrain Set: Application of Equation(2.3.3)
It has been shown, in section 2.2.2, that the mirror separation must be set at 104 cm., with an accuracy of $\pm$0.5 cm., for a reasonably placed focal plane. Thus, in applying equation (2.3.3) the mirror separation, d, is plotted around this value to give the Cassegrain field in the relation shown in figure 2.3.3. Cassegrain set parameters are given in table 2.3.2. The full field of the Cassegrain, according to figure 2.3.3, is 27 to 28 mrads, greater than the Newtonian field and nearly twice the full angle of

divergence of the laser.

2.3.1(c) Field of the Cassegrain Primary/Newtonian Secondary Combination

The Cassegrain type primary was retained but the Newtonian flat secondary was substituted. The secondary position was determined by a field analysis similar to that in 2.3.1(a), given in 2.3.1(c). The parameters for the Cassegrain primary and Newtonian flat combination are given in table 2.3.3. Equation (2.3.4) is applied to restrict separation to a maximum of 109 cm., allowing a full field of 18 mrads. Equation (2.3.3) is applied for this particular mirror combination to give the field/mirror separation relation in figure 2.3.3. Since the focal lengths of the Newtonian set primary and Cassegrain set primary are similar, their fields of view are practically identical. However, the Cassegrain type primary, with its central hole, has great advantage as a means of sighting the telescope, a principal requirement, as described in chapter 7 on transceiver integration.

2.3.2 Conclusions on Telescope Field of View

With reference to figure 2.3.3, the Cassegrain telescope set would be the choice for a large field of view if the image size were small enough. Otherwise the Newtonian or Newtonian/Cassegrain combination would do. The latter was preferred for the reason stated above. This combination gives adequate field if the mirror separation is great enough. However, to ensure an accessible focal plane position the separation is restricted to a maximum of 109 cm. A lower limit depends upon the laser divergence but telescope field should be maximised anyway. The effect of mirror separation on image size is discussed below, in section 2.4.

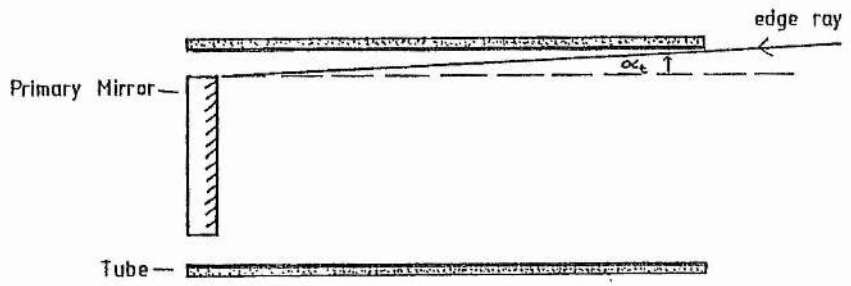

Figure 2.3.1 Field limited by the telescope tube

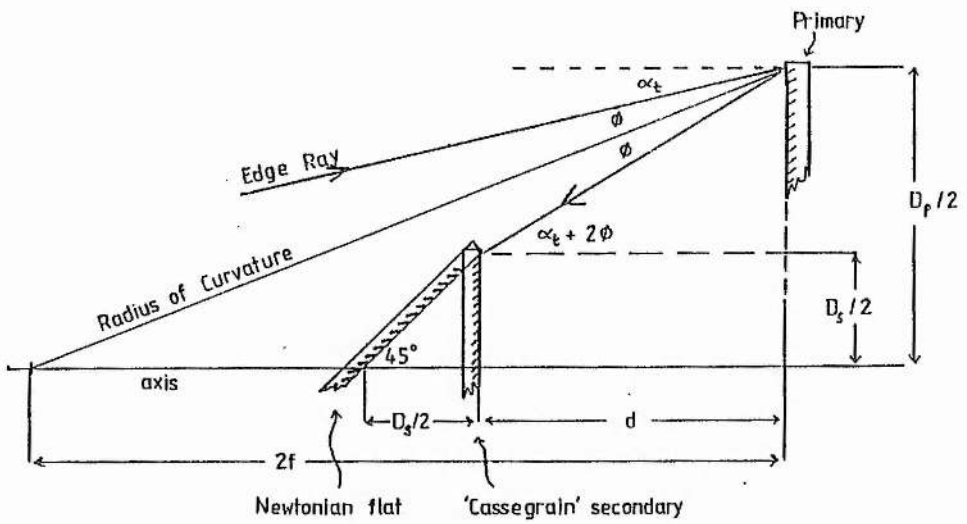

Figure 2.3.2 Ray diagram for defining the general telescope field equation in relating field to mirror separation

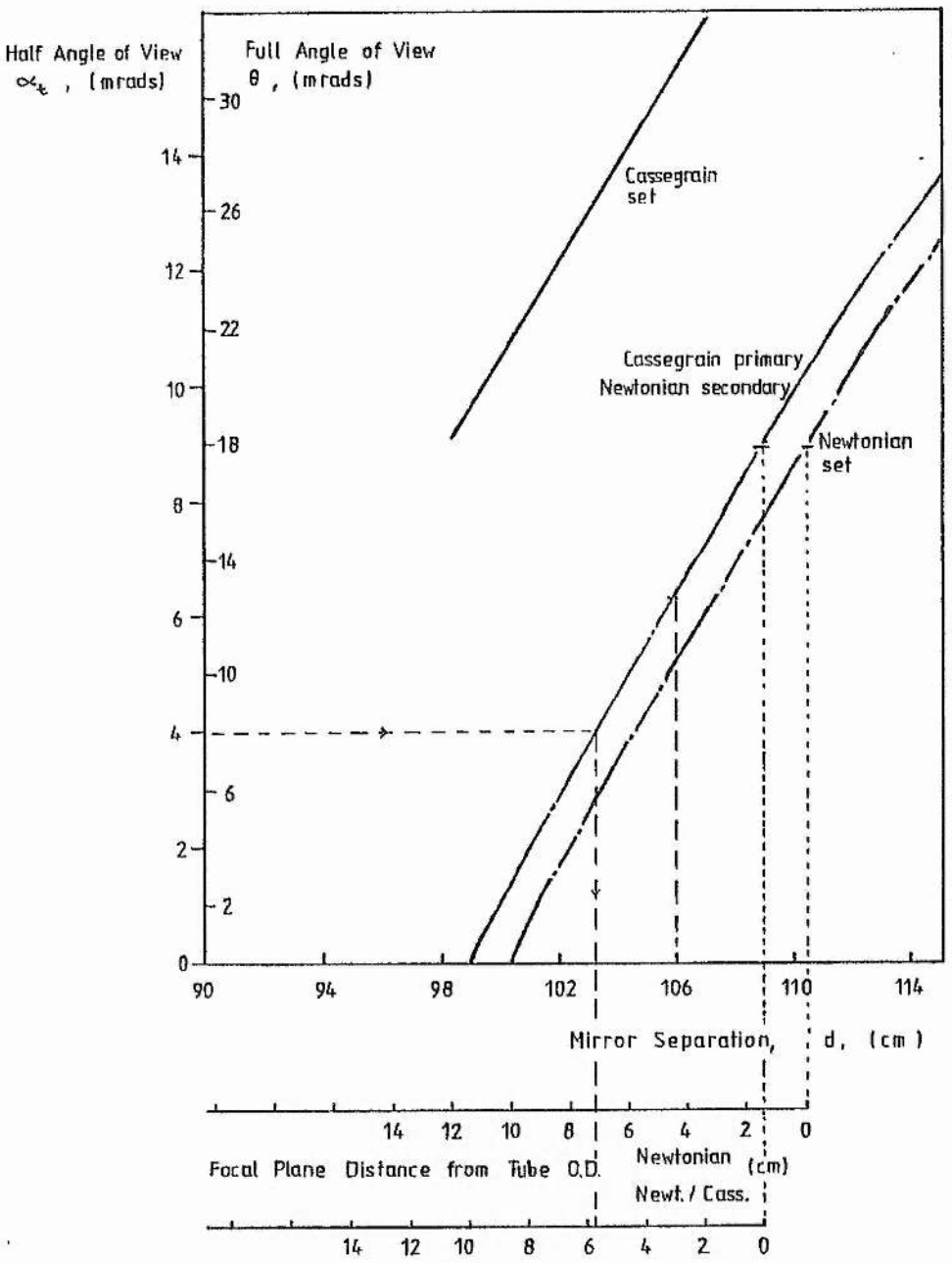

Figure 2.3.3 Variation of the field of view with the mirror separation or the focal plane position (Newtonian focus) for different mirror sets

Table 2.3.1 Newtonian Mirror Set Parameters

Primary diameter	D_p	25.4 cm
Primary focal length	f	129.5 cm
Secondary diameter (minor axis)	D_s	5.7 cm

Table 2.3.2 Cassegrain Mirror Set Parameters

Primary diameter	D_p	25.4 cm
Primary focal length	f	128 ± 0.5 cm
Secondary diameter	D_s	7.6 cm
Secondary focal length (virtual)	f'	29.5 ± 0.9 cm

Table 2.3.3 Newtonian/Cassegrain Mirror Set Parameters

Primary diameter	D_p	25.4 cm
Primary focal length	f	128 ± 0.5 cm
Secondary diameter (minor axis)	D_s	5.7 cm

2.4 Image Size and Detector Position

In the preceeding section the fields of the Newtonian and Cassegrain mirror sets and the field of the Cassegrain primary in a Newtonian configuration (described as the Newtonian/Cassegrain combination) are compared. The work described in this section defines image size to allow appropriate detector positioning for efficient use of the light gathering power of the telescope. In sub-section 2.4.1 an analysis of image size is applied to the Cassegrain set and Newtonian/Cassegrain in comparison; the Newtonian set is rejected because of its slightly less favourable field of view and the lack of the sighting facility. In sub-section 2.4.2 the detector position, with respect to the focal plane, is defined for the Newtonian/Cassegrain telescope.

2.4.1 Image Size

Two equivalent expressions are derived (appendix A2.1) to relate the system image size to the mirror separation for application to either the Cassegrain or the Cassegrain/Newtonian sets.

2.4.1(a) Cassegrain Image Size

The situation for the Cassegrain and its secondary magnification is shown in the ray diagram of figure 2.4.1. The useful relation between system image size, d_i, and mirror separation, d, is given by (equation A2.1.12)

$$d_i = D_s - 2(b + d).\tan[\tan^{-1}(D_p - D_s)/2d - 2\tan^{-1}(D_s/4f')] \qquad (2.4.1)$$

and is plotted for the Cassegrain parameters (table 2.3.2) in figure 2.4.2 (b is given for d by equation 2.2.6).

At the mirror separation of 104 cm., which was selected in sub-section 2.2.2, figure 2.4.2 gives an image diameter of 18.8 cm., which is greater than the primary hole diameter. In addition, the detector is nowhere near large enough, further restricting the effective full primary field. Field of view and effective (detected) image size are related by combining equations (2.3.3), (A2.1.9), (A2.1.10) and (A2.1.11) to give

$$\alpha_t = 2\tan^{-1}(D_p/4f) = 2\tan^{-1}(D_s/4f') = \tan^{-1}(D_s - d_i)/2(b + d). \quad (2.4.2)$$

The photomultiplier (EMI G26H314LF) has a cathode diameter of 1.6 cm. which, upon insertion for d_i in equation (2.4.2), gives a field of view which is less than zero.

This analysis explains why the Cassegrain set was rejected. The problem arises with the magnification of the primary image by the secondary mirror. The solution, to replace the convex secondary mirror by a flat Newtonian secondary, is tested in the following image size analysis for the Newtonian secondary and Cassegrain primary combination.

2.4.1(b) Newtonian Secondary/Cassegrain Primary Image Size

The relation between system image size and defined mirror separation, d, is the same as that for the primary image size, given by (equation A2.1.3)

$$d_F = (dD_p + fD_s - fD_p)/d \quad (2.4.3)$$

and plotted for the Newtonian/Cassegrain parameters (table 2.3.3) in figure 2.4.3.

The detector diameter of 1.6cm., on figure 2.4.3, restricts the maximum

mirror separation to 106 cm. On figure 2.3.3 this gives an adequate full field of 13 mrads. and a focal plane position at 3 cm. from the tube O.D. As the focal plane in this case would be so near to the tube (any further out and the field is reduced, according to figure 2.3.3) then difficulty could have been encountered upon inclusion of an interference filter and iris in front of the detector. Further analysis is given below in subsection 2.4.2 to determine how far away from the focal plane the detector may be before the field is restricted.

2.4.2 Detector Position with respect to System Focal Plane

The effective image size, as the detector "sees" it, increases away from and on each side of the focal plane of the telescope as is shown for the edge rays in figure 2.4.4, where the focal plane image size is d_I and the effective image size is d_I' at an axial distance, x, from the focal plane. It is useful to determine the distance that the detector can be placed from a focal plane of known size. Similar triangles in figure 2.4.4 give

$$(D_p - d_I)/f = (d_I' - d_I)/ x. \qquad (2.4.4)$$

The maximum allowable distance, x_{max}, is defined for a detector size which gives $d_I'_{max}$ in the expression

$$x_{max} = f(d_I'_{max} - d_I)/(D_p - d_I), \qquad (2.4.5)$$

which is plotted for $d_I'_{max} = 1.6$ cm., $D_p = 25.4$ cm. and $f = 128$ cm. in figure 2.4.5.

Figures 2.4.5 and 2.3.3 are considered. If the focal plane is close to the tube it is difficult to place the detector. However, if the focal plane

were moved away from the tube by reducing the mirror separation then the field would suffer (figure 2.3.3). Therefore, to fix a detector near to a focal plane near to the tube it was necessary to know how accurately the positioning should be , given the mirror separation as the base specification.

A most useful way of expressing the distance x is to use it to calculate the permissible range of detector distance, e , from the tube O.D. The maximum is given by

$$e_{max} = f - D_s/2 - p - d + x_{max}, \qquad (2.4.6)$$

where p is defined in sub-section 2.3.1(a). The minimum permissible distance is given by

$$e_{min} = f - D_s/2 - p - d - x_{max}. \qquad (2.4.7)$$

Equations (2.4.6) and (2.4.7) express the situation shown in figure 2.4.4. They are plotted in figure 2.4.6, showing that there is no freedom of positioning at d = 106 cm. which corresponds to an image size of 1.6 cm., (figure 2.4.3) the detector diameter.

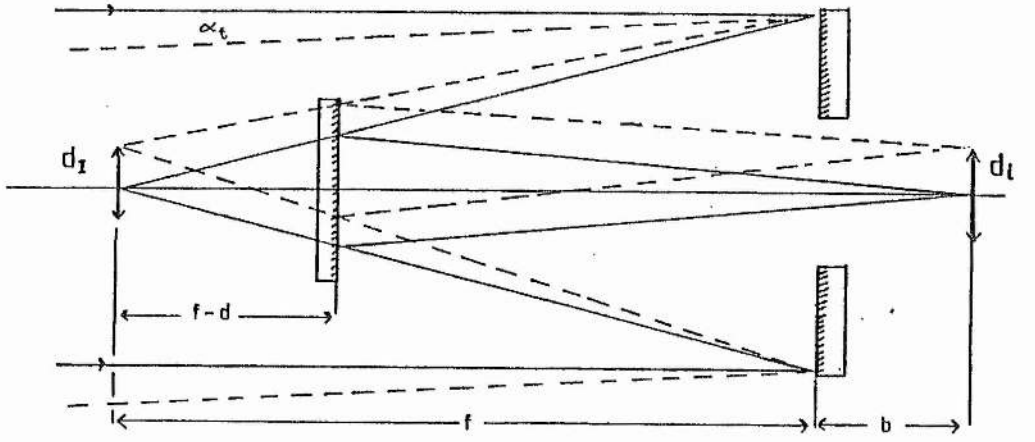

Figure 2.4.1 Ray diagram showing the image size formed by the edge rays in the Cassegrain telescope

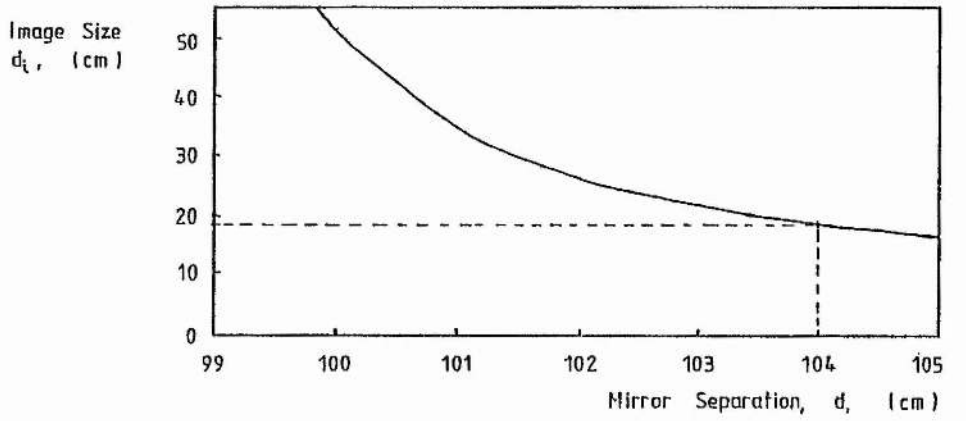

Figure 2.4.2 Variation of the focal plane image size with mirror separation in the Cassegrain telescope

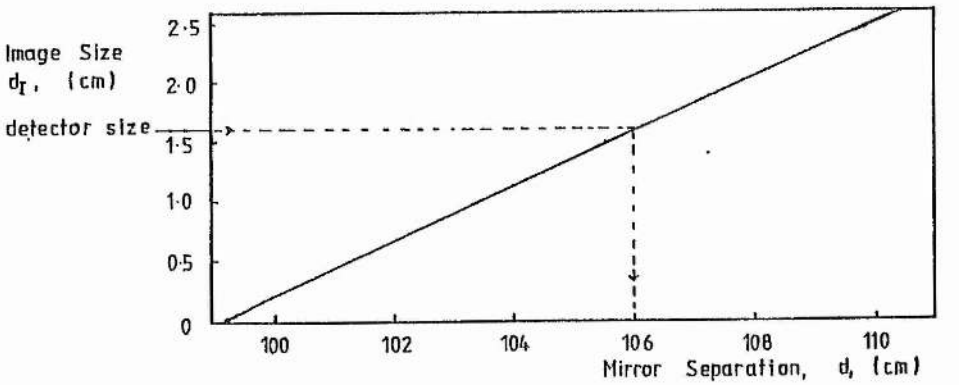

Figure 2.4.3 Variation of the focal plane image size with mirror separation in the Newtonian/Cassegrain telescope system

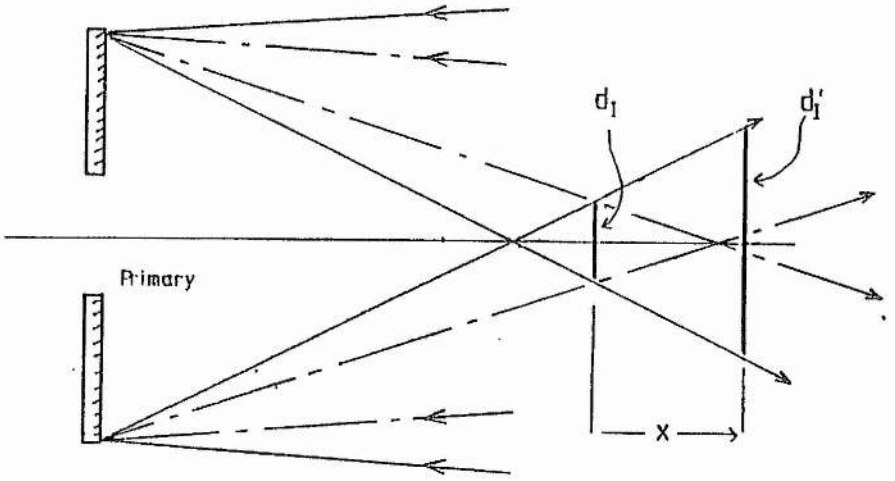

Figure 2.4.4 Effective telescope image size away from the focal plane

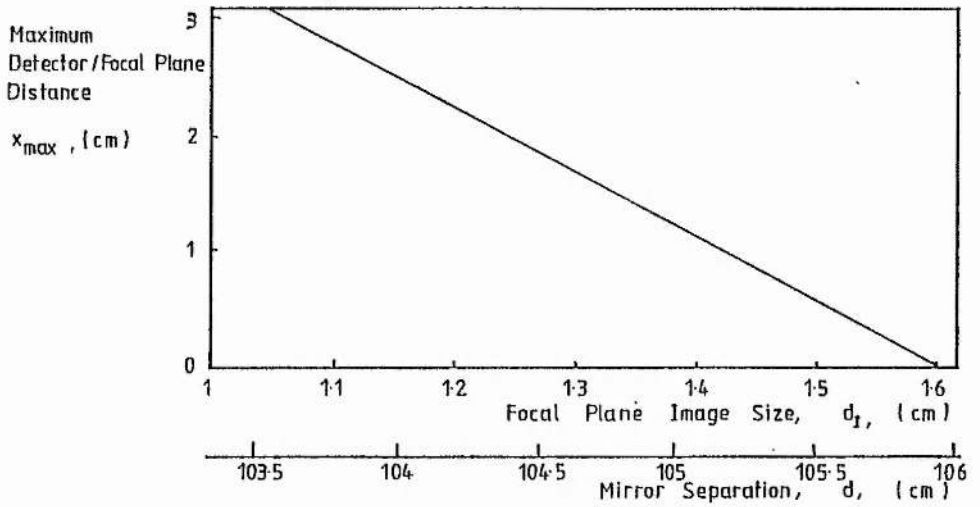

Figure 2.4.5 Allowable detector to focal plane distance in the Newtonian/ Cassegrain telescope, for image size or mirror separation

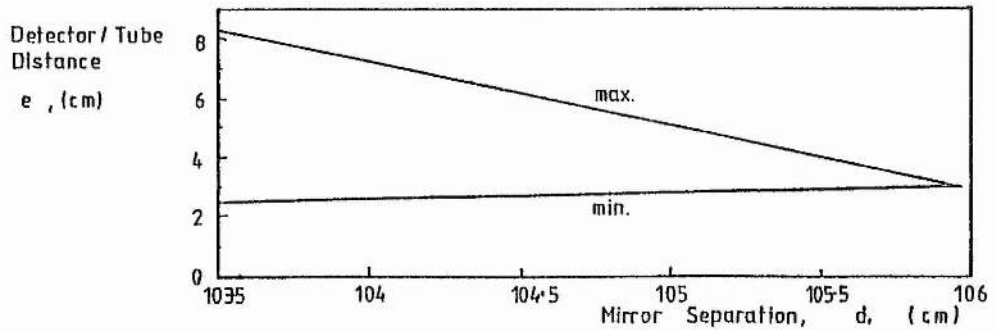

Figure 2.4.6 Allowable detector position with respect to the tube O.D, depending on mirror separation

2.5 Construction of the Lidar Telescope

2.5.1 Result of the Telescope Work Prior to Construction

The Cassegrain type primary and the Newtonian flat secondary mirrors were selected for the lidar telescope as the means of satisfying field of view and image size requirements. However, the unique feature of this configuration is the facility for direct telescope/target alignment when used with a reflective filter near the focal plane (chapter 7).

The principal restriction on maximum mirror separation is image size. If the latter was to be kept less than 1.6 cm. at the focal plane then the mirrors were not to be greater than 106 cm. apart, according to figure 2.4.3. To preserve an adequate field of view the separation was to be great enough. As a guide, the full field was limited to a minimum of 8 mrads. by ensuring that the separation, according to figure 2.3.3, never falls below 103.5 cm. The limits on separation are then denoted by

$$103.5 \text{ cm.} < d < 106 \text{ cm.}, \qquad (2.5.1)$$

giving the coresponding full field of view range, given by figure 2.3.3, as

$$8 \text{ mrad.} < \alpha_t < 13 \text{ mrad.} \qquad (2.5.2)$$

It was possible to set the mirror separation by the limits of (2.5.1) and then use figure 2.4.6 to define the limits on the detector position. Alternatively, the detector to tube distance could be set, placing a maximum on mirror separation according to the maximum in figure 2.4.6. The latter idea was followed because the housed detector, with filter, iris and mounting, effectively set the distance, e, between photocathode and

telescope tube. Ideally, the detector would be set at the focal plane to maximise field of view. The telescope was constructed so that the separation could be varied within the prescribed limits of (2.5.1). The detector mounting was designed to be moved to stay aligned with the optical axis.

2.5.2 Telescope Construction

The lidar equipment in general was designed to be as reliable and as service free as possible. To this end the telescope, illustrated in the schematic of figure 2.5.1, was made from simple, yet fully adjustable, components.

The primary mirror was mounted on an aluminium base plate which is secured by adjusting screws to the telescope end plate against a compressed O-ring (figure 2.5.2(a)). The secondary mirror mount was constructed to the same principle. A three legged spider mount, secured to the tube, carries the mirror below it (figure 2.5.2(b)), stuck and clipped to a solid aluminium base. A rubber block, under compression between the two sections, provides a pivot for adjustment by three screws. The fastenings of the spider to the tube (figure 2.5.1) were made so as to provide adjustment of the secondary mirror along the optical axis so that mirror separation, d, could be varied between the limits of (2.5.1). It was vital to remember that the actual centre-to-centre mirror separation is given by $d + D_s/2$. Facility is provided on the main spider body to attach either the Cassegrain or the Newtonian secondary. The secondary mount was designed to support the Cassegrain and Newtonian mirrors simultaneously, one on each side, if the laser "beam" was required to be transmitted co-axial to the telescope (figure 2.5.3).

The tube, enclosing all the components, is derived ,in keeping with the low cost nature of the project, from P.V.C drainpipe with a 30.5 cm. I.D and 1 cm. thickness.

The telescope optical component details are listed in table 2.3.3, the general specification in table 2.5.1.

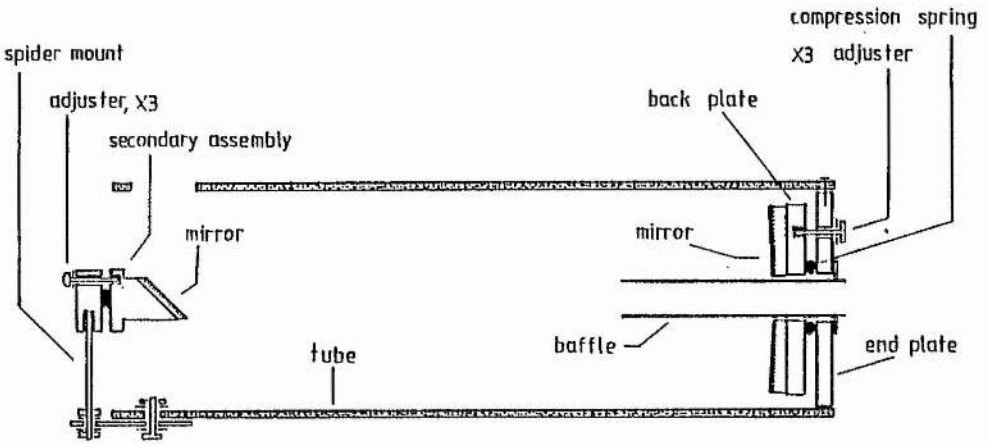

Figure 2.5.1 Sectional schematic of the Newtonian/Cassegrain lidar 'scope

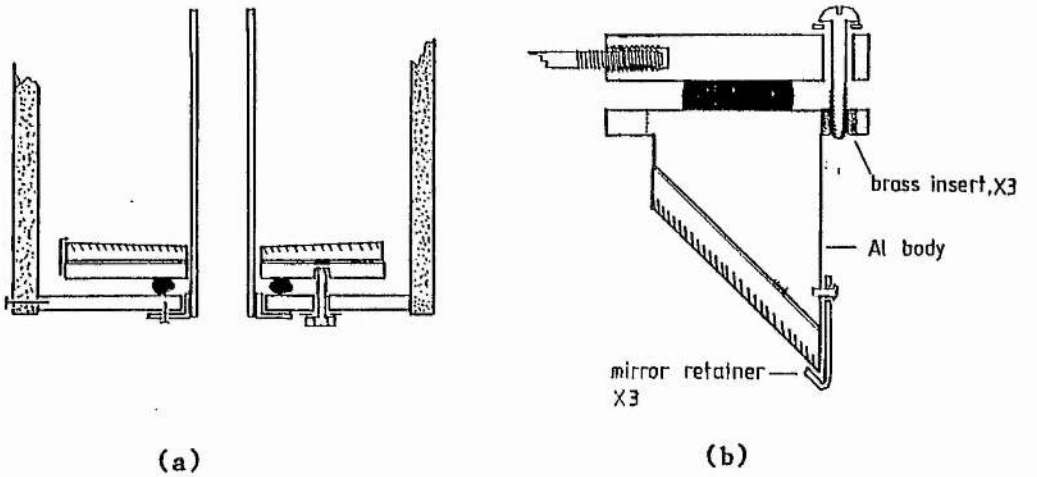

Figure 2.5.2 Sectional schematic of (a) the primary mirror mount
(b) the secondary mirror mount

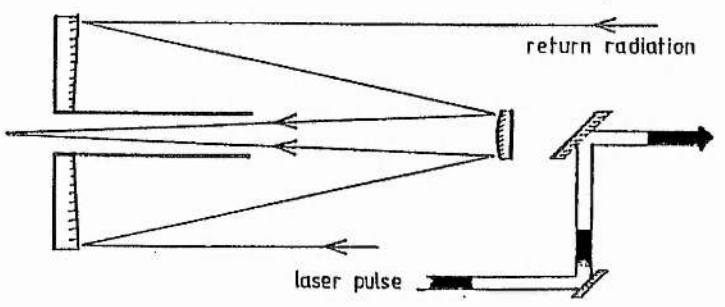

Figure 2.5.3 Schematic showing the facility for co-axial transmission of the laser pulse using a Cassegrain receiver

Table 2.5.1 The Lidar Telescope Specification

Component	Description	Specification
Focus	Newtonian	
Primary mirror	Cassegrain type; spherical concave; 4cm hole.	
	diameter	25.4 cm
	focal length	128 ± 0.5 cm
	focal ratio	f:5
Secondary mirror	Elliptical flat	
	minor axis	5.7 cm
	major axis	8.0 cm
System focal ratio		f:5
Tube	PVC	
	wall thickness	1 cm
	length	120 cm
Mounting	Steel frame alt-azimuth with laser bracket.	

References for Chapter 2

Hamilton P.M; The Application of a Pulsed Light Rangefinder (lidar) to the Study of Chimney Plumes, Philos.Trans.R.Soc.London A, 265, p.153-172, (1969)

Kruse P.W, M^{c}Glaughlin L.D and M^{c}Quistan R.B; Elements of Infra-red Technology, Wiley, New York

Northend C.A, Honey R.C, and Evans W.E; Laser Radar (Lidar) for Meteorological Observations, Rev.Sci.Instrum.,37, 4, p.393, (April 1966).

Optical Society of America; Handbook of Optics

Chapter 3 The Photomultiplier and Detector Head

In DIAL the return photon distribution is often very weak, particularly when receiving a signal from an extreme range. The detection process for such signals must include an amplification stage. A photomultiplier incorporating high cathode sensitivity with low noise, high bandwidth and high gain is most suitable for the task. This chapter describes the general features of photomultiplier operation and provides information leading to the choice of a photomultiplier specifically for this work. A general discussion of operating conditions is applied to specifying the operating environment of the chosen tube. The final sections describe the physical environment of the photomultiplier in the lidar system, including an investigation into the scattered solar spectrum at ground level.

3.1 Photomultiplier Structure and Operation

The study described in this section provides a general background knowledge of each working aspect of the photomultiplier with a bias towards the properties necessary for detection of pulses of ultra-violet wavelength. The tube gain is analysed generally in the appendix with regard to the interstage voltages set by the divider chain resistances. This allows tube gain to be defined for later application. An investigation of pulse transfer in its transduction from optical to electrical form gives the effect of temporal resolution in pulse reproduction. The photomultiplier

structure types associated with time response are compared.

3.1.1 Introduction to the Photomultiplier

The action of a photomultiplier is illustrated in the block schematic of figure 3.1.1. A photon current incident upon the photo-cathode causes photo-emission of electrons with a wavelength dependent quantum efficiency describing the efficiency of photon to electron transfer. The cathode current is amplified in an electron cascade by a series of dynodes, each made of a secondary emitting material. The electrons collected at the anode after multiplication constitute the anode current which may be processed directly in current mode or analysed in voltage mode as the potential developed across a load resistor. Processes in photomultiplier operation are explained in the following sub-sections.

3.1.2 Window, Cathode and Spectral Response

The main features of concern as regards the photomultiplier window and cathode are the respective wavelength dependent transmission and photo-emissivity.

Correct selection of window material becomes important towards the UV below about 375 nm. The most common windows in, for example, EMI tubes are of borosilicate or Corning 9741. Borosilicate is suitable only to 350 nm. but the Corning glass gives about 95% transmission at this wavelength, tailing off to 50% at about 200 nm. Figure 3.1.2 shows the spectrally dependent window transmission of some window materials which are supplied for UV detection. The best are the fluorides which transmit at least 65% down to 150 nm. In most wavelength regions it is possible to select a window to give transmission of more than 80%.

The spectral response of the photocathode is represented numerically by its quantum efficiency; that is the ratio of the number of emitted photoelectrons to the number of incident photons. The sensitivity can also be defined by the radiant cathode sensitivity (mA/W), a function of wavelength or the luminous cathode sensitivity (μA/lumen), independent of wavelength. Cathode material selection is made according to the requisites of wavelength or range of wavelengths to be detected. The quantum efficiency of some materials can approach a peak of 25%. The low work function of these types means that it is sensitive over a broad wavelength range. This may be a problem in cases where unwanted background is present. Photocathodes of high work function are supplied for response to UV wavelengths with a cut-off on the edge of the visible band. However, these solar blind cathodes have a peak quantum efficiency of no more than 10% and they have a much narrower spectral response range. The high work function also gives the advantage of low thermal dark current. It must be noted that the low wavelength response materials are only available in low cathode diameters, a factor which may be important in photometry of a large image size. Figure 3.1.3 gives examples of the spectral response of some materials (EMI catalogue, 1979; Hamamatsu catalogue, 1980; RCA catalogue, 1979).

3.1.3 Gain

A photomultiplier generally has a maximum gain, by electron multiplication, of between 10^4 and 10^8 times depending on the secondary emitting dynode material, the number of amplifying stages, the dynode configuration and the operating voltage. The dynode configuration has a much more significant effect on tube time response and is discussed in the next section.

EMI tubes use dynodes of cesium antimonide (CsSb) or berylium oxide on a

copper substrate (Be-O-Cu or alternatively, BeCu). The former provides a higher gain for the same applied voltage but its response is not as linear as that of BeCu. High gain dynodes are useful if equipment has to be operated at the lower voltage from a battery as may be the case in a portable, hand-held detector.

High gain tubes employ up to 14 secondary emitting stages. However, a tube with more stages is more susceptible to greater overall gain changes in the event of any variation in interstage voltage producing changes in electron multiplication which are then amplified further. In such a device the critical stage voltages are stabilised.

The voltage between each dynode stage, a prime factor in the secondary emission process, is applied by dividing an overall voltage across a chain of resistors. Zener diodes are usually used to set a voltage where it is critical at, for example, the first stage between the cathode and the first dynode. Any fluctuation in gain created here would be amplified by the rest of the multiplier. Derivations of tube gain expressions for each of two circuits are given in the appendices A3.1 and A3.2 for application to any tube given the divider chain resistances, zener voltages, the overall voltage and the secondary emission coefficients.

The circuit of figure 3.1.4 is a resistive divider chain of n stages with only the cathode-to-first-dynode voltage set by a zener diode. The resistive chain voltage is given by

$$V_R = V_o - V_{Zk} \,, \qquad (3.1.1)$$

where V_{Zk} is the zener voltage and V_o is the overall applied voltage. The

gain equation for this circuit, derived in appendix A3.1, is given as

$$G = f.A^{n}[V_{Zk}.V_{R}^{n-1}.R_{2}R_{3}....R_{n}/R_{T}^{n-1}]^{B} , \qquad (3.1.2)$$

where A and B are constants which can be found for a particular tube, R_n is the resistor before the n^{th} dynode, R_T is the total chain resistance and f is the cathode-to-first-dynode collection efficiency incorporated with the constant A. Equation (3.1.2) is re-arranged to give resistive voltage for a gain G in

$$V_R = [(G/f.A^{n})^{1/B}.R_{T}^{n-1}/V_{Zk}.R_{2}R_{3}....R_{n}]^{1/n-1} \qquad (3.1.3)$$

used in conjunction with (3.1.1) to define overall voltage for a desired gain.

In the circuit of figure 3.1.5 the cathode-to-first-dynode voltage and the three final stage voltages are set by zener diodes, allowing variation of gain at high signal pulse currents without losing linearity of response (explained in section 3.2). Equation (3.1.1) above now takes the form

$$V_R = V_o - (V_{Zk} + V_{Z1} + V_{Z2} + V_{Z3}). \qquad (3.1.4)$$

The gain equation for this circuit, derived in appendix A3.2, is

$$G = f.A^{n}[V_{Zk}.V_{Z1}....V_{Zm}.V_{R}^{n-m-1}.R_{2}.R_{3}....R_{n-m}/R_{T}^{n-m-1}]^{B}, \qquad (3.1.5)$$

where there are m+1 final-stage zeners. Equation (3.1.5) is re-arranged to give

$$V_R = [(G/f.A^n)^{1/B} R_T^{n-m-1}/V_{Zk}.V_{Z1}....V_{Zm}.R_2.R_3....R_{n-m}]^{1/n-m-1}. \quad (3.1.6)$$

This is used with (3.1.4) to define the overall voltage necessary for a desired gain.

Both of these examples are available for defining the gain of particular photomultiplier and divider circuits, given the overall operating voltage. Alternatively, the operating voltage may be set for a desired gain. The constants $f.A^n$ and B are found by solving (3.1.2) simultaneously for two values of gain at respective operating voltages. The method assumes that the manufacturers specification was obtained using a standard divider circuit, defining the resistor chain and zener voltages. Once the constants have been found, they apply to any variation from the standard circuit. Section 3.4 includes an application of the equations and method to the selected photomultiplier. A circuit for the DIAL system was designed according to operational limitations defined in section 3.2 and applied in section 3.4.

3.1.4 Time Response and the Dynode Structure

This sub-section provides the informative basis for selecting a tube (section 3.3) with the time resolution and gain linearity required for spatial resolution and accurate power representation in lidar. The time spread of the tube is expressed in sub-section 3.1.5.

The time response of a photomultiplier is described by the rise-time and the full width at half maximum (shortened to fwhm) of an output arising from the multiplication of a single cathode electron. The magnitudes of these factors are dependent on the structure of the dynode chain. Photocathode response time can be assumed to be negligible in the face of

the time spread arising from differing electron paths between the dynodes. This spread is reduced in certain types of focused multiplier structures where all electrons traverse the same path length. Four types of multiplier are illustrated in figures 3.1.6(a) to (d) (EMI catalogue, 1979; Photo-electronic Devices, Dance). The dynodes of figures 3.1.6(a) are called venetian blind, each being made of several plates inclined at 45° to the tube axis and having a grid to collect stray, low energy electrons. This type has the advantage of large input area though it has the relatively slow response of 5 to 10 ns. rise time and 15 to 20 ns. fwhm (EMI catalogue, 1979). The box and grid structure of figure 3.1.6(b) has an even slower response, with a rise-time of 12 to 20 ns. and a fwhm of 30 to 50 ns. This arrangement forms the internals of a narrow photomultiplier tube. Figure 3.1.6(c) is of the linear focused chain, giving a typical rise-time of 1.8 to 2.2 ns. and a fwhm of 2.7 to 5.5 ns. The circular focused structure of figure 3.1.6(d), the only one without a transparent cathode, is the most compact and is used in small tubes with a side window. This is the fastest tube, with a rise-time of 1 to 2 ns. and a fwhm of 2 to 5 ns. However, it does not have as high a potential for gain as the linear focused configuration.

Another variable depending on the type of multiplier structure is the linearity of response over the range of signal currents. The best linearity is obtained with a linear focused structure, followed by the circular focused then the venetian blind and the box and grid configurations.

3.1.5 The Pulse Transfer Function

A transfer function is derived to describe the passage, amplification and time spread of a signal from its form as a time-dependent photon distribution, incident upon the photocathode, to a time-dependent current

function at the anode. The anode current is predicted for a delta function current emitted from the cathode, leaving the transfer function to be found by a Fourier transform convolution technique. The transfer function can be applied to any form of cathode function to determine the form of the photomultiplier output.

The transfer function is derived in appendix A3.3 to give

$$H = (G/\sqrt{2\pi}\,\tau_2).\exp(-t^2/2\,\tau_2^2), \qquad (3.1.7)$$

which has a transform

$$\mathcal{F}H = G.\exp(-\omega^2\,\tau_2^2/2); \qquad (3.1.8)$$

τ_2 is the standard deviation of the Gaussian function associated with pulse spread along the tube. Thus, the transfer function describes the Gaussian time response and gain G of the photomultiplier tube and can be applied in convolution with a cathode current function or any optical function expressed as a photon current to derive the form of the anode current. More importantly, the transfer function can be deconvolved with an anode current function to obtain, more precisely, the form of the original optical signal.

Appendix A3.4 outlines the application of the transfer function to the cathode pulse arising from incidence of a Gaussian photon current of the form

$$n'(t) = (n_1/\sqrt{2\pi}\;\tau_o).\exp(-t^2/2\,\tau_o^2), \qquad (3.1.9)$$

to give the form of the anode current as

$$i_a = [\eta e n_i G/\sqrt{2\pi}\,(\tau_o^2 + \tau_2^2)^{1/2}].\exp[-t^2/2(\tau_o^2 + \tau_2^2)], \qquad (3.1.10)$$

assuming negligible cathode response time. In this equation, η is the cathode quantum efficiency, τ_o is the standard deviation of the original pulse and n_i is the total number of incident photons. Equation (3.1.10), in temporal comparison with (3.1.9), shows the time spread imposed by the photomultiplier on an original pulse width, transforming according to

$$fwhm_{pulse}=(fwhm^2_{pulse}+fwhm^2_{photomultiplier})^{1/2} \qquad (3.1.11)$$

If tube time spread, given by the standard deviation, τ_2, occuring in equation (3.1.7), is insignificant when compared with the optical pulse width, expressed in (3.1.9) by the standard devation τ_o, then in this case the anode current of (3.1.10) is a replica in time of the incident pulse of (3.1.9). More generally, the transfer function of equation (3.1.7) becomes merely the tube gain, becoming the equivalences

$$H=G \qquad (3.1.12)$$

$$\mathcal{F} H \equiv G \qquad (3.1.13)$$

under the conditions

$$\tau_2 \ll \tau_o \qquad (3.1.14)$$

Appendix A3.5 describes the application of the transfer function, given in equation (3.1.7), in convolution with the function describing any incident

photon distribution, given by the photon current n'(t). The transfer equation gives the transorm of the anode current, i_a, in

$$\mathcal{L} i_a = \eta e \mathcal{L} n'(t) . \mathcal{L} H. \qquad (3.1.15)$$

The result of the transfer on the Gaussian in the previous paragraph showed the time spread on the pulse in passage through the dynode structure. If this spread is much smaller than the incident pulse width, according to the conditions of (3.1.14), then the transfer function is simplified to the gain, as in (3.1.12) and (3.1.13). In this way equation (3.1.15) can be approximated to give the anode current as

$$i_a \simeq \eta e G n'(t) \qquad (3.1.16)$$

under the conditions of inequality (3.1.14).

3.1.6 The Photomultiplier Output Circuit

This sub-section gives a guide to the form of the output voltage, given a certain anode current function. The results can be applied to predict the form of the signal voltage arising from a lidar return function. The output circuit of the photomultiplier is a load resistor, R_L, and a parallel stray capacitance, C_L, as shown in figure 3.1.7. The following analysis for output voltage is based on the equivalent output circuit in figure 3.1.8, where the anode is considered as an ideal current generator (EMI catalogue, 1979).In general, the anode current, i_a, in the circuit is given by

$$i_a = V/R_L + C_L . dV/dt \qquad (3.1.17)$$

If the time spread of the photomultiplier can be ignored, as described in sub-section 3.1.5, then equation (3.1.16) gives the anode current for substitution into (3.1.17), thus linking the photon current with the output voltage in the expression

$$\eta eGn'(t)=V/R_L+C_L.dV/dt \qquad (3.1.18)$$

The form of n'(t) in lidar is given by the lidar equation in chapter 8.

3.1.6(a) <u>The Output Voltage Arising from a Gaussian Optical Pulse</u>

Equation (3.1.17) is specified for a Gaussian optical pulse by equation (3.1.10) to become

$$[\eta en_1G/\sqrt{2\pi}\,(\tau_o^2+\tau_2^2)^{1/2}].\exp[-t^2/2(\tau_o^2+\tau_2^2)] = V/R_L + C_L.dV/dt \qquad (3.1.19)$$

Equation (3.1.19) is considered with respect to the relation between the R_LC_L time constant of the output circuit and the standard deviation which describes the anode current pulse width (equation (A3.4.3)).

If the constant R_LC_L is much larger than $(\tau_o^2+\tau_2^2)^{1/2}$, then the pulse is integrated in that the anode capacitance is charged to a voltage V_C. Integration of equation (3.1.19) in the limit

$$R_LC_L >> (\tau_o^2+\tau_2^2)^{1/2} \qquad (3.1.20)$$

gives the maximum voltage as

$$V_C = \eta en_1G/C_L. \qquad (3.1.21)$$

In the event that the output circuit response matches the speed of the pulse, in the equality

$$R_L C_L = (\tau_o^2 + \tau_2^2)^{1/2}, \tag{3.1.22}$$

then equation (3.1.19) gives the peak voltage as

$$V_{pk,1} = \eta e n_i G / \sqrt{2\pi}\, C_L. \tag{3.1.23}$$

Thus, the peak is lowered in comparison with the maximum obtained through the pulse integration described above.

When the $R_L C_L$ constant is reduced further, a lowering of the peak response is expected in addition to a narrowing of the output pulse towards the width of the original optical pulse. If $R_L C_L$ is considered negligible, in the limit

$$R_L C_L \ll (\tau_o^2 + \tau_2^2)^{1/2}, \tag{3.1.24}$$

then equation (3.1.19) gives an expression for the peak voltage in

$$V_{pk,2} = \eta e n_i G R_L / \sqrt{2\pi}\, (\tau_o^2 + \tau_2^2)^{1/2}, \tag{3.1.25}$$

which is merely Ohms law applied to the peak anode current.

3.1.6(b) The Output Voltage Arising from a General Optical Pulse

A detected distribution, described generally by the photon current, $n'(t)$, can be assumed to give rise to an output voltage given by equation (3.1.18), which is

$$\eta eGn'(t) = V/R_L + C_L.dV/dt. \qquad (3.1.26)$$

If the constant, $R_L C_L$ is small in comparison with the duration of temporal changes, dt, in $n'(t)$ then equation (3.1.26) can be approximated (dt large) to give the peak voltage response in the expression

$$V_{pk,max} = \eta eGR_L n'(t). \qquad (3.1.27)$$

A large constant integrates the entire photon distribution and is not usually desirable in a lidar application where range resolution is required. However, for short pulsed returns and where range averaging is acceptable, the signal may be integrated over its whole extent in charging the anode capacitance. The maximum voltage attained across the output is given by

$$V_C = \eta eG/C_L \int_{t_1}^{t_2} n'(t)dt. \qquad (3.1.28)$$

This is the general form of equation (3.1.21) and effectively measures the total number of photons collected.

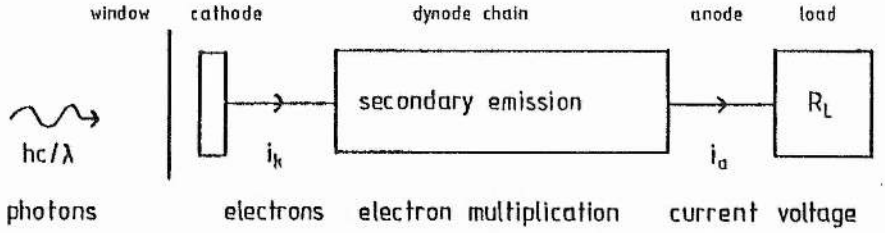

Figure 3.1.1 Block schematic of photomultiplier action

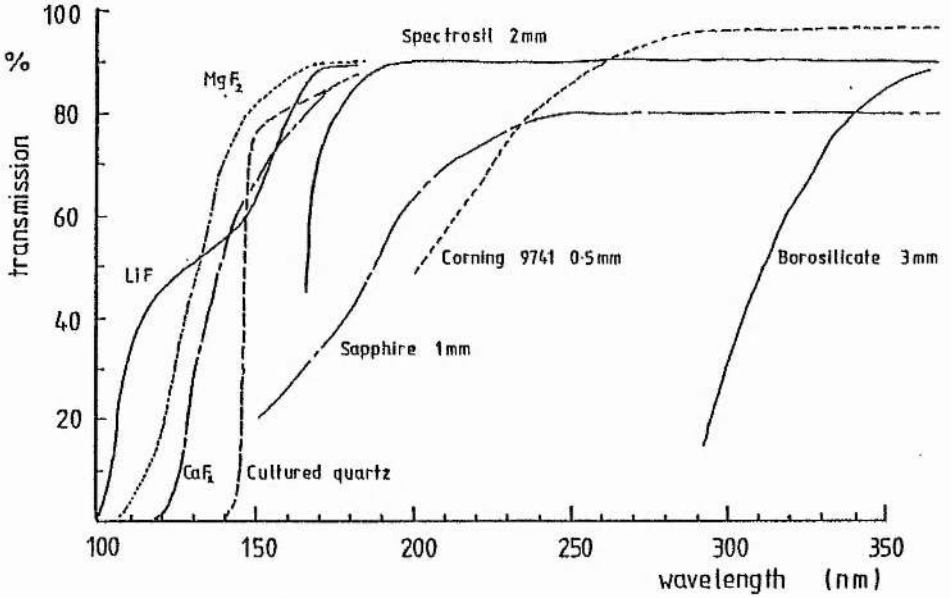

Figure 3.1.2 Spectral transmission characteristics of photomultiplier windows (EMI catalogue, 1979)

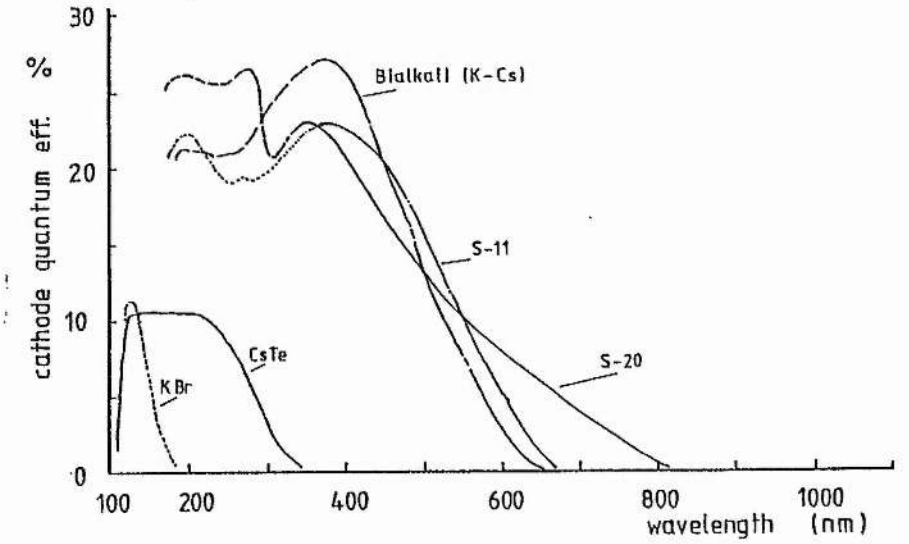

Figure 3.1.3 Spectral response of photocathode materials (EMI catalogue, 1979, Hamamatsu catalogue, 1980, RCA catalogue, 1979)

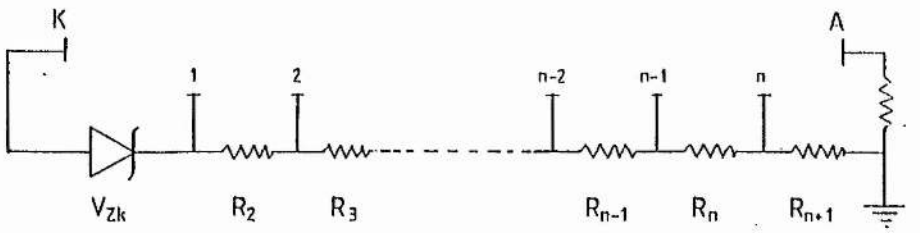

Figure 3.1.4 A mainly resistive photomultiplier voltage divider chain for n dynodes

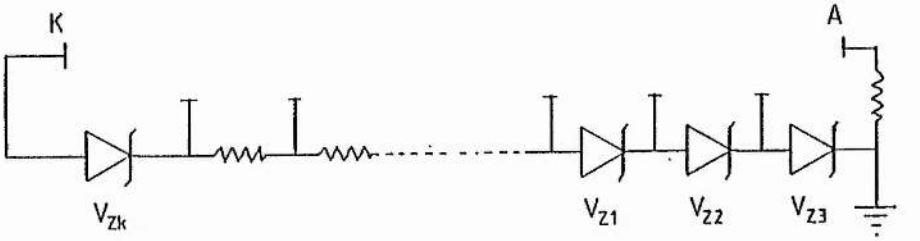

Figure 3.1.5 A resistive photomultiplier voltage divider chain for n dynodes but with first and final stage zener voltages for better stability

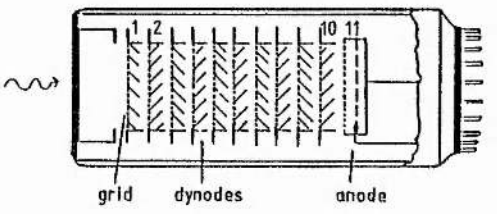

(a) Venetian blind

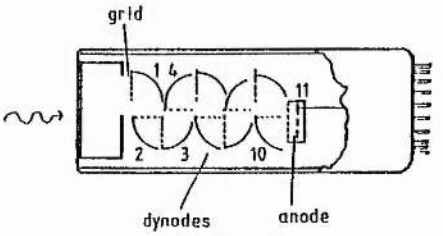

(b) Box and grid

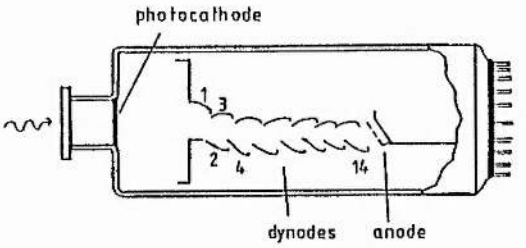

(c) Fast linear focused

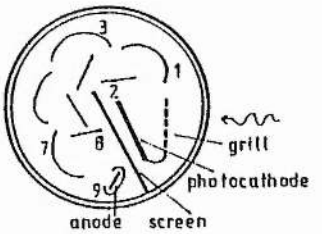

(d) Circular focused

Figure 3.1.6(a) to (d) Four types of dynode multiplier structure

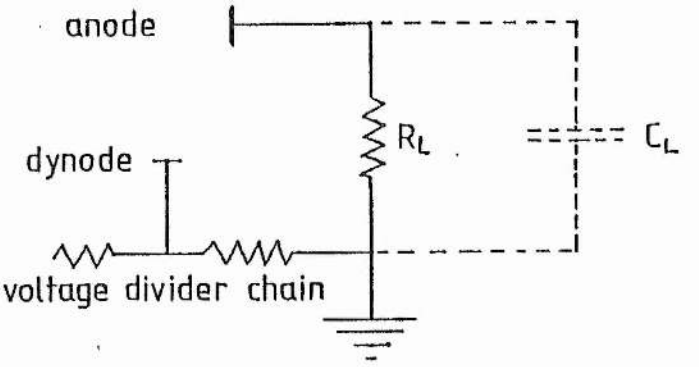

Figure 3.1.7 Photomultiplier O/P circuit showing the stray load capacitance

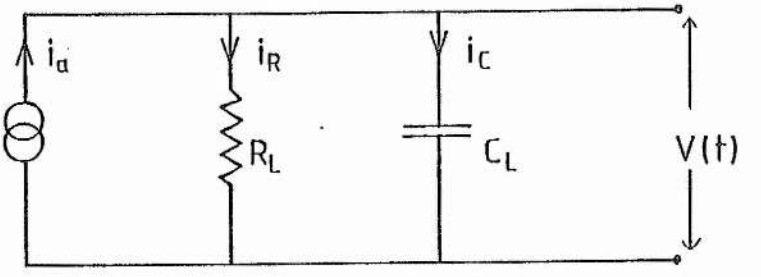

Figure 3.1.8 An equivalent O/P circuit for the photomultiplier

3.2 Photomultiplier Operating Conditions

A photomultiplier has certain limitations which must be observed to ensure device longevity. These limits are readily obtained from manufacturers recommendations. It is also important to consider those operational parameters which restrict the handling of the detected signal. All the factors are combined to decide upon tube operation parameters (voltage, divider chain resistances, output cicuit) and to define signal limitations (maximum input power decided by anode or cathode limits or from response linearity requirement). The tube itself must be chosen to be compatible with the optical signal to be detected and to give the required electrical output for analysis. The main areas for consideration are outlined, with a summary of the associated problems, in table 3.2.1. This section is concerned with the points mentioned in table 3.2.1 to provide a recipe for operating the lidar system photomultiplier, applied in section 3.4. Detailed descriptions of the factors to consider are given in the appendices A3.6 to A3.12 and the conclusions are outlined in the sub-sections below.

3.2.1 Summary of Photomultiplier Operating Conditions

This sub-section lists the equations which have been derived in the preceding appendices of the section for application to photomultiplier operating limits and divider circuit design. Additional points and manufacturers recommendations are included. Specific notes apply to pulse detection. The general circuits outlined in figures 3.2.1 and 3.2.2 are examples which were evolved from the procedure followed here and they are in fact standard EMI configurations.

3.2.1(a) Preventing fatigue of the cathode and the anode

Given average current maxima $i_{k\ max}$ and $i_{a\ max}$, the pulse repetition rate, S, and cathode and anode charge, Q_k and Q_a respectively, are limited according to expressions derived in appendices A3.6 and A3.7 to give

$$(Q_k S)_{max} = \bar{i}_{k\ max}, \tag{3.2.1}$$

$$(Q_a S)_{max} = \bar{i}_{a\ max}; \tag{3.2.2}$$

The charge Q_a arises from a cathode charge pulse Q_k after a gain G. In considering $Q_{k\ max}$ and $Q_{a\ max}$ given by (3.2.1) and (3.2.2), the lower **effective** signal level sets the limit on the incoming signal intensity.

3.2.1(b) Maximum overall voltage

A maximum voltage is set by the manufacturer or by experiment to eliminate after-pulses and breakdown.

3.2.1(c) Cathode-to-first-dynode voltage set by zener diode

3.2.1(d) Final stage voltages

The requirement for linearity under conditions of high current signal pulses necessitates that final dynode voltages are increased by using higher divider resistances, as shown in figures 3.2.1 and 3.2.4. Alternatively, the final voltages can be stabilised for linearity by using zener diodes in the arrangement in figure 3.2.2, allowing high current pulses. The limits concern divider current, i_d, anode charge and duration, Q_a and $fwhm_{anode}$ respectively, and pulse repetition rate, S. Using equations (A3.10.15) and (A3.10.16) with (A3.7.2) and (A3.7.3) these limits are given as

$$Q_a S < i_d, \tag{3.2.3}$$

$$Q_a / fwhm_{anode} >> i_d, \tag{3.2.4}$$

where i_d is given by chain voltage and resistance as $i_d = V_R/R_T$.

3.2.1(e) First-to-second-dynode divider resistance

The first-dynode-to-second-dynode voltage, V_1, is set at a minimum of 100 volts (EMI catalogue, 1979) by a zener diode or a minimum resistance in the divider, depending on minimum likely overall voltage, $V_{o\ min}$. In the non-evaluated circuit of figure 3.2.1, this impedance, R_1 is given by

$$R_1 = 16.5RV_{1\ min}/(V_{0\ min} - V_{k-d1} - V_{1\ min}). \tag{3.2.5}$$

The value of R is defined by the circuit configuration and the total chain resistance.

3.2.1(f) Total divider circuit resistance and resistor values

The total divider circuit resistance is restricted by the linearity requirement, L, and the maximum resistor power rating, W, in the expression (from (A3.10.12))

$$2V_{R\ max}^2/n_R W < R_T < L.V_{R\ min}/(Q_a S)_{max}, \tag{3.2.6}$$

where V_R is the voltage across the resistive stages, n_R is the number of dynodes, S is the pulse repetition rate and Q_a is the charge in the anode pulse. The product $(Q_a S)_{max}$ is subject to satisfying the fatigue conditions of (3.2.1) and (3.2.2). The total resistance of the circuit in figure 3.2.1 is, in general, given by

$$R_T = 16.5R + R_1. \qquad (3.2.7)$$

3.2.1(g) Maximum load resistance

If linearity, L, is to be maintained, the load resistance, R_L, cannot exceed a certain value, given by equation (A3.11.3) as

$$R_{L\ max} = L.V_{n\ min}/\bar{i}_{a\ max}, \qquad (3.2.8)$$

where $V_{n\ min}$ is the minimum likely voltage across the final stage, to ground (figure 3.2.4).

3.2.1(h) Final stage capacitors

Capacitors on the final stages help to maintain linearity, as explained in appendix A3.12. The final stage capacitance value is chosen to remain within the limits set by inequalities (A3.12.4) and (A3.12.5), giving

$$Q_{a\ max}/V_{n\ min}L < C_d < 1/R_cS_{max}, \qquad (3.2.9)$$

where R_c is the charging voltage fixed in the determination of the total circuit resistance (see figure 3.2.3) and circuit configuration. In applying (3.2.9) C_d is maximised and the lower limit is only applied as a guard on $Q_{a\ max}$, the signal level, to protect the linearity requirement. The use of de-coupling capacitors allows the peak pulse current to far exceed the divider current as long as the average current is much lower. This is described by signal vs divider current limits in (A3.10.13) and (A3.10.14) which are expressed using (A3.7.2) and (A3.7.3), relating pulsed to average current values, to give

$$Q_a S \ll i_d \tag{3.2.10}$$

and

$$Q_a / fwhm_{anode} \gg i_d. \tag{3.2.11}$$

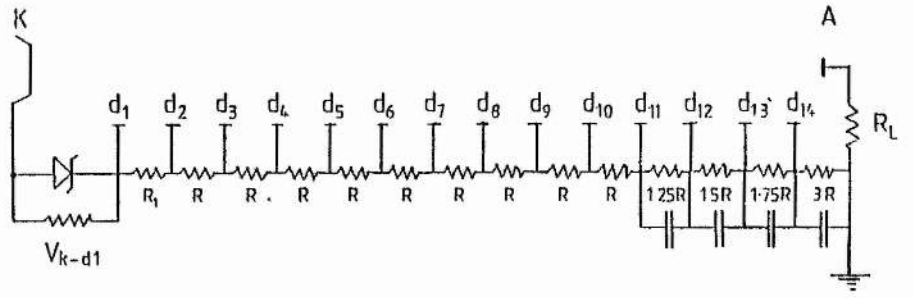

Figure3.2.1 A mainly resistive divider circuit configuration for a 14-stage photomultiplier used in the detection of fast pulses

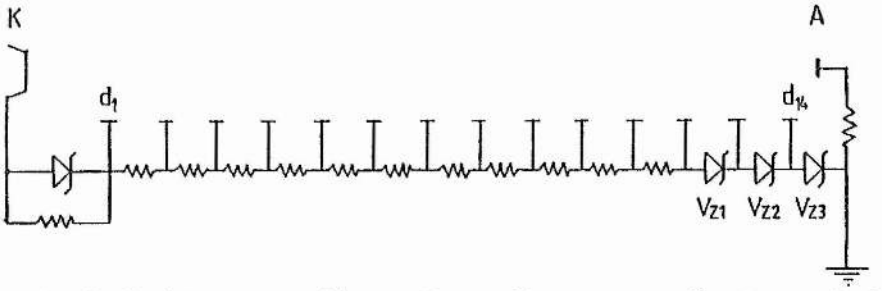

Figure 3.2.2 A divider circuit configuration for a 14-stage photomultiplier used in the detection of fast pulses but with the use of final stage zener voltage stabilisation to allow overall gain adjustment whilst maintaining response linearity

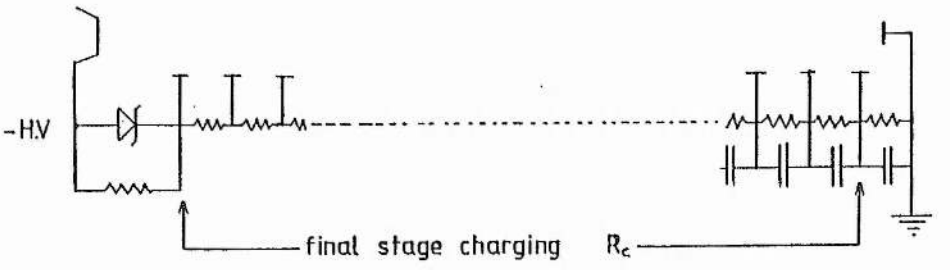

Figure 3.2.3 Re-charging of the final stage de-coupling capacitors, indicated on a divider circuit layout

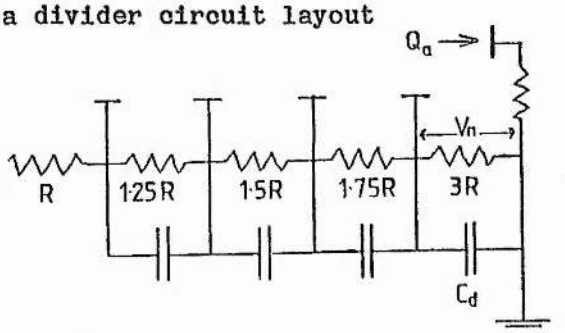

Figure3.2.4 De-coupling capacitors and increased voltages on the final stages of a photomultiplier divider circuit

Table 3.2.1 Summary of Photomultiplier Operating Limits

Parameter	Location	Problem
Cathode current	Cathode	Cathode fatigue
Cathode-to-first-dynode voltage	Multiplier structure	After pulsing from residual gas ionization
Interdynode voltage		Loss of linearity from space charge effects
Overall voltage		Feedback current
Anode current	Anode	Anode fatigue
		Loss of linearity
Load resistance	Output circuit	Pulse repetition rate
Load capacitance		Pulse pile-up
Zener voltages	Divider circuit	Linearity
Resistances		Linearity, circuit heating
De-coupling capacitances		Linearity

3.3 Choosing a Photomultiplier for DIAL

The aspects of photomultiplier structure and operation which are applicable to various requirements are discussed in the main in section 3.1. This section describes the selection of the photomultiplier especially for the requirements of the $XeCl^*$ excimer laser differential absorption lidar.

3.3.1 Window

The radiation to be collected, at the $XeCl^*$ laser wavelength of around 308 nm., necessitated a U.V transmitting window like those examples given in figure 3.1.2. A transmission of at least 90% was to be expected.

3.3.2 Photocathode

According to figure 3.1.3 a considerable choice of photocathodes, if used with a U.V window, give a lower wavelength response, at 308 nm., with a quantum efficiency ranging between 15% and 25%. However, there are tubes with high work function cathodes, of CsTe or RbTe, which have a response cut-off at about 360 nm. Although the quantum efficiency is only about 1%, this partially solar blind feature (solar radiation extends down to 310 nm.; section 3.6) is used with a narrow band filter and iris to cut out the background radiation which would otherwise interfere with lidar operation in daylight. Another useful property of this type of cathode is the low level emission of thermal electrons, so that a typical dark current is much less than 1 nA, thus avoiding the necessity of cooling the tube. A circular cathode shape is more efficiently employed at the focal plane of the lidar telescope, supporting the choice of the head-on, rather than the side-on, type of photocathode.

3.3.3 Dynodes and Multiplier Structure

The choice of dynode material and configuration influences tube gain, response time and gain linearity. The high gain desired in measuring low level lidar signals from greater ranges or from high absorption volumes necessitates as many multiplying stages as possible. There is a requirement for high temporal and therefore high spatial resolution in defining a sample element in gas concentration measurement. To these ends the most suitable type of dynode structure is the fast linear focused, illustrated in figure 3.1.6(c). The dynode material itself is chosen according to linearity, a factor which is important in DIAL where the concentration is calculated from the difference between signals of different intensity. It is for this reason that BeCu dynodes are preferred to those of CsSb.

3.3.4 Tube Choice

The products of three manufacturers were considered; all end window types with fast, linear focused multiplier structure. These are listed in table 3.3.1. The EMI G26H314LF was selected in preference to the others on the grounds of higher gain, faster response and greater cathode area. The specification of this tube is given in table 3.3.2.

Table 3.3.1 Photomultipliers suitable for DIAL

EMI	G26H314LF	Solar blind, special U.V
Hamamatsu	R 821	Solar blind
RCA	C 70128	

Table 3.3.2 Specification of the EMI G26H314LF P-M

Spectral Response	110 nm to 360 nm
Cathode material	CsTe
Window material	MgF_2
Cathode quantum efficiency	
@ 180 to 220 nm (peak)	15%
@ 300 nm	1.3%
@ 350 nm	0.25%
Gain at 1326 volts	10^5
Gain at 1605 volts	10^6
Dynode structure	14 stage, linear focused
Rise time	2.2 ns
Pulse width (fwhm)	3.4 ns

3.4 Theory Applied to Operating the EMI G26H314LF Photomultiplier

The divider circuit is designed using the summary in sub-section 3.2.1, taking each factor for evaluation. The operating limits on applied voltages and acceptable signal levels (in terms of the anode signal) are defined. The gain equation (3.1.2) of sub-section 3.1.3 is applied.

3.4.1 Divider Circuit Design and Definition of the Operating Limits

3.4.1(a) Fatigue and space charge limitation

The absolute maximum average values (in a 30 second period) of cathode and anode currents quoted by EMI are

$$\bar{i}_{k\ max} = 5\ nA, \tag{3.4.1}$$

$$\bar{i}_{a\ max} = 200\ \mu A. \tag{3.4.2}$$

The anode limitation is reached if the maximum cathode current is amplified by only 4×10^4 times, lower than the expected minimum operational gain of 10^5. Thus, the limit on signal level is imposed by the anode current. The limit on the anode current under operating conditions is kept to 1/100 of the fatigue limit so that the charge/repetition rate product given by equation (3.2.2) is

$$Q_a S < 2\ \mu A. \tag{3.4.3}$$

3.4.1(b) Maximum overall voltage

The manufacturer indicates a maximum of 3000 volts overall and a typical voltage of 2300 volts. However, experience of after-pulses with another EMI fast linear focused tube (9594 QUB) suggested that it should be kept below 1800 volts. The gain of the supplied photomultiplier was specified at 1600

volts overall.

3.4.1(c) Cathode-to-first-dynode voltage

The cathode-to-first-dynode voltage (stabilised by zener diodes) recommended by EMI is

$$V_{k-d1} = 300 \text{ volts.} \qquad (3.4.4)$$

3.4.1(d) Final stage voltages

The four final stage voltages are elevated by higher resistances 1.25R, 1.5R, 1.75R and 3R respectively (figures 3.2.1 and 3.2.4). The value of R is defined by the total resistance in 3.1.4(f).

3.4.1(e) First-to-second-dynode divider resistance

EMI recommend a voltage minimum, $V_{1\ min}$, of 100 volts between the first and second dynode. The appropriate resistance, R_1 is set by using equation (3.2.5) with equations (3.4.4) and (3.4.6), below to give

$$R_1 = 1.83R. \qquad (3.4.5)$$

3.4.1(f) Total divider circuit resistance and resistor values

The total divider resistance limits are given by (3.2.6). EMI quote gain figures for the tube as 10^5 at 1326 volts and 10^6 at 1605 volts. Therefore the overall voltage minimum is set by

$$V_{o\ min} = 1300 \text{ volts.} \qquad (3.4.6)$$

The resistive voltage minimum, by equation (3.1.1) for $V_{Zk} = 300$ volts, is

$$V_{R\ min} = 1000 \text{ volts.} \qquad (3.4.7)$$

The absolute voltage maximum is set by the manufacturers handbook at

$$V_{o\ max} = 2300 \text{ volts,} \qquad (3.4.8)$$

giving

$$V_{R\ max} = 2000 \text{ volts.} \qquad (3.4.9)$$

Circuit components are defined using the information outlined. For compactness, 1/2 watt resistors are the most suitable. This assumes that 1/2 watt is dissipated, on average, via each of $n_R = 14$ resistors. The signal limitation, $(Q_a S)_{max}$, is given by equation (3.4.3). Linearity is restrained to within 1%. With these values equation (3.2.6) gives the bounds on total resistance as

$$1.14M < R_T < 5M\Omega. \qquad (3.4.10)$$

Bearing in mind that the lower limit is set by the power restriction for a maximum voltage which is not likely to be applied it was advantageous from a linearity point of view to set the resistor chain at the value

$$R_T = 1.14M\Omega. \qquad (3.4.11)$$

The total resistance of the divider circuit in figure 3.2.1 is expressed by equation (3.2.7) which, combined with equation (3.4.5) gives

$$R_T = 18.33R\Omega. \qquad (3.4.12)$$

Applying a total resistance of 1.14MΩto this, gives

$$R = 62k\Omega, \qquad (3.4.13)$$

allowing each resistor to be set to the standard values closest to that indicated in figure 3.2.1. The divider circuit, with component values, is illustrated in figure 3.4.1. The total resistance is now 1.135MΩ. R_1 is evaluated according to (3.4.13) and (3.4.5) to give the nearest standard at

$$R_1 = 110k\Omega. \qquad (3.4.14)$$

The resistors across the zeners are set to drop a voltage which is a few percent greater than the 300 volts.

3.4.1(g) Maximum Load Resistance

Equation (3.2.8) is used to define the maximum load resistance if a linearity of 1% is not to be exceeded. The final stage voltage, $V_{n\ min}$, shown in figure 3.2.4, is defined by circuit resistances and the minimum voltage to give

$$V_{n\ min} = V_{R\ min}3R/18.33R. \qquad (3.4.15)$$

This is used in (3.2.8) with values from (3.4.2) and (3.4.7) to give

$$R_{L\ max} = 818k\Omega. \qquad (3.4.16)$$

3.4.1(h) Final Stage Capacitances

Capacitance values on the final stages are maximised to maintain linearity at high pulsed levels. The upper limit is set in (3.2.9) by the resistive chain and the maximum pulse repetition rate. The maximum pulse repetition rate is limited in laser operation and is given by

$$S_{max} = 20 \quad \text{pps.} \tag{3.4.17}$$

In the circuit in figure 3.4.1 the four capacitors each charge through the resistances making up R_c as given in the table 3.4.1 which lists the respective upper limits on each capacitance. This sets all four final stage capacitors at

$$C_d = 47 \text{ nF.} \tag{3.4.18}$$

This value of capacitance, applied in the lower limit of (3.2.9), using (3.4.15) for $V_{n\,min}$, gives the maximum anode charge pulse, limited by the 1% linearity requirement to

$$Q_{a\ max} = 7.69 \times 10^{-8} \text{ coulombs.} \tag{3.4.19}$$

If the product $(Q_a S)_{max}$ is formed from (3.4.19) with (3.4.17) then a value of 1.54 μA is obtained as the maximum allowed charge/repetition rate product, falling within the fatigue limit defined by (3.4.3).

3.4.1(i) Circuit Construction

The circuit in figure 3.4.1 was constructed and housed in a shielded box with connections to the photomultiplier via a D-plug, providing a totally shielded assembly and the option of changing the circuit without disturbing

the tube. The voltages expected and measured between photomultiplier stages are listed in table 3.4.2, including the corresponding pin and D-plug numbers. The load resistor is mounted within a fuse holder, allowing it to be changed at will (as long as the value is kept withim limits set by (3.4.16).

3.4.2 Gain Equations (section 3.1.3) Applied

Equation (3.1.2) for gain is applied to the EMI G26H314LF photomultiplier and the divider circuit resistances shown in figure 3.4.1. Equation (3.1.2) gives

$$G = f.A^{n}(V_{Zk}V_{R}^{n-1}R_{2}R_{3}....R_{n}/R_{T}^{n-1})^{B}, \qquad (3.4.20)$$

where V_R is given by the overall voltage and the zener voltage in equation (3.1.1), re-written as

$$V_{R} = V_{o} - V_{Zk}, \qquad (3.4.21)$$

where (3.4.4) gives the value of V_{zk}. The constants A and B are found by simultaneous equations of (3.4.20) set up from the specification supplied with the tube. EMI quote a gain of 10^5 at an overall voltage of 1326 volts and a gain of 10^6 at an overall voltage of 1605 volts. Thus (3.4.20) becomes

$$10^{5} = f.A^{14}(9.595 \times 10^{25})^{B}, \qquad (3.4.20a)$$

and

$$10^{6} = f.A^{14}(2.188 \times 10^{27})^{B}. \qquad (3.4.20b)$$

Equations (3.4.20a) and (3.4.20b) give

$$f^{1/14}A = 0.0978 \qquad (3.4.22)$$

and

$$B = 0.7365. \qquad (3.4.23)$$

The gain equation for the photomultiplier and constructed circuit, allowing for variable voltage, is given by

$$G = 7.324 \times 10^{-15}[6.872 \times 10^{-14}(V_o - 300)^{13}]^{0.7365}. \qquad (3.4.24)$$

The gain is plotted for overall voltage in figure 3.4.2.

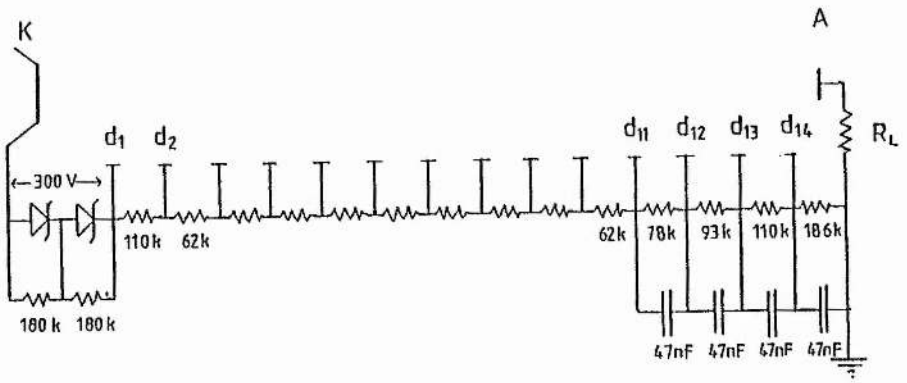

Figure 3.4.1 The divider chain circuit for application to the EMI G26H314LF photomultiplier in XeCl* excimer laser DIAL

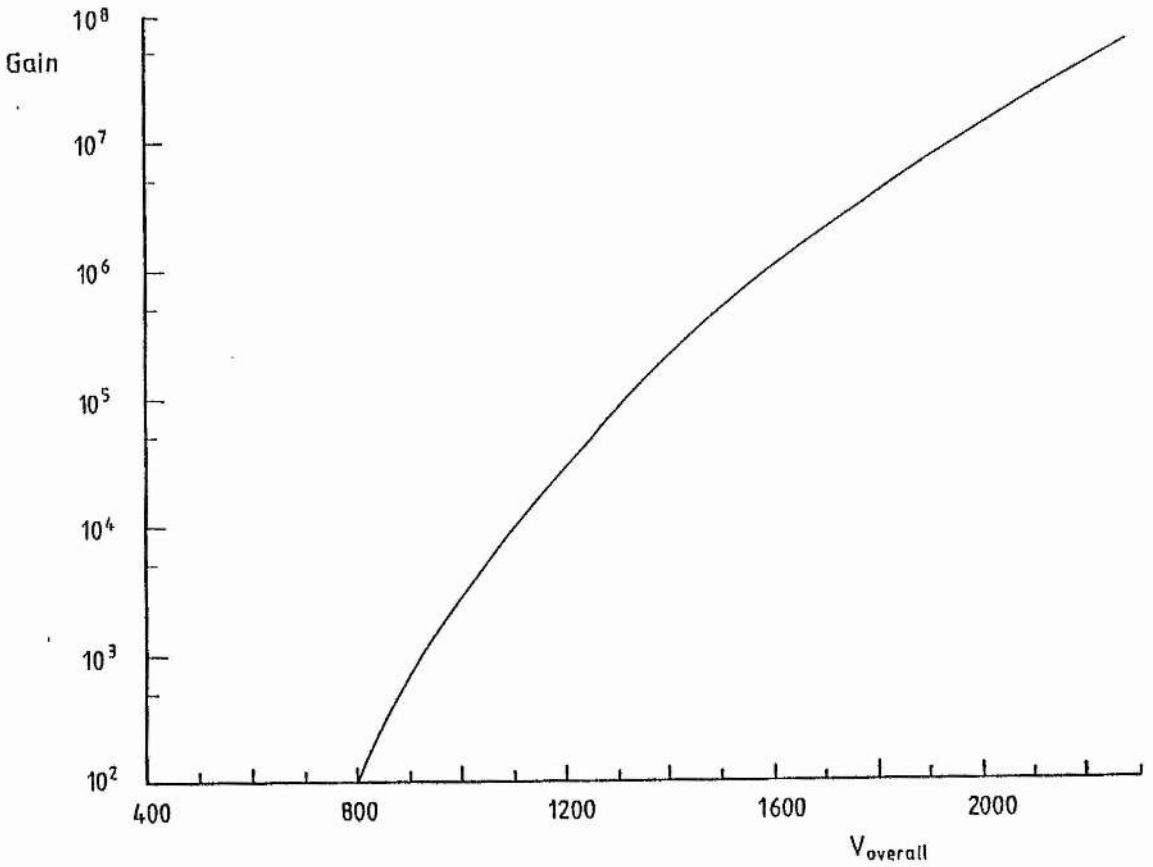

Figure 3.4.2 Gain/voltage characteristic (expected) in the EMI G26H314LF photomultiplier using the divider circuit of figure 3.4.1

Table 3.4.1 Maximum final stage capacitance values set by the linearity requirement at high current pulses

Stage	Divider Stage Resistance, R_d(kΩ)	Charging Resistance, R_c(MΩ)	Maximum $C_{d\ max}$(nF)
d_{14} to earth	186	0.949	52.7
d_{13} to d_{14}	110	1.025	48.8
d_{12} to d_{13}	93	1.042	48.0
d_{11} to d_{12}	78	1.057	47.3

Table 3.4.2 Photomultiplier Divider Circuit Voltages

Stage	Pins	D-plug	Resistance		Voltages @ 1300/1600 V			
			nom.	meas.	calculated		measured	
					1300	1600	1300	1600
k-d_1	19-2	2-4	Zener		300	300	299	301
d_1-d_2	2-16	4-6	120	122	107	139	106	138
d_2-d_{11}(9)	16-7	6-22	558	553	485	630	476	619
d_{11}-d_{12}	7-11	22-20	75	75.5	66	86	65	85
d_{12}-d_{13}	11-8	20-18	91	93.5	82	107	81	105
d_{13}-d_{14}	8-10	18-16	120	117.6	103	134	102	132
d_{14}-earth	10-earth	16-earth	180	180.8	158	206	156	203

3.5 Housing and Shielding

The mounting of the photomultiplier and the way in which it is shielded from external noise is described. The object was to mount the photomultiplier in a light-tight unit which provided shielding from r.f radiation, a cooling facility, filter and iris mounting and easy divider circuit access for servicing and alteration. The reasons for employing a filter and iris are contained within section 3.6. Figure 3.5.1 is a sectional schematic showing the layout of the final detector unit.

The graphite-coated envelope of the photomultiplier is connected to raise it to cathode potential to prevent internal variable background from electro-luminescence.

The photomultiplier is surrounded by a grounded cylindrical shield contained within another grounded housing of heavy gauge brass, with the ends closed off by a plate containing the external connection and by a close-fitting mount holding the filter. This arrangement encloses and screens the detector, except for where the filter is placed, and allows an external divider circuit to be plugged in at the female screened D-plug connector. The divider circuit, described in previous sections, designed in this work for the lidar application, is mounted within a small screen enclosure fitted with the male D-plug connector for the photomultiplier supply and with the H.V input and signal output sockets. This feature of divider circuit configuration isolates the detector from circuit heating and permits circuit interchangeability for any change in detection mode (eg. DC detection) and allows easy servicing.

The cooling facility was included in the apparatus to reduce dark current

arising from thermal emission of electrons from the photo-cathode. In the end the precaution was unnecessary due to the vanishingly small anode dark current in the chosen tube, stated by the manufacturer to be 4×10^{-12} A (specification, table 3.2.2). However, the option exists to cool the tube if the lidar system was operated in a hot environment, allowing the temperature to be maintained at around $15^{\circ}C$. Temperature stabilisation in any event is improved by brass blocks which are brazed onto the screen casing. Cooling is by a thermoelectric frigistor array, using the Peltier effect, whereby one side is cooled and the other side is heated when a high current, typically 15A to 20A, is passed through the elements. Heat is removed from the frigistor by air cooling, with the option of fan assistance.

The adjustable iris is positioned just outside the filter, giving control over the extent of the detected received field. The entire detector unit is secured to a frame which is adjustable on the telescope to permit coincidence of the photocathode with the telescope focal plane region. The position of the photocathode with respect to the telescope optical axis is determined by field of view and image size limitations, described in chapter 2, on the telescope dimensions.

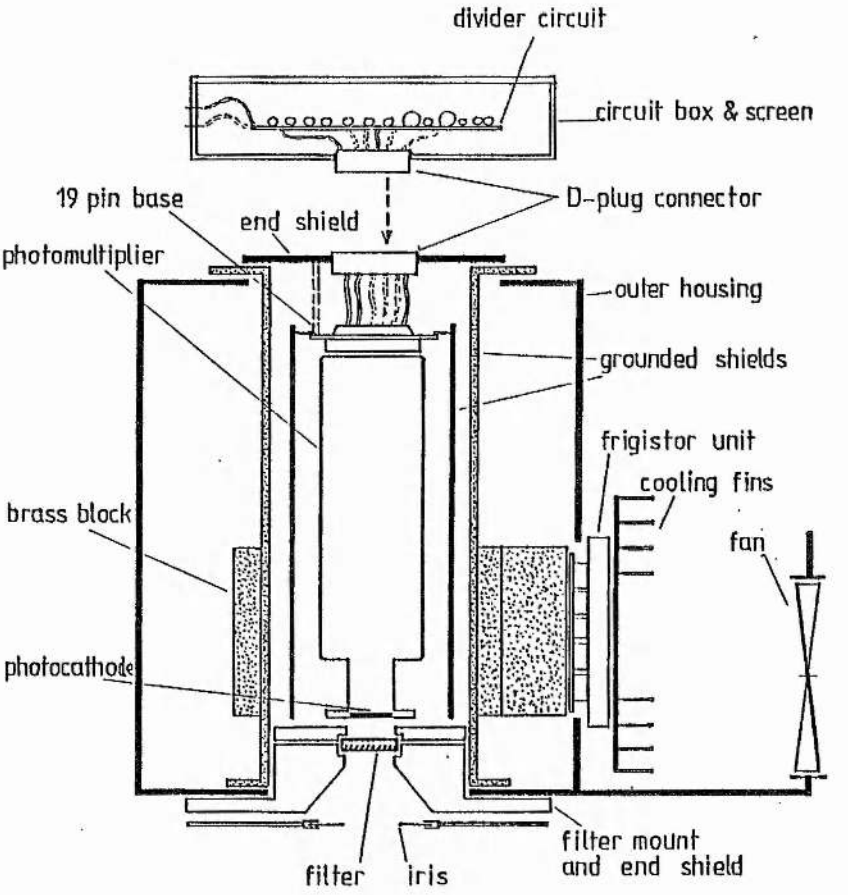

Figure 3.5.1 Schematic of the photomultiplier in its screened housing, showing the positioning of the divider circuit

3.6 Solar Background Precautions

In measuring the low light levels of a lidar return signal any background interference is to be avoided. The solar radiation, scattered or direct, reaching the ground can present a problem in lidar detection necessitating the use of a narrow band filter centred on the detected wavelength. Experiments at the nitrogen laser wavelength of 337.1 nm suffered from background problems. The selection of a near solar blind photomultiplier for this work eliminated any background from 360 nm to higher wavelengths. Before selecting the filter an experiment was performed to take a spectrum of scattered solar radiation at ground level to find the wavlength cut-off by ozone absorption in relation to the lidar operating wavelengths around 308 nm. This experiment and the narrow band interference filter is described in this section.

3.6.1 Solar Spectrum at Ground Level

A spectrum of scattered daylight was recorded with a Carl Zeiss Q24 Spectrograph possessing a range capability of 200 to 570 nm, although the region of interest is 300 to 400 nm. The Carl Zeiss G11 Microdensitometer and G1 B1 Potentiometric Recorder were used in combination to make a plot of the plate density with respect to wavelength, part of which is reproduced in figure 3.6.1(a). Quantitative calibration for atmospheric transmission would have been unnecessarily tedious in an investigation to certify merely the existence of certain wavelengths at ground level. However, figure 3.6.1(b) is a more useful guide, having been derived from figure 3.6.1(a) by applying a logarithmic correction to the ordinate axis, justified by the expected logarithmic correlation between the density of the developed spectrogram and the level of incident radiation. The spectrum shows absorption due to the Huggins and Hartley bands of electronic

transitions in ozone with some finer structure from the vibration-rotation bands (Kondratyev, Radiation in the Atmosphere, 1969). The trace proves the presence of radiation at 337.1 nm but at 308 nm on the edge of the Hartley band (Uchino et al, 1979) it shows none, unless obscured by noise. This ozone absorption is very helpful in reducing background in the $XeCl^*$ laser DIAL system but it restricts application to lidar range heights below about 10 km where the ozone layer starts to build up to its maximum at about 22 km (Green, 1964). At these altitudes the absorption cross section near 308 nm is of the same magnitude as that for SO_2 (Houghton, 1977, The Physics of Atmospheres).

3.6.2 Narrow-band Filter

A filter is required at the detector to eliminate background radiation from around 308 nm to the solar blind photomultiplier cut-off around 360 nm. The ideal pass-band of a filter is as narrow as possible but broad enough to allow passage of the $XeCl^*$ laser spectrum, with peaks at 307.92 and 308.17 nm, with low loss. A narrow band filter, centred on 308.05 nm, with a 0.3 nm fwhm, would have been ideal but costly as a custom made component. In view of the low background level around 308 nm (see figure 3.6.1(b)) a much cheaper, "off the shelf", Corion Corp. (Laser Lines) filter with a fwhm of 10 nm, centred at the zinc line at 307.1 nm, is quite adequate. A peak transmission of 20% is greater than that of a filter of narrower bandwidth.

Figure 3.6.2 shows the passband of the selected filter. Figure 3.6.3 is an interpretation of the solar spectrum from the corrected trace of figure 3.6.1(b), drawn on the same wavelength scale as figure 3.6.2. Figure 3.6.4 is of the solar radiation expected to be passed by the filter, peaking around 312 nm. This is passed at the side of the filter pass-band so that, occuring where solar radiation is at a low level (figure 3.6.1(b)), the

background detected by the photomultiplier is expected to be low. This is confirmed by a lidar experiment with the $XeCl^{\#}$ laser system (chapter 8) where no background was measureable.

In assessing the suitable application of the zinc line filter it was useful to investigate the effect of a cone of convergence at the telescope focus on shifting the peak of transmission to lower wavelength. the shift is described by the expression (Oriel filter catalogue)

$$\lambda_1/\ \lambda_o = [1 - (1/2)(n_e/n^{\#})^2 \sin^2(\tan^{-1}(1/2f:))], \qquad (3.6.1)$$

where λ_o and λ_1 are the original and lower peak wavelengths respectively, n_e and $n^{\#}$ are the refractive indices of the environment and the filter substrate respectively and f: is the focal ratio of the non-parallel beam. For the f:5 focal ratio of the DIAL telescope and a substrate index of 1.45 the shift of the peak from 307.1 nm is by 0.24%, a shift to lower wavelength of only 0.7nm.

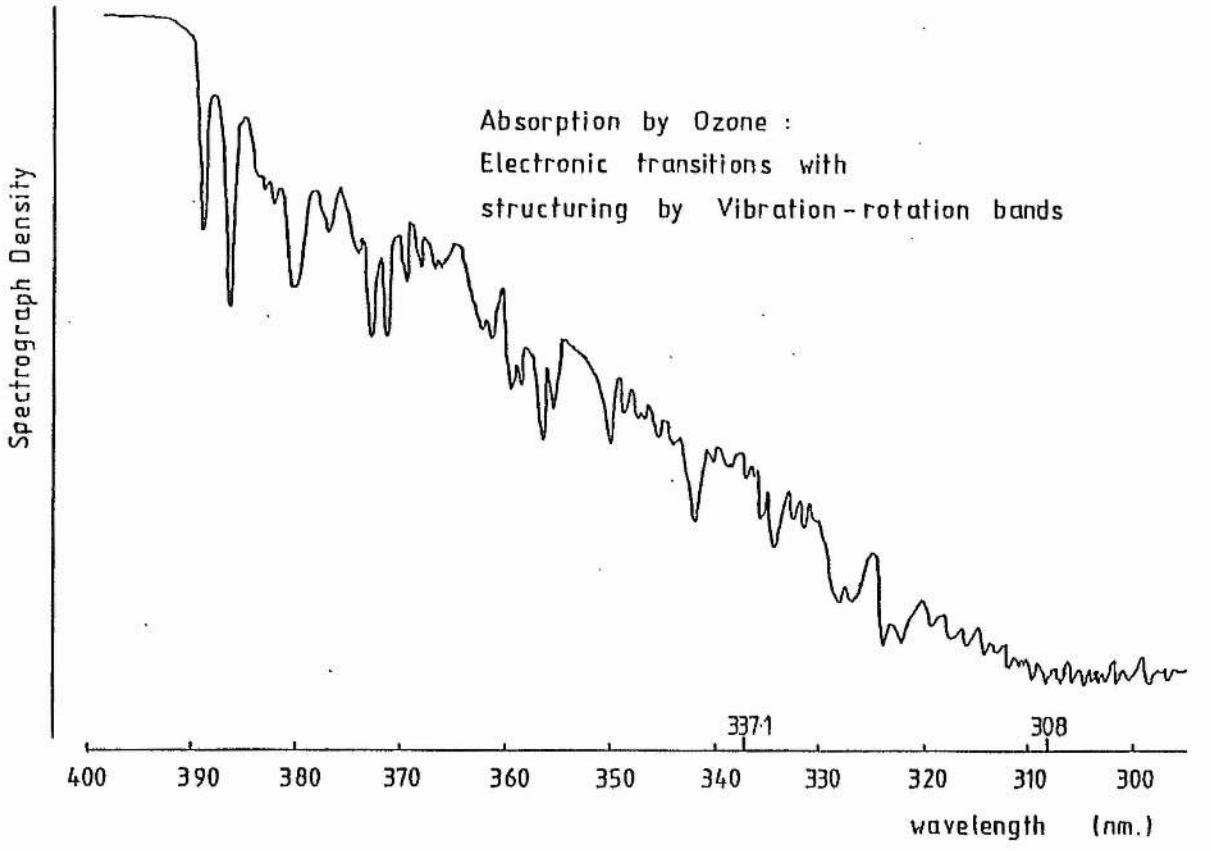

Figure 3.6.1(a) Micro-densitometer trace from a spectrogram of the solar spectrum

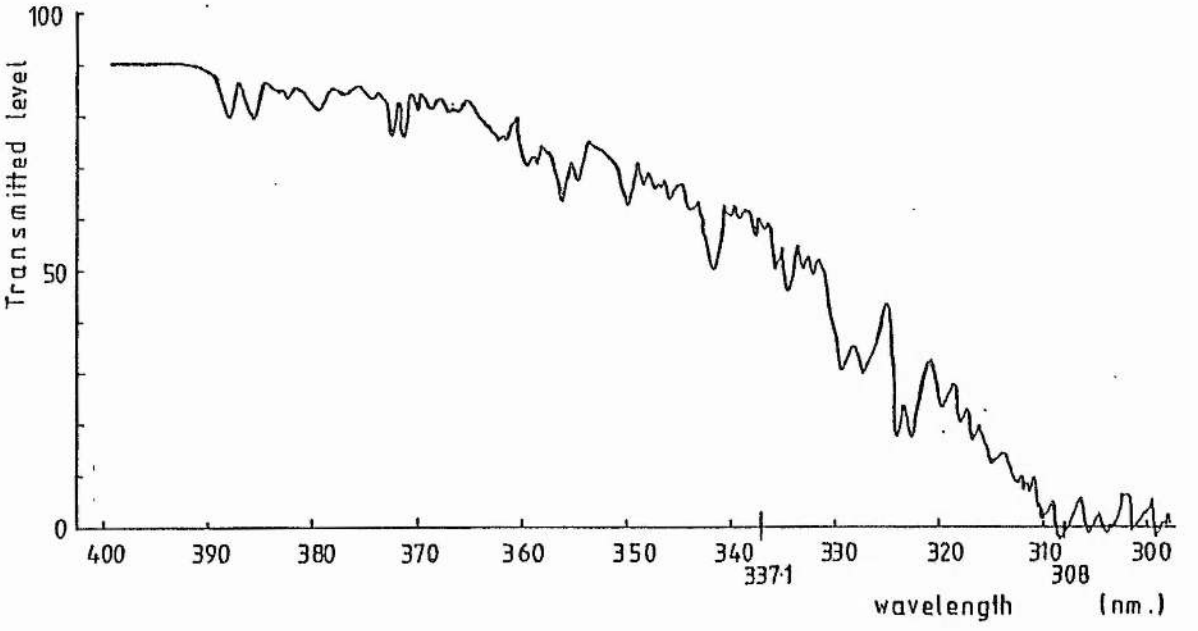

Figure3.6.1(b) Micro-densitometer trace of figure 3.6.1(a) adjusted in the ordinate for intensity to give a more realistic estimateof relativespectral atmospheric transmission ofsolar radiation to ground level

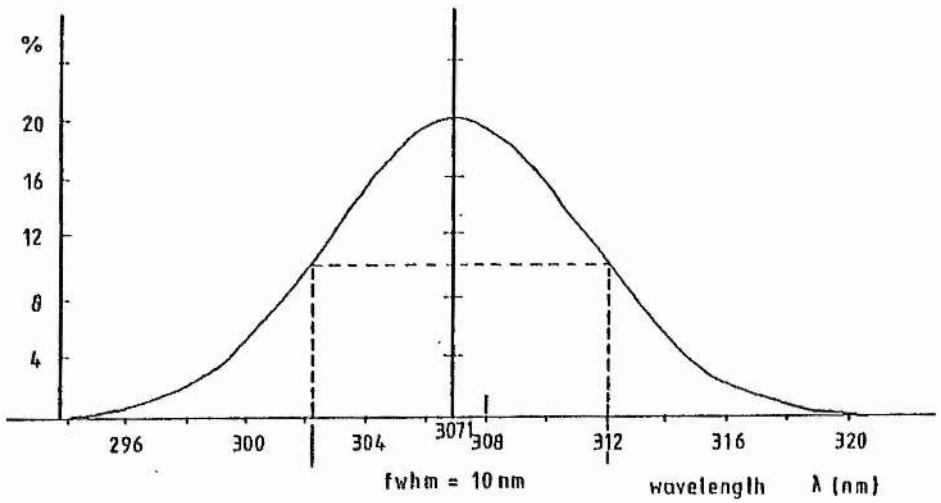

Figure 3.6.2 Passband of the zinc line narrow band filter at 307 nm (est.)

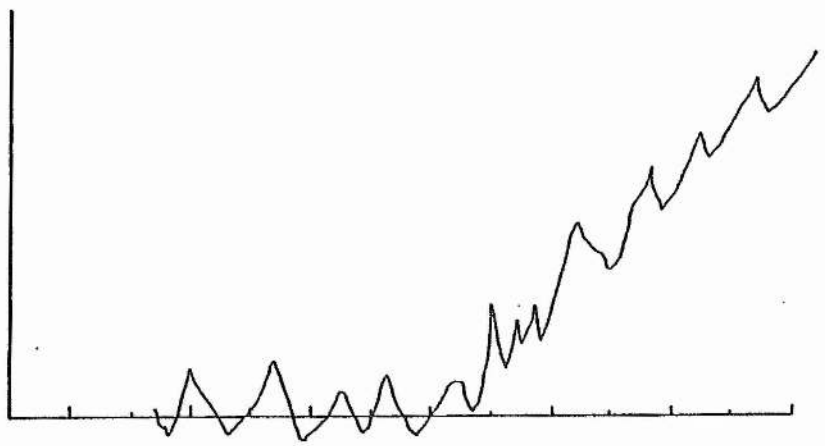

Figure 3.6.3 Solar spectrum in the region of 308 nm (from figure 3.6.1(b))

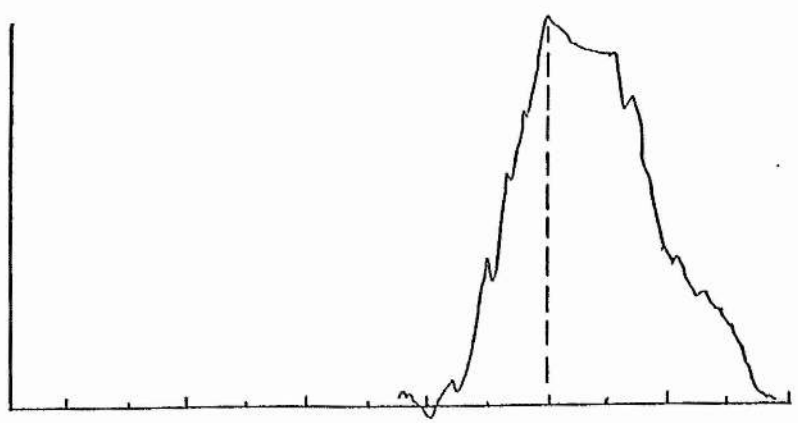

Figure 3.6.4 The portion of the solar spectrum passed by the zinc line filter

References for Chapter 3

Dance J.B; Photo-electronic Devices, 1969

EMI Photomultiplier Catalogue, 1979

EMI; Photo-electric Cells and Photomultipliers, 1961

Green Alex E.S; Attenuation by ozone and the earth's albedo in the middle ultra-violet. Appl.Opt., 3, 2, 203-208, (February, 1964)

Hamamatsu Photomultiplier Catalogue, 1980

Houghton J.T; The Physics of Atmospheres, 1977

Kondratyev; Radiation in the Atmosphere, 1969

Oriel Filter Catalogue, 1975

RCA Photomultiplier Catalogue, 1979

Uchino Osamu, Maeda Mitsuo, Hirono Motokazu; Application of excimer lasers to laser radar observations of the upper atmosphere. IEEE J.Quantum Electron., QE-15, 10, 1094, (October, 1979)

Chapter 4 The $XeCl^{*}$ Excimer Laser

A $XeCl^{*}$ excimer laser was designed for the DIAL system. The laser system is shown, installed in the lidar transmit/receive head, in figures 4.1.2. The sections below introduce this type of laser and describe the development of this lidar laser.

4.1 A Brief Review of Excimer Lasers

This short account of the excimer laser indicates its function and its history. The final paragraph of this section outlines the development of the type over a period of three years up to the form of the Xenon Chloride laser upon which this lidar laser is based.

Once formed, an excimer molecule possesses a bound upper state and a weakly bound ground state. The latter dissociates very rapidly, assisting the maintenance of population inversion under laser conditions during a high rate of spontaneous emission. A particular type of excimer molecule is formed between some rare gases and mono-halides, providing a lasing medium for pulsed ultra-violet radiation up to megawatt levels. Lasing is more likely and is stronger with a combination of the heavier rare gas and lighter halogens. Table 4.1.1 lists the known major lasing wavelengths for rare gas/halogen excimers. Figure 4.1.1 shows all the main excimer wavelengths with an arbitrary ordinate to indicate the relative obtainable peak powers.

Excimer molecules are formed by exciting a mixture of the rare gas and halogen donor, diluted by a buffer gas such as helium or argon to a pressure of up to several atmospheres. The excitation, by electron beam or transverse electric discharge, forms excited states and ions of the rare gas. The excimer is then formed by either the "harpooning" reaction involving the rare gas excited state in

$$2R^{*} + 2MX \longrightarrow 2RX^{*} + M_2, \qquad (4.1.1)$$

or by dissociative attachment of electrons to the halogen in

$$2e^{-} + 2MX \longrightarrow 2X^{-} + M_2, \qquad (4.1.2)$$

followed by three body ionic recombination

$$2R^{+} + 2X^{-} + M_2 \longrightarrow 2RX^{*} + M_2. \qquad (4.1.3)$$

The possibility of rare gas/halide lasers was suggested by Velazco and Setser at the beginning of 1975. By the middle of that year Searles and Hart (1975) had reported the first radiation in an electron beam pumped XeBr mix. Within a month Ewing and Brau (1975) described lasing from a similarly pumped XeCl laser using molecular chlorine as the halogen donor. Electron beam excitation systems are large and expensive. The transverse electric discharge, already well developed for CO_2 lasers was first applied to the excimer by Burnham et al (1976) when they obtained XeF excitation, reported in January 1976. The electrically discharged XeCl laser, of prime interest in this project, came onto the scene in the literature of 1977

with Kudryavtsev and Kuz'mina (1977) and Ishchenko et al (1977). Burnham (1978) made significant improvement over Ishchenko on laser energy by using HCl as the halogen donor instead of BCl_3. This, the best choice of halogen donor (to date) was confirmed by a report of Sze and Scott (1978) in the latter half of 1978.

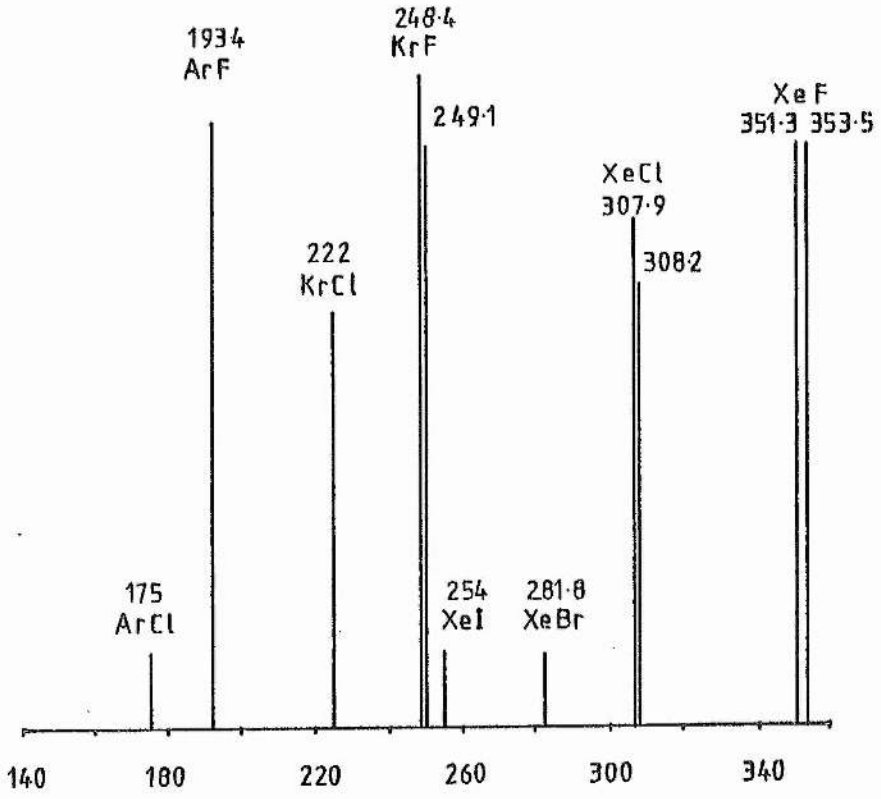

Figure 4.1.1 Major excimer lasing lines

Table 4.1.1 Major excimer lasing wavelengths

	He	Ne	Ar	Kr	Xe
F			193.4	248.4 249.1	351.3 353.3
Cl			175	222	308.2 307.9
Br					281.8
I					254

Figure 4.1.2(a) and (b) The $XeCl^*$ excimer laser installed in the lidar transmit/receive head

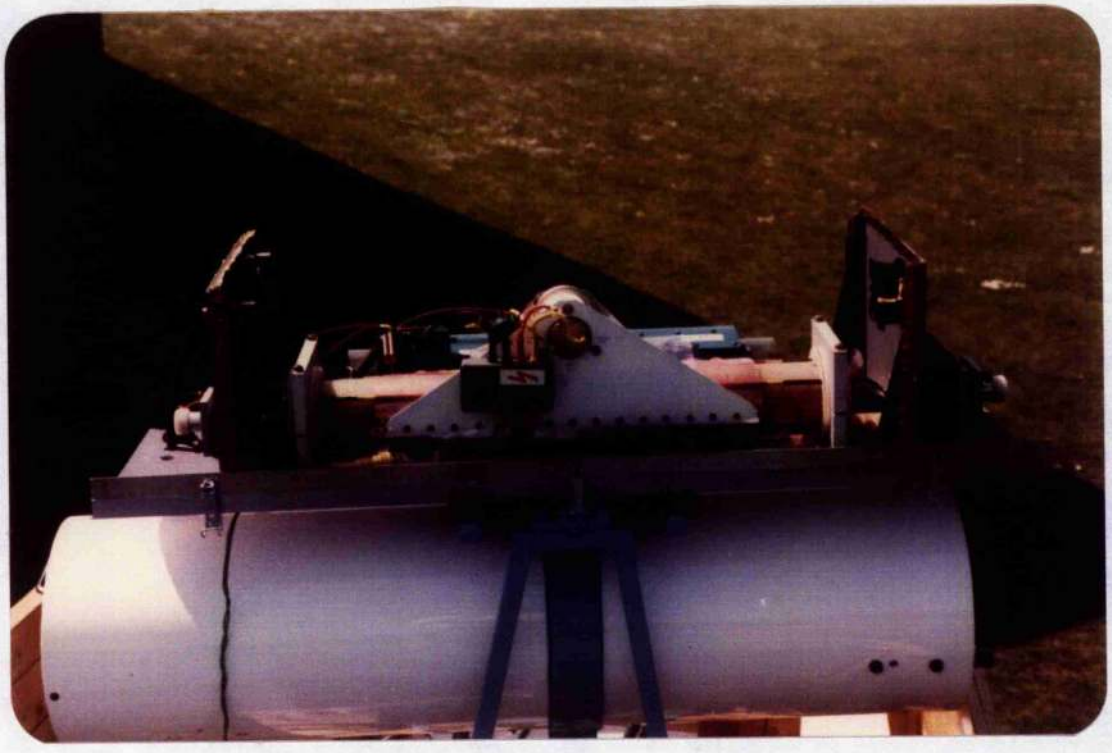

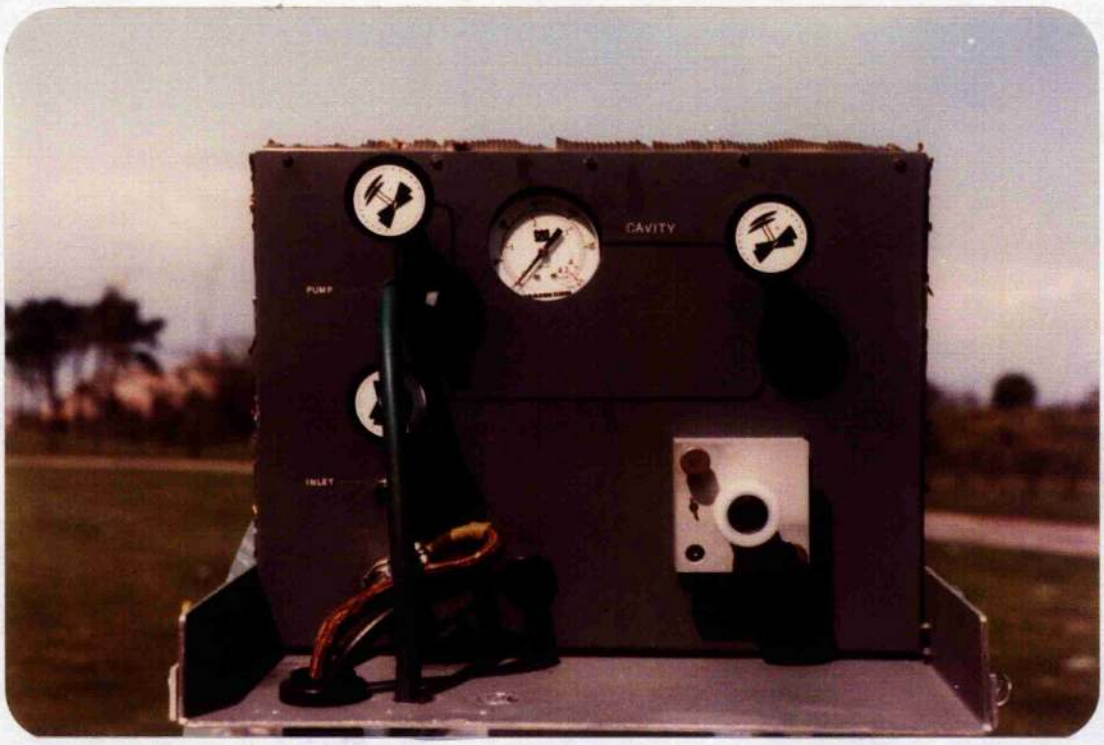

Figure 4.1.2(c) The laser gas handling panel

(d) The laser output coupler

4.2 Requirements for the DIAL Laser

The XeCl excimer laser was chosen as the radiation source in DIAL monitoring of SO_2 on the basis of the latter's absorption cross-section differential between the wavelengths of the two main lasing peaks, described in Chapter 1. The method of excitation was limited practically to a transverse electric discharge supplied by a fast capacitative discharge circuit. Space and weight restriction in a transceiver head for mobile lidar called for a compact but well insulated (for safety) laser structure. The necessary reliability and serviceability was obtained through simplicity in structure, electrical systems and gas handling components.

The main laser requirement is a high pulse peak power, giving high received signal-to-noise-ratio, for greatest lidar range, target penetration and best sensitivity to SO_2. Thus the electrical circuit requires a low loop size, low inductance discharge path for optimum energy transfer efficiency. The necessity for reliability and good pulse to pulse reproduceability meant a relatively low operating voltage to reduce component stress and internal arcing. The highest possible pulse repetition rate is desireable for fast signal averaging in DIAL operation. To this end a gas recirculation system was considered. However the repetition rate in a static fill has proved adequate. To reduce the weight and complexity of the mobile system the gas systems were split between a dedicated laboratory based refill station and the essential laser based handling equipment. A stable optical cavity was adopted to minimise difficulties in mirror alignment. The mirrors themselves are isolated from the damaging gas mix by UV transmitting windows, mounted at the Brewster angle to reduce reflection losses. The complete laser is housed in a shielded, earthed enclosure to reduce r.f interference emitted by the discharge. Further noise reduction

precautions were taken in filtering leads passing in and out of the laser housing. To prevent pick-up, earth loops are avoided in nearby circuits. Noise reduction is discussed in chapter 7.

Section 4.3 outlines the materials considered for the laser systems. Sections 4.4 to 4.7 describe the construction of the laser, followed by sections 4.8 and 4.9 on its operation and specification. The final section, 4.10 summarises problems and their remedies.

4.3 Materials Review for the Laser Systems

This section describes how various materials were considered for fabrication of the laser and the gas handling components. The cavity of the excimer laser operated by transverse electric discharge contains metallic conductors as electrodes and supply lines with the addition of insulators as structural parts. Other parts of the laser are seals, windows and gas handling components. It was necessary to choose materials with regard to the use of corrosive hydrochloric acid gas (anhydrous), high voltage (<25kV), high pressure (<4 atmospheres absolute), and UV radiation. Each system component is treated in the sub-sections below with a discussion leading to determination of a suitable fabrication.

4.3.1 Laser Gas Cavity Material

The structural design of the cavity is explained in section 4.4. It was possible to construct the cavity in a single material or in a hybrid construction where an inner layer, resilient to the gas, is contained within a pressure vessel. The necessity for an insulator suggests the use of glasses and/or plastics. However the difficulties in engineering a glass for vacuum sealing and high pressure operation, plus the likelihood of acid attack, pointed towards the selection of a suitable plastic. A range of easily obtainable plastics is listed in Table 4.3.1 which includes a comparison, where available, of chemical resistance, elongation, yield stress, reaction to high voltage stress and reaction to UV radiation. Further factors affecting the choice of a material are the expense and availability in the desired form and dimension. The rest of this sub-section is a discussion of the choice of plastics concluding with the selected type.

ABS and polypropylene, the latter obtainable as gas supply pipe, are unsuitable since they are not resilient to attack in an acid environment. Nylon is readily available but it becomes stressed and embrittled near regions of high electric stress (>1.5 MV/m). This has been observed in a Nylon cavity constructed in this research group (D.Wheatley). Cracks ocurring near to the discharge electrodes reduced the material strength and created leak problems. Nylon is still useful if used away from high electric stress and with minimal machining. PVC (PolyVinylChloride) is very easy to obtain in a wide range of sizes as tubing. Its resistance to hydrochloric acid and it's strength are good enough for use in the excimer laser. However some doubt has been cast (Chemistry Dept.,St.Andrews) as to the suitability of PVC under the effects of UV. radiation which may produce, in photolysis, inter cavity contaminants, to the degradation of the discharge. PTFE (PolyTetraFluoroEthylene) is a good choice in a high purity laser system due to its excellent insulative properties and resistance to chemical attack. It does, however flow considerably under pressure and can therefore only be used in a long term system if it is supported by an outer pressure vessel. The flow of a PTFE slab to the extent of pressure loss has been observed over a period of three days in a sandwich type cavity (section 4.4) constructed within the group. Poly-Tri-Fluoro-Chloro-Ethylene has similar properties to PTFE. The most attractive material for the $XeCl^*$ laser cavity proved to be PVDF (PolyVinyliDeneFluoride) combining all the desired physical properties, including easy machining. Its cost was slightly less than for PTFE but it was not as readily available. A tube of PVDF was purchased for fabrication of the laser cavity.

4.3.2 Window Material

The windows situated at the gas cavity ends must satisfy three

requirements. They must be strong enough to withstand cavity pressures; they must be resistant to the corrosive gas component with no blooming; they must give good transmission of UV at 308 nm.. The immediate options as to glass type are quartz, Spectrosil B, Calcium Fluoride or Magnesium Fluoride. Quartz and Spectrosil B are liable to surface damage after exposure to the hydrochloric acid in the gas mix. Other users in the group have observed, after exposure of the windows to the air, the formation by hydration of a contaminant on the window surface. Calcium fluoride windows were chosen for their resistance to the gas and for optimum transmission of the laser radiation.

4.3.3 Electrode and Corona Wire Materials

Electrodes, situated in the corrosive environment may be of aluminium, stainless steel or monel, the latter being a nickel/copper alloy. Monel is chosen in a high purity system where there is to be a minimum release of gas contaminants by chemical action. Components which are made of monel and exist in the presence of hydrochloric acid are not subject to the weakening corrosion that attacks alternative materials. Thus the alloy is the best choice for stressed parts. The only apparent physical drawback is noticed in small diameter monel tubes after exposure to air when a green slime of unknown composition forms on the surface. Another disadvantage is the relative expense and unavailability of the material in the desired form. Aluminium has already been widely used as a metallic component within laser cavities containing HCl. A surface coating of anhydrous aluminium chloride forms, to be hydrated to a fine greasy film upon exposure to the moisture in the air. This has not impaired laser performance since the cavity materials are allowed to passivate in an atmosphere of the gas mix, thereby reaching reactive equilibrium. Aluminium is the cheapest metal, it is easily machined and it was in stock at the time of construction. Thus it

was adopted for the electrodes of the XeCl* laser. Stainless steel, a more expensive substance, has not been seen to have any advantage as an electrode material.

Corona wires are most suitably of nickel but stainless steel is cheaper and more readily available. Fastenings can be of aluminium or stainless steel according to type.

4.3.4 Sealing Materials

Vacuum tight (to 0.01 torr) and high pressure (to 5 atmospheres) seals between cavity sections are O-rings and strip seals. In a non-corrosive environment these would be made of neoprene but under these laser conditions they are of Viton (trade mark), employed for longevity and to avoid gas contamination.

4.3.5 Gas Handling Equipment Materials

Valves, tubing and gauges had to be corrosion resistant and designed for a working pressure of at least 75 p.s.i.(absolute). Materials available for these components are stainless steel or monel metal. Monel is the prime choice for safety at high pressures after exposure to HCl. However some stainless steel components were used for cheapness and after considering that the very low HCl concentration (typically <0.5% by volume) will not create corrosion problems where moisture is excluded. It is necessary to use monel where the HCl is not diluted, as in the metering valve and connection to the acid cylinder. It was found necessary, after one year of use in the field, to replace, with monel where possible, those stainless steel components, such as quick connects, which are often in contact with the air. Corrosion, after attack by hydrated HCl, has created leaks at the external terminals.

Table 4.3.1 Properties of plastics in the XeCl* laser cavity environment

Material	Chemical resistance to HCl	Elongation (%)	Yield Stress (psi)	Reaction to H.V	Reaction to U.V
ABS Acrylonitrile ButadieneStyrene	poor	1 - 20	4000 - 9000		
PVC PolyVinylChloride	fair/good	2 - 40			poor
PTFE PolyTetra FluoroEthylene	excellent	200 - 400	1000 - 2000		
PTFCE PolyTriFlouro ChloroEthylene	excellent	250	4200		
Polypropylene					
Nylon				poor (embrittles)	
PVDF PolyVinylidene Fluoride	excellent (PTFE formed)				

4.4 Structure of the Cavity, Electrodes and Windows

This section considers each part of the cavity structure as to the design options, in particular, the cavity configuration, electrode shape, sealing and electrical connections. The cavity and electrodes were designed to contain a pre-ionized transverse electric discharge in a corrosive gas mix at a pressure of two or three atmospheres. Windows were fitted to survive the hostile environment and to transmit ultra-violet laser radiation with wavelength around 308 nm.

4.4.1 Cavity and Windows

The cavity options fall into two categories; a sandwich type, with cross-section as in figures 4.4.1(a) to (c) or one based on a cylinder, as in figures 4.4.1(d) to (e). Suggested variations on either theme are in a combination of materials chosen from nylon, PTFE, PVC, aluminium or monel. The layout and shape of the components was to satisfy sealing requirements, electrical connections and the discharge specification. Figure 4.3.1(a) is of the basic sandwich type with large elongated O-ring seals between the central insulator and each of the metal plates to which the electrodes are attached. Lasers of this type have been constructed within the group, (by Govindanunny.T, C.A.Pirrie, A.B.Duval) the insulator being of perspex, nylon or PTFE and the plates being aluminium or monel. However, for this work the desired energy output, fill lifetime and general reliability could not be achieved except in the form of a cumbersome, high purity device and the lasers were liable to leak or suffer stress fractures in the insulator. Monel plates could have been employed in a high purity vessel for longer gas lifetimes although a considered option was to employ a PTFE lining as in figures 4.4.1(b) and (c). The low volume cavity in figure 4.4.1(b) would have the advantage of high replenishment rate in a closed cycle

recirculated gas system. Figure 4.4.1(c) shows the inclusion of a spacer to provide a discretely variable electrode gap. After due thought these sandwich types were rejected on four main points. Gas purity is likely to be lost in lined cavities due to gas seepage between the metal/PTFE interface. A configuration like that in figure 4.4.1(b) would be impossible to machine. The high metal content of the construction makes for a heavy laser, unsuitable for a portable device. Finally, the number of plate securing bolts would make servicing a tedious job.

A more attractive proposition was to use a cylindrical cavity with a cross-section as in figure 4.4.1(d) and with end caps carrying the windows. Figure 4.4.1(e) shows the option of building in an inner lining for high purity, made of perhaps PTFE, though this would be difficult to accomplish. The answer was to find an easily machined plastic, PVDF (materials section 4.3) which is relatively inert to HCl gas and which has the desired strength in an obtainable cylinder of appropriate dimension. The latter was defined by electrode gap and length, given below, and any space required for gas inlet/outlet ports and corona wire fittings.

Nylon, as a convenient material, was adopted for the ends of the cavity. The problems with nylon as a cavity material, explained in section 4.3 are not encountered at the end plates where there are no unduly high mechanical or electrical stresses. The seal between the end cap and the cavity end is made with a Viton O-ring sitting in a groove machined into the cap (figure 4.4.2), following the principle of maximising the machining on the cheapest components. Four steel rods clamp both ends together (figure 4.4.6).

Windows are mounted at a Brewster angle to reduce reflection losses and to polarize the emitted radiation. The polarization is useful in the event of

tuning with an etalon or birefringent filter (see chapter 5). The Brewster angle, θ for transmission from air to the window is given by

$$\tan \theta = n_w/n_a, \qquad (4.4.1)$$

where n_w is the refractive index of the window and n_a is the refractive index of the surrounding air. Windows of CaF_2 (section 4.3) were selected for its high UV transmission and compatibility with HCl gas. The refractive index of CaF_2, 1.45 at 300nm., gives the Brewster angle as

$$\theta = 55^{\circ}\ 29'. \qquad (4.4.2)$$

This sets the angle of the aluminium Brewster mount shown in section in figure 4.4.2. The window is secured to the mount against a reinforced Viton O-ring. The mounts themselves are screwed into each end plate and sealed with a Viton O-ring.

4.4.2 Electrodes and Corona Wires

Electrodes of aluminium were adopted as described in section 4.3. This sub-section discusses the electrode profile, their sealed fitting to the tube, their electrical connections, dimensions and separation. The corona wires and fittings, used for pre-ionizing the gas mix, are described. The reasons for choosing the corona wire from the options are explained in sub-section 4.5.4.

The electrode length is fixed at a convenient 50cm. Separation is considered on the basis of the maximum operating voltage of 20 kV, set as low as this to ensure capacitor longevity and a high repetition rate. The expected ratio of electric field to cavity pressure is expected to be given

by

$$E/P = 820 \text{ V/m.T}, \qquad (4.4.3)$$

as derived from the works of Maeda et al and Sze and Loree in electric discharge excimer lasers. The ratio is expressed as

$$E/P = V_{max}/d_{max}.P. \qquad (4.4.4)$$

By setting the maximum voltage

$$V_{max} = 20 \text{ kV} \qquad (4.4.5)$$

at a pressure of 2 atmospheres (1520 torr) and for the E/P ratio given in equation (4.4.3) then the electrode gap is limited by

$$d_{max} = 16 \text{ mm}. \qquad (4.4.6)$$

The electrode separation was set at 15 + 1 mm. as a maximum. The lasers within this group had used 20mm. gaps but with higher applied voltages, indicating that this setting is reasonable.

The electrode profile shown in section in figure 4.4.3 was made semi-circular rather than given the usual Rogowski profile. The reason for this "sharpening" is to create a more intense electric field along the cavity and to confine the discharge to a narrower volume. Hindsight suggests that a Rogowski profile should have been used (see section 4.10). Electrical connections to the electrodes are made via threaded studs, every 3cm. passing through the cavity wall.

Vacuum and high pressure sealing is made by trapping a Viton strip between the flattened electrode base and the inside curvature of the tube (figures 4.4.4 and 4.4.5). An optional method is to use compound (Dowty) seals tightened down round the studs on the outside of the tube. However this would allow gas to penetrate into the electrode/cavity interface.

Two stainless steel wires are employed to provide a pre-ionizing corona from positions in a plane perpendicular to that of the electrodes. The position of the corona wires is shown in the cavity section of figure 4.4.3. A compromise was taken between the high field of a very thin wire and the large electron emitting surface area of a thicker wire. The fitting of two wires in the restricted space inside the cavity presented problems in keeping a taut wire and a sealed terminal to the exterior. The eventual method, illustrated in figure 4.4.2 but in detail in figure 4.4.3 was to fix four O-ring sealed stainless steel attachments into each of the end plates and to stretch each wire between the fittings via stainless steel springs. Each spring is shorted to remove the inductance. The method ensures the correct tension with less risk of breaking by external adjustment. Electrical connections are made to each fitting by an external screw.

4.4.3 The Complete Cavity

The final cavity, having been described in component form is shown in longitudinal section in figure 4.4.6, including the gas port positions. The space between the electrode ends and the end plates was a contingency for accommodating large diameter recirculation ports should such a system have been necessary for high repetition rate and long gas life.

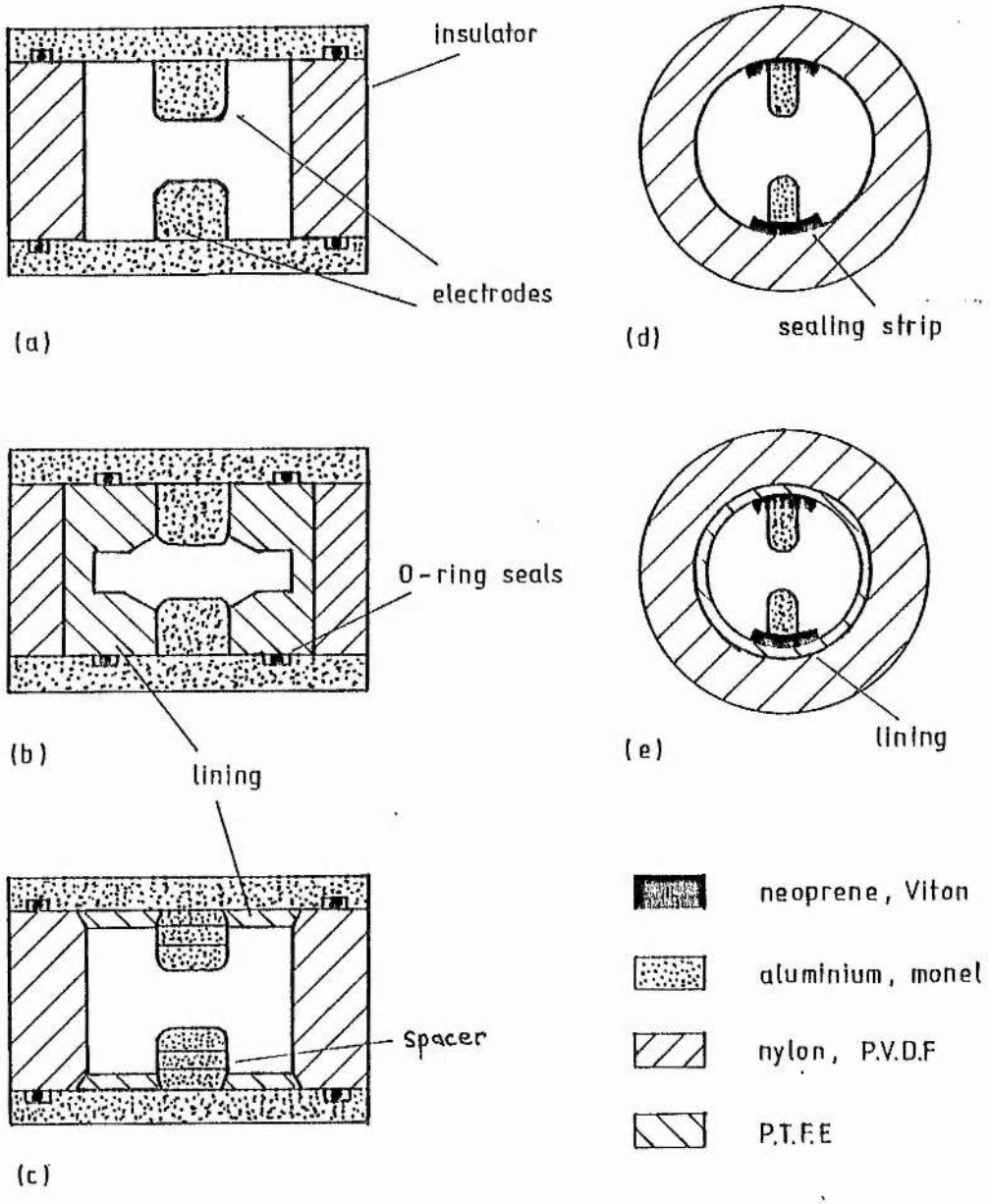

Figure 4.4.1(a) to (e) **Transverse cross-sections of suggested laser cavities**

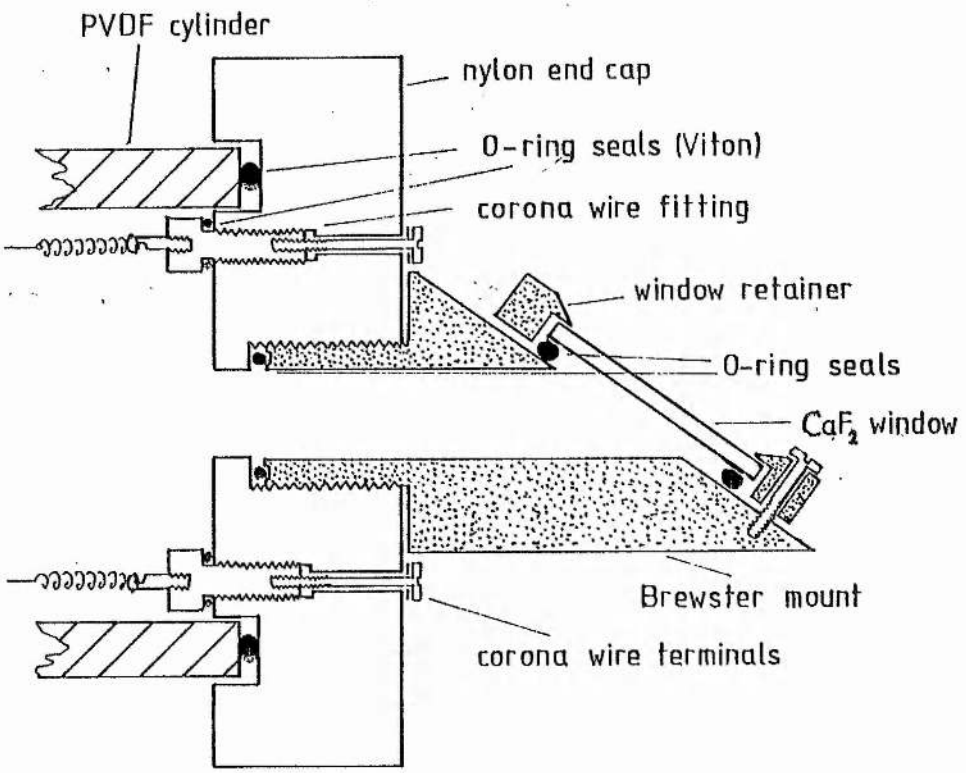

Figure 4.4.2 Cavity end plate, Brewster mount, window and corona wire fitting

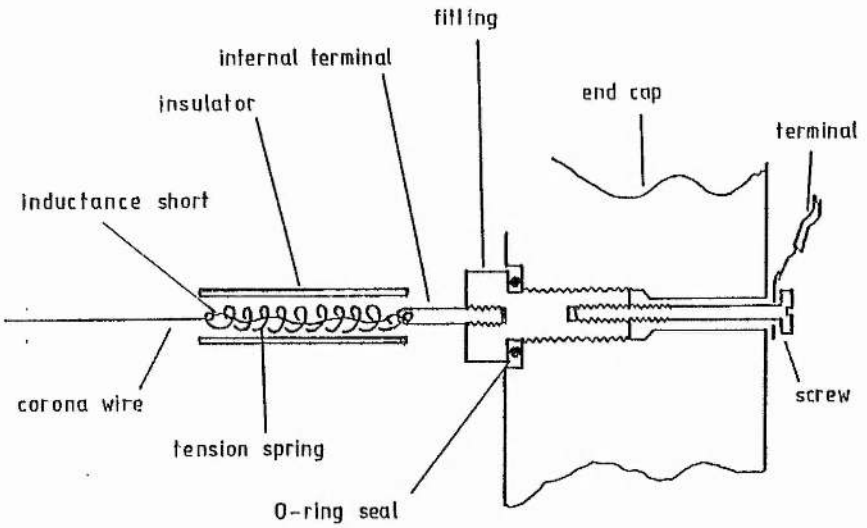

Figure 4.4.3 Corona wire fittings

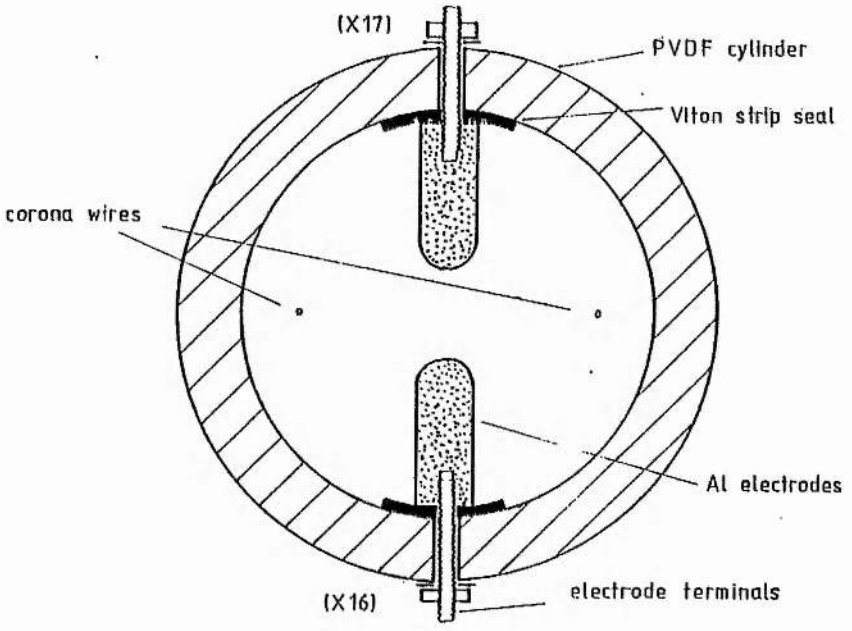

Figure 4.4.4 Laser cavity and electrode cross-section

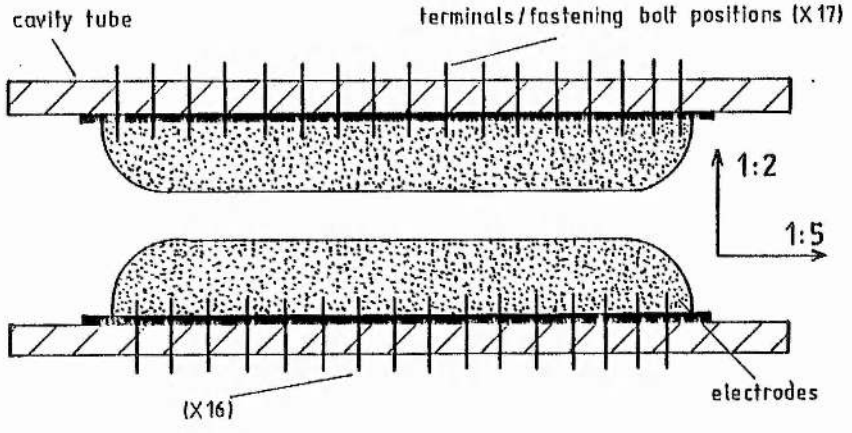

Figure 4.4.5 Cavity and electrode longitudinal cross-section

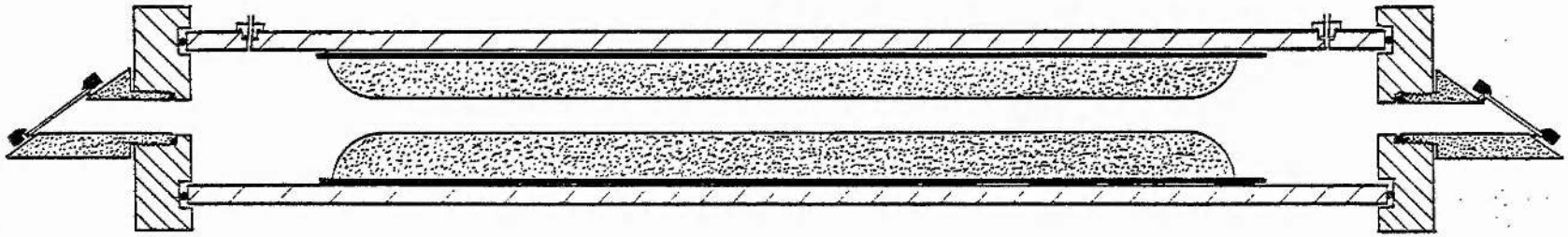

Figure 4.4.6 Longitudinal section of the $XeCl^{*}$ laser cavity and end cap assemblies

4.5 The Laser Circuits

The design of the capacitative discharge and pre-ionization circuits is described after consideration of the options. The adopted circuits are illustrated in figure 4.5.6 and the layout is shown schematically in figure 4.5.5. A brief investigation into circuit characteristics is outlined in section 4.8.

4.5.1 Discharge Circuit Types

There are three possibilities for the discharge circuit of a transverse excited gas laser. These are drawn in figure 4.5.1, without a pre-ionization circuit. The LC inversion circuit has been used successfully with excimer lasers by Burnham and Djeu (1976), Sze and Loree (1978), Maeda et al (1978) and in the XeCl laser used in some of the laboratory stages of this work (C.A.Pirrie,1980). The Blumlein has been applied by Ishchenko et al (1977), Waynant et al (1977) and Sutton et al (1976). These and the C-to-C transfer circuit have been compared with regard to their suitability in this particular application. A prime consideration in circuit choice is the overvolting of the laser electrode gap. That is, taking the voltage to well above the breakdown potential before the discharge occurs. In this way the transfer of energy to the gas is optimised. To this end a short rise time, obtainable from a low inductance discharge circuit was sought. The LC inversion circuit of figure 4.5.1(a) was discounted on the basis of a relatively long rise time (70 to 100 ns.) in comparison with the two other types. A further disadvantage is the voltage doubling and subsequent overstressing of the circuit components. The Blumlein, with a very low inductance is the faster of the remaining circuits. However, the layout is necessarily bulky. One idea in applying figure 4.5.1(b) is given in the sectional sketch of figure 4.5.2 in which the capacitors are each two

parallel plates with a single di-electric in a rigid construction. Even if the capacitors were folded or, if flexible, wrapped around the cavity, the result would be unsuitable for the lidar laser where compactness, robustness and serviceability were to be combined. The conclusion was to use discrete capacitors in a C-to-C transfer circuit of the form of figure 4.5.1(c).

4.5.2 C-to-C Transfer Circuit: RC Components

This sub-section outlines circuit operation, defines the quantities involved in this application and describes the capacitors and resistors which have been adopted.

With reference to figure 4.5.1(c), C_s is the value of the storage capacitor and C_d is the value of the discharge capacitor. The resistance R_s across the cavity allows C_s to be charged to a voltage $+V$. The switch, called S, either a spark gap or a thyratron, earths the positive side of C_s and sets an effective overvolting potential of $-V$ across the cavity. If the overvoltage is to be maximised, the storage capacitor to cavity circuit has to be of minimum inductance. The charge from C_s is tranferred to C_d , mounted close to the cavity where it forms a very low inductance circuit, thus allowing fast dumping of energy into the discharge for population inversion. It is necessary that C_d is smaller than C_s if, by charge conservation, the effective cavity overvoltage is not to be lowered and if C_d is to charge fast enough before breakdown. The discharge capacitance C_d must not be so much smaller that it is dumping a smaller energy into the gas. An impression of the ideal voltage pulse is shown in figure 4.5.3. A rule-of-thumb satisfying the conditions gives the limits

$$3C_d < C_s < 4C_d. \qquad (4.5.1)$$

In selecting the capacitances, C_s is set for the energy requirement and C_d is set according to the limits (4.5.1).

An optical energy of 50mJ was aimed at, after an estimated electrical to optical efficiency of about 0.5%. The energy stored in the storage capacitor is given by

$$E = C_s V^2 / 2. \qquad (4.5.2)$$

An operating voltage of up to 20kV is assumed, giving the requirement on minimum storage capacitance as

$$C_{s\ min} = 50\ nF. \qquad (4.5.3)$$

Thirty eight "doorknob" capacitors, with barium titanate di-electric, are assembled into a compact, low inductance unit to give an expected total capacitance of about 75 nF. The discharge capacitance is set at about 25 nF using smaller barium titanate capacitors. These are assembled in parallel pairs along the entire electrode length, between one electrode's connections and an earth sheet (connected to the other electrode) enclosing the cavity, as illustrated in the schematic section of figure 4.5.5. They are arranged with sixteen pairs on one side of the electrode and seventeen pairs on the other side to provide discharge loops of opposing direction to minimise inductance. Capacitances and breakdown voltages are outlined in table 4.5.1.

The charging resistance R_s is set to allow full charging of the storage capacitor at the maximum likely repetition rate, S pps; R_s is defined using

the inequality

$$R_S < 1/C_S \ S. \qquad (4.5.4)$$

A maximum likely repetition rate of 20 pps gives the requirement

$$R_S << 667 \ k\Omega. \qquad (4.5.5)$$

A high wattage resistor of 21.8 kΩ was installed. A further resistor of 300 MΩ was connected across the storage capacitor.

4.5.3 Switching the C-to-C Transfer Circuit

A triggered spark gap or a gas filled thyratron are options for switching the high peak currents in the C-to-C transfer circuit. A spark gap has the apparent benefits of simplicity, cheapness and higher operating voltage than a thyratron but it is liable to overheating at repetition rates greater than 1 pps unless a gas (nitrogen) is flowed between the electrodes. The latter is a complication to be avoided. This laser was not designed to use a voltage greater than 20 kV, permitting the selection of a thyratron as a more reliable and controllable switch. An English Electric Valve Co. deuterium filled thyratron, type CX1180, was chosen.

4.5.3(a) Basic Thyratron Principles

A thyratron is a gas filled switch, closing when an ionised column of gas is extended between the thermionically emitting cathode and the anode. The column is initiated when a sufficient positive potential is applied to grid 1 (see figure 4.5.4). The switch is kept open when a negative hold-off potential is applied to grid 2. This hold-off is removed in switching by applying a positive cancelling pulse to grid 2. Gas pressure is kept

constant by a heated gas reservoir. The cathode and reservoir heater supplies, grid biasing and trigger pulse source are described below.

4.5.3(b) Thyratron Heaters, Bias Circuits and Trigger Unit

One transformed supply provides 6 V.a.c. for the heaters. A d.c. supply biases grid 1 at +150 V. and grid 2 at -150 V. The grid 2 trigger pulse is derived from a thyristor switched capacitor circuit operated by a relaxation oscillator, allowing variable pulse repetition rate or a manual single shot. A synchronisation pulse is provided to trigger any ancillary units. These circuits are included in the entire laser system circuit diagram of figure 4.5.6 with specification in table 4.5.1.

4.5.3(c) Thyratron Circuits; Precautionary Measures

The thyratron is just suitable for switching 20 kV at around 5 pps. However a higher switching rate of up to 20 pps necessitates a lowering of the voltage towards 15 kV if thyratron internal arcing and switching failure is to be avoided. A fan is provided for cooling over long running periods at high repetition rate and/or high voltage or current operation. The thyratron is mounted close to the cavity tube to minimise the size of the inductance loop (see figure 4.5.5). Dimensions in general are minimised for faster switching times. All circuits are completely fused. Careful earthing of the circuits prevent the formation of loops through which large r.f fluxes from the discharge can induce severe noise problems and possibly cause damage to sensitive components in signal recording circuits. Wherever there was any possibility of removing the earth from a live circuit a fail-safe switch was provided to connect an alternative ground. The main earth circuits are illustrated in the heavy line of figure 4.5.6. The main system ground is provided through the laser operating unit via the high voltage supply.

4.5.4 Pre-ionization of the Laser Gas Mix

In the excimer laser, a pre-ionization of the gas is required just before and as the main discharge occurs to ensure a uniform electron and ion distribution for a uniform discharge. An adequate pre-ionization removes the inhomogeneities formed at positions of high electric stress where arcs can otherwise develop to provide a discharge of poor optical quality.

The first discharge excited excimer lasers of Burnham et al and Ewing and Brau ($XeCl^*$) used UV pre-ionization generated from a flashboard made of a series of spark gaps. These were supplied prior to the main discharge by a separate circuit allowing variation in the interval. Most excimer lasers to date seem to have been pre-ionized in this way. A simpler method was proposed and tested by H.M.von Bergmann et al in 1975 in which a corona was produced from razor blade electrodes prior to the breakdown of high pressure nitrogen. It was suggested that the idea was suitable for application to other UV lasers. The advantage of avoiding duplicated discharge circuitry and the necessary delay technique is reinforced by the minimisation of material introduced into the laser cavity. The latter lowers the possibility of gas contamination by impurities and allows better passivation. Indeed, Sze and Loree reported a gas fill lifetime reduced by a factor of 2 or 3 after using a high power flashboard in KrF and ArF lasers. However the extent of ionization is lower in the simple corona technique with the result that lower laser pulse energies are obtained.

Pulsed corona pre-ionization was adopted for the lidar laser, designed for simplicity, reliability and serviceability. Two wires are employed, parallel but in a plane perpendicular to that of the electrodes so that the corona is directed to the oppositely poled electrode. The position and

mounting method is shown in figures 4.4.2 and 4.4.3 of section 4.4.

4.5.4(a) Pre-ionization Circuit

The best way of connecting the corona wires was found empirically. At first each end of the wires was connected via a 0.75 nF capacitor to the live side of the cavity (connections to the earthy side caused arcing). In later efforts to increase laser energy, a resistor was included to charge the capacitor (figures 4.5.5 and 4.5.6) before the thyratron is switched. Internal arcing was often evident until one end of the corona wires was left connected in the way described but with the other end connected directly to the live side of the cavity.

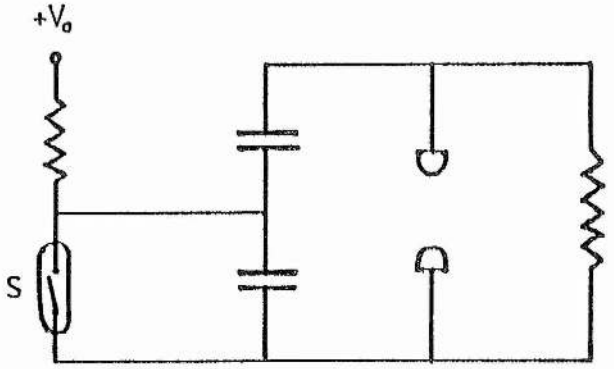

(a) LC inversion circuit

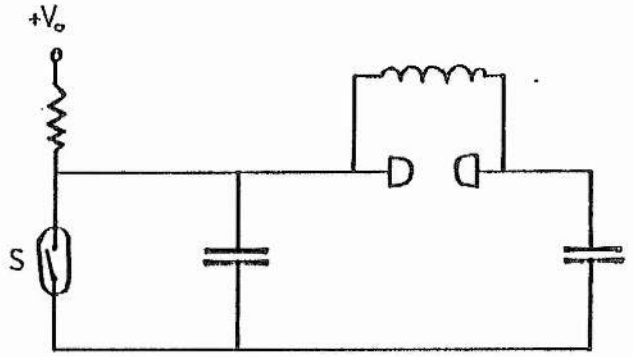

(b) Blumlein circuit

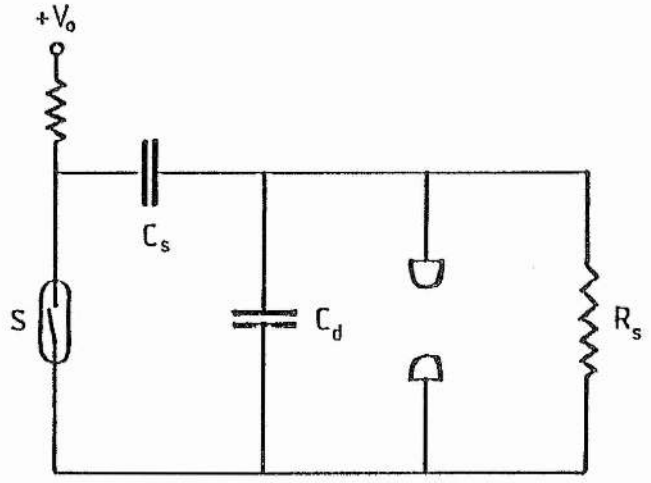

(c) C to C transfer circuit

Figure 4.5.1 Basic laser discharge circuits

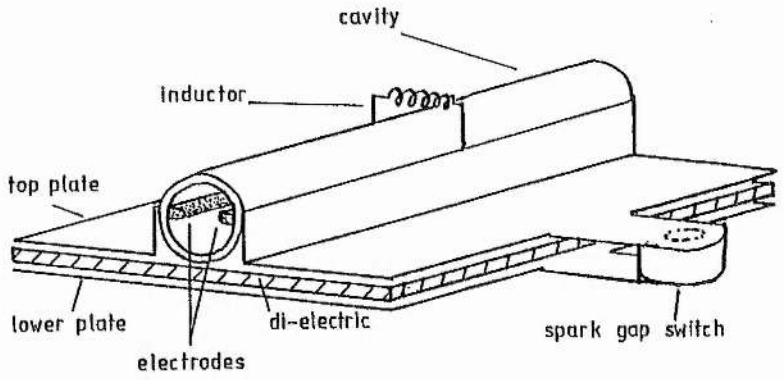

Figure 4.5.2 Layout of a Blumlein circuit

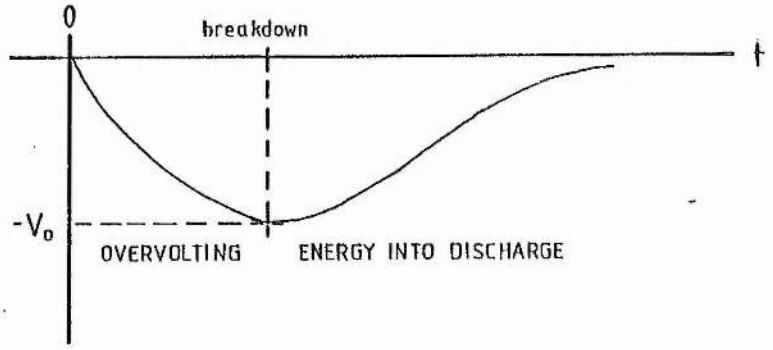

Figure 4.5.3 Cavity voltage transient

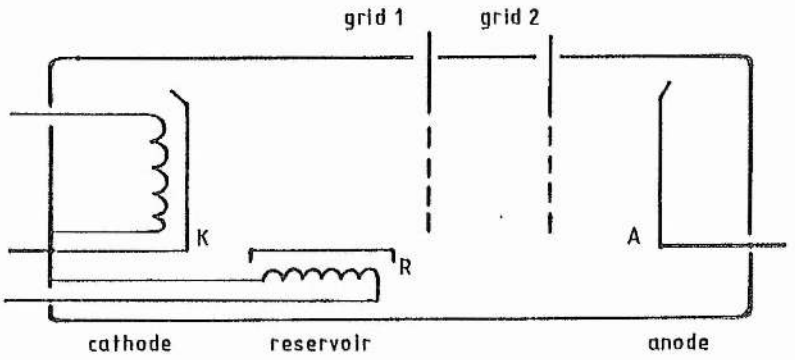

Figure 4.5.4 Thyratron internal structure

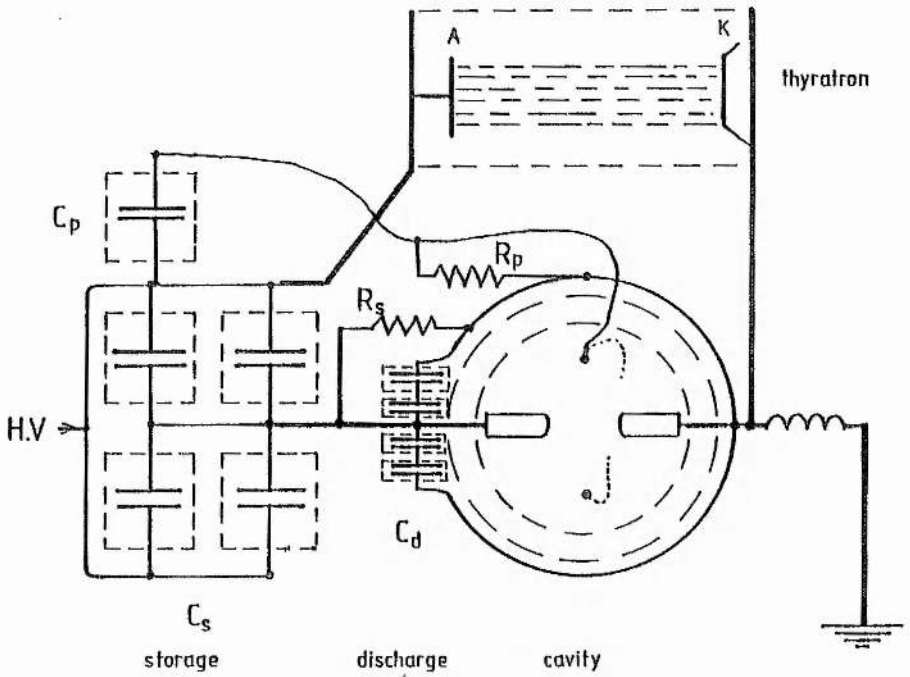

Figure 4.5.5(a) Representation of the $XeCl^*$ laser discharge circuit showing the cavity in cross-section

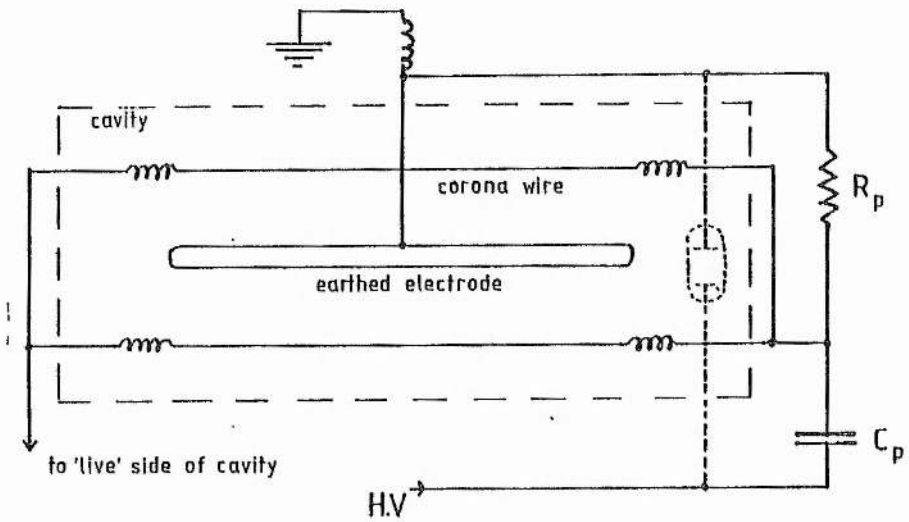

Figure 4.5.5(b) Longitudinal representation of the laser pre-ionization circuit showing two corona wires and the position of the earthed electrode

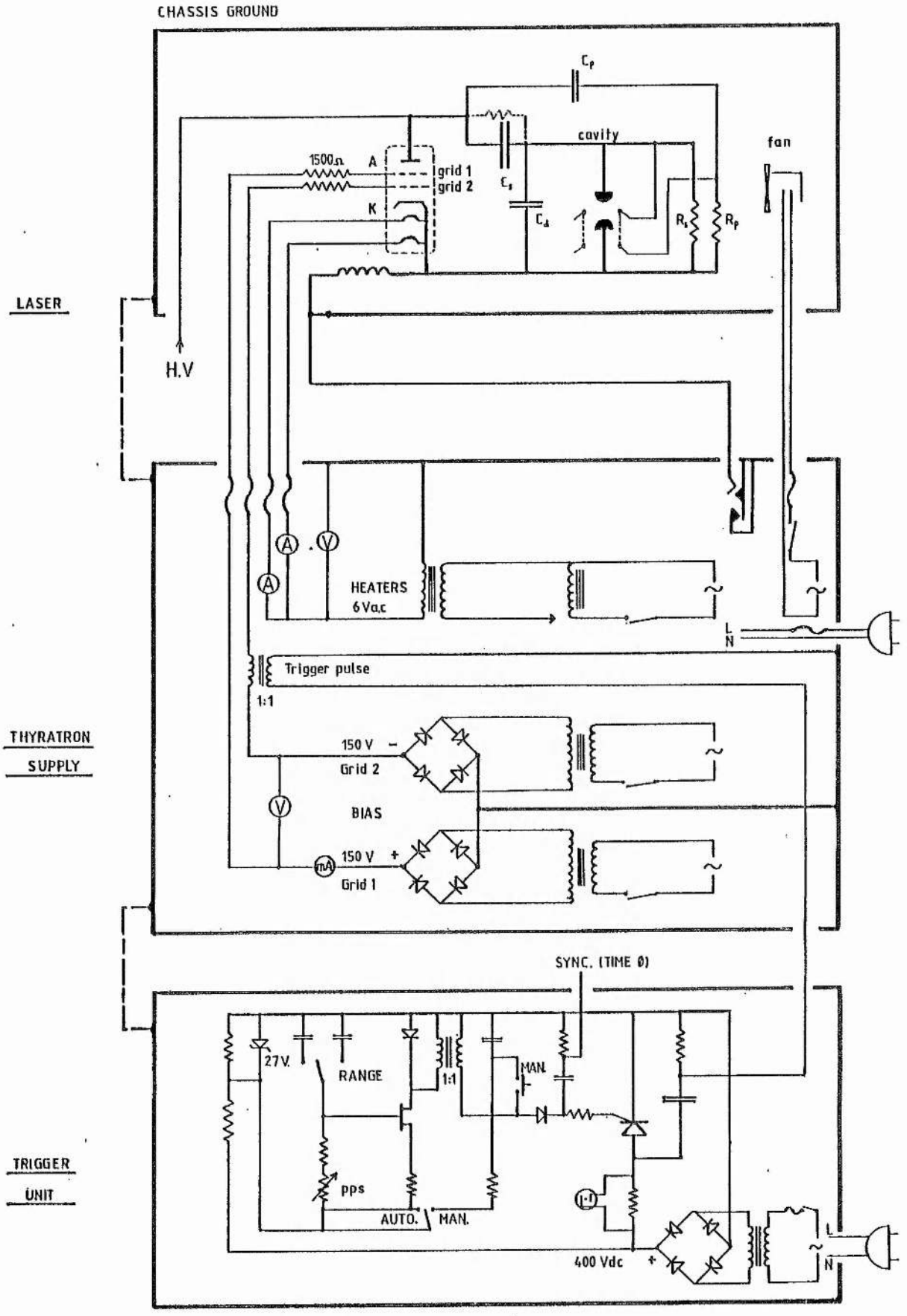

Figure 4.5.6 Lidar laser circuits

Table 4.5.1 Lidar laser circuit parameters

Function	Value or operating V, R, I, C	Duration	Rate (pps)	Limits
Heaters				
Cathode	6.3 Vac, 12 A			
Reservoir	6.3 Vac, 6 A			
Bias				
Grid 1	+150 Vdc, 100 mA			
Grid 2	-150 Vdc			
Trigger pulse				
Grid 2	+250 Vpk net	>1 μs		
Trigger unit				
Trigger pulse O/P	+400 V	1.5 μs	0.3 - 3.3 3 - 36	
Sync. pulse	+15 V	12 μs		
Laser circuit				
Discharge capacitor	23 nF			24 kV max
Storage capacitor	70 nF			30 kV max
Storage charging R	21.8 kΩ			
Preionization C	1.45 nF			24 kV max
Preionization charging resistance	37.5 MΩ			
Operating voltage	15 - 20 kV			20 kV max

4.6 Laser Mirrors

The mirrors are mounted outside the Brewster windows of the gas cavity to allow ease of adjustment, replacement and the prevention of chemical reaction with the surface in the presence of UV. A total reflector and an output coupler are used in a stable optical cavity configuration, allowing for easy mirror alignment. The total reflector (actually 98% at 308nm) is a di-electric coated component with a 2m. radius of curvature. The fraction of radiation transmitted through the back end (<2%) is useful as a pulse intensity sample for normalization of the lidar pulse output. The output coupler is a quartz flat situated about 95 cm. from the back mirror.

4.7 Gas Systems

The laser gas systems are defined by the cavity mix requirement and the application to DIAL. The requirement for a compact laser and mobile unit led to the construction of two separate gas systems. A dedicated laboratory based gas mixing station containing the metering valves, low pressure gauge, gas cylinders and rotary pump is used to charge a high pressure (up to 20 atmospheres) cylinder with sufficient gas for several pre-mixed laser refills. The laser gas system is merely filled from this cylinder via input and cavity shut-off valves. A pressure gauge on the cavity allows the operating pressure to be set and provides a monitor for leaks. Evacuation of the laser in situ is provided by a small rotary pump.

The layouts of the gas handling systems are shown in figure 4.7.1. All connections and piping, except pump lines are 1/4" O.D. components. The

laser cavity and high pressure refill cylinder were tested hydraulically to about twice the expected working pressure. Gas mixing and system integrity is discussed in the following sections.

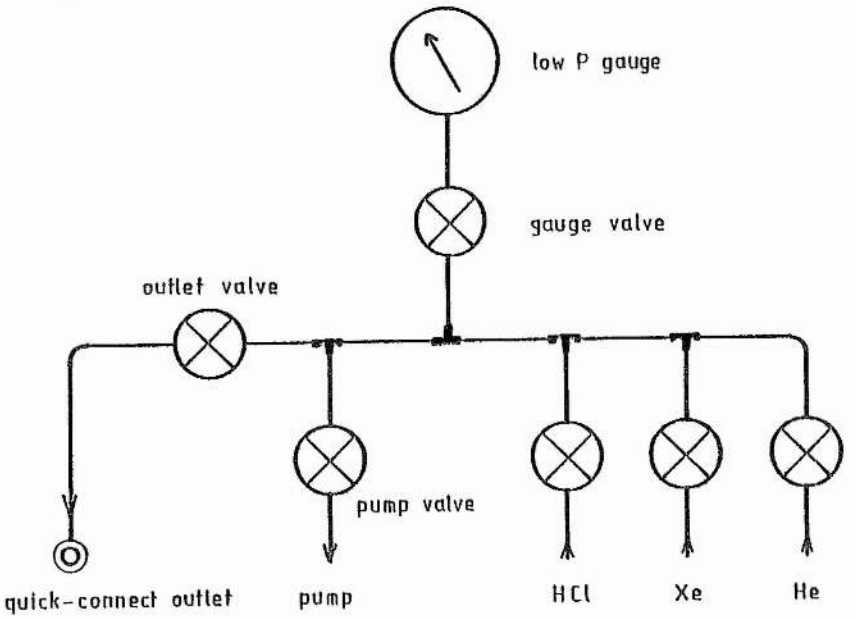

(a) Gas mixing station

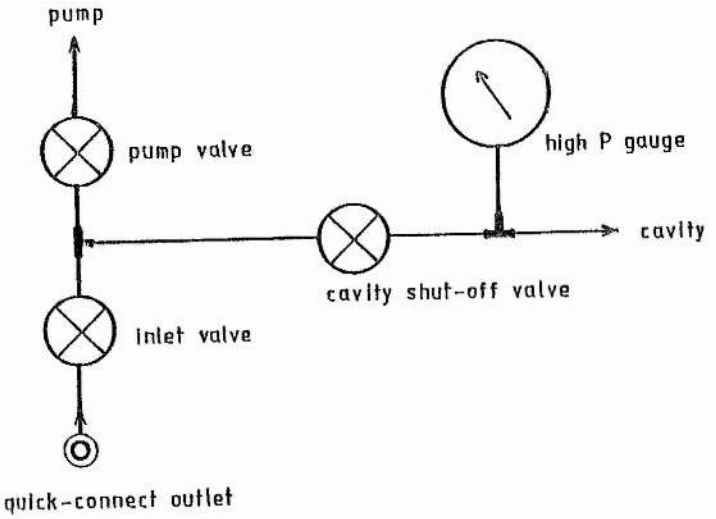

(b) Laser gas system

Figure 4.7.1 $XeCl^*$ laser gas systems

4.8 Laser Commissioning

4.8.1 Obtaining Lasing

The primary discharge circuit was checked by acheiving lasing at 337 nm. with nitrogen at a pressure of around 100 torr. The effectiveness of the pre-ionization was proved by obtaining an arc free helium discharge at pressures in the range 2 to 3 atmospheres and at voltages of 10 to 20 kV. Oscillographs of the cavity voltage in figure 4.8.1 show reasonably efficient energy dumping, in about 30 ns., into the discharge at voltages greater than 15 kV, in comparison with a relatively sluggish transfer over about 50 ns. at 10 kV. The transfer takes place on the positive-going slope after the first negative cavity overvolting. The swing over to a positive voltage is caused by ringing due to the mismatch between the capacitors and the cavity.

A preliminary mix of hydrogen chloride, xenon and helium in the respective proportions of 3 torr, 10 torr and 3 atmospheres was left in the cavity for a day or two to allow establishment of chemical equilibrium between the gas and the cavity materials. This passivation of the cavity continues while the gas is present and is aided by the discharge which tends to clear-up some impurities. Passivation must be repeated after the internal components have been exposed to air. Lasing was obtained at the 308 nm. region with the stated gas mix. The gas proportions necessary for optimising the output energy were obtained by experiment following a review of other works. The results outlined below were from a repeated investigation after improvement of the pre-ionization circuit (sub-section 4.5.4(a)) had boosted the pulse energy by about 350%.

4.8.2 The $XeCl^*$ Laser Gas Mix

Gas mix proportions which have been adopted in some $XeCl^*$ lasers are reviewed in table 4.8.1. The most applicable figures are those refering to transverse discharge excitation where hydrogen chloride is the chlorine donor. On the whole, the references of table 4.8.1 indicated partial concentrations set within the ranges given by

$$0.07\% < [HCl] < 0.2\% \qquad (4.8.1)$$

and

$$0.9\% < [Xe] < 5\%, \qquad (4.8.2)$$

respectively. However, preliminary attempts at lasing with these ranges of levels failed due to excessive arcing. Eventually the arcing was removed by lowering the xenon concentration to below the 0.9% of (4.8.2). Gas partial pressures tried in mix optimisation were based on the range in (4.8.1) for HCl and a lower xenon component than the minimum in (4.8.2). The apparent discrepancy with the xenon component may be due to an inadequate level of pre-ionization with a higher xenon concentration, spoiling the homogeneity of the discharge. Discharge voltage is limited by the component specifications to 20 kV thus allowing a voltage variation down to that at the threshold of lasing. Overall helium pressure is limited mechanically to about 3.5 atmospheres (50 psi). Different proportions of Xe and HCl were tried over a range of voltage and helium pressure and the laser pulse energies were measured. One channel of a laser energy ratiometer (Laser Precision Corp. Rj 7200) was employed to average 10 pulse energies. The number of pulses measured per fill did not exceed about 600, avoiding innacuracies due to energy degradation through gas lifetime problems.

Figure 4.8.3(a) shows the variation of maximum energy per mix with partial pressures of Xe for different HCl partial pressures, at 16 kV and an overall pressure of 3 atmospheres. It is desirable to operate at maximum voltage and pressure for highest energy output. However, the restriction on these parameters is imposed to avoid arcing and subsequent loss of pulse reproducability. Figure 4.8.3(b) gives the same result as 4.8.3(a) but the partial pressure of HCl is varied for different Xe pressures. Figures 4.8.3(a) and (b) specify an operating point, given in table 4.9.1, including the acceptable partial pressure ranges giving 90% of the optimum energy. Partial pressures should be set to an accuracy of about 30%. The concentration as a percentage is applied in charging the refill cylinder to a maximum overall pressure of 20 atmospheres.

4.8.3 Discharge Characteristics

The oscillographs of figure 4.8.1 serve to check on the speed of energy transfer into a helium discharge. A similar check on the excimer discharge for an operating voltage of 16 kV is the oscillograph of figure 4.8.2 where the current flows for about 35 ns. after overvolted breakdown. This is roughly the expected period for energy transfer.

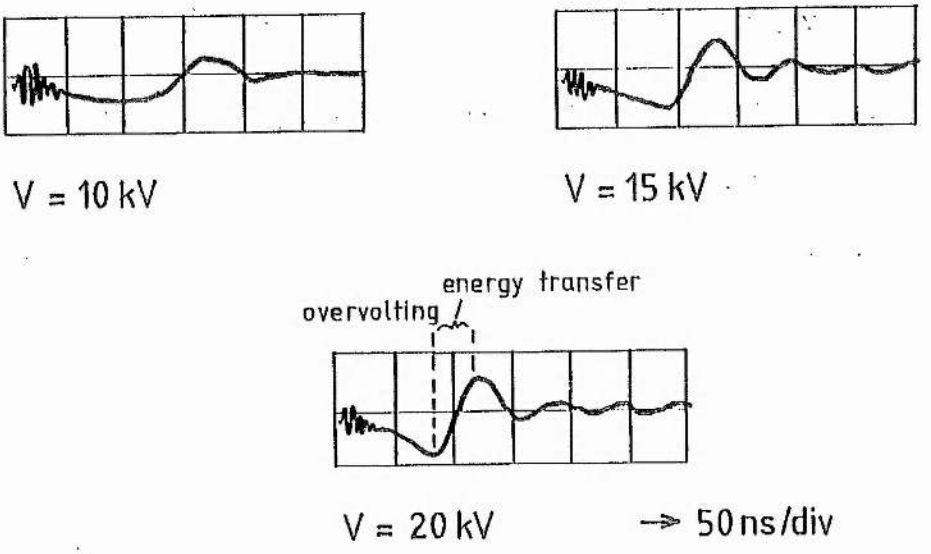

Figure 4.8.1 Cavity voltage transients across a helium discharge

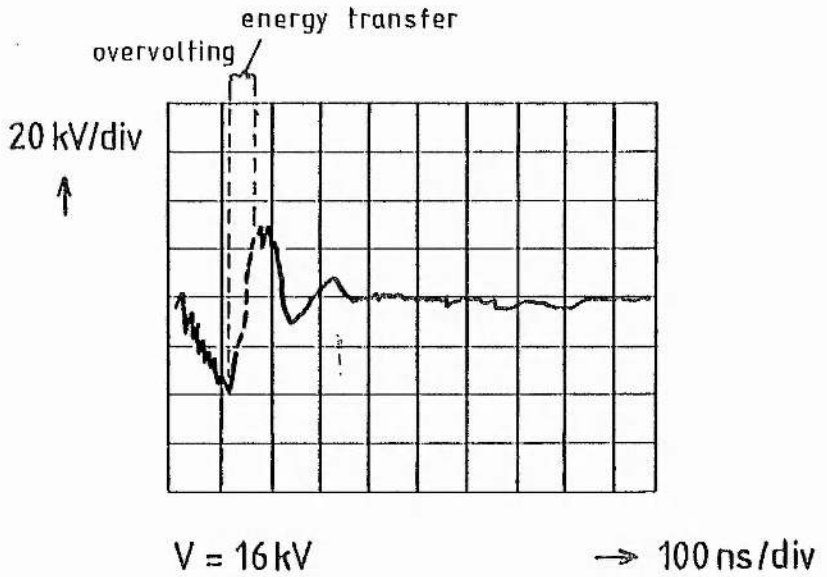

Figure 4.8.2 Cavity voltage transients across $XeCl^{*}$ lasing discharge

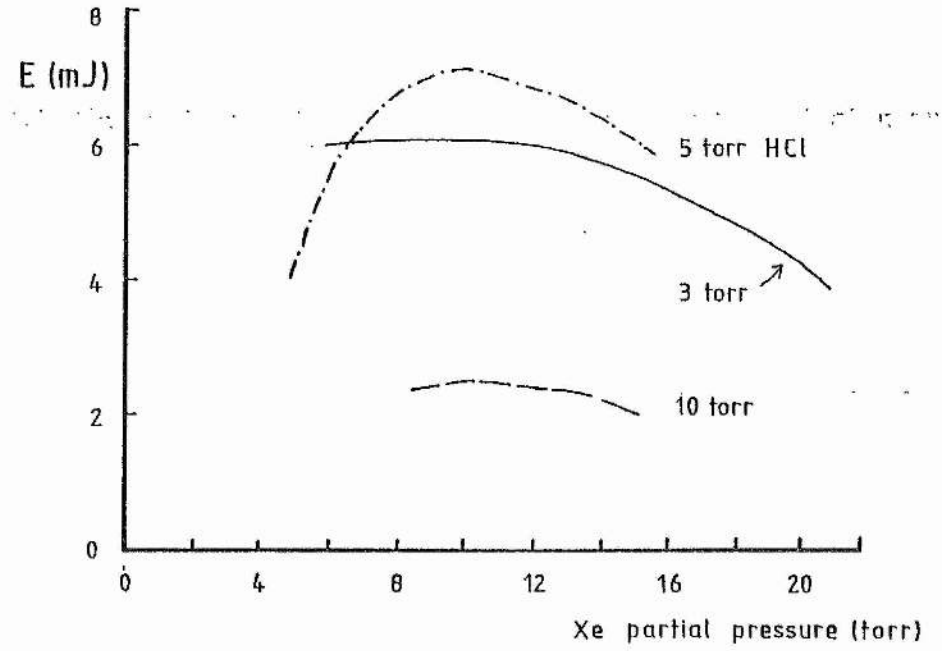

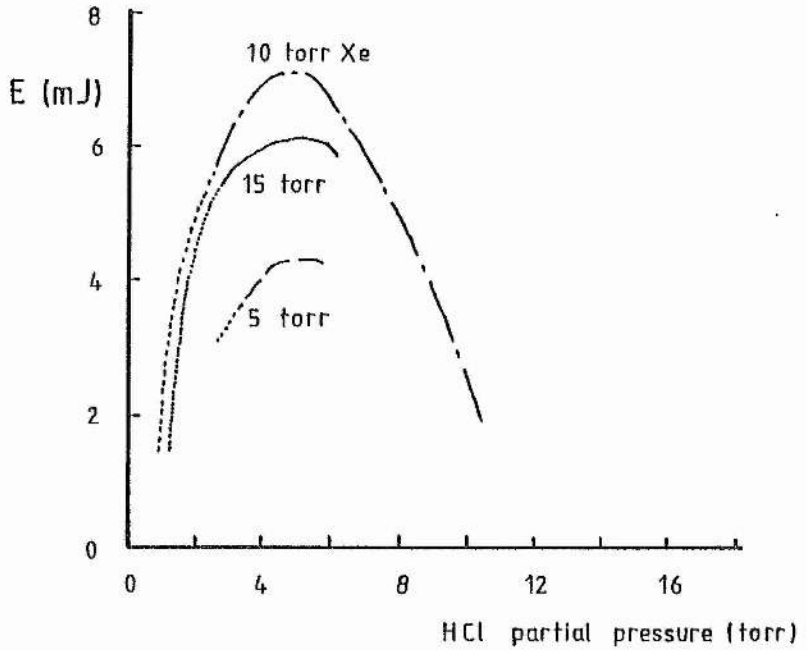

Figure 4.8.3(a) and (b) Effect of gas mix proportions on lasing energy at 16kV and 3atm He pressure

Table 4.8.1 $XeCl^{*}$ lasing gas mix proportions by reference

Investigator	Discharge Method	Pre-ion Method	Halogen Donor	Xenon	Buffer	E (mJ)	kV	P (at)
Ewing & Brau (1975)	e-beam	e-beam	Cl_2 0.1% 2 T	10% 207 T	Ar 89.9%	n/a	n/a	2.72
Sze & Scott (1978)	t.e.d	spark	HCl 0.2% 5 T	5% 124 T	He 94.8%	180	48	3.27
			HCl 0.2% 5 T	1% 25 T	He 98.8%	90	48	3.27
Maeda at al (1978)	t.e.d	spark	BCl_3 0.13% 3 T	0.88% 20 T	He 98.99%	4	25	3
			BCl_3 0.2% 3 T	1.32% 20 T	He 98.48%	12	25	2
Burlamacchi (1979)	t.e.d	n/a	Chlorinated hydrocarbon 0.13% 1 T	5% 40 T	n/a 94.87%	7	12	1
Champagne (1979)	n/a	n/a	HCl 0.067% 1.5 T	1% 22.8 T	Ne 98.93%	n/a	n/a	3

4.9 $XeCl^{*}$ Excimer Laser Parameters

The primary operating points defining gas mix proportions and voltage have been discussed in 4.8. This section outlines the determination of the rest of the laser parameters, summarised in table 4.9.1.

4.9.1 Pulse Repetition Rate

Repetition rate should be as high as possible for fast signal acquisition from a single target sample prior to averaging in DIAL. High temporal resolution may also be an advantage if the target is dispersed rapidly. The pulse repetition rate was found to be limited in practice to a maximum of 20 pps, at the maximum voltage, when severe arcing and thyratron misfire occured. Another restriction on the rate is imposed by the power capability, W_V, of the high voltage supply, given by

$$S = 2W_V / C_S V^2_{max}, \qquad (4.9.1)$$

where V_{max} is the maximum tolerable voltage. Equation 4.9.1 is used to define the permissible combination of operating voltage and repetition rate where the supply is the limiting factor.

4.9.2 Gas Lifetime

It is useful to know the gas-fill lifetime in terms of the pulses available before the energy is too low for lidar use. It is convenient to define the lifetime by the number of pulses emitted before the energy is reduced to one half of its initial value. The degradation, obtained empirically is shown in figure 4.9.1.

4.9.3 Beam Divergence

An important operational factor in a lidar system is the full angle of divergence of the laser beam. It should be smaller than the full field of the telescope if radiation is to be collected from the whole target area. This eliminates the need for a correction term in the geometric collection efficiency given in the lidar equation. The full angle of divergence, θ was measured as 8.2 milliradians, close enough to the roughly expected 10 mrads in this cavity configuration. The acceptance angle (field angle) of the telescope is greater than the transmission angle of the laser so that all the radiated target is "seen".

4.9.4 Temporal Pulse Width

The temporal width of the laser pulse was measured in the laboratory, using a fast linear focused photomultiplier (EMI 9594 QUB), giving a fwhm of 32ns. The oscilloscope trace is shown in figure 4.9.2. A correction was made, on the original measurement, allowing for the time spread due to the photomultiplier time response (2.2ns rise-time). The temporal width, τ , of the laser pulse is required as a spatial length, given by $c\tau/2$, as the definition of the minimum resolveable lidar range element. The significance of this is described more fully in the lidar and DIAL chapters 8 and 9.

4.9.5 $XeCl^*$ Excimer Laser Output Spectrum

The $XeCl^*$ excimer lases on two main lines around 308 nm.(Brau and Ewing, 1975). Experiments were carried out to verify the spectral characteristics of the emission and to evaluate the relative intensities of the two peaks. The latter (as a ratio, n_1/n_2) is a parameter in the differential lidar equation and its definition is required automatically per pulse pair during signal acquisition and processing in a return pulse normalization procedure. However a value for n_1/n_2 was wanted for insertion into a model

predicting differential lidar results. The experiments also yielded information on pulse to pulse energy variation.

Two instrument systems used in these investigations were a Carl Zeiss Q24 spectrograph, a G1 microdensitometer, and a G1B1 potentiometric recorder and a B & K optical spectrum analyser (OSA).

4.9.5(a) Primary Lasing Wavelengths (Q24 experiments)

Table 4.9.2 lists $XeCl^{\#}$ peak wavelengths as determined by previous workers. The Q24 prism spectrograph was used here to record the $XeCl^{\#}$ spectrum. Spectral calibration of the plates on the instrument is done with a wavelength scale transparency. However, a more precise calibration was obtained by the superimposition of a mercury vapour spectrum. The microdensitometer and potentiometric recorder allowed the spectra to be recorded on paper, as reproduced in figure 4.9.3. Measurements of the traces gave wavelength peak values, given in table 4.9.2 in close agreement with references and verifying the results of Sze and Scott (1978) at 307.92 nm. and 308.17 nm. Higher resolution traces allowed peak separation to be measured, giving the values in table 4.9.2.

4.9.5(b) Relative Intensities of Lasing Peaks (OSA experiments)

In the OSA system a grating disperses the radiation onto a vidicon diode array. Light falls on each diode and depletes the existing charge content. The instrument measures relative intensity by monitoring the amount of charge necessary to replenish the contents of each diode. Intensity is expressed digitally as the a number of counts. Resolution with the grating used is about 0.3 Å., this being the approximate spectral coverage of each diode or channel. Thermal drift of the display baseline led to incorrect count numbers. However, the results were obtained by measurements on X/Y

recorder traces delivered by the OSA's print facility. A typical trace is reproduced in figure 4.9.4. Superimposition of many such spectra allowed quantification of pulse to pulse variation, described below.

Peak intensity ratios are valid for a single output. The error in the ratios given in table 4.9.3 is the standard deviation of the series of ratio results (not of the mean ratio). A value intended for insertion into the model of chapter 9 is improved by applying Chauvenets theorem to reduce the error to that in 17 selected readings. The uncertainty in the average of all readings arises from the pulse-to-pulse variation. The effect of this variation, as an uncertainty in lidar return intensities, can be removed if the return is normalized by a measurement of the lidar output pulse.

4.9.5(c) Pulse-to-Pulse Variation (OSA experiments)

Figure 4.9.4 shows the variation in intensity between pulses. Twenty nine traces of this type provided quantification of the pulse-to-pulse variation at the peaks. The results are given in table 4.9.4. Pulse-to-pulse variation is given as the mean of the error measurements. The maxima and minima are obtained from the error mean by adding and subtracting, respectively, the standard deviation of the measurement errors. The most useful values are the maxima. They can be applied to determine DIAL accuracy if no pulse energy normalization is used.

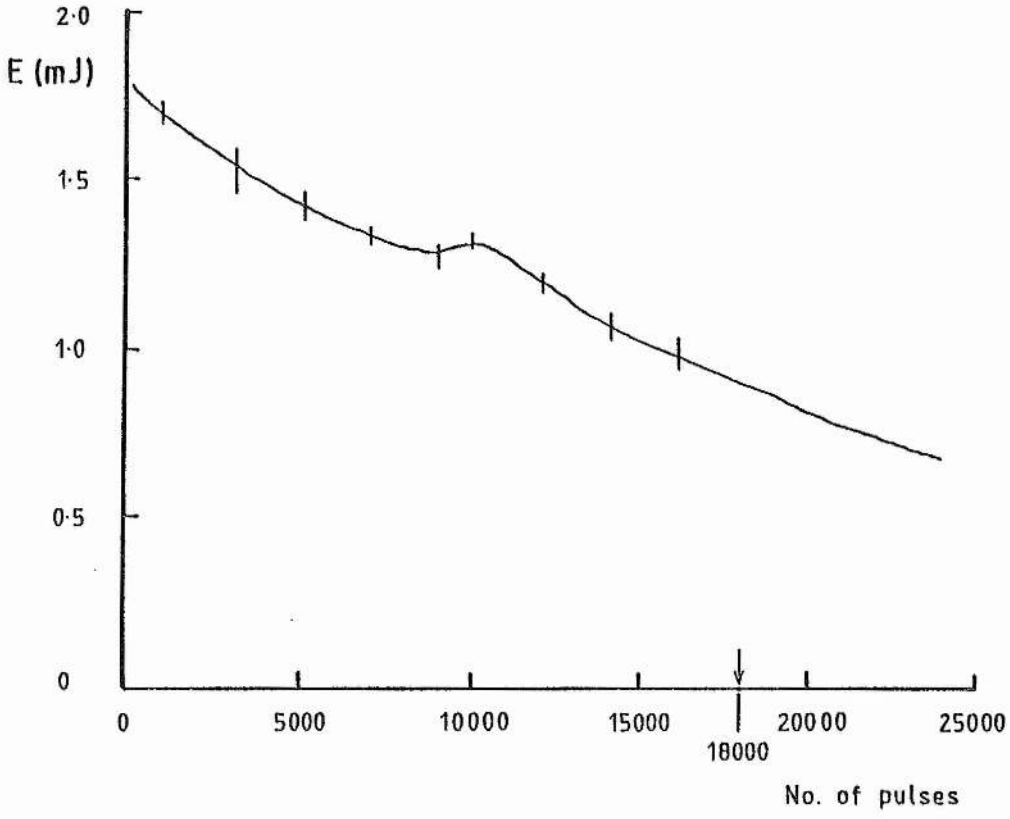

Figure 4.9.1 Pulse energy degradation defining laser gas fill pulsing lifetime

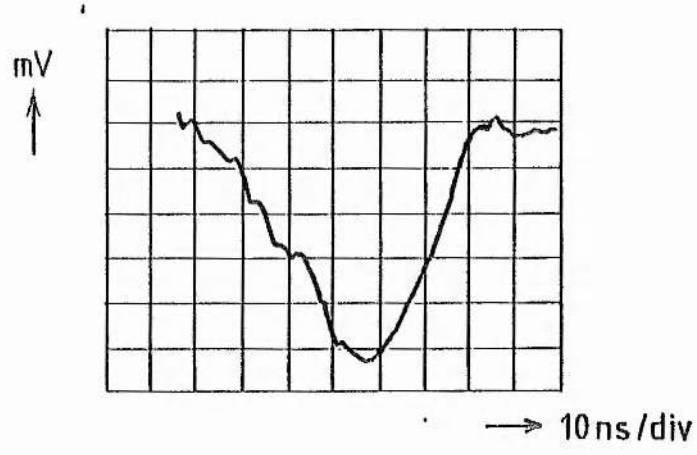

Figure 4.9.2 Temporal width of $XeCl^{*}$ laser pulse, by experiment. O/P from EMI 9594 QUB fast photomultiplier (2.2ns rise)

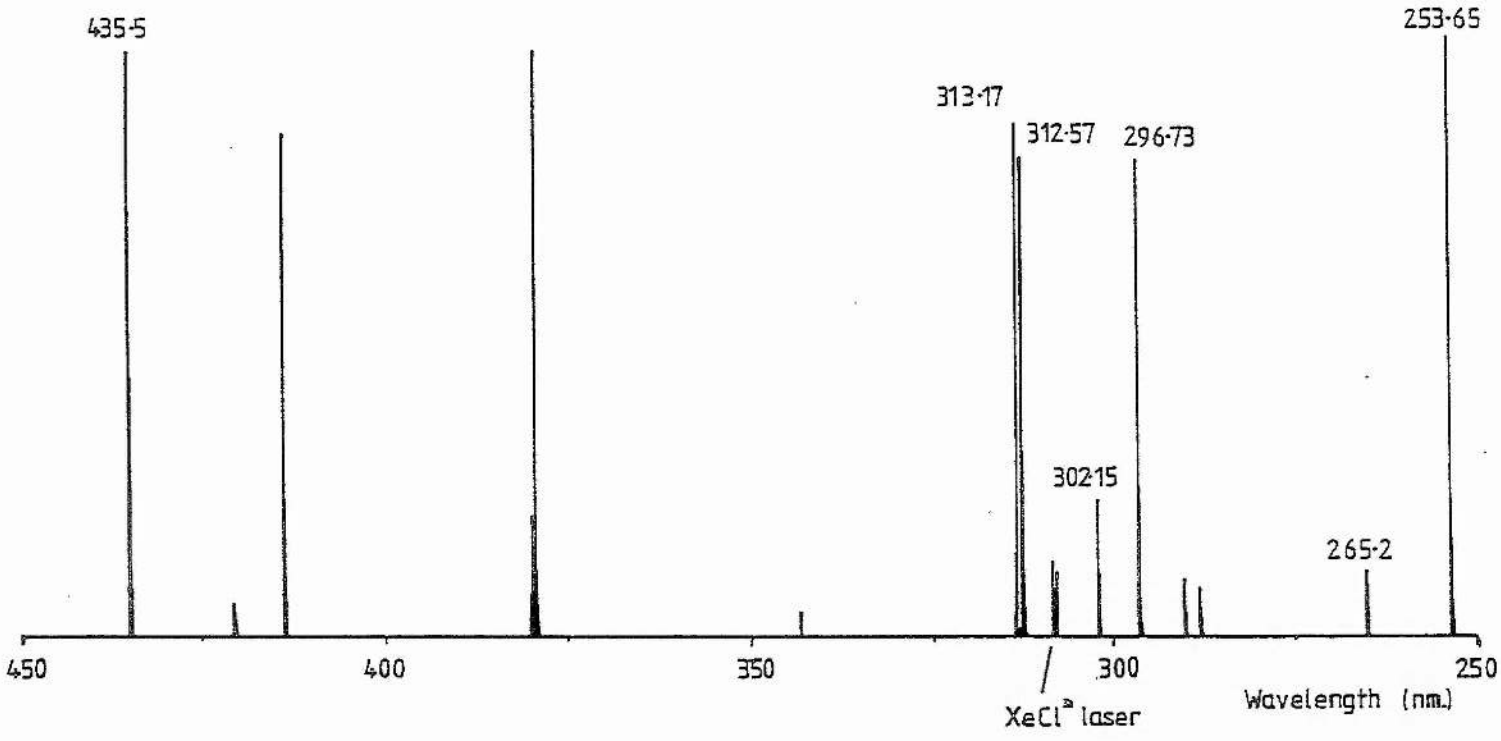

Figure 4.9.3 Microdensitometer trace of $XeCl^{*}$ lasing lines and Hg reference lines. (The region around 308nm was expanded for calibration)

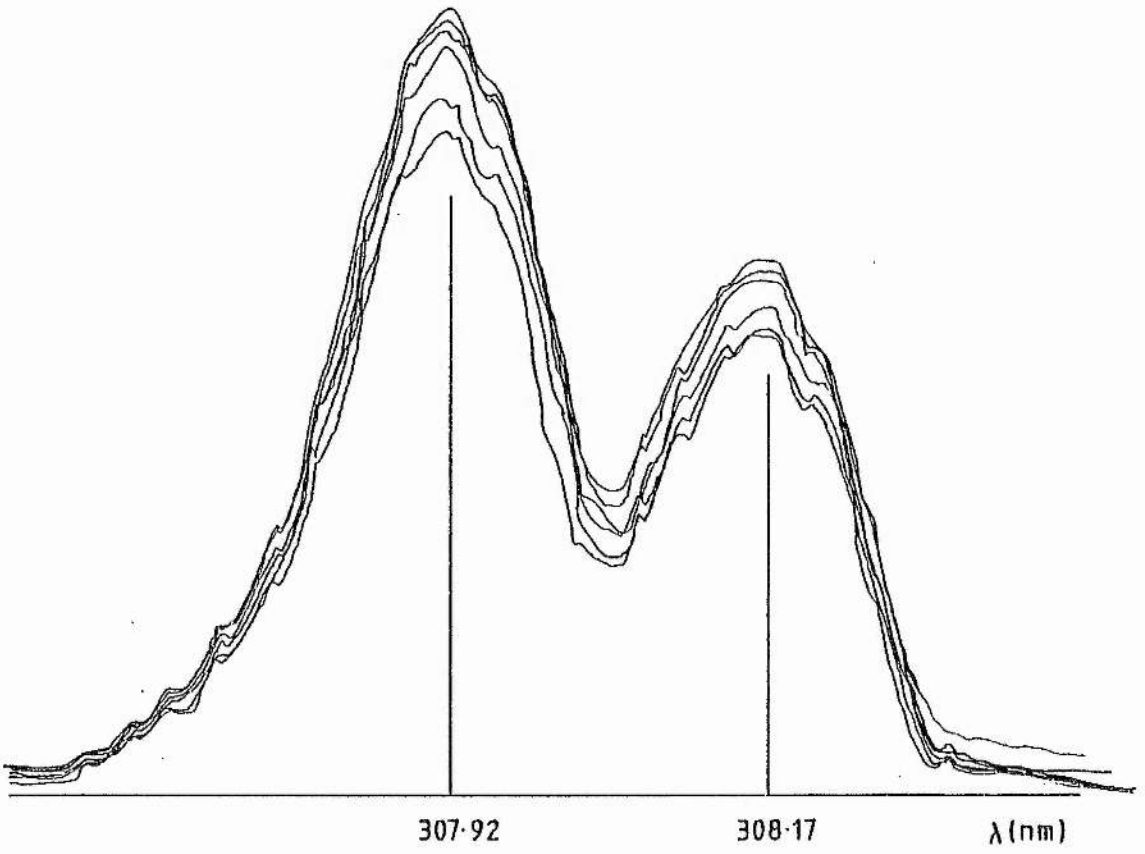

Figure 4.9.4 Optical Spectrum Analyzer (OSA) output of the XeCl* lasing spectrum

Table 4.9.1 Laser operating parameters and properties

	Setting Point	Range
Voltage (kV)	16	15 to 18
HCl pressure (torr)	5	3 to 6.3
(%)	0.22	0.13 to 0.28
Xe pressure (torr)	10	7 to 14
(%)	0.44	0.31 to 0.61
He pressure (atm)	3	1 to 3.5
Repetition Rate (pps)	-	< 20 @ 17 kV max. < 15 @ 20 kV max.
Pulse Width (fwhm) (ns)	32 ± 1	
Energy (mJ)		5 to 8
Number of pulses to half energy	18,000	
Beam divergence (mrad)	8.2	
Discharge volume (l)	1.85	
Max. energy emission per unit discharge vol. (mJ/l)	2.7	

Table 4.9.2 $XeCl^*$ laser spectral dimensions

Investigator	Peak Wavelengths		Separation	Method
	λ_1	λ_2(nm)	(Å)	
Sze & Scott	308.17	307.92		microdensitometer
Maeda et al	308.2	307.9		microdensitometer
This work	308.2	307.95	2.4 ± 0.5	microdensitometer

Table 4.9.3 $XeCl^*$ laser: Dual wavelength intensity ratios

Ratio n_1(308.2nm)/n_2(307.9nm)	% Error	Source
0.6970	7 (S.D)	average of 29 readings
0.6915	4.4 (S.D)	average of 17 readings after removal of extremes.

Table 4.9.4 $XeCl^*$ laser: Dual wavelength peak intensity variation

Quantity	Pulse to pulse variation		
	Average(%) Error	Minimum(%) (from S.D of errors)	Maximum(%)
Error, $\Delta n_1/n_1$, in peak at 308.17 nm wavelength	7.0	3.5	10.5
Error, $\Delta n_2/n_2$, in peak at 307.92 nm wavelength	5.2	1.1	9.3
Error, $(\Delta n_1 + \Delta n_2)/(n_1 + n_2)$ in total output	5.9	2.9	8.9

4.10 Problems in the Laser System

This section is concerned with some system malfunctions and shortcomings and the action taken to remedy the situation.

4.10.1 Noise Emission

To reduce the amount of rf noise transmitted to the detection system, disc ceramic capacitors were fitted to the leads as high pass filters to the earthed enclosure. The supply leads were shielded within their conduits. An inductor between the earthy side of the laser cavity and the enclosure served to prevent large voltage spikes from artificially raising the ground. These precautions have proved to be effective in minimising external noise.

4.10.2 Leaks in the Laser Cavity

The only major leak occured where a cavity window seal became ineffective. The high pressure gas containing HCl was forced between the O-ring and the aluminium window mount resulting in very localised corrosion of the metal, worsening the leak. The plates of figures 4.10.1(a) and (b) show the build up of $AlCl_3$ and the resulting pit at the leak point. The hole was filled with Araldite and the window was resecured.

4.10.3 Leaks in the Gas System

Gas system leaks at the quick connect outlet/inlets were caused by corrosion of the stainless steel by HCl in the presence of moisture from the air. The rust prevented good metal to O-ring contact. Corrosion occurred in the same way in the stainless steel bellows of the shut-off valve in the re-charge cylinder causing a perforation. This valve was replaced by a monel unit. If monel replacements are not obtainable then

quick connect lifetime may be prolonged by efficient purging with helium before exposure to the air. Otherwise the quick connects may be replaced by "Swagelock" couplings of monel.

4.10.4 Laser Pulse Energy

Although an output energy of 50 mJ was aimed at (see section 4.5.2) only one tenth of this was achieved in practice. It is suspected that this was due in part to the reduction of discharge volume by the adoption of sharper profile electrodes rather than those of flatter, "Rogowski" profile. An additional shortcoming may be the lack of adequate pre-ionization, mentioned earlier with respect to the low optimum xenon concentration. Corona wire pre-ionization could be improved upon by a spark board technique, although this was discounted on the grounds of complexity. Higher energies would be possible at voltages higher than 20 kV if this was allowed by component tolerances, bearing in mind the reliability feature. An energy discrepancy is apparent from the reduction in effective capacitance of the barium titanate components when operated at anything other than low voltage. The reduction in effective capacitance is expected for voltages greater than about 40% of the rated figure (Sprague catalogue; K.Matsumoto et al 1980).

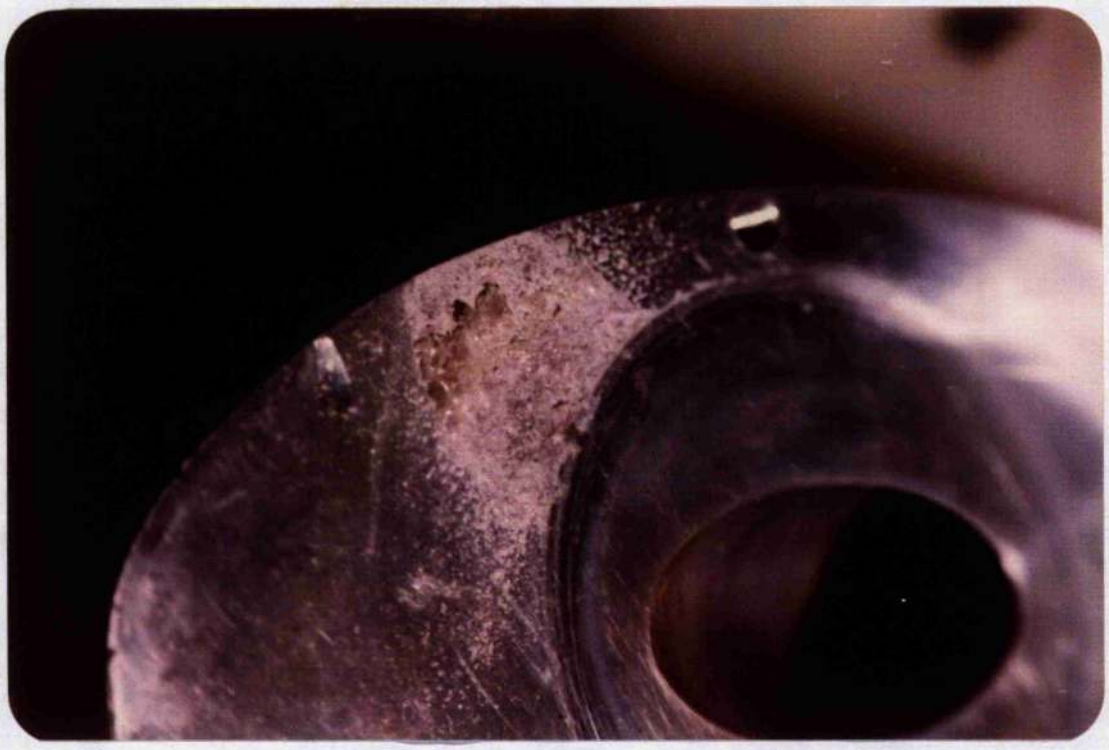

Figure 4.10.1(a) Build-up of $AlCl_3$ at a leak point of the laser window

(b) The resulting pit in the window mount

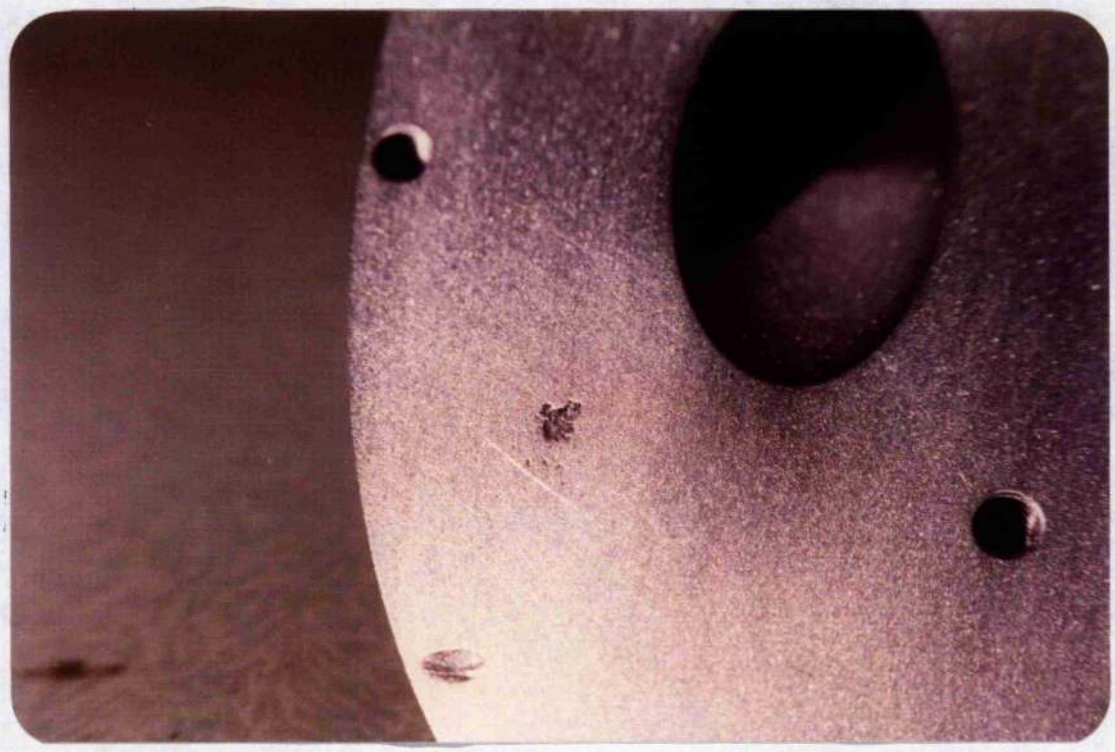

References for Chapter 4

Burlamacchi L; Long-life operation of a XeCl excimer laser. Appl.Phys. Lett., 34, 1, 33, (January 1979)

Burnham R and Djeu N; Ultraviolet preionized discharge pumped lasers in XeF, KrF and ArF. Appl.Phys.Lett., 29, 11, 707, (December 1976)

Burnham R, Harris N.W and Djeu N; Xenon fluoride laser excitation by transverse electric discharge. Appl.Phys.Lett., 28, 2, 86, (January 1976)

Burnham R; Improved performance of the discharge-pumped XeCl laser, Opt.Commun., 24, 2, 161, (February 1978)

Champagne L.F, Palumbo L.J and Finn T.G; Absorption processes in the XeCl laser. Appl.Phys.Lett., 34, 5, 315, (March 1979)

E.E.V, Hydrogen Thyratrons, Descriptive catalogue, (1980)

Ewing J.J and Brau C.A; Laser action on $^2\Sigma^+ \rightarrow {}^2\Sigma^+$ bands of KrF and XeCl. Appl.Phys.Lett., 27, 6, 350, (September 1975)

Ischenko V.N et al; Efficient discharge pumping XeCl laser. Opt.Commun., 21, 1, 30, (1977)

Kudryavtsev and Kuz'mina; Sov.J.Qu.El., 7, p.173, (1977)

Maeda M, Yamashita T and Miyazoe Y; High power XeCl excimer laser by discharge pumping. Japan.J.Appl.Phys., 17, 5, 969, (1978)

Searles S.K and Hart G.A; Stimulated emission at 281.8 nm. from XeBr. Appl.Phys.Lett., 27, 4, 243, (August 1975)

Pirrie C.A; Private communication (1980)

Sutton D.G, Suchard S.N, Gibb O.L and Wang C.P; Fast discharge initiated KrF laser. Appl.Phys.Lett., 28, 9, 522, (May 1976)

Sze R.C and Scott P.B; Intense lasing in discharge excited noble gas monochlorides. Appl.Phys.Lett., 33, 5, 419, (September 1978)

Sze R.C and Loree T.R; Experimental studies of a KrF and ArF discharge laser. IEEE J.Quantum Electron., QE-14, 12, 944, (1978)

Velazco and Setser; Bound-free emission spectra of diatomic xenon halides. J.Chem.Phys., 62, 5, 1990, (1 March 1975)

von Bergmann H.V; Pulsed corona excitation of high power U.V nitrogen lasers at pressures of 0 - 3 bar. Appl.Phys.Lett., 27, 10, 553, (1975)

Waynant R.W; A discharge pumped ArCl superfluorescent laser at 175.0 nm. Appl.Phys.Lett., 30, 5, 234, (March 1977)

Chapter 5 Laser Spectral Modification

The dual wavelength output of the $XeCl^*$ laser, described in chapter 4, is applied to differential absorption lidar. Other DIAL systems have used tunable lasers (see chapter 1), giving a unique wavelength at any instant. (The simultaneous emission of two wavelengths, in work by Inomata and Igoroshi, 1975, is an exception in dye laser DIAL.) If the $XeCl^*$ laser is to provide a single wavelength per pulse then it is necessary to apply a method of wavelength selection, either at the receiver or at the transmitter. The method must be fast enough to allow the tuning operation to occur between adjacent pulses, at a rate of up to 10pps.

Selection techniques available for consideration include dispersion by a grating, a Fabry-Perot type etalon or a method using a birefringent filter. The birefringent filter is investigated as having potential for a practical design. A further and novel idea for some sort of wavelength content modification (rather than distinct wavelength selection) was devised and is applied in preference to the existing methods. More consideration is given to using this method, where an absorption cell is inserted within the laser cavity. This chapter indicates the feasibility for application of each technique to this DIAL system in the field.

5.1 Transmission Grating

A transmission grating would not be used as a laser tuning element. However, it is possible to apply it to separating the excimer wavelengths at the receiver, either as a moveable grating supplying one detector, or as a fixed element supplying two detectors, as shown in figure 5.1.1. The method is only feasible if the angular separation, $\Delta\theta$, between the dispersed paths is large enough, say a few degrees. The grating equation for normal incidence is

$$\sin\theta_\lambda = m\lambda/a, \qquad (5.1.1)$$

where a is the separation of the grating lines, m is the order of diffraction and θ_λ is the angle of diffraction. The dispersion equation, obtained by differentiation of (5.1.1) is

$$\Delta\theta/\Delta\lambda = m/a.\cos\theta_\lambda. \qquad (5.1.2)$$

A combination of (5.1.1) and (5.1.2) gives the angular separation for a wavelength separation of $\Delta\lambda$ in the expression

$$\Delta\theta = m\,\Delta\lambda\,/a.\cos(\sin^{-1}m\lambda/a). \qquad (5.1.3)$$

At a grating line spacing of $a = 5 \times 10^{-7}$m. the angular separation of lines at 307.92 nm. and 308.17 nm. (from table 4.9.2), in the first order, is only a very small fraction of a degree. This small separation was deemed to make a transmission grating an impossible proposition.

5.2 Reflection Grating

The possibility of using a reflection grating at the detector or for tuning the laser was rejected for reasons similar to those mentioned in section 5.1. A reflection grating would be used in the position shown in figure 5.2.1.

5.3 Etalon Tuning

A Fabry-Perot etalon, operating on the principle of multiple interference, can, in theory, be applied to selecting the $XeCl^{*}$ wavelengths, separated by about 2.5 angstroms. The arrangement is shown in figure 5.3.1. The plate separation would be adjusted by voltage ramped, piezo-ceramic transducers. However, a unit with such fine resolution requires suitable di-electric multi-layered coatings to sharpen the transmission peaks. The piezo-ceramics themselves are subject to expansion and contraction with temperature variation. Some experiments with a readily constructed etalon proved its suspected susceptibility to temperature and shock variation. It was concluded that the type of etalon system required for this application would be unsuitable in field equipment of the type required.

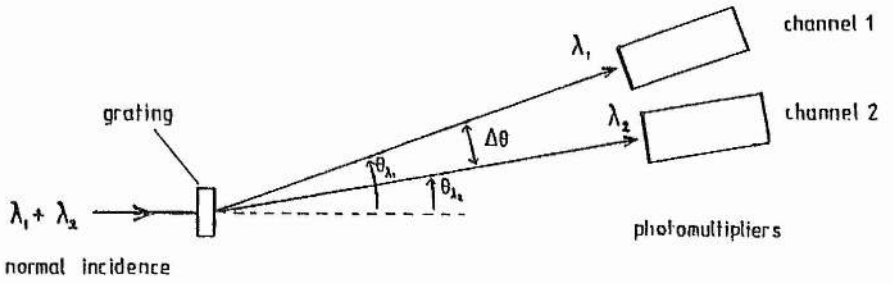

Figure 5.1.1 A transmission grating at the DIAL receiver

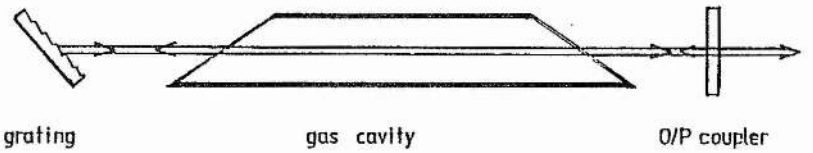

Figure 5.2.1 A blazed reflection grating as the back mirror for laser tuning

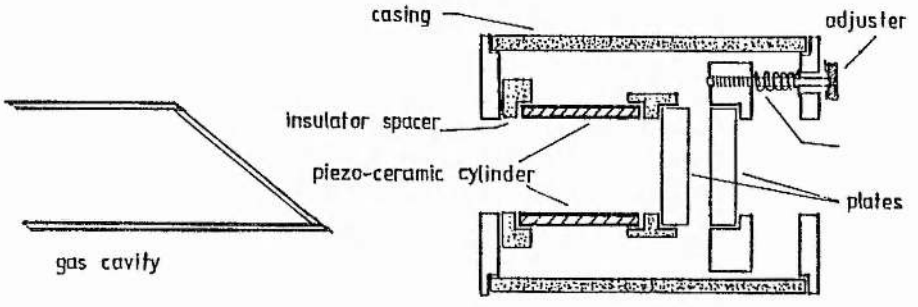

Figure 5.3.1 A Fabry-Perot etalon for laser tuning
The etalon doubles as the output coupler

5.4 Birefringent Filter

A birefringent filter is a combination of retardation plates and polarizers to create a transmission characteristic of equally spaced pass bands. Filter design dictates passband separation and width. This type of wavelength selection is discussed in more detail than the previous methods as it seems to offer the best practical conventional solution to the problem. However, a precise design in this application was rejected in favour of the technique finally adopted for the project, and which is described in section 5.5. A simple birefringent filter is designed in the sub-sections below (after Evans, 1949), illustrating the suitability of the type for $XeCl^{*}$ DIAL. Reference is made to a simple example which has been applied to the tuning of a dye laser (Yarborough and Hobart, 1975). The theory behind the birefringent filter is given in appendices A5.1 to A5.3.

5.4.1 Birefringent Filter Design

In a simple birefringent filter with no tuning facility the polarizer axes are parallel. The birefringent element slow axes are parallel but at 45° to the polarizer axes. This gives a true zero transmission between pass bands (Evans, 1949). The principal features for a birefringent filter design are the passband width, B_{λ} , and the passband separation, $\Delta\lambda$. These depend upon the thickness of the thinnest birefringent element, d_1, the number of units, M, in the filter and the difference between the extra-ordinary and ordinary indices of refraction of the crystal. The radiation and its E-vector (see figure A5.1) are transmitted into the plate in a direction which is perpendicular to the axes of refraction; ie. the crystal is cut along the plane of the axes of refraction. The limit on the thinnest element is set by the minimum requirement on passband separation requiring derivation of a relation between $\Delta\lambda$ and d_1. The bandwidth requirement

determines the thickness of the thickest birefringent element and therefore sets the number of units (by equation (5.4.3). Thus, B_λ is related to d_1 for different M. These relations are shown in figures 5.4.1, plotted from the analysis below with regard to wavelength selection between the dual wavelength $XeCl^*$ laser output. The birefringent filter description and analysis given in appendices A5.1, A5.2 and A5.3 provides the equations for filter design.

The passband width, B_λ , is related to thinnest element thickness, d_1, in conjunction with the number of elements, M, by equation (A5.2.4a), expressed as

$$B_\lambda = \lambda_1^2/(2^M d_1(n_f - n_s) + 2\ \lambda_1), \qquad (5.4.1)$$

where $(n_f - n_s)$ is the relative retardation of the birefringent material and λ_1 is the passband peak wavelength. In application to the $XeCl^*$ laser spectrum, where the two wavelengths, at 307.92nm and at 308.17nm, are separated by 2.5 Å, passband widths around 2.5 Å are considered. Practical birefringent element thicknesses and numbers per filter are considered. Equation (5.4.1) is used, at the wavelength region of 308nm, to plot figure 5.4.1(a) (where quartz is considered as the birefringent material, giving $n_f - n_s = 0.009$; E.Hecht, Optics; Evans, 1949).

The passband separation, $\Delta\lambda$, is shown in relation to the thinnest element thickness, d_1, by figure 5.4.1(b), obtained by equation (A5.2.7a), given as

$$\Delta\lambda = \lambda_a^2/(d_1(n_f - n_s) + \lambda_a), \qquad (5.4.2)$$

where λ_a is the principal wavelength of interest, at 308nm in this case.

Figure 5.4.1 is used to design the $XeCl^*$ laser tuning filter. The thickness of the M^{th} birefringent element, based on that of the thinnest element, is given by equation (A5.1.9) as

$$d_M = 2^{M-1} d_1. \qquad (5.4.3)$$

Tuning of the filter is described in appendix A5.3, with the method shown in application to tuning the $XeCl^*$ laser output, given in section 5.4.2(b).

5.4.2 Birefringent Filter for $XeCl^*$ Laser Tuning

5.4.2(a) Basic Design (passband consideration)

The $XeCl^*$ lasing spectrum is given in figure 4.9.4, showing the peaks at 307.92nm and at 308.17nm. The passband separation must be large enough to exclude all emitted radiation, occurring within a wavelength region of 10 Å. Thus, the value for $\Delta\lambda$ should be limited to a minimum of 10 Å, so that, by figure 5.4.1(b), the thinnest plate thickness, d_1, is limited to a maximum of 10mm. The thickest plate (by combination of the number of units, M, and the thickness, d_1) determines the passband width, B_λ. The $XeCl^*$ lasing peaks are separated by 2.5 Å. If the pass bandwidth were to be limited to 1.5 Å and just 3 units were to be employed, then figure 5.4.1(a) gives a thinnest element thickness of 8.5mm. The thickest element in this case is 34mm thick, by equation 5.4.3. The passband separation (figure 5.4.1(b)) is now 12 Å. The birefringent element thicknesses and filter specifications are listed in table 5.4.1. The plates are drawn in section in figure 5.4.2.

5.4.2(b) Tuning Method

Tuning of the filter designed above is carried out by introducing a retarding quarter-wave plate per element of the filter, after Evans (1949). The principal axis of the quarter-wave plate is positioned parallel to the axis of the preceeding polarizer, of the same unit. The mechanics of the method involve rotation of each element by a different angle. The following analysis describes how the angular variation between the units is quantified for tuning the output from the $XeCl^*$ laser. The basis for the analysis is given in appendix A5.3. A schematic diagram for the tunable filter is given in figure 5.4.3. The first unit (M=1) remains fixed with respect to the instrument axis. The second unit (M=2) is rotated through an angle θ_1, relative to the instrument axis. The third unit (M=3) is rotated through an angle θ_2, relative to the axis. The final polarizer is rotated through an angle θ_3.

Equation (A5.3.10) is applied to the $XeCl^*$ laser wavlength at 308.17nm, using the specification of the fixed spectrum birefringent filter, designed above, to give the desired angle between the axis of the M^{th} quarter-wave plate and the axis of the following polarizer; ie. the angle between successive units of the filter. Thus, the respective angles are given by equation (A5.3.10) in

$$\rho_M = 2^{M-1}(\pi\, d_1(n_f - n_s)/\lambda_a) - \pi \cdot \text{integer value of } 2^{M-1}(d_1(n_f - n_s)/\lambda_a) \qquad (5.4.4)$$

which provides the appropriate relative angles with values less than 180^o. The relative angles between units, in this case, for tuning a transmission peak onto 308.17nm, are $\rho_1 = 67.8^o$; $\rho_2 = 135.6^o$; $\rho_3 = 91.2^o$. The angle,

θ_M, which each unit must be set to, with respect to the instrument axis, is given by the sum of the preceeding relative angles, given by (A5.3.8) as

$$\theta_M = \sum_M \rho_M . \qquad (5.4.5)$$

Equation (5.4.5) is evaluated to set the units at the angles shown in figure 5.4.3; $\theta_1 = 67.8^o$ (247.8^o); $\theta_2 = 203.4^o$ (23.4^o); $\theta_3 = 294.5^o$ (114.5^o). The bracketed figure are the 180^o equivalents, if such a direction were to be more conveniently applied in a physical situation. These directions would be shown on a graduated scale on the units.

The wavelength shift, necessary to tune the $XeCl^*$ laser, is 2.5 Å. This shift is achieved by adjusting the angles between the filter units. The additional relative angle between units is given by (A5.3.2) as

$$\rho_M = 2^{M-1}(\rho_a + \Delta\rho), \qquad (5.4.6)$$

where ρ_a is the original angle between the first two units, when tuned to the wavelength λ_a and where $\Delta\rho$ is the added angle between the first two units, creating a wavelength shift over the transmission spectrum. The shift of the transmission peak from wavelength λ_a to λ_ρ is related to the corresponding angular rotation, $\Delta\rho$, between the first and the second units in the expression (by (A5.3.6))

$$\Delta\rho = \pi d_1(n_f - n_s)(\lambda_a - \lambda_\rho)/ \lambda_a\lambda_\rho , \qquad (5.4.7)$$

which is used to set the new relative angles of all the units for the desired wavelength shift. Thus, the angles, θ_M, about the instrument axis, are defined by using equation (5.4.5). The necessary angular rotation for

each unit ($\Delta\rho_1$, $\Delta\rho_2$, $\Delta\rho_3$) is plotted for wavelength variation in figure 5.4.4, (showing the shift to the 307.92nm laser peak) which includes the relative angles and settings, with respect to the instrument axis, for tuning a peak to 308.17nm. Figure 5.4.4 shows that the tuning accuracy which may be expected if the angular movement could be controlled to, say, within 2^{o}, is 0.14 Å. The angles ρ_M and θ_M, for tuning to 308.17nm, and the shifts, $\Delta\rho_M$, for tuning to 307.92nm, are given in table 5.4.1.

In the final filter, in each unit, illustrated in figure 5.4.3, the polarizer axis and quarter-wave plate principal axes are parallel but at 45^{o} to the principal axis of the birefringent element. Tuning is carried out by rotating each unit (the first one, M=1, is fixed) and the final polarizer. Filter specification is given in table 5.4.1.

A relatively simple and tunable birefringent filter was the subject of a United States Patent by Yarborough and Hobart (1975) who designed a 3 element unit for the intra cavity tuning of a dye laser. The necessity for polarizers was avoided by operating the filter at Brewster's angle to the optical axis, given by

$$\tan \phi_B = n_b/n_a, \qquad (5.4.8)$$

where n_b is the refractive index of the birefringent element and n_a is the refractive index of the surrounding air. The tuning method utilises the inclination of the filter. Appendix A5.1 gives the theory behind birefringent filter operation which must preceed the following explanation. Figure 5.4.5 shows one birefringent plate inclined at the Brewster angle. The fast (F) and slow (S) axes have been resolved into the fast component (f) and the slow component (s). Although the radiation is not incident

along either the fast or the slow axis it can be resolved into a fast component and a slow component, creating a certain phase shift on passage through the crystal. If the element is rotated about its slow (S) axis, the effective slow component of the radiation is unaltered while the change in the effective fast index of refraction changes the fast radiation component. The new difference in phase, thus induced, shifts the peaks of the transmission spectrum, the filter having been tuned to another wavelength series. The filter elements, in the example of Yarborough and Hobart, follow a different increment (4^{M-1} rather than 2^{M-1}) to that suggested in the design following Evans, probably because it was applied to a dye laser with a broader spectral gain curve. The suggested plate thicknesses of the original design, above, would be adhered to but the polarizers would be omitted in operating the filter at the Brewster angle.

5.4.3 Application to the DIAL System

The birefringent filter may be used to select the appropriate $XeCl^{*}$ wavelength, either by its insertion within the laser optical cavity, where the non-linear nature of the gain would sharpen the tuning curve of the filter. Further application of the birefringent filter would require calculation of this effect. A more complex type, beyond the design scope of this work, is the reflecting birefringent filter, of split elements (Evans, 1949; F.K.von Willisen, 1966), which may replace the total reflector at the back of the laser cavity. The operation of the filter as a tunable part of the cavity would probably allow greater powers for the output pulse. All in all, the birefringent filter, in one form or another, is an option for wavelength selection in $XeCl^{*}$ DIAL.

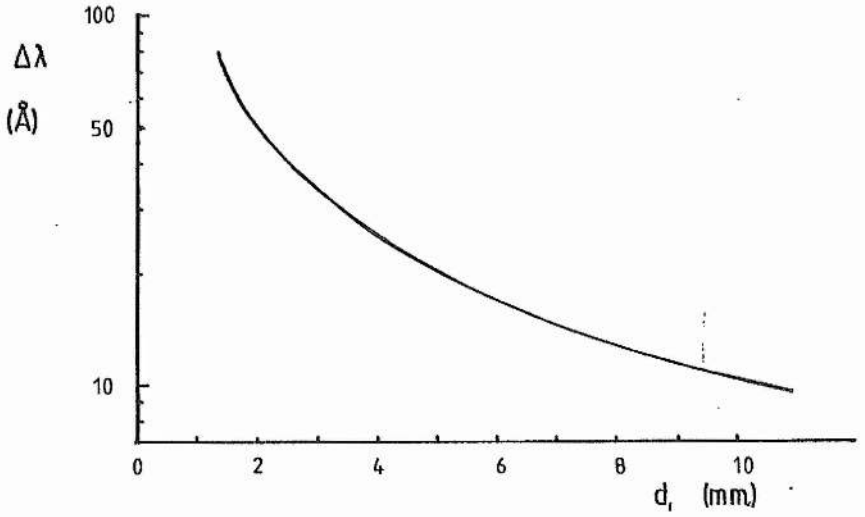

(b) Passband separation vs. thinnest element thickness

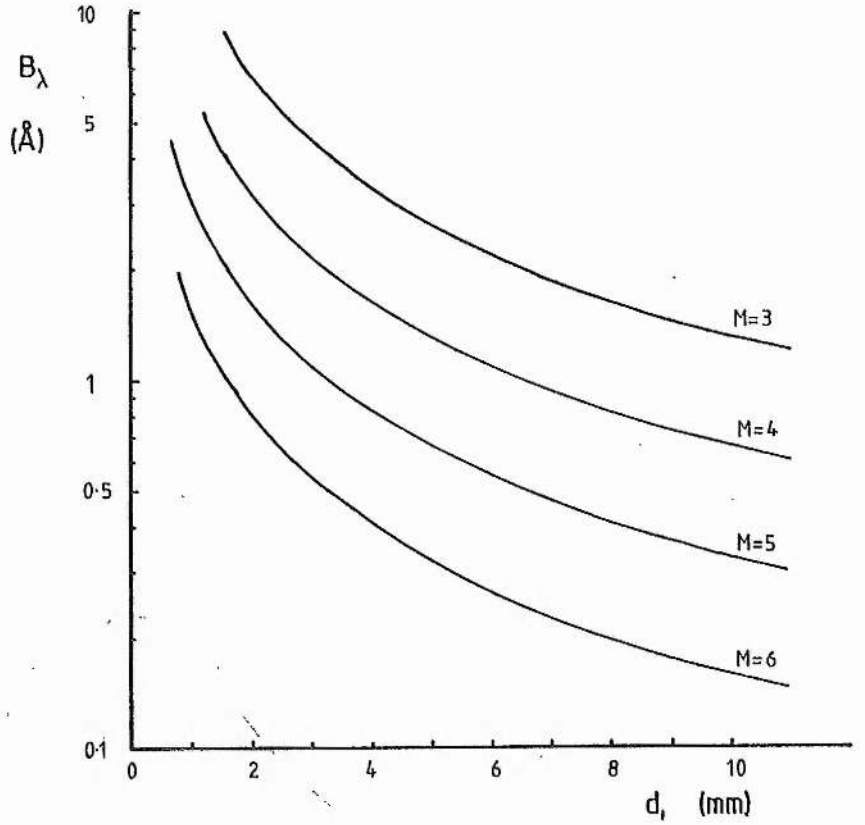

(a) Passband-width vs. thinnest element thickness for different numbers of units

Figure 5.4.1 Spectral transmission characteristics of quartz plate birefringent filter as a function of the birefringent element thicknesses and number of units

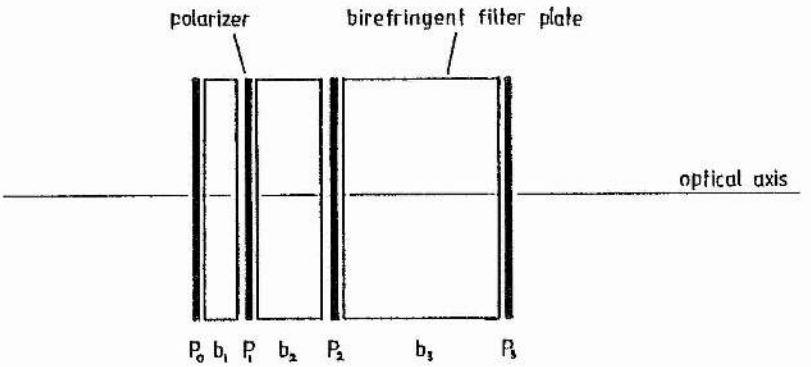

Figure 5.4.2 Schematic of a simple, 3 unit, birefringent filter

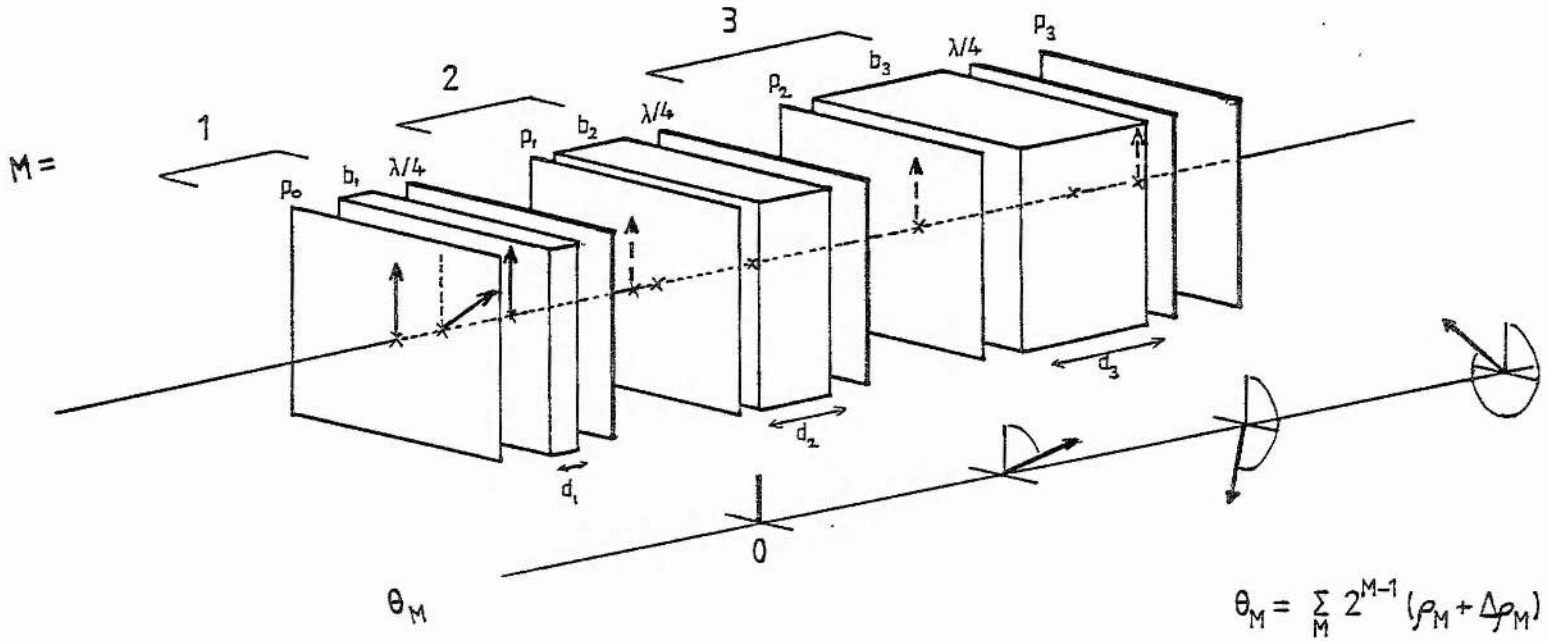

Figure 5.4.3 Schematic representation of a 3 unit, tunable, birefringent filter for application to XeCl* laser tuning

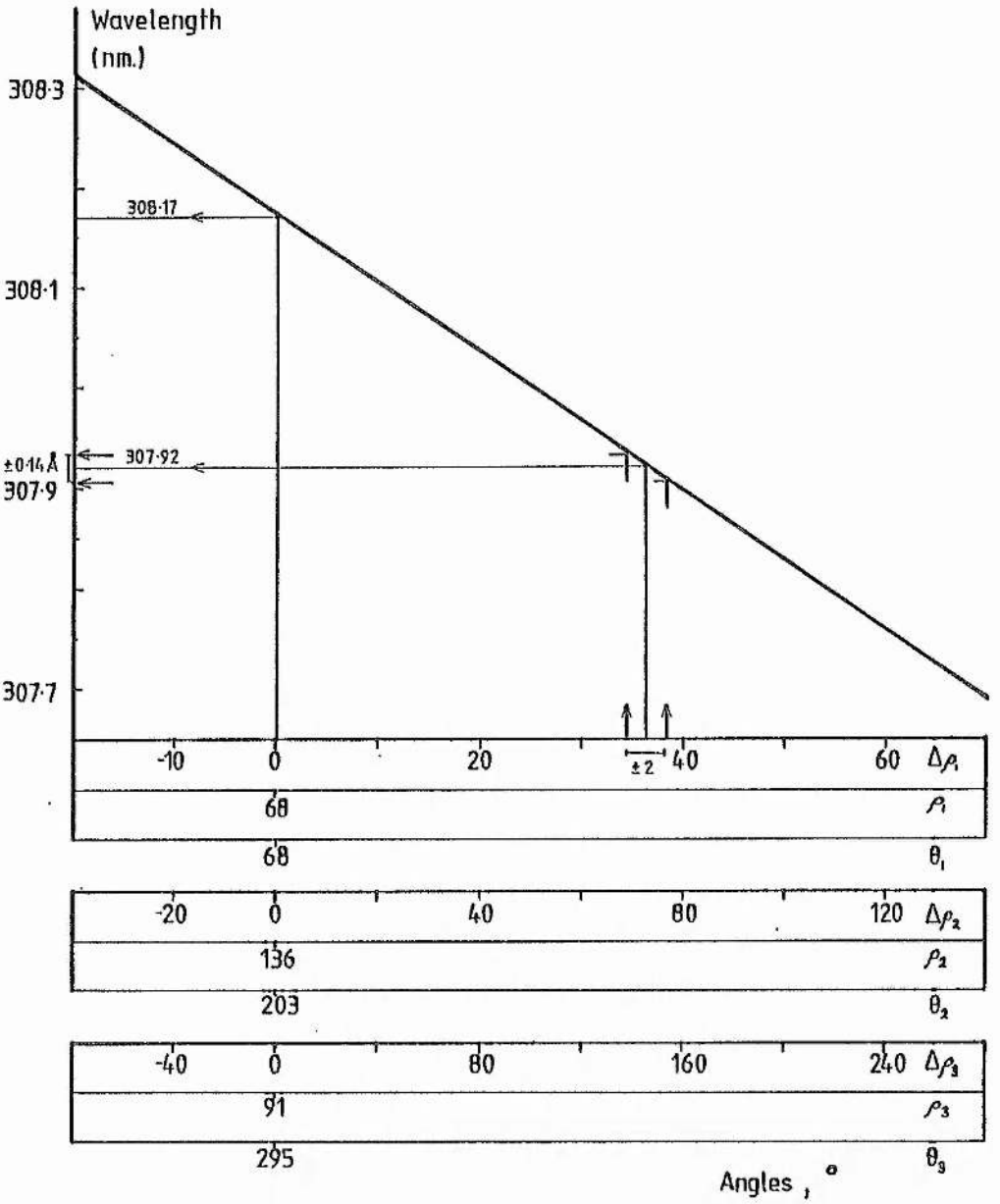

Figure 5.4.4 $XeCl^{*}$ laser tuning by birefringent filter. The angular variation between the axis of each quarter-wave plate and the axis of the following polarizer, between the three units of a birefringent filter. The respective wavelength shifts, $\Delta\rho$ from a position tuned to 308.17nm, the relative angles, ρ, between units tuned to the 308.17nm peak, and the angular settings, θ, at 308.17nm, with respect to the instrument axis

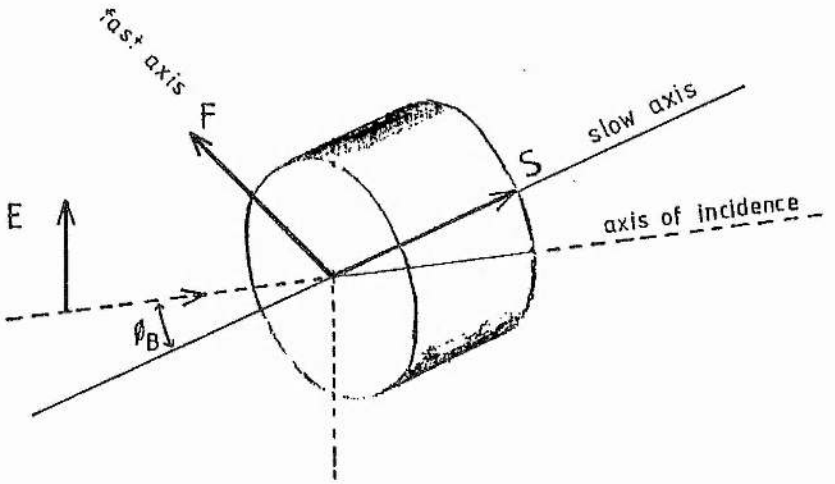

Figure5.4.5 A birefringent plate operated as a filter at the Brewster angle for easy tuning (Yarborough and Hobart, 1975)

Table 5.4.1 Specification of a Birefringent Filter XeCl* Laser Wavelength Selection.

Parameter	Symbol	Value
Bandwidth	B_λ	1.5 Å
Passband Separation	$\Delta\lambda$	12 Å
Number of elements	M	3
Element thickness	d_1	8.5 mm
	d_2	17.0 mm
	d_3	34.0 mm
Angle between units for tuning to 308.17nm	ρ_1	67.8°
	ρ_2	135.6°
	ρ_3	91.2°
Angle of units about instrument axis for tuning to 308.17nm	θ_1	67.8° (247.8°) *
	θ_2	203.4° (23.4°)
	θ_3	294.5° (114.5°)
Angular increment for shifting passband to 307.92nm	$\Delta\rho_1$	36.3°
	$\Delta\rho_2$	72.6°
	$\Delta\rho_3$	145.1°

* Bracketed angles are 180° equivalents

5.5 Absorption Cell (SO_2)

Differential absorption lidar (DIAL) has traditionally used two pulses, each of unique wavelength, per sample. Chapter 9 describes DIAL theory applied to this case, pointing out the cancellation of atmospheric effects by ratioing return signal powers. The methods of distinct wavelength selection and their application, where possible, to the dual wavelength $XeCl^*$ emission (figure 4.9.4) have been described in the preceeding sections. Chapter 9 also describes a novel method, in DIAL, where the relative intensities of the two peaks are modified for one of the pulses. The other pulse is an unaltered dual wavelength transmission. This section explains the method of modification by inserting, within the optical cavity, a cell containing a gas which has different absorption cross section at the two $XeCl^*$ laser lines. The gas chosen for the cell is SO_2.

5.5.1 Cell Coefficients

Laser output is considered as the number of photons, n_1, emitted at wavelength λ_1 and the number, n_2, emitted at wavelength λ_2. An unaltered laser output emits $n_1 + n_2$ photons. If a cell of a differentially absorbing gas is inserted within the laser optical cavity as shown in figure 5.5.1 then the component at the wavelength λ_1 is modified by a coefficient, a, less than unity and the component at λ_2 is modified by a similar coefficient, b, so that the entire pulse is of $an_1 + bn_2$ photons. The coefficients a and b are expressed by considering the net amplification of photons in travelling within the bounds of the optical cavity of figure 5.5.1. If no cell is present, then an initial number of photons, n_i, of wavelength λ_1 are amplified to give n_1 photons emitted according to the expression

$$n_1 = n_i.\exp(\mathcal{N}_c \alpha \ell).\mathcal{R}''^{((\mathcal{N}_c-1)/2)}.\mathcal{R}'^{((\mathcal{N}_c-1)/2)}.(1-\mathcal{R}''), \qquad (5.5.1)$$

where $\mathcal{N}_c$ is the number of single passes of the gas cavity which has an active length ℓ, α is the net amplification coefficient of the laser medium and $\mathcal{R}'$ and $\mathcal{R}''$ are the back mirror and output coupler reflectivities, respectively. If an absorption cell is inserted, then equation (5.5.1) is modified by the absorption term due to the cell material itself and to the gas to give

$$an_1 = n_i.\exp(\mathcal{N}_c \alpha \ell).\mathcal{R}''^{((\mathcal{N}_c-1)/2)}.\mathcal{R}'^{((\mathcal{N}_c-1)/2)}.(1-\mathcal{R}'').K.\exp(-\mathcal{N}_c \sigma_1 N_T x), \qquad (5.5.2)$$

where σ_1 is the absorption cross-section at wavelength λ_1, x is the gas path length, N_T is the cell gas molecular number density and K is the generalised factor to account for cell material absorption and other losses. Taking the ratio of equations (5.5.1) and (5.5.2) gives the appropriate cell coefficient as

$$a = K.\exp(-\mathcal{N}_c \sigma_1 N_T x). \qquad (5.5.3)$$

Similarly, for wavelength λ_2, the other cell coefficient is given by

$$b = K.\exp(-\mathcal{N}_c \sigma_2 N_T x), \qquad (5.5.4)$$

where σ_2 is the absorption cross-section at λ_2. It is convenient to express the gas number density as pressure, P(torr) so a conversion is applied, with derivation given in appendix A9.1 (A9.1.7) to give

$$a = K.\exp[-9.657 \times 10^{24}.\mathcal{N}_c.\sigma_1.x.P(\text{torr})/T(^{o}K)] \qquad (5.5.5)$$

and

$$b = K.\exp[-9.657 \times 10^{24}.\mathcal{N}_c.\sigma_2.x.P(\text{torr})/T(^{o}K)], \qquad (5.5.6)$$

where $T(^{o}K)$ is the cell temperature.

5.5.2 Application of the Absorption Cell

The feasibility of the SO_2 cell in DIAL is justified on an operational basis in chapter 9, using the expressions (5.5.5) and (5.5.6). Its physical suitability is based on its robustness and low cost. Wavelength modification is obtained by simply placing the cell within the optical cavity, between the Brewster window and the output coupler. A quartz cell was fitted with a flexible connection to a bellows valve to permit adjustment of pressure. The cell is mounted on a disc which is rotatable between the "in" and "out" positions by a two position motor. A photograph of the housing containing the cell assembly and peripherals is shown in figure 5.5.2. Cell switching is accomplished by a motor drive supply unit operated by logic circuits from a synchronising trigger pulse taken from the main laser trigger unit. The circuit, drawn in figure 5.5.3, allows the cell to be placed within the optical cavity for every alternate laser pulse. In the adopted method, the cell was inserted as described and then removed to allow free passage of the dual wavelength laser pulse. The effect of the cell itself must be taken into account by the factor K. An alternative procedure would be to insert an evacuated cell for the unmodified pulse, allowing easy cancellation of the factor K in the DIAL analysis. For the purpose of a model the value of K is defined by experiment.

5.5.2(a) Cell Specification

The dimensions of the quartz cell are indicated in table 5.5.1. Experiments have established the optimum SO_2 cell pressure for the cell between 30 and 100 torr. In chapter 9 a theoretical treatment of DIAL SO_2 measurement, using the absorption cell technique, defines an optimum cell pressure for desired accuracy and sensitivity to SO_2 concentration. The mechanical switching rate with the present set-up allows a maximum laser repetition rate of 10 pps for adjacent transmission of DIAL pulse pairs. This is a point to be improved upon, considering that static fill lasing can be taken to 20 pps (see chapter 4).

5.5.2(b) Modification of the $XeCl^*$ Laser Output Spectrum

The expressions (5.5.5) and (5.5.6), applied to a cell of SO_2, can show the theoretical relative lowering of the peaks of the $XeCl^*$ lasing spectrum if a reasonable value for the number of single passes of the cavity, N_c, is used. An unaltered lasing spectrum is shown in figure 4.9.4. Experiments were carried out using an optical spectrum analyser (OSA) with a hard copy facility to investigate the modification of the lasing spectrum by the SO_2 absorption cell. Examples of the modified spectrum for different cell pressures are shown compared to the unmodified spectrum in figure 5.5.4 with an arbitrary intensity scale. The ratio of the two wavelength peaks is plotted against a variation in cell pressure. In this way, by ratioing, in the theory, equations (5.5.5) and (5.5.6) the factor K is eliminated. The modified experimental ratios, obtained from figure 5.5.4 at different pressures, are tabulated with the respective cell pressures in table 5.5.2(a) and are plotted in figure 5.5.5. The natural, unmodified ratio, $n_1/n_2 = 0.6757$, is that at a cell pressure of zero, where $a = b = K$. This sets the zero pressure ratio to be applied in a theoretical application, although more rigorous experimental evidence gave a ratio of 0.6915 (table

4.9.3) for use in a DIAL model (chapter 9). The theoretical ratios, using (5.5.5) and (5.5.6), are given by

$$an_1/bn_2 = (n_1/n_2).\exp[-9.657 \times 10^{24}.\mathcal{N}_c x(\sigma_1 - \sigma_2)P(\text{torr})/T(^oK)]. \quad (5.5.7)$$

Known parameter values for equation (5.5.7) are given in table 5.5.1, leaving the value of $\mathcal{N}_c$, the number of single passes of the cavity, to be defined. The maximum value for $\mathcal{N}_c$ is given by the temporal fwhm of the laser pulse, 32 ns., which is entered into the expression

$$\mathcal{N}_{c\ max} = c\tau/L \quad (5.5.8)$$

to give

$$\mathcal{N}_{c\ max} = 10. \quad (5.5.9)$$

The experimental evidence stated in table 5.5.2(a) is used in equation (5.5.7) to define a value for $\mathcal{N}_c$, as an average obtained from the three values given per cell pressure in table 5.5.3. The values, seemingly, do not follow a pressure dependent distribution, already verifying the validity of equation (5.5.7), and they are averaged to give

$$\mathcal{N}_c = 2.36. \quad (5.5.10)$$

This value of $\mathcal{N}_c$ can now be used in equation (5.5.7) to predict the normalized theoretical spectrum peak ratios, tabulated in table 5.5.2(b) and plotted as a function of cell pressure in figure 5.5.5 (including the experimental plot). The slight variation between experimental and theoretical plots is the result of averaging to find $\mathcal{N}_c$.

The value of K is estimated from measurements of the peak intensities as obtained without an intra cavity cell and with an evacuated intra cavity cell. The measurements, given in table 5.5.4 for each peak are on an arbitrary scale but are ratioed in the general expression

$$K = (a,b.n_{1,2})_{\text{cell vacuum}}/(n_{1,2})_{\text{no cell}}, \qquad (5.5.11)$$

where $a = b = K$ for an evacuated cell and $a = b = 1$ where there is no cell. This gives an average value of 0.82 for K, applicable to a lidar model.

The exercise in defining the parameters $\mathcal{N}_c$ and K, above, is of prime value in lidar and DIAL models. However, the data handling technique of the operational DIAL system should contain a method for their automatic determination or correction for inaccuracies.

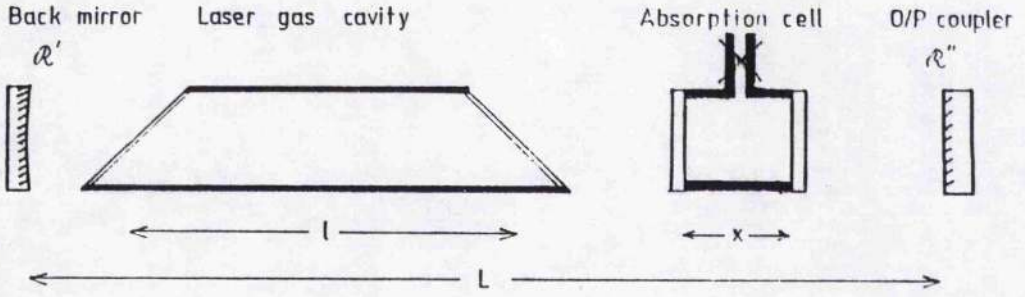

Figure 5.5.1 Schematic of the absorption cell within the laser optical cavity

Figure 5.5.2(a) Absorption cell housing and laser output coupler

(b) The absorption cell in situ

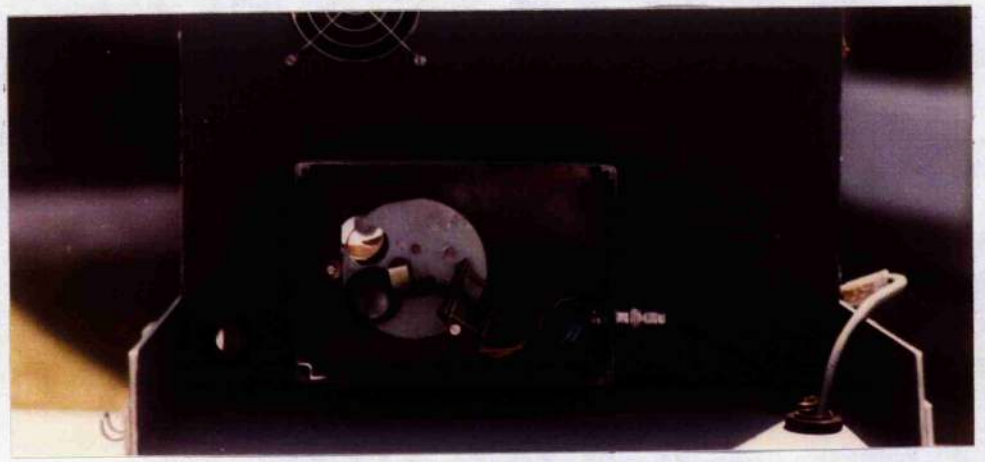

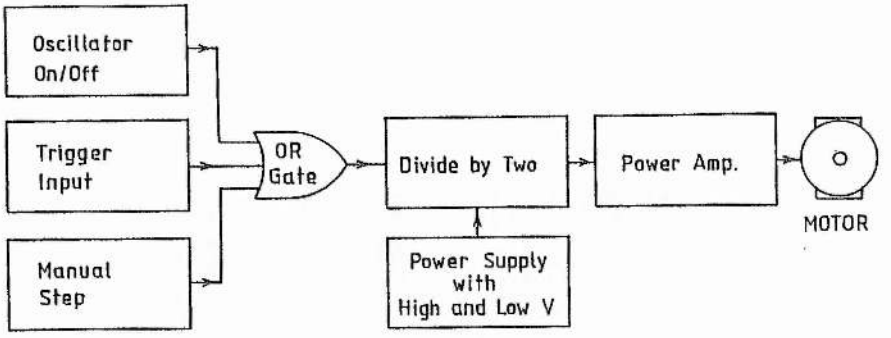

Figure 5.5.3 Block diagram of the circuit of the cell switching unit. The cell motor is switchable by an external trigger or an internal, variable rate, oscillator.

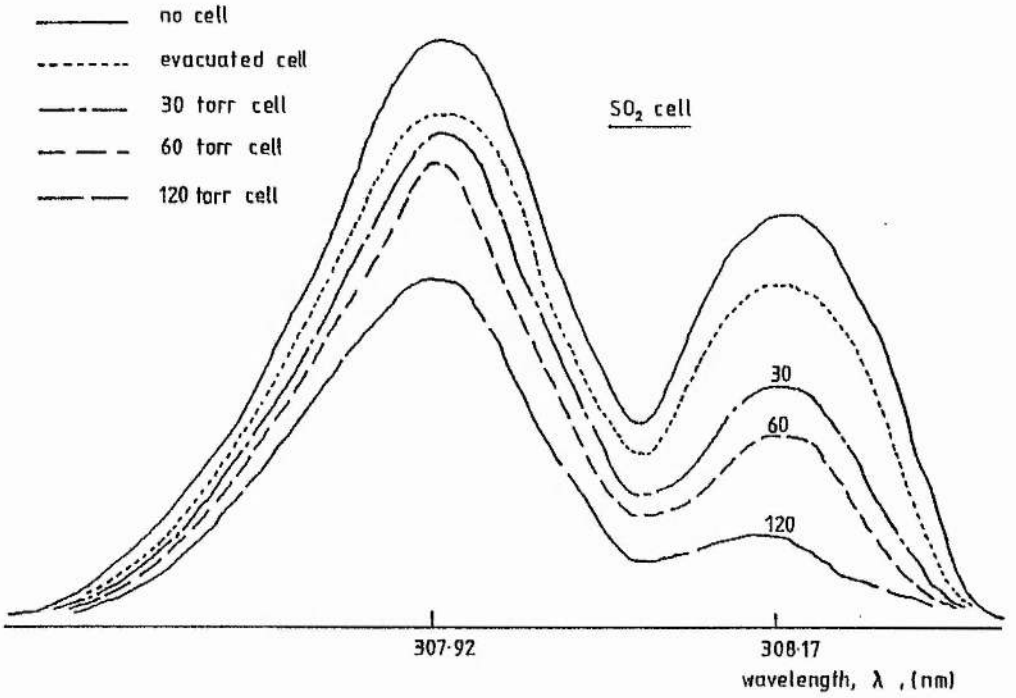

Figure 5.5.4 Modification of the XeCl* lasing spectrum by an absorption cell within the optical cavity.

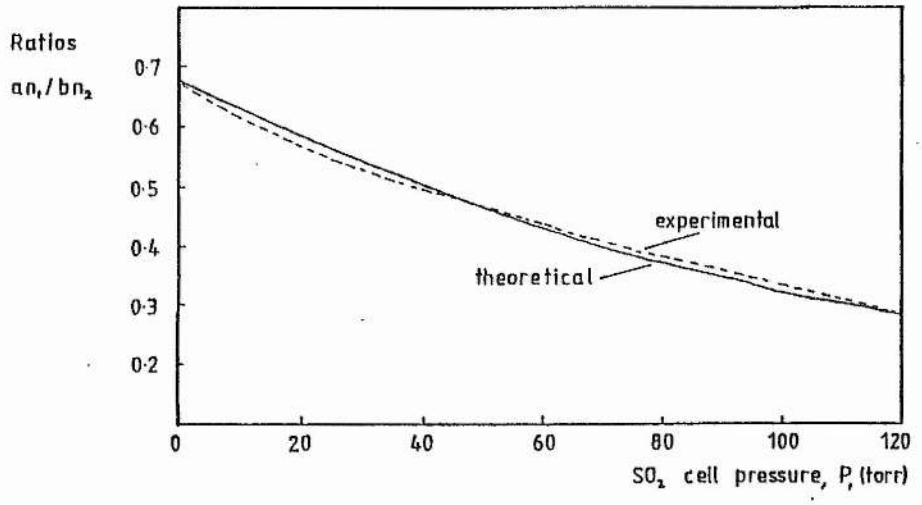

Figure 5.5.5 Modified peak ratios as a function of cell pressure

Table 5.5.1 Modification of the $XeCl^*$ Laser Output Spectrum by an Intra-cavity Absorption Cell: Parameter Values for a Theoretical Treatment using Equation (5.5.7).

Parameter	Symbol	Value
Unmodified peak ratio	n_1/n_2	0.6757
Active cell length	x	0.01 m
Cell temperature (lab)	T	290 ^{o}K
X-section difference(Brassington),	$\sigma_1 - \sigma_2$	9.5×10^{-24} m^2
Laser optical cavity length	L	0.95 m
Pulse fwhm	γ	32 ns

Table 5.5.2 Cell Pressure vs. Modified Peak Ratios

Cell Pressure	Ratio an_1/bn_2	
P, (torr)	Experimental (a)	Theoretical (b)
0	0.6757	0.6757
30	0.5288	0.5400
60	0.4453	0.4316
120	0.2826	0.2757

Table 5.5.3 Experimental N_c Values (no. of single passes of the laser cavity) per cell pressure.

Pressure, P (torr)	N_c
30	2.58
60	2.20
120	2.30
	(2.36)

Table 5.5.4 Intensities of the Peaks (arbitrary units) as Obtained with an Evacuated Cell and with No Cell to give the Cell Effect expressed by the factor K.

Situation	an_1	bn_2
no cell (a=b=1)	117	166
evacuated cell (a=b=K)	95	139

5.6 Conclusion of Chapter 5

In all the methods of wavelength selection or tuning of the $XeCl^*$ laser the emphasis was placed on finding a technique for which the equipment could be designed and manufactured "in house". The requirement, in certain cases, of precisely made gratings, etalons or birefringent plates would have necessitated the specifying and purchasing of such costly items at the risk of finding the method unsuitable for this particular application. The equipment finally constructed for the DIAL system meets the twin requirements of tuning and insensitivity to shock and misalignment.

The previous sections of this chapter have discussed the considered options, and have rejected the transmission and reflection gratings and the etalon. A tentative look at the specification of a simple birefringent filter indicated its suitability, given the necessary funds. The technique which was eventually used for this DIAL set-up, in keeping with the relative simplicity of the rest of the system, was the use of an absorbing gas cell, inserted into the laser cavity to modify the spectral distribution of the laser output.

References for Chapter 5

Brassington D.J; Tunable Dye Laser Measurements of the SO_2 Absorption Spectrum Between 290 and 317 nm., C.E.R.L Lab. Note No.RD/L/2055N81, Job No.VC 299, June 1981; Sulphur Dioxide Absorption Cross-section Measurements from 290 nm. to 317 nm., Appl.Opt., 20, 21, (1981)

Evans J.W; The Birefringent Filter, J.Opt.Soc.Am., 39, 3, 229, (1949)

Hecht E; Optics, Schaum's Outline Series, M^{c}Graw-Hill

Inomata and Igorishi; Japan.J.Appl.Phys., 14, 11, pp.1751-60, (1975)

von Willisen F.K; A Tunable Birefringent Filter, Appl.Opt., 5, 1, 97, (1966)

Yarborough J.M and Hobart J.L; Improved Tuning Apparatus for a Dye Laser,United States Patent 3,868,592, 25 Feb., (1975)

Chapter 6 Signal Handling

This chapter describes how the lidar return signals are stored and interpreted to give SO_2 concentration measurements. Description is made of the signal handling circuits and the micro-computer control and analysis of data. Operational details are given in chapter 10.

6.1 Requirement for Signal Measurement

In DIAL, the measurement of return signal levels provides data from which atmospheric SO_2 concentrations can be evaluated. The signal returned from the smoke plume target is reproduced as a voltage pulse (typically 10mV to 300mV; see chapter 8) across the output load resistor of the photomultiplier. In the present form of this DIAL system the pulse is used to define the range location of the target sample, requiring measurement of the peak voltage as representative of the return level. This is defined in the rest of this thesis as the return photon curents n' and n", for the respective pulses of a DIAL pair. In order to provide the range resolved target measurement the presence of the ambient SO_2, over the range to the target, is measured in a preliminary DIAL sequence, giving an integrated-range result away from the target. The results are used in the analysis of a repeat sequence, measuring the integrated-range return from the target, to subtract the ambient absorption, leaving a range resolved result.

Measurement of pulse peaks is the simplest, cheapest and most reliable way in which return measurements can be made in the present $XeCl^*$ laser DIAL system. If return signal levels are to be measured at intervals along the

return distribution (where the pulse width may be only 100ns), then an expensive, fast sampling system of at least 10 MHz bandwidth, would be necessary. Peak voltage levels are necessarily digitised for immunity from interference and for storage in micro-computer memory, from which they are retrieved for averaging in error reduction. Interpretation of the measurements as SO_2 concentration is achieved by insertion into a DIAL algorithm, introduced in equation (1.3.6) but developed for a distinct wavelength case and for a mixed wavelength case in chapter 9 to give equations (9.1.10) and (9.5.8) respectively.

The data acquisition and analysis in the $XeCl^*$ laser DIAL system is carried out by an Acorn Atom micro-computer which controls a signal measurement and digitising circuit driven by the photomultiplier and laser energy detector. Presentation of the results is via VDU and printer. The signal handling system is described in detail below.

6.2 Signal Handling Circuit and Hardware

The process by which the signal handling circuit accepts photomultiplier output signals, to provide signal return level data, is described. The signal handling circuits are illustrated and their function is explained.

6.2.1 Signal Measurement and Digitising

The signal handling circuit, interfacing between the detectors and the micro-computer, is in three functional parts. These are the analogue, the digital and the logic control circuits, shown in the block diagram of figure 6.2.1. Figure 6.2.1 simplifies the explanation of the complete circuit, illustrated in figure 6.2.3. The logic circuit paths are shown in figure 6.2.2.

Two input channels are provided for analogue signals. One of these is for the photomultiplier signal originating in the atmospheric return and the other accommodates the ouput from a solid state detector situated outside the laser optical cavity, where it measures part of the laser output. This serves as a monitor of laser pulse energy, allowing the measurement to be used to normalize the corresponding measured return level, providing automatic compensation for pulse energy degradation and pulse-to-pulse variation.

During measurement of the laser energy, the incoming pulse peak voltage is measured by a FET sample-and-hold stage. After 10X amplification, the peak level is sampled by a commercial sample-and-hold circuit which posesses a lower droop-rate but which would not be fast enough to "catch" the original peak. The return signal channel has an ultra-fast buffer stage followed by

a fast, X10 gain, amplifier with a bias adjustment facility. A high-quality, fast, sample-and-hold circuit measures the incoming peak voltage. This channel is capable of measuring a pulse peak where the rise-time is greater than 200ns. The final voltage measurement from each sample-and-hold channel is switched to the A-to-D converter input at an appropriate time, defined by an externally sourced trigger (from the laser trigger synchronisation pulse).

A 12-bit analogue to digital converter, in "stand alone" mode is used to pass the measured information to the input/ouput bus of the Acorn Atom computer, using 8 bits on port A and 4 bits on port B. The Read/Convert enable pulse, initiated by the trigger pulse, is switched by the logic circuit for the return signal measurement, and by a computer-sourced pulse for the laser energy measurement. The use of a 12-bit measurement, instead of an 8-bit, gives an improvement on accuracy by a factor of 16, from a digitising error of 0.39% to one of 0.024%. This uncertainty should be insignificant as it is much smaller than any expected error arising from other sources (eg. shot noise, background noise; a complete discussion of noise sources is given in chapter 9, section 9.3).

6.2.2 Circuit Control by Logic IC's

Timing and operation of the analogue and digital circuits is carried out by pulses and high and low status signals from monostable and bistable outputs of the logic circuit, shown in part of figure 6.2.3. Logic circuit operations, described below, are simplified in figure 6.2.2 and are summarised in table 6.2.1, where the signals are numbered for clarity.

Synchronisation of the arrival of an analogue I/P signal with the hold enable pulses (2a and 2b), the Read/Convert instruction (4) to the A-to-D

converter, and the computer interrupt (3), enabling data measurements to be read into the computer, is initiated by the trigger (time 0) pulse (1) from the synchronisation output of the laser trigger unit, operating via monostables. The interrupt pulse to the computer is allowed only when a software synchronised pulse (5) has been passed from the computer, initiating a bistable level change (6), which indicates "on line" status. This ensures that the computer is operative for data collection and handling. The "on/off line" signal (5) is also used to connect and disconnect the printer to the computer port. The Read/Convert operation is enabled, either by the (time 0) trigger initiated pulse (4a) or by a signal (4b) from the computer (7). The (4a) performs the Read/Convert operation for the signal return measurement in channel 1 and the computer-sourced pulse (4b) performs the operation after switching to the analogue channel 2. The analogue sample channel is switched (8) by a logic pulse (8a) originating in the interrupt enable and first Read/Convert operation. Timing for time 0 trigger initiated operations is shown in figure 6.3.1.

Identification of the DIAL pulse (whether or not the laser pulse has been modified by the intra-cavity absorption cell) is performed by a cell position sensor, the output (11) of which is buffered into the logic circuit to provide the computer with a logic 1 or 0 (12), respectively, if the cell is in or out. This allows direction of signal level data to the appropriate memory location, even if a cell switching malfunction causes adjacent pulses to be of the same identity.

The logic circuits are initiated (10) by reset/clear signals from the computer (9a), before each sample operation, or by manual operation (9b) before each new interrupt run. During each interrupt run, a signal pulse return level and the laser energy sample is measured.

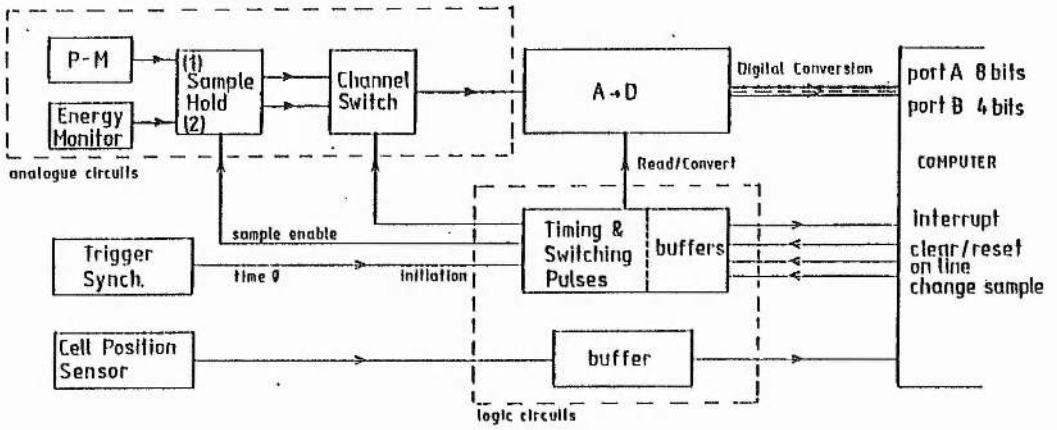

Figure 6.2.1 Block diagram of the XeCl* laser DIAL signal handling circuit, showing the detection and processing system.

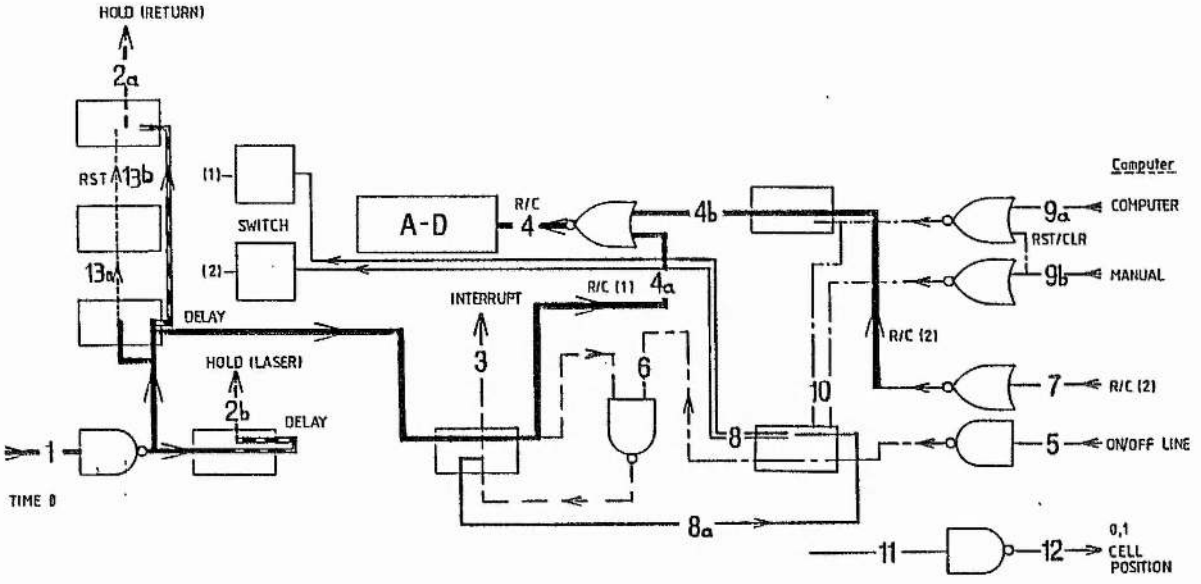

Figure 6.2.2 Logic circuit paths within the signal handling unit.

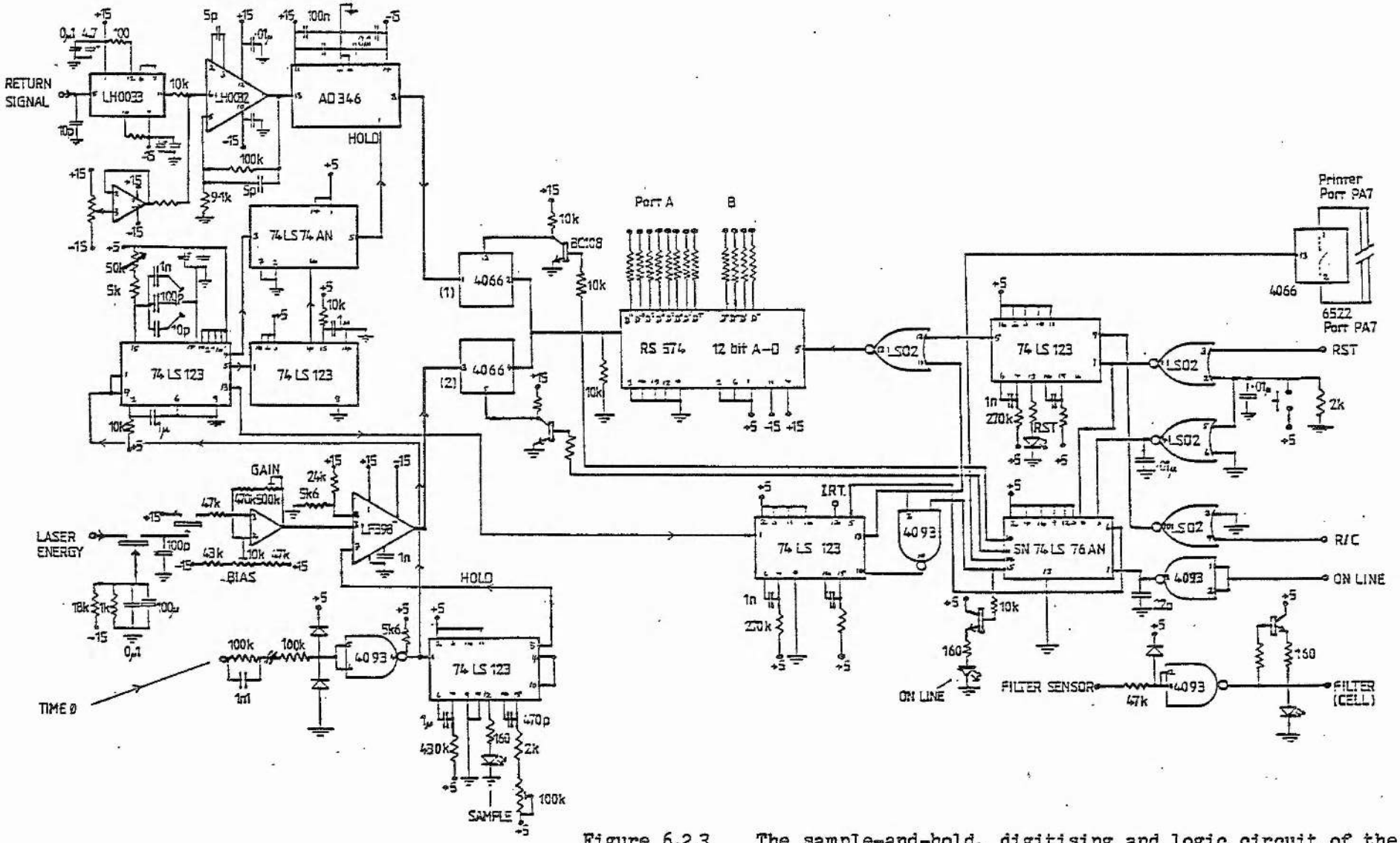

Figure 6.2.3 The sample-and-hold, digitising and logic circuit of the XeCl* laser DIAL signal handling unit.

Table 6.2.1 Logic Operations in the Signal Handling Circuit (refer to figure 6.2.2)

I/P to logic	Source	Destination	O/P function from logic
time 0 pulse (1)	laser trigger unit	sample and hold circuit	hold enable (2a and 2b)
		*A to D R/C buffer	Read/Convert enable (4a)
		* A to D	Read/Convert (4)
		computer	interrupt pulse (3) permitted in "on line" mode
		*flip-flop	change analogue channel (8a)
		*switch	analogue channel select (8)
on/off line (5)	computer	*interrupt monostable	(6) permits interrupt in "on line" mode
Read/Convert (7)	computer	*A to D R/C buffer	Read/Convert enable (4b)
		A to D	Read/Convert (4)
reset/clear (9a)	computer	*monostables bistables	reset/clear (10) logic circuit
(9b)	manual	"	"
absorption cell position (11)	cell position sensor	computer	cell position indicator for DIAL pulse identity (12)

* operations within the logic circuit.

6.3 Control, Data Storage and Analysis by Micro-Computer

The role of the Acorn Atom micro-computer in signal handling control, data storage and data analysis is described.

6.3.1 Computer Control of the Signal Handling Circuit in Data Acquisition

The sampling and analogue to digital conversion of signals in the DIAL system is carried out by the circuit shown in figures 6.2.1, 6.2.2 and 6.2.3 and the procedure described in section 6.2. Circuit operation is initiated by a "time 0" pulse from the synchronisation output of the laser trigger unit. However, the circuit only works in conjunction with appropriately-timed pulses from the computer. Before a data acquisition run, the computer program sends an "on line" pulse (5), connecting the computer to the circuit through the input/output port and data bus. It also allows a time 0-pulse-initiated interrupt command (3) and channel change (8 and 8a) to take place. The second Read/Convert operation (labelled 4b in figure 6.2.2), to digitise the laser power measurement, is initiated by a computer pulse (7). The computer sends a reset pulse (9a) at the end of each lidar return acquisition process (one "time 0" initiated sequence) to reset and initialise the switching circuit. At the end of each data acquisition run (m pulse pairs) an off line pulse (5) disconnects the circuit from the computer prior to data analysis. The cell position sensor provides a signal (12) to a computer input port to allow correct identification of the DIAL pulse (whether the cell is "in" or "out").

The sequence of control events in "time 0"-pulse-initiated data acquisition and analogue-to-digital operations is given in the timing diagram of figure 6.3.1. The lidar return signal and the laser power peaks are measured at an

appropriately-set time in their respective sample-and-hold circuits in channels 1 and 2 (figure 6.2.2). The lidar return measurement conversion (A to D) is enabled by the "time 0" synchronise pulse. On receipt of the interrupt pulse (3) from the logic circuit, the computer reads the 12-bit data for this result off the computer ports and then stores the information. The other analogue channel (2) is then switched to drive the A to D converter input before the computer enables a new Read/Convert operation. This data is then passed to the appropriate computer memory. The logic circuit is reset in preparation for the next measurement (corresponding to the other laser absorption cell position) which provides the data from the other pulse of the DIAL pair.

Measurements are taken for averaging (if necessary) to give two results; the return signal peak level ratio of the first and second DIAL pulses (asigned to the floating point variable %R); and the ratio of the laser power measurement corresponding to the first and second DIAL pulses (asigned to the floating point variable %P).

6.3.2 Computer Programs for Circuit Checks, Data Acquisition and Analysis

The software in the XeCl* laser DIAL system computer provides three distinct categories of functions; system test; data acquisition and storage; and data analysis. The functions are listed in table 6.3.1. Test and data acquisition programs are in machine code and the analytical program is in BASIC. All programs are stored on a single ROM memory, avoiding the necessity for program retrieval from tape or disc.

The test program displays the function menu and allows the signal handling system to be checked for correct operation. Test functions and the appropriate responses are summarised in tables 6.3.1 and 6.3.2. The test

program itself is listed in appendix A6.1(a).

The data acquisition program, listed in appendix A6.1(b) (continuation of A6.1(a)), controls the operation of the logic circuit in the way described in sub-section 6.3.1, figure 6.3.1 and tables 6.3.1 and 6.3.2. Data is stored in memory locations and retrieved to produce return signal and laser energy ratios (program variables %R and %P respectively).

The analytical program, listed in appendix A6.2, interprets the measured return signal levels and, if necessary, the laser power measurements to give the concentration of sulphur dioxide in units of ppm. The access and function of the program is given in table 6.3.1.

6.3.3 Data Analysis and Presentation

The data measurements can be interpreted to give a result as the average SO_2 concentration over an integrated range or, by selection of the appropriate program mode, to give range-resolved results. A range-integrated result is a measurement of an ambient SO_2 concentration, obtained by taking a lidar return pulse from a target with zero differential absorption (eg. wall; NOT a smoke plume). The range-resolved result, taking the return from an SO_2 laden plume, requires a previous data acquisition run followed by analysis in integrated range mode, providing the stored ambient level data for compensating the smoke plume return measurement. The results are presented by VDU and miniature dot-matrix printer. An example of a printed data analysis output, showing range-integrated then a range-resolved analysis, is given in figure 6.3.2. The algorithms for the analytical program are derived from work on the mixed wavelength DIAL equations, described in chapter 9.

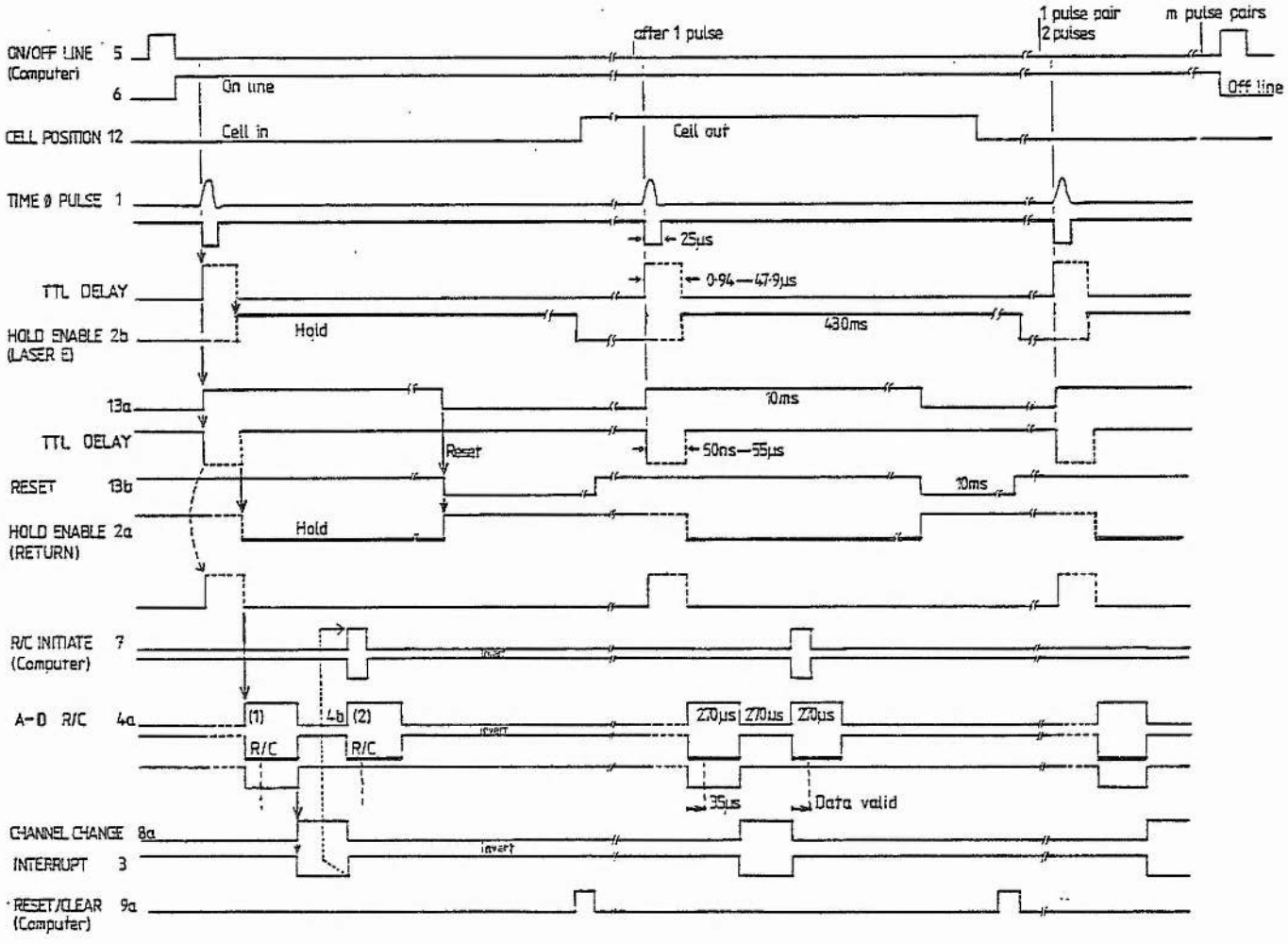

Figure 6.3.1 Timing diagram for laser synchronised (time 0) and computer initiated logic pulses in the $XeCl^*$ laser DIAL signal handling sytem.

```
XeCl Laser DIAL

ENTER M (1-253)=?20

%R  1.56754058E-1
%P  1.54681951E-1
SELECT REQUIRED MODE
0 Integrated Conc.
1 Range Resolved Conc.
?0
Integrated Conc.
ENTER LIDAR RANGE (m)
?40
Cell P/T ratio
3.50000000E-1
ENTER CELL P/T RATIO?.33
5
No. of single passes
2.36000000
Cell attenuation factor
8.00000000E-1
Laser peak ratio
6.91500000E-1
IS NORMALIZATION REQUIRE
D? Y or N?Y
Normalizing laser peak r
atio
7.08530680E-1
Pressure     1013 mbar
Temperature      283 oK
ENTER PRESSURE?1013
ENTER TEMPERATURE?273
Is pressure/height compe
nsation  required? Y or
N?N
Return signal ratio
1.56754058E-1

Sulphur dioxide conc. of

4.75721617 ppm
averaged over range
      40 metres
```

```
XeCl Laser DIAL

ENTER M (1-253)=?20

%R  1.79267399E-1
%P  1.48434589E-1
SELECT REQUIRED MODE
0 Integrated Conc.
1 Range Resolved Conc.
?1
Range Resolved Conc.
Cell P/T ratio
3.50000000E-1
ENTER CELL P/T RATIO?.34
5
No. of single passes
2.36000000
Cell attenuation factor
8.00000000E-1
Pressure     1013 mbar
Temperature      283 oK
ENTER PRESSURE?1013
ENTER TEMPERATURE?273
Is pressure/height compe
nsation  required? Y or
N?N
IS THE AMBIENT CONC. RAT
IO KNOWN? Y or N?Y
Ambient return ratio is
1.56754058E-1
Output circuit R and C
      100
3.35000005E-10
ENTER LOAD RESISTANCE?10
0
Return signal ratio
1.79267399E-1

Sulphur dioxide conc. of

110.504229 ppm
in minimum range element

20.5178815 metres
at a range of
      40 metres
```

Figure 6.3.2 An example of a print-out of the data analysis routine for an integrated range measurement followed by a range-resolved result.

Table 6.3.1 Computer Program Functions

The functions are listed in order of occurrence during the signal handling and analysis routine.

Function Mode	Language	Access (enter)	Function
TEST	machine	"LINK #A000"	display menu numbered 1 - 6
TEST PORT		"1"	tests I/O ports of VIA
TESTKEYBOARD		"2"	testscomputerkeyboard
TEST PRINTER		"3"	tests printer operation
TEST MEMORY		"4" "#8000" "#8200"	tests memory accessibility
TEST INTERFACE		"5" press RETURN press RETURN press SHIFT	tests reset operation tests on/off line operation tests cell position sensor
(press RETURN after each test to return to menu)			
DATA ACQUISITION AND STORAGE	machine/ BASIC	"6" "RUN"	asks for m, the number of pulse pairs to be measured, to be entered
		enter m press RETURN	system "on line" until data is collected data ratioed and averaged to give %R and %P, displayed and printed
DATA ANALYSIS	BASIC		asks for selection of required analysis mode
		"0" for range integrated or "1" for range resolved SO_2 concentration analysis. (Note: range resolved analysis requires stored data from a range integrated analysis)	takes measured values and interprets them to give a range integrated or range resolved SO_2 concentration. (options: pulse power normalization where %P is used; target sample height compensation; alteration of system and environmental parameters)

Table 6.3.2 (a) Correct Response in Test Sequence

(b) Display During Data Acquisition

Events are listed in order of occurrence

(a) TEST

Test Mode	Response
PORT	(VDU) "Port Okay"
KEYBOARD	(VDU) correct characters displayed
PRINTER	(VDU; print-out) full character sequence printed
MEMORY	(VDU) "Memory Okay"
INTERFACE	
RST	(Signal Handling Unit) RST led flashes
ON LINE	" ON LINE led on and off
CELL POSITION	(Signal Handling Unit) CELL led on (out) and off (in) (VDU) "Cell in" or "Cell out" displayed

(b) DATA ACQUISITION

Location	Display
Before start	(VDU) request for number of measurements, m
Start (no laser)	(Signal Handling Unit) ON LINE led on CELL led off (VDU) Screen "interference" with double apostrophe character at top (data acquisition indicator)
Data Acquisition Sequence Running (laser) *	(Signal Handling Unit) TIME 0 led blinks RST led flashes CELL led on (VDU) Data acquisition indicator changes to exclamation mark (Signal Handling Unit) TIME 0 led blinks RST led flashes CELL led off (VDU) Data acquisition indicator changes to apostrophes
End	(Signal Handling Unit) CELL led on or off ON LINE led off (VDU) Averaged (over m data sets) values for %R and %P displayed and analytical mode entered

* repeated m times

6.4 Calibration

The linearity of the signal handling circuits, shown in figure 6.2.3, including amplifier performance and signal digitisation, is shown.

6.4.1 Setting-up the Circuit

The amplification stage of the return signal and the laser energy measurement circuits are biased to zero and gain is set in each at about X10. Biasing of the return signal channel is controlled by a pre-set on the front panel of the signal handling unit.

In each channel, the time at which the sample circuit is switched to "hold" mode is variable according to the time of arrival of the respective pulse. The "hold" step, causing measurement of the return pulse, is set for each lidar situation, allowing for variation in target range. A logic output to the oscilloscope is available to show the time of occurrence of the "hold" step, allowing synchronisation with the desired part of the return signal. The "hold" step, causing measurement of the laser energy signal, is set, similarly, by using a pre-set on the front panel.

6.4.2 Calibration

The computer-displayed measurement, with a full-scale of 4095, has been calibrated for a d.c voltage which was applied at the input of each signal channel (negative into the return channel; positive into the laser energy channel).

The calibration for the signal return circuit is given in figure 6.4.1, which shows the voltage/reading calibration for a negative d.c input. In this case, the full scale reading is obtained at -965 mV. Figure 6.4.1(b)

is the calibration for d.c inputs up to 10 mV, showing the potential accuracy of linearity to be less than 0.2 mV, applying over the entire input range. Accuracy was judged on the basis of the difference between two readings arising from the same input voltage.

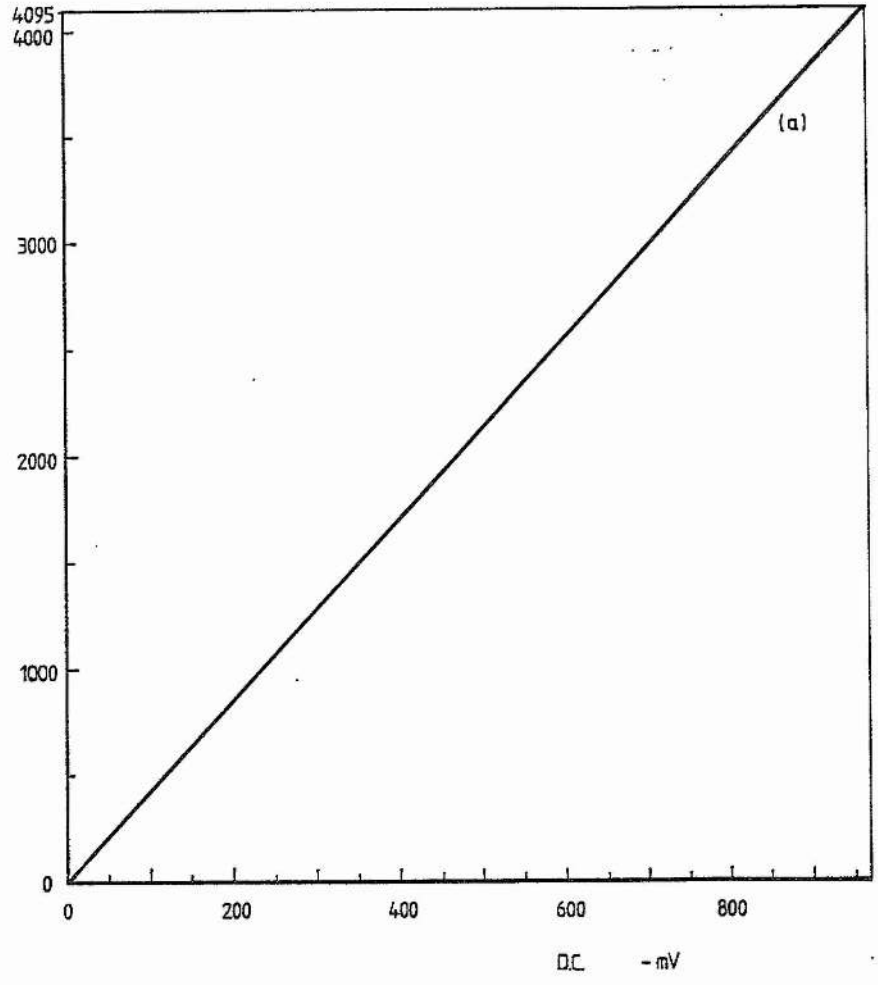

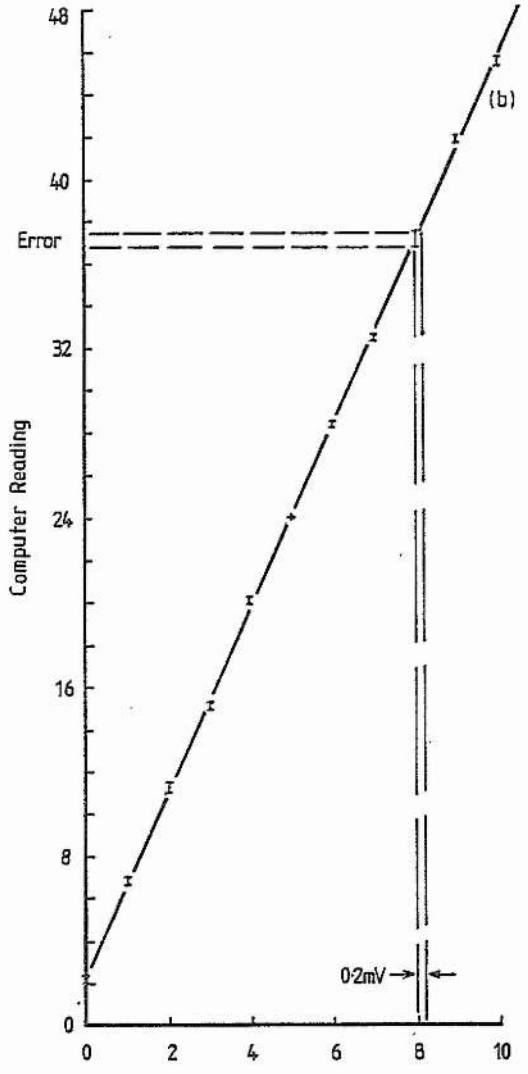

Figure 6.4.1 D.C calibration of the signal measuring system;
(a) full scale
(b) low input level (0 to 10mV)

Chapter 7 System Integration

This chapter is concerned with the assembly and combined operation of the laser system, telescope, photomultiplier detector and signal processing equipment, each described in previous specialised chapters 2 to 6 (inc.), to form the trailer-based $XeCl^*$ laser DIAL system for use at power station sites. Signal and supply paths are shown but special emphasis is placed on the design of the grounding system, developed for noise and pick-up elimination. The physical layout of the components is a key factor in noise reduction, in easy laser/telescope/target alignment and in serviceability.

7.1 System Function, Equipment Wiring and Grounding

7.1.1 System Function

All major signal paths, including that of the laser trigger pulse, the transmission, backscatter and reception of the laser optical pulse and the signal handling and data production routes, are illustrated in the flow chart of figure 7.1.1, which shows the basic simplicity of the system. Optical and electrical paths are shown.

7.1.2 Equipment Wiring

The interconnections between the components of the system are shown in figure 7.1.2. Laser and peripheral control circuits are grouped together, as are the detector and signal processing circuits, and are arranged to reduce coupling between the noisy laser circuits and the low level detection circuits. All connections between screened units are made via co-

axial or fully screened cables to reduce the effects of pick-up of r.f from the laser discharge (see 7.1.3). Leads between the laser/telescope head and the supply units are enclosed in heavy duty reinforced conduit for neatness and safety.

7.1.3 System Grounding and Screening

The primary noise source is the high frequency r.f emission ($\triangleq$ 10 Mhz), emanating from the laser discharge and capable of inducing several volts in nearby conductors. An example of noise induced in the input cable of an oscilloscope, about 3m from a badly grounded and screened $XeCl^*$ laser, is reproduced in the oscillograph trace of figure 7.1.3. The maximum zero to negative peak voltage of this example is about 400mV, which would certainly obscure a strong smoke return signal voltage pulse of 250mV (from chapter 8). System grounding and screening is summarised in figure 7.1.4 but the basis for the design of the grounding circuit is described below.

In order to reduce noise at source the laser is housed within a mild steel screen, surrounded by an aluminium outer casing which is fitted with flexible brass screening seals. The 'ground' side of the cavity itself is d.c connected as the return path to the laser supplies via a large inductor (several nH) which prevents further propagation of a noisy ground. All leads to and from the laser (figure 7.1.2) are screened with the ground connection made at the end nearest supply earth (Ott, Noise Reduction Techniques in Electronic Systems, 1976). Care is taken in providing grounded shields, especially for leads carrying weak signals, to avoid earth loops which would act as a reception aerial for r.f radiation. Where possible, high frequency shield grounding is completed on cables longer than about 1m by a 0.1 μF capacitor. High voltage leads to the laser are fitted at each end with high frequency ceramic capacitors (0.2 μF) to earth

to prevent them acting as rf transmission aerials. Other leads in the system, other than fast pulse carriers, are similarly fitted to reduce the effects of pick-up.

The parts of the system most vulnerable to noise are the low level detection and signal processing circuits. These require careful consideration of lead filtering, screening hardware and grounding connections. The cell position sensors and the laser power detector supplying the signal processing circuits are uniquely housed and the screens are grounded to the processing unit. The photomultiplier screening, incorporating the divider circuit return path, is earthed to the H.V supply. However, the signal output circuit of the photomultiplier is grounded to the signal processing unit, avoiding the relatively noisy and high current path of the photomultiplier H.V supply. The computer power supply and VDU are grounded directly to the supply earth, removing a source of noise from the ground of the low level circuit.

Once designed, slight alterations were made to the grounding circuit until the laser could be operated at full voltage without false flashing of signal processor mode indicators and, more importantly, until a test program could be run in a loop without corruption or loss.

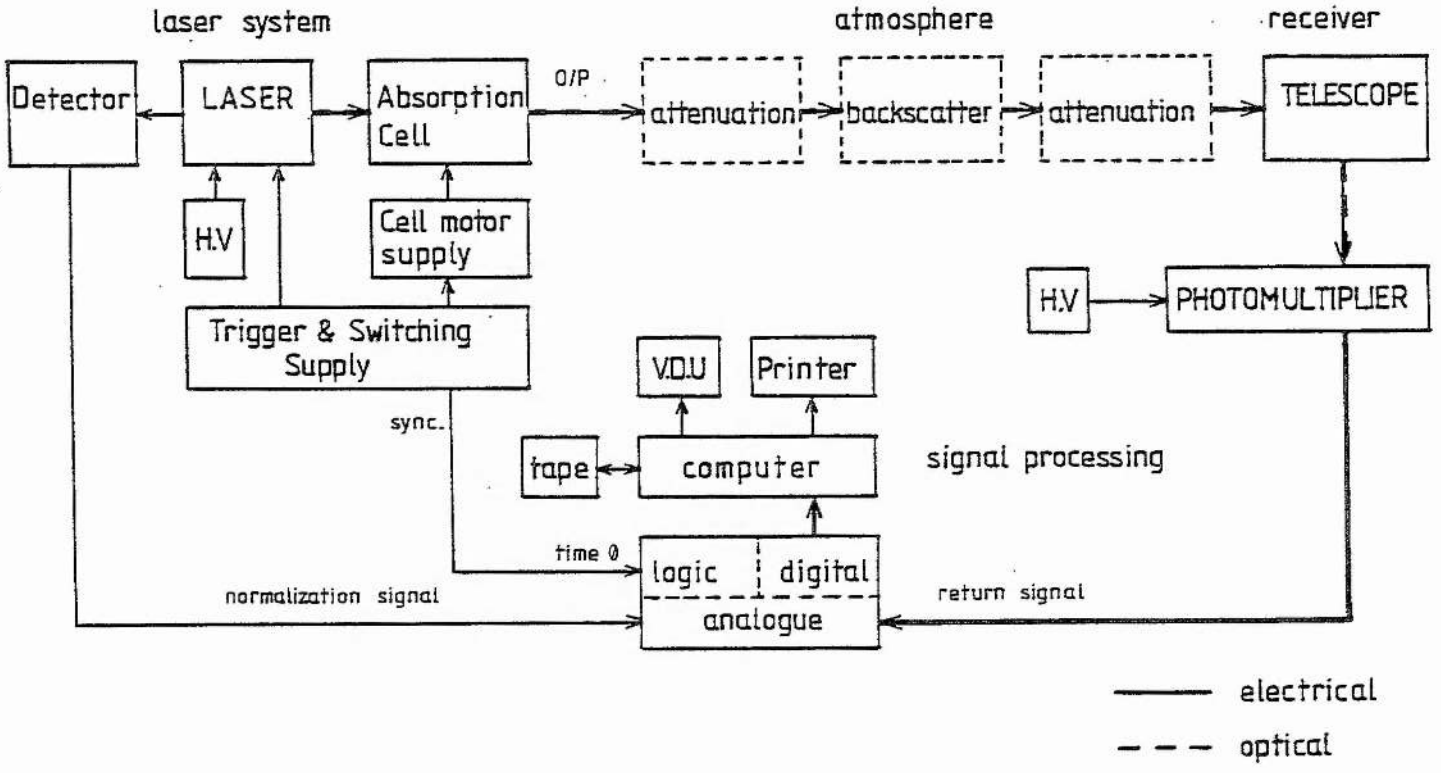

Figure 7.1.1 Block diagram illustrating the flow of optical and electrical signals in the XeCl* laser DIAL system

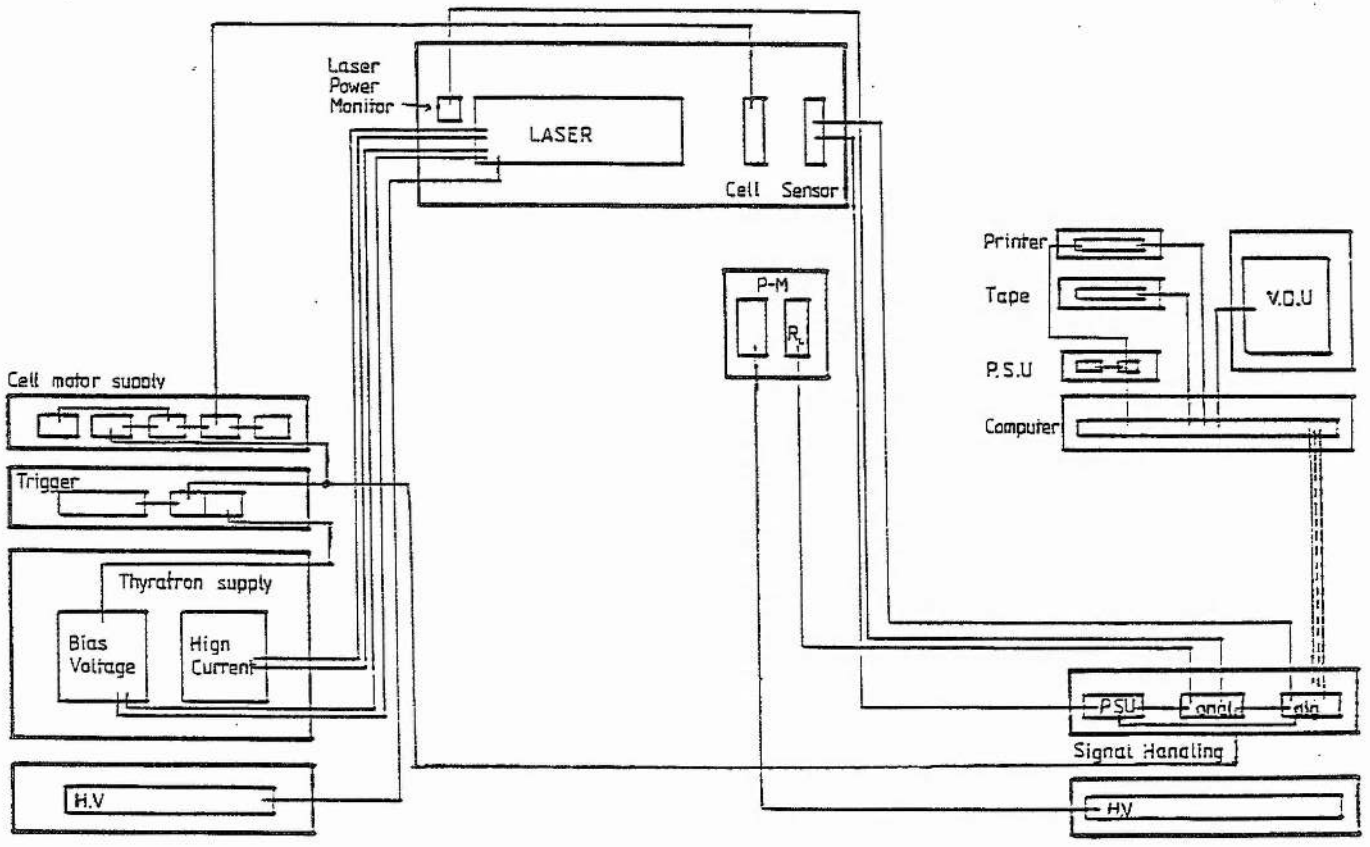

Figure 7.1.2 Block diagram of the $XeCl^{*}$ laser DIAL system components and interconnections

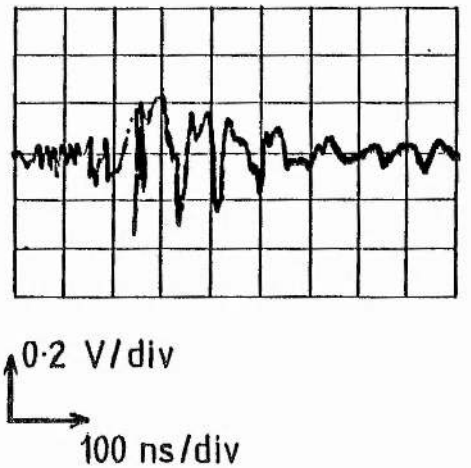

Figure 7.1.3 An oscillograph trace of noise due to pick-up of rf emitted by a badly-screened $XeCl^*$ laser discharge

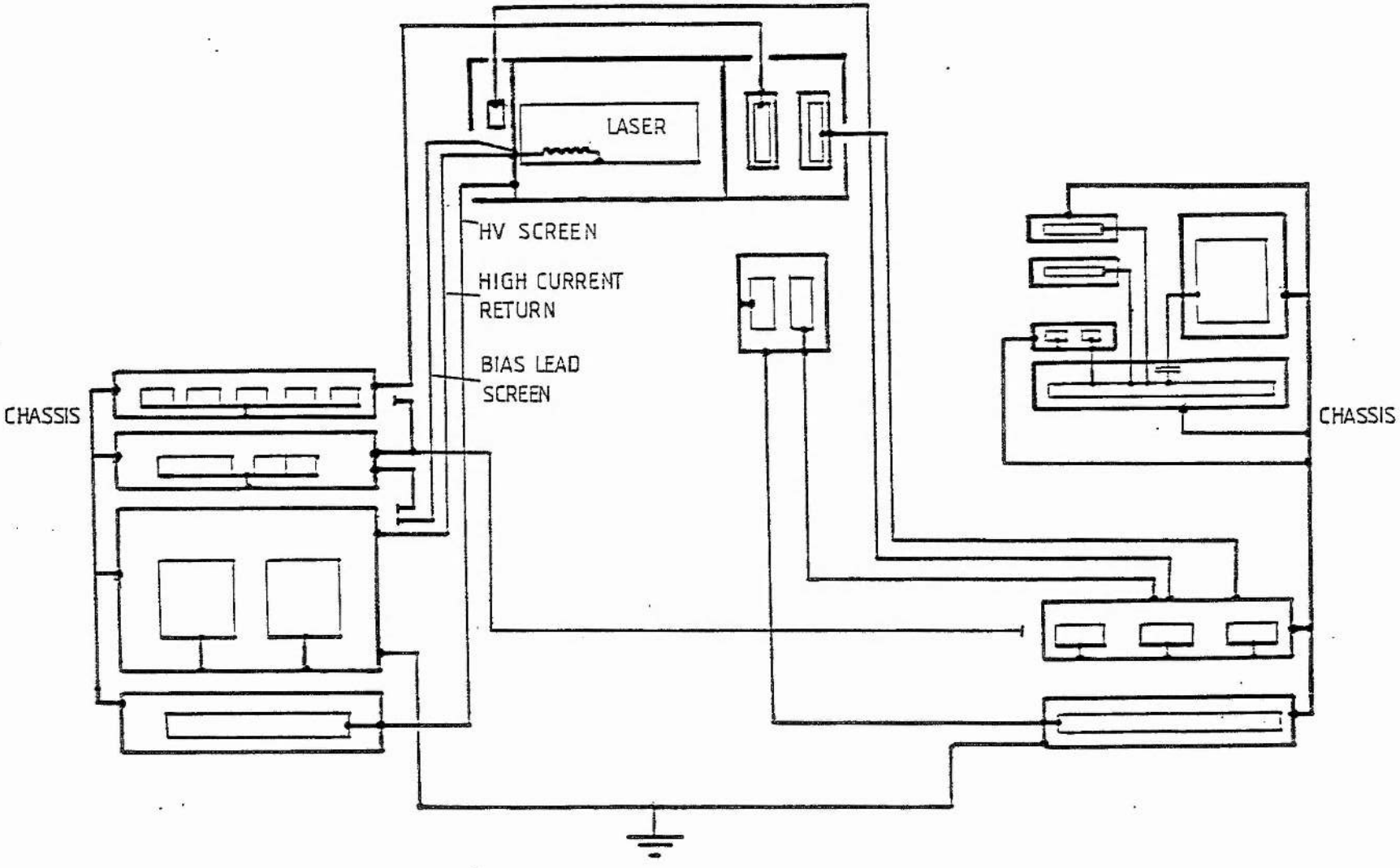

Figure 7.1.4 Block diagram of the XeCl* laser DIAL system grounding and screening connections

7.2 Physical Layout of the DIAL System

7.2.1 Physical Assembly

The system electrical and electronic components and units shown in the block diagrams of figures 7.1.2 and 7.1.4 are assembled into the laser/telescope/detector head, a laser supply and switching cabinet and a signal detection and processing cabinet. The system, including a rotary pump for laser evacuation and a high pressure gas mix refill cylinder, is all accomodated within a purpose-built trailer in a layout according to the plan of figure 7.2.1. A gas mixing station is laboratory based.

7.2.1(a) The Laser, Telescope and Photomultiplier Receiver

The laser and receiver are rigidly mounted together to enable the laser field of coverage to be aligned within the telescope field of view to optimise signal collection. The arrangement also permits the option of co-axial laser transmission, shown schematically in figure 2.5.3. The cradle carrying the laser/telescope/detector head is mounted upon a rotating frame, permitting adjustment in altitude and azimuth. Laser-to-telescope mounting is by four rubber blocks, each secured by a central bolt. Compression of the blocks, as appropriate, by the adjusting nuts allows laser/telescope alignment. The photomultiplier housing, complete with iris and narrow band interference filter, is situated near the Newtonian focus of the telescope and is adjustable, with the secondary mirror, in a direction parallel to the telescope axis.

A feature of the system is the easy, cheap facility for direct sight alignment of the laser/telescope and target, avoiding the use of unnecessary sophistication or a time consuming method. The laser is aligned upon the target by direct sighting along the optical cavity, enabled by the

visibly transparent di-electric mirror at the rear of the cavity. The telescope is also sighted by eye by looking through the central hole from the rear of the primary mirror. The novelty lies in the use of a narrow band interference filter, with a surface which reflects visible light, at the telescope focus. This 'sees' an image of the target, via the primary mirror, then the secondary, and then reflects it via the secondary down the the primary aperture, as illustrated in figure 7.2.2.

An addition to the laser assembly is the fast p-i-n diode detector for pulse power monitoring. The output of the detector is used to normalize the DIAL return signal.

7.2.1(b) The Laser Supply Units and Trigger Source

One cabinet houses the laser control circuits and the motor supply for switching the absorption cell in and out of the laser optical cavity. The laser is supplied by the thyratron heaters and bias circuits and the high voltage unit used to charge the laser capacitors. The primary trigger unit and oscillator provides the thyratron trigger pulse for controlled laser repetition rate. A lower voltage pulse, synchronised with the triggering pulse, is used as an initiating pulse for the signal handling circuit (time 0) and to switch the cell motor supply on and off.

7.2.1(c) Photomultiplier Supply and Processing Units

The second cabinet contains the low level circuits associated with detection and signal processing. The signal processing circuits, described in chapter 6, are mounted with the micro-computer and display system. A H.V unit supplies the photomultiplier interdynode voltage divider circuit. However, maximum isolation of the high voltage supply from the low level section is provided to minimise noise coupling.

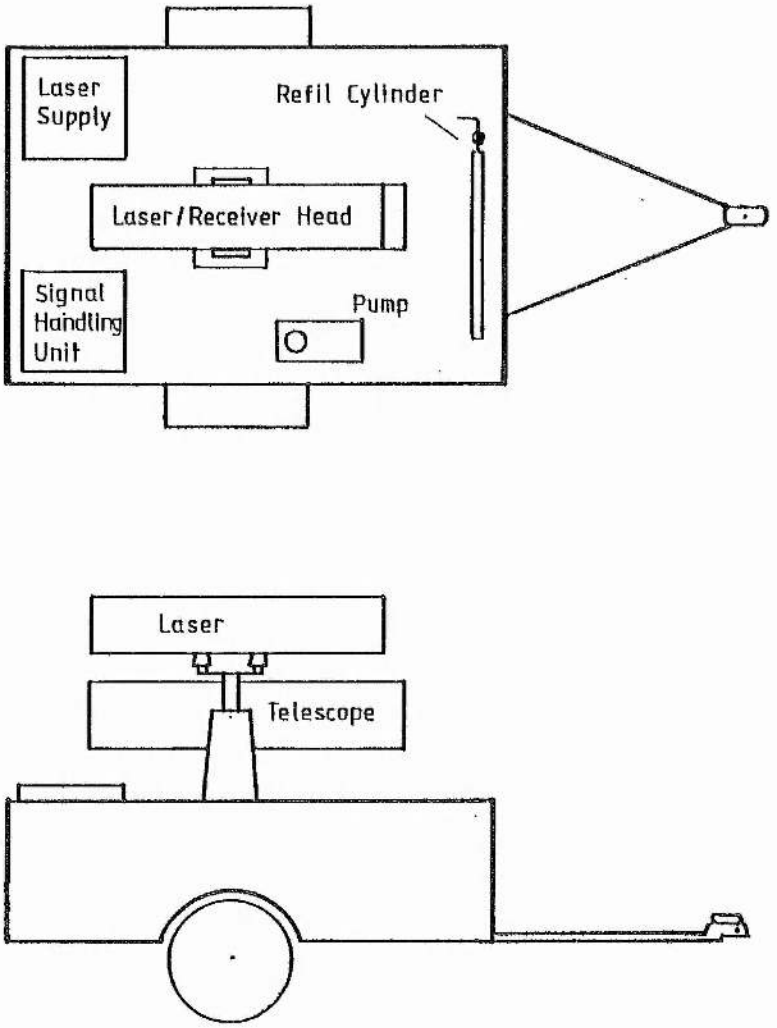

Figure 7.2.1 The layout of the XeCl* laser DIAL system in a trailer

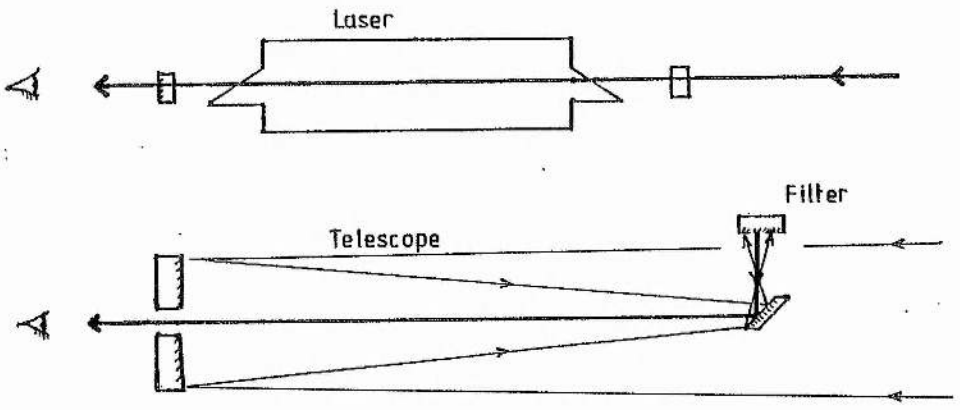

Figure 7.2.2 Schematic illustration of laser/telescope/target alignment in the XeCl* laser DIAL system

7.3 Procedure for Operating the XeCl* DIAL System

Figure 7.3.1 is a photograph of the system installed in the trailer. The procedure, from arrival on site to obtaining SO_2 concentration measurements, is summarised in figure 7.3.2. Power for the system is provided by a petrol generator of at least 1.3 kW output.

It has been usual to prepare a fresh laser fill at St.Andrews before transporting the equipment to the test site. However, assuming an old or contaminated gas mix or low pressure, then it is necessary to replenish the laser in the field. A rotary pump has been installed to evacuate the laser discharge tube and the pipework. The laser is filled with the pre-mixed gas to an absolute pressure of between 2 and 3 atmospheres before the cylinder is disconnected for storage.

The electrical system is switched on to allow the thyratron to warm-up for about 5 minutes. This must be done before the high voltage is applied and the trigger unit and cell motor supply are switched on. Laser output is verified by checking for fluorescence from incidence of the pulse onto a suitable material (white handkerchief or white paper). If necessary, the back mirror and output coupler kinematic mounts are adjusted to optimise the laser output.

The laser trigger is disabled before the photomultiplier high voltage unit, the signal processing unit and the computer and its peripherals are switched on. The signal processing equipment, the computer memories and the computer peripheral interface devices are checked to ensure correct operation before the system is set for signal reception.

When the laser, telescope and target have been aligned, the system is ready to measure SO_2 concentrations. The laser trigger is initiated and the signal processing system is operated by the data collection program (chapter 6). After the required sequence of pulse pairs has been run, the collected data is analysed to give SO_2 concentration. Information is delivered via the VDU and/or the printer to the operator.

The procedure for SO_2 concentration measurements is given in section 10.3.

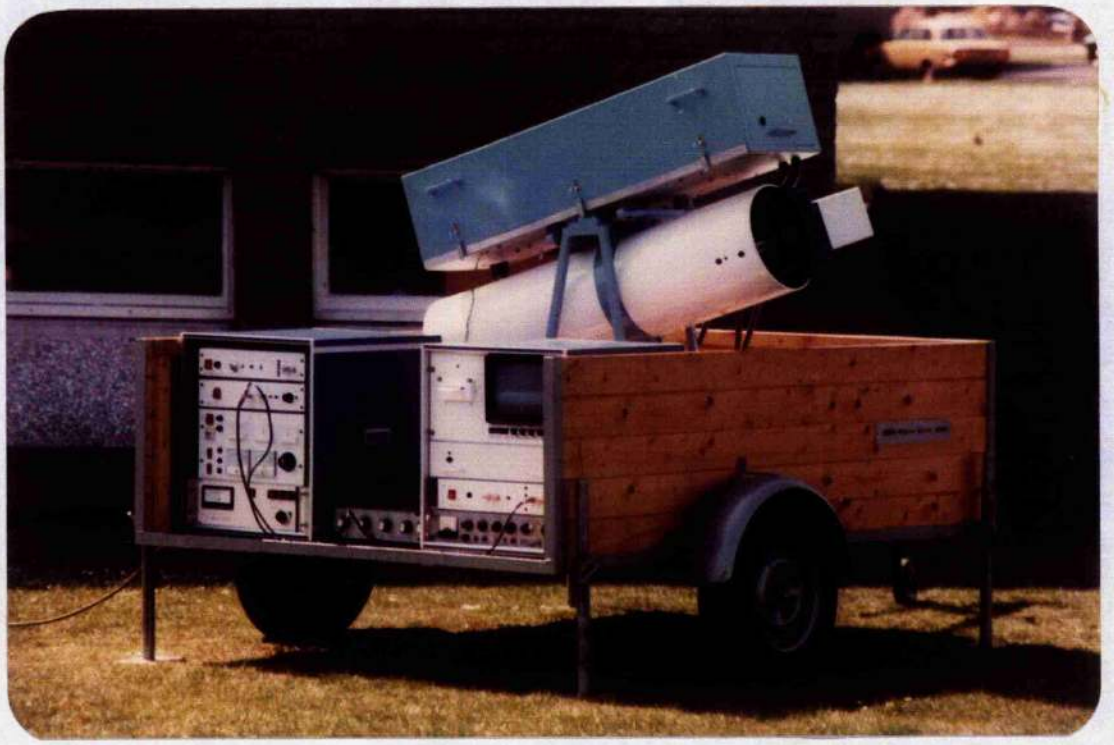

Figure 7.3.1(a) The $XeCl^*$ laser DIAL system installed in the trailer

(b) Front view of the laser, telescope and detector head (laser cover removed)

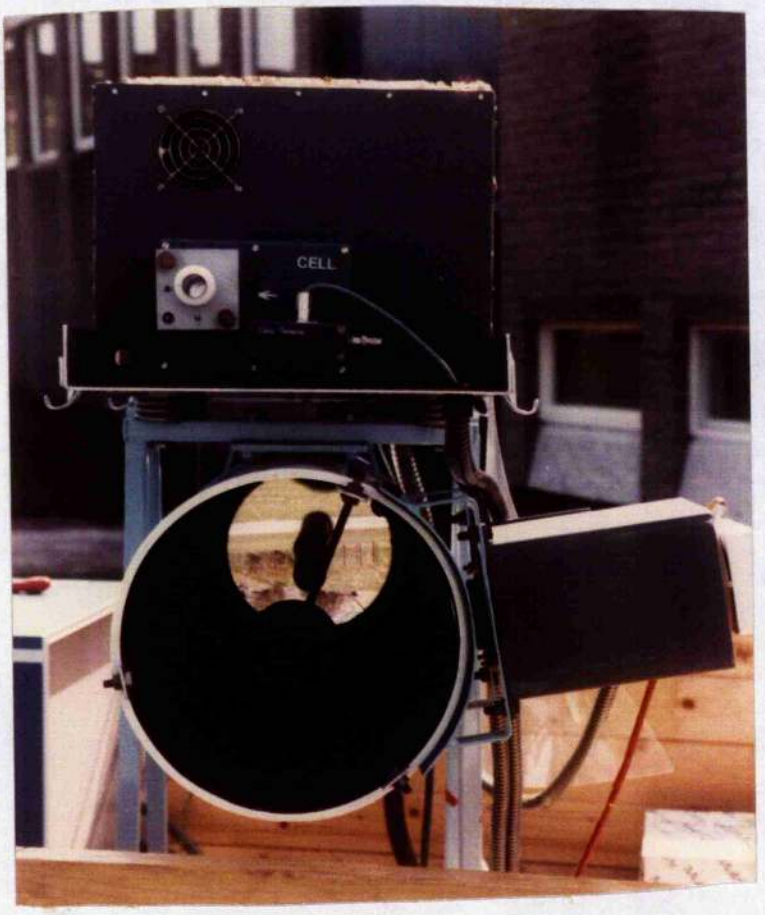

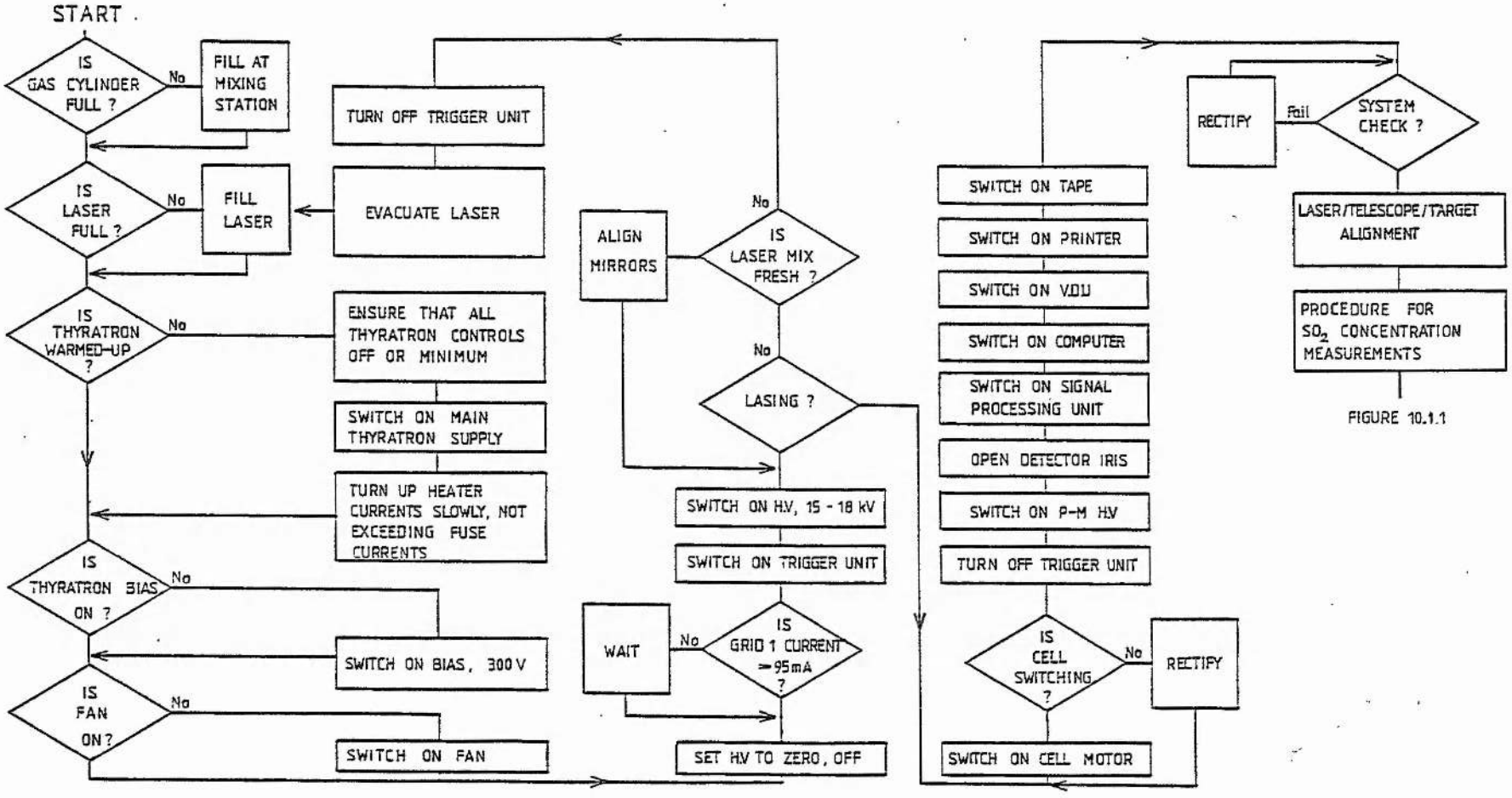

FIGURE 10.1.1

Figure 7.3.2 Flow chart defining the switch-on procedure and operation of the XeCl laser DIAL system

References for Chapter 7

Ott, Noise Reduction Techniques in Electronic Systems, (1976)

Chapter 8 Derivation and Application of the Lidar Equation

The transmission of a laser pulse into a scattering atmosphere and the subsequent reception of photons as a function of range is described, approximately, by the single pulse, single wavelength lidar equation, derived below after an introduction to atmospheric scatter and attenuation. The major point of obtaining a lidar equation is for its application in the differential absorption lidar theory used to analyse returns for SO_2 concentration. A general atmospheric transfer function is derived for possible convolution with any known time-dependent laser pulse function, to obtain, if necessary, an accurate representation of the return distribution. The simple lidar equation is applied to a model of the lidar return from a scattering atmosphere containing a smoke plume. A single pulse scattering experiment carried out at Methil power station, Fife, is described and compared with the modelled return.

8.1 Introduction to Rayleigh and Mie Scattering in the Lower Atmosphere

Atmospheric scattering, particularly through a scatter angle of 180°, is important as the mechanism for giving a lidar return signal. Scatter is also responsible, with absorption, for attenuation of the lidar radiation by removing it from its path in passing to and from the atmospheric target. Two mechanisms are Rayleigh, or molecular scattering and Mie scattering by the larger particles, the aerosols. This section provides expressions for Rayleigh and Mie scattering coefficients.

8.1.1 Rayleigh Scattering

The method of derivation of the Rayleigh coefficients, given in appendix A8.1, is based on the emission of radiation from a volume element in a dipole interaction between the photons and the molecules. The incident light is described, very simply, as exciting the molecules prior to re-emission at the same wavelength but with a certain angular distribution (Kondratyev, Radiation in the Atmosphere, 1969). The extent of scatter is spectrally dependent and a function of pressure and temperature. Mathematically, the scattering is a function of the angular term and a term which describes the interaction between molecules and radiation. Rayleigh scatter is predominant under conditions of good visibility, though it becomes less important at longer wavelengths. A coefficient which describes the scatter along unit length into a unit solid angle and in a direction at an angle θ is expressed as (A8.1, equation (A8.1.29)) a function of range, r in

$$\alpha_{R,\theta}(r) = 5.939 \times 10^{-8} \cdot P_r (1 + \cos^2\theta) / \lambda(\mu m)^{4.09} \cdot T_r \quad m^{-1} sr^{-1}. \qquad (8.1.1)$$

This function is plotted in figure 8.1.1. The total space Rayleigh scatter, or extinction, coefficient, obtained by integrating equation (8.1.1), is given by

$$\alpha_R(r) = 9.951 \times 10^{-7} \cdot P_r(mbar) / \lambda(\mu m)^{4.09} \cdot T_r(^oK) \quad m^{-1} \qquad (8.1.2)$$

for direct application in an attenuation term. Equation (8.1.1) is applied for a scatter angle of π radians to give the backscatter coefficient, given by

$$\beta_R(r) = \alpha_{R,\pi}(r) \qquad (8.1.3)$$

which is conveniently expressed in terms of the total space scatter coefficient as

$$\beta_R(r) = 3\alpha_R/8\pi \quad m^{-1}sr^{-1}. \qquad (8.1.4)$$

Equations (8.1.2) and (8.1.4) are applied in the lidar equation in section 8.2.

8.1.2 Mie Scattering

Atmospheric particles, between radius $10^{-2}\mu$,larger than single molecules, and 10μ ,at least a magnitude smaller than, say, a grain of sand, are termed aerosols. The scatter of light from such aerosols is described by the theory of Mie scattering (G.Mie, 1909). Any analysis of the scattering, as for example, in providing an extinction coefficient, requires determination of the aerosol size distribution in combination with a spectral dependence and angular distribution. The difficulty in providing a rigorous analytical solution has prompted an empirically derived function for the linear Mie scatter coefficient (Kruse et al, 1962), the form of which has been justified in this work (appendix A8.2). Thus the Mie coefficient to be applied at range r is expressed as

$$\alpha_M(r,\theta) = [(3.912/V(m)) - \alpha_R(0.55)].[0.55/\lambda(\mu m)]^q \quad m^{-1}, \qquad (8.1.5)$$

where q is given by

$$q = 0.585.V(km)^{1/3} \quad \text{for} \quad V < 10 \text{ km} \qquad (8.1.5a)$$

$$q = 1.3 \quad \text{under average seeing conditions.} \qquad (8.1.5b)$$

The visibility, V, is defined as the visual range at which the target contrast equals the threshold contrast of the eye. The Rayleigh coefficient, arising as a correction in the visibility term, is given by equation (8.1.2). The Mie backscatter term is given (equation(A8.2.19)) in terms of the scatter coefficient as

$$\beta_M = \alpha_M/8\pi \quad m^{-1}sr^{-1}. \tag{8.1.6}$$

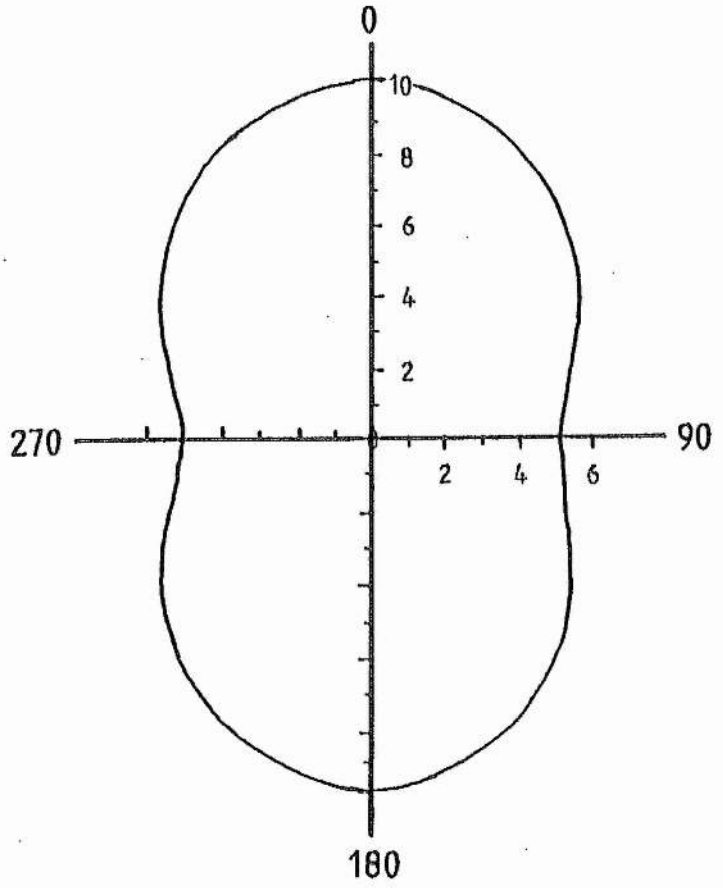

Figure 8.1.1 Normalized plot of the angular Rayleigh scatter coefficient

8.2 The Lidar Equation for Atmospheric Transmission of a Laser Pulse

A lidar equation describes the distribution of the signal return as a time or range dependent photon current after transmission of a single wavelength pulse into a scattering atmosphere. The following derivation is approximate in that it assumes a rectangular laser pulse. In appendix A8.3 a comparison between a Gaussian function and a rectangular photon function of the same duration shows the approximation of peak Gaussian photon power to the peak and average photon power of the rectangular function. Single scattering is assumed, as distinct from multiple scattering, in that any photons removed by scatter from the incident light path do not re-enter the path apart from those scattered through 180°. Multiple scattering is evident where photons are scattered in the forward direction ($\theta = 0$) or where photons re-enter the light path.

Each atmospheric or system property involved in the equation is discussed in the following sub-sections as a proportionality to the instantaneous photon current received from a range r. The subsequent functions are combined to give the lidar equation.

8.2.1 Attenuation by Scatter and Absorption

Scattering, as discussed in section 8.1, contributes to the attenuation of the pulse by removing photons from the light path. Absorption by atmospheric gases can be evident in certain regions of the spectrum and within certain altitude ranges. At around 308 nm. the major ambient gaseous absorber would be ozone, which is only a problem where it is increasingly present above the troposphere, outwith the region of this system (Fleagle and Businger, p.168, fig.4-20). (This is consistent with the absence of ground level radiation around 308 nm., investigated spectrographically and

described in chapter 3). Both attenuation terms take the form of a Beer-Lambert exponential as a function of range. Thus, in a non-uniform atmosphere the linear scatter coefficients of equations (8.1.2) and (8.1.5) are applied over a two way path to give the instantaneous received photon current as

$$n'(r) \propto \exp[-2\int_o^r (\alpha_R(r) + \alpha_M(r))dr]. \qquad (8.2.1)$$

This applies to the extremely inhomogeneous atmosphere containing a smoke plume, where the scatter coefficient varies widely along the optical path. The absorption coefficient is expressed as an absorption cross-section, σ, and number concentration, N, so that, for a number, i, of absorbing species, the attenuation term is expressed as

$$n'(r) \propto \exp[-2\int_o^r \Sigma_i \sigma_i N_i(r)dr]. \qquad (8.2.2)$$

8.2.2 Collection Efficiency and Backscatter to the Receiver

The size of the return signal collected by the telescope is proportional to the mirror area, the amount of backscatter given by the coefficients in equations (8.1.4) and (8.1.6) and the scattering length which gives rise to an instantaneous return signal.

The solid angle which is subtended at range r by a mirror of area A is given by

$$\omega = A/r^2 \quad \text{sr}, \qquad (8.2.3)$$

as is shown in figure 8.2.1. The length of the backscatter medium which

gives an instantaneous return power is one half of the spatial pulse length of the laser, defined by the space-time diagram for the pulse path in figure 8.2.2. This range sample length, or minimum resolvable range, is given as

$$\Delta r = c\tau/2 \quad m, \tag{8.2.4}$$

where τ is the temporal full width at half maximum of the laser pulse (fwhm). Thus the Rayleigh and Mie backscatter coefficients are included with equations (8.2.3) and (8.2.4) to give

$$n'(r) \propto Ac\tau(\beta_R(r) + \beta_M(r))/2r^2 \tag{8.2.5}$$

which is more conveniently expressed, using equations (8.1.4) and (8.1.6), as

$$n'(r) \propto Ac\tau(3\alpha_R(r) + \alpha_M(r))/16\pi r^2. \tag{8.2.6}$$

Some sources quote equation (8.2.6) in the form

$$P'(r) \propto (A/4\pi r^2)(1.5\alpha_R(r) + \alpha_M(r))(c\tau/2) \tag{8.2.6a}$$

with a modified backscatter coefficient given by

$$\beta'(r) = 1.5\alpha_R(r) + 0.5\alpha_M(r). \tag{8.2.7}$$

The range dependence allows application to the non-uniform atmosphere.

8.2.3 Optical Efficiences of the System

A correction is allowed for the efficiences of the transmitting and receiving optics. Two reflection efficiences for the telescope are combined with the transmission efficiency of the narrow band filter to give a reception efficiency t_R. The output efficiency, t_T, is unity in this system where the pulse is emitted directly. Thus, including the average or peak photocurrent, $n_o'(t)$, transmitted at time zero, we get

$$n'(r) \propto n_o'(r) t_T . t_R \qquad (8.2.8)$$

8.2.4 The Lidar Equation

The lidar equation, upon combination of proportionalities (8.2.1), (8.2.2), (8.2.6) and (8.2.8), describing the backscatter and attenuation of photons up to range r, gives the instantaneous photon current, received from range r, in the expression

$$n'(r) = n_o'(t) t_T . t_R A c \tau (3\alpha_R + \alpha_M) . \exp[-2\int_o^r (\alpha_R + \alpha_M + \Sigma_i \sigma_i N_i(r)) dr] / 16\pi r^2 \qquad (8.2.9)$$

for the single pulse, single wavelength case. Some of the indications of range dependence have been omitted. The equation is of the same form as that given in other lidar works. This is only a reasonably good approximation if the function $n_o'(t)$, for the laser output pulse, represents an average photon current over the temporal width. Equation (8.2.9) gives the instantaneous photon current arising from scatter by a range element Δr, between ranges r and $r + \Delta r$ (see figure 8.2.2). The expression is more valid where the scattering length, Δr, is much less than the range r. The minimum range element, defined by the laser pulse duration, is given in equation 8.2.4. The backscattering from a real laser

pulse is a function of the pulse's temporal shape and is not simply uniform over a finite length. A rigorous approach to an analysis of the atmospheric transfer effect on a known pulse may utilise an atmospheric transfer function, a form of which is derived in section 8.3. However, in the simple case discussed here, equation (8.2.9) should be re-written as if for a rectangular laser pulse of relatively short duration Δt, consisting of n_o photons. Equation (8.2.9) is re-written to describe the signal obtained from such a pulse. The components are re-arranged to give the expression

$$n'(r) = (n_o/\Delta t)(1.5\alpha_R+0.5\alpha_M)(c\Delta t.A.t_T t_R/8\pi r^2).\exp[-2\int_o^r(\alpha_R+\alpha_M+\sum_i \alpha_i N_i)dr] \quad s^{-1}. \qquad (8.2.10)$$

This form of the simplified lidar equation is applied to calculate the return signal from a scattering atmosphere, including the scatter from a smoke plume. In section 8.4 a computer modelled prediction of the return distribution is given, in conjunction with the photomultiplier output analysis of chapter 3. The exponential attenuation term contains scatter coefficients which are considered as having a continuous range dependence. However, for the sake of the model, the backscatter coefficients are defined for each of the backscattering range elements, expressed as

$$\Delta r = c\,\Delta t/2. \qquad (8.2.11)$$

Adjacent target elements give return signals separated by time element, Δt, as indicated on the space-time diagram of figure 8.2.3. A supposed return distribution in figure 8.2.4(a) is modelled by the vertical bars of 8.2.4(b). When the path of a laser pulse is split into range elements in this fashion, a model atmosphere, including a smoke plume, can be set up, element by element, to predict a lidar return distribution (section 8.4).

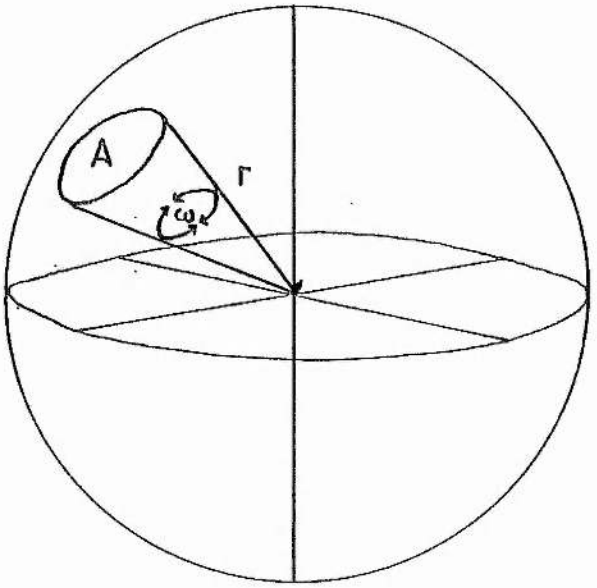

Figure 8.2.1 The solid angle of scattered photons subtended by an area A at range r

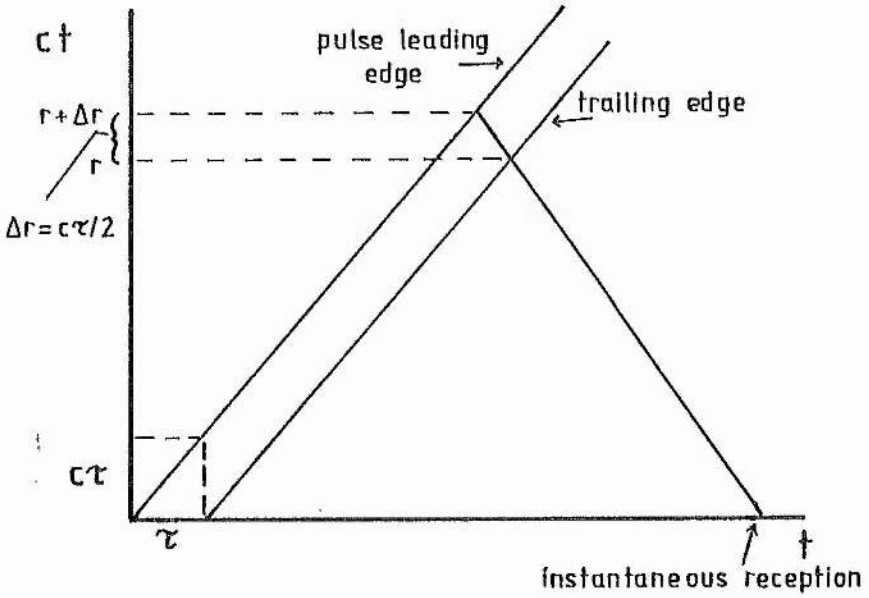

Figure 8.2.2 Space-time diagram of the laser pulse

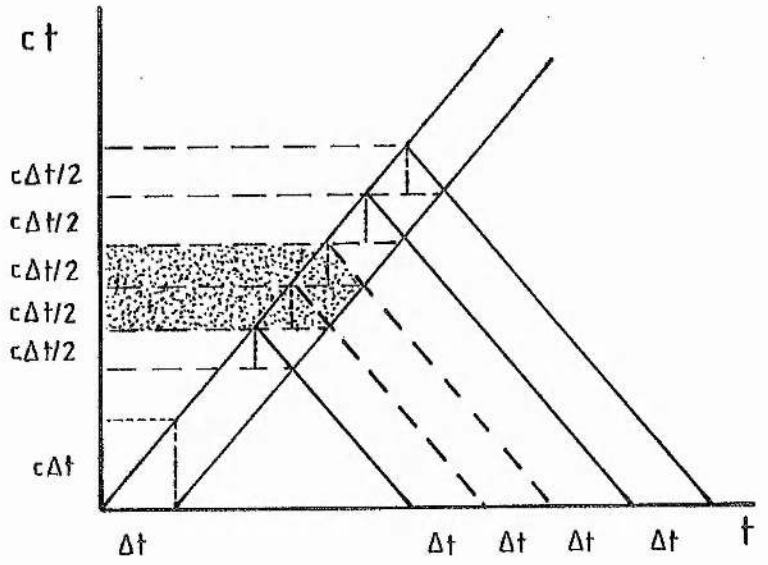

Figure 8.2.3 Space-time diagram of the laser pulse showing the scattering elements

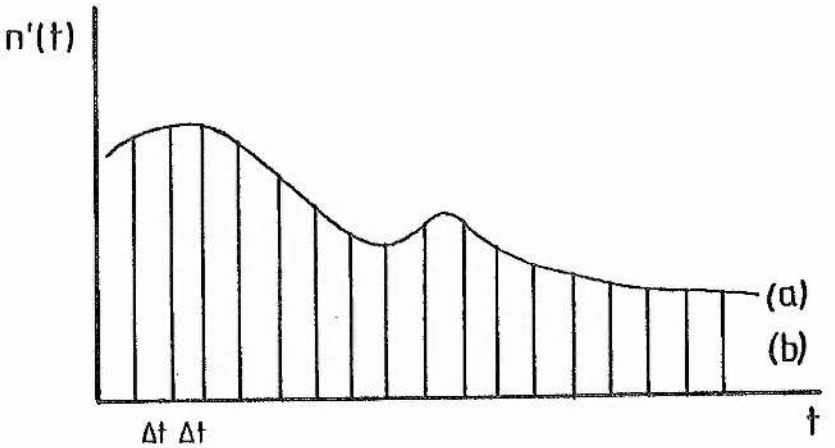

Figure 8.2.4 (a) A continuous lidar return distribution
(b) A modelled, discrete return distribution

8.3 The Lidar Transfer Function

The lidar equation (8.2.10) is useful as it stands but ,in the event of requiring a more accurate result with any known laser pulse function, then a general transfer function is desirable for convolution with that laser function. The atmospheric transfer function in the time domain, $H_a(t)$, or in the range domain, $H_a(r)$, describes the atmospheric and systematic properties involved in lidar pulse propagation from laser to detector. The basis for finding the transfer function lies in the prediction of a return function, $n'(t)_{\delta t}$ which results from the supposed transmission into the atmosphere of a pulse which is approximated to a delta function of photons. The photon delta function is a rectangular pulse of infinitesimal duration. A transfer convolution is applied to the delta function in a general sense and the result is compared with the lidar equation after it has been applied to predict the result of a delta function transmission.

The analysis is founded upon a general expression for pulse transfer in lidar, from a form given in appendix A8.4, which is given as the product of Fourier transforms in the convolution

$$\mathcal{F}\, n'(t) = \mathcal{F} n_o'(t) . \mathcal{F} H_a(t), \qquad (8.3.1)$$

where $n'(t)$ is the time dependent return function and $n_o'(t)$ is the laser output function.

8.3.1 Transfer of an Infinitesimal Rectangular Laser Pulse

The form of the rectangular laser pulse, illustrated in figure 8.3.1, is given by the equation

$$n_o'(t)_{\delta t} = n_o/\Delta t \qquad (8.3.2)$$

which can be re-expressed as a delta function in the limit

$$n_o'(t)_{\delta t \Delta t \to 0} \; n_o \, \delta(t), \qquad (8.3.3)$$

where n_o is the total number of output photons. The form of the delta function is evident in the integral

$$\int_{-\infty}^{\infty} 1/\Delta t \; dt = 1. \qquad (8.3.4)$$

Equation (8.3.1) is applied to the transmission of the delta function output of the form of (8.3.3) to give

$$\mathcal{F}\, n'(t)_{\delta t} = \mathcal{F} n_o \delta(t) . \mathcal{F} H_a(t). \qquad (8.3.5)$$

The transform of the delta function, shown in appendix A8.5, is applied to equation (8.3.5) and the inverse transforms are taken to give the impulsive transfer equation

$$n'(t)_{\delta t} = n_o H_a(t). \qquad (8.3.6)$$

8.3.2 The Impulsive Transfer Equation Compared with the Lidar Equation

The lidar equation of (8.2.10) is in a form which can be applied to the transmission of an impulse. In the limit that the pulse duration , Δt, tends to zero, equation (8.2.10) is compared with equation (8.3.6) as a function of range to give the transfer function as a function of range in

$$H_a(r) = (1.5\alpha_R + 0.5\alpha_M)(cAt_T t_R/8\pi r^2).\exp[-2\int_o^r(\alpha_R+\alpha_M+\Sigma_i\sigma_i N_i)dr]. \quad (8.3.7)$$

This equation can be re-expressed in terms of time elapsed, at the receiver, using the identity $r = ct/2$, to become

$$H_a(t) = (1.5\alpha_R + 0.5\alpha_M)(A.t_T t_R/8\pi ct^2).\exp[-2c\int_o^t(\alpha_R+\alpha_M+\Sigma_i\sigma_i N_i)dt]. \quad (8.3.8)$$

It is interesting to note that the backscatter function, $(1.5\alpha_R+ 0.5\alpha_M)$, is complete and operative only upon convolution with the laser function.

8.3.3 How to Apply the Transfer Function

If the function of (8.3.8) is to be convolved with a laser function according to the transfer equation (8.3.1), then the Fourier transform of the transfer function must be taken. This sub-section presents just an approximate result, for the sake of completeness, but it was done with the possibility of requiring it in a further analysis. The Fourier transform of the transfer function of (8.3.8) is expressed as the equation

$$\mathcal{F} H_a(t) = (1.5\alpha_R + 0.5\alpha_M)(A.t_T t_R/8\pi c).\mathcal{F}(1/t^2).\exp[-2c\int_o^t(\alpha_R+\alpha_M+\Sigma_i\sigma_i N_i)dt]. \quad (8.3.9)$$

It is assumed that the scatter coefficients in the backscatter function are uniform over the temporal width of a laser pulse and so they are not included within the transform function. A further simplification is

introduced in the transform function by assuming a uniform scattering and absorbing atmosphere up to and beyond a smoke plume, thus allowing the approximation given by

$$\exp[-2c\int_o^t(\alpha_R + \alpha_M + \sum_i \sigma_i N_i)dt] \longrightarrow \exp[-2(\alpha_R + \alpha_M + \sum_i \sigma_i N_i)ct]. \qquad (8.3.10)$$

Furthermore, if there is a local scatter and absorption term applicable only between the limits, t_1 and t_2, of a smoke plume, then the attenuation exponential for s active constituents is given by

$$\exp[-2c\int_{t_1}^{t_2}((\alpha_R + \alpha_M)_s + \sum_s \sigma_s N_s)dt] \longrightarrow \exp[-2c(t_2-t_1)((\alpha_R + \alpha_M)_s + \sum_s \sigma_s N_s)]. \qquad (8.3.11)$$

Equation (8.3.9) becomes, using (8.3.10) and (8.3.11),

$$\mathcal{L} H_a = (1.5\alpha_R + 0.5\alpha_M)(At_T t_R/8\pi c).\exp[-2c(t_2-t_1)((\alpha_R + \alpha_M)_s + \sum_s \sigma_s N_s)] \times \mathcal{L}(1/t^2).\exp[-2(\alpha_R + \alpha_M + \sum_i \sigma_i N_i)ct] \qquad (8.3.12)$$

which is transformed (Campbell and Foster, p.68, 606.1, 1961) to the result

$$\mathcal{L} H_a = (1.5\alpha_R + 0.5\alpha_M)(At_T t_R/8\pi c).\exp[-2c(t_2-t_1)((\alpha_R + \alpha_M)_s + \sum_s \sigma_s N_s)] \times (\omega - 2c(\alpha_R + \alpha_M + \sum_i \sigma_i N_i)). \qquad (8.3.13)$$

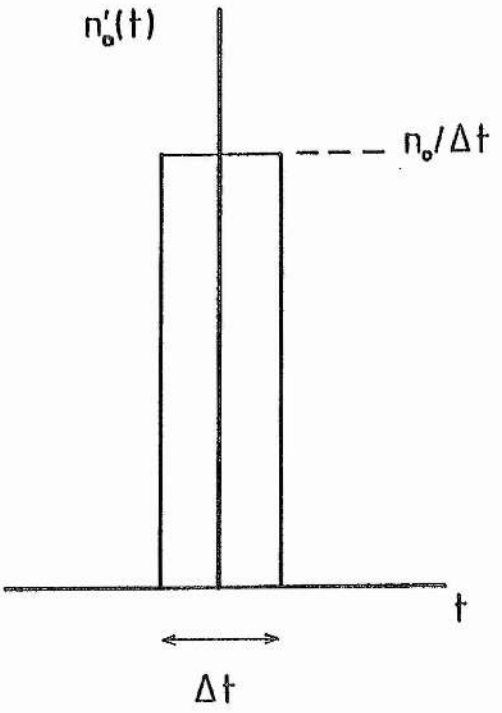

Figure 8.3.1 An impulsive laser function

8.4 A Model of the Lidar Return from a Scattering Atmosphere

Equation (8.2.10) is applied in combination with the photomultiplier output equation (3.1.27) to model, on an Acorn Atom micro-computer, the oscilloscope trace of a lidar return from a smoke plume. In section 8.6 a comparison is made between the modelled returns and those obtained in single pulse scattering experiments described in section 8.5.

8.4.1 Background to the Model

The basis to the model atmosphere is introduced in sub-section 8.2.4 and figures 8.2.3 and 8.2.4. A micro-computer program is set up in BASIC to give the photomultiplier output voltage arising from a range element Δr_j. Equations (8.2.10) and (3.1.27) give the voltage corresponding to photons from range r as

$$V(r) \geqslant n_o \eta e G R_L (1.5\alpha_R + 0.5\alpha_M)(cAt_T t_R / 8\pi r^2).\exp[-2\int_o^r (\alpha_R + \alpha_M + \textstyle\sum_i \sigma_i N_i)dr] \qquad (8.4.1)$$

which is valid in the equality for an output time constant, $R_L C_L$, which is much less than any temporal changes in the return signal. In the event that such a limit fails, then the voltage given by V(r) must be considered as a minimum value to appreciate that a strict expression would give higher peak response for greater $R_L C_L$ through signal integration. The return signal is calculated for each range element by considering the backscatter coefficient at the element. The attenuation term is given by the sum of the scatter and absorption depths up to the j^{th} element and is re-expressed, for one absorbing species, by

$$\exp[-2\int_{o}^{r}(\alpha_R + \alpha_M + \sum_i \sigma_i N_i)dr] \longrightarrow \exp[-2\sum_j(\alpha_{Rj} + \alpha_{Mj})\Delta r_j - 2\sum_j \sigma N_j \Delta r_j]. \quad (8.4.2)$$

For the purpose of the model, equation (8.4.1) is expressed as

$$V(r_j) = n_o \eta e G R_L . (1.5\alpha_{Rj} + 0.5\alpha_{Mj})[cAt_T t_R / 8\pi(j.\Delta r_j)^2] \times \exp[-2\sum_j(\alpha_{Rj} + \alpha_{Mj})\Delta r_j - 2\sigma\sum_j N_j \Delta r_j], \quad (8.4.3)$$

where the range element is given by (8.2.4) as

$$\Delta r_j = c\tau/2. \quad (8.4.4)$$

The application of the minimum resolveable range element ignores system bandwidth, the justification being in the use of a 100Ω load resistance, R_L. The range of interest is expressed as the total of the range elements covered. A model atmosphere along the pulse path, indicated in figure 8.4.1, is defined per range element in terms of an appropriate atmospheric visibility and concentration of SO_2 in ppm. The Rayleigh scattering coefficient is defined by equation (8.1.2) and the visibility is used in equation (8.1.5) to give the Mie coefficient. The presence of a smoke plume is entered by reducing the visibility value for a series of range elements to cover the spatial extent of the plume. Sulphur dioxide concentration within the plume, entered in ppm, is converted by equation (A9.1.5) to a number concentration for use in the attenuation term of (8.4.3).

8.4.2 Program Operation

Each parameter of (8.4.3) is evaluated in a sub-routine. A final evaluation is made per range element, followed by a plot, on a graphics display, of voltage as a function of range. The return from the entire range is built

up by steady increments of the quantity j in repetition of the analytical program. Table 8.4.1 lists the parameters used in the program. Constants are entered with the program listing but system parameter values are entered when the program is run. The model atmosphere is set up by entering the values of array variables for visibility and SO_2 concentration over defineable sections of the range. After a return has been modelled a re-run can be made for different parameters. The program is listed in appendix A8.6.

8.4.3 Modelled Returns

The lidar model was used to predict the lidar signal, as an oscilloscope output voltage distribution, from an atmosphere containing a smoke plume and SO_2 absorber. The smoke plume was simulated by lowering the visibility in that region, thereby increasing smoke density. The plume models were based on the relative spatial SO_2 concentration distribution given in figure 8.4.2(a) and the local visibility distribution of figure 8.4.2(b), giving a hypothetical plume cross-section like that in figure 8.4.3, as would be observed from a direction perpendicular to the light path. Experiments at Methil power station took lidar returns from a smoke plume, at a lidar range of about 200 m., from the chimney top to about 100 m. along the plume. The model was based on the experimental situation with a view to matching theoretical and empirical results to check the validity of equations (8.4.1) and (8.4.3) and checking that the signal acquisition system was operating correctly.

System parameters and conditions pertaining to the modelled situation are listed in table 8.4.2. The accuracies of these parameters alone suggests an uncertainty of ±16% in applying equation (8.4.1). Visibility and SO_2 level range distributions are given in table 8.4.3 and the modelled returns are

reproduced in figures 8.4.4(a) to (e). A clear sky is assumed to have a visibility of 20 km. The full plume extent is set at 45m, with a denser centre of width 9m.

Figures 8.4.4(a), (b) and (c) are realistic predictions of the signals expected from a power staion plume at a range of 220 m., based on the knowledge that SO_2 concentrations at the chimney top of Methil power station may be expected to fall within the range 700 to 1400 ppm (output figure, SSEB 1977). The three modelled plumes are identical apart from the SO_2 burdens. Peak voltages are noted for comparison with experimentally obtained returns. No return is predicted from beyond the plume due to the attenuative effects of scatter and absorption.

Figures 8.4.4(d) and (e), on different voltage scales, are not attempts at modelling a real situation. In each, the dense scattering medium, starting at 200 m., is continued beyond that range. The medium in 8.4.4 (d) carries an SO_2 burden which prevents a return from beyond several metres optical depth. In 8.4.4(e) the absence of SO_2 gives a stronger signal and allows a return to be detected from the denser atmosphere. This shows the predominantly $1/r^2$ proportionality which will impose an upper limit on practical lidar range. However, a greater problem appears to be in probing deep into an SO_2 laden atmosphere, because of strong absorption.

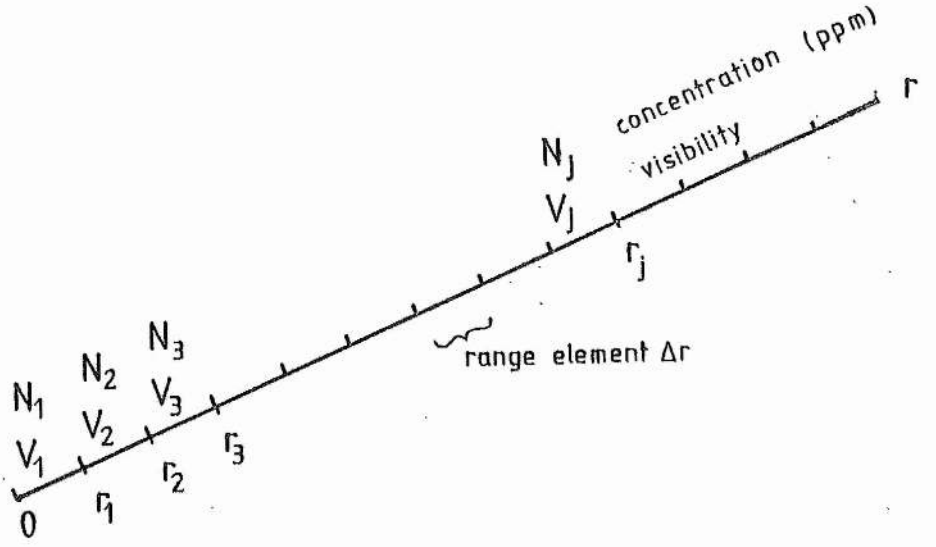

Figure 8.4.1 A model scattering and absorbing light path based on range elements

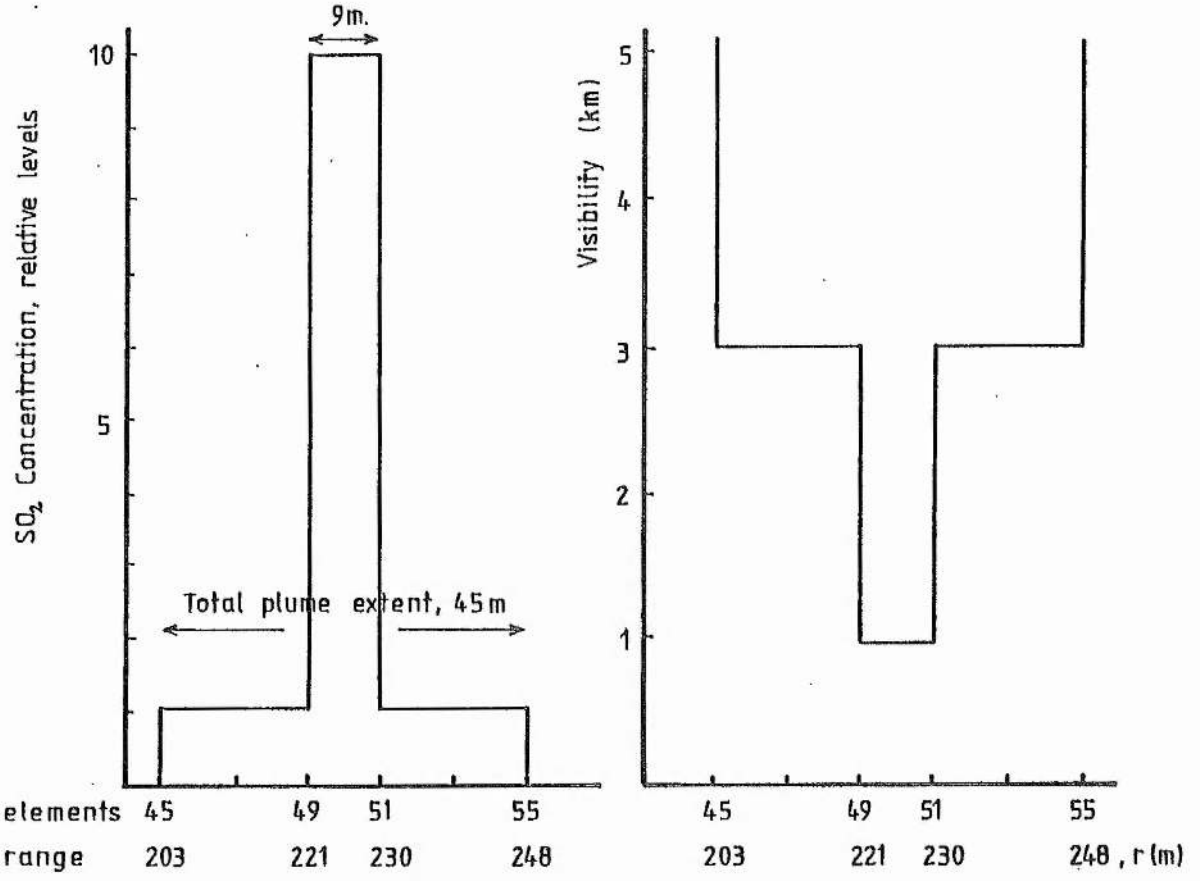

Figure 8.4.2 (a) Relative spatial and sectional distribution of SO_2 concentration for a lidar model

(b) Relative spatial and sectional distribution of visibility for a lidar model

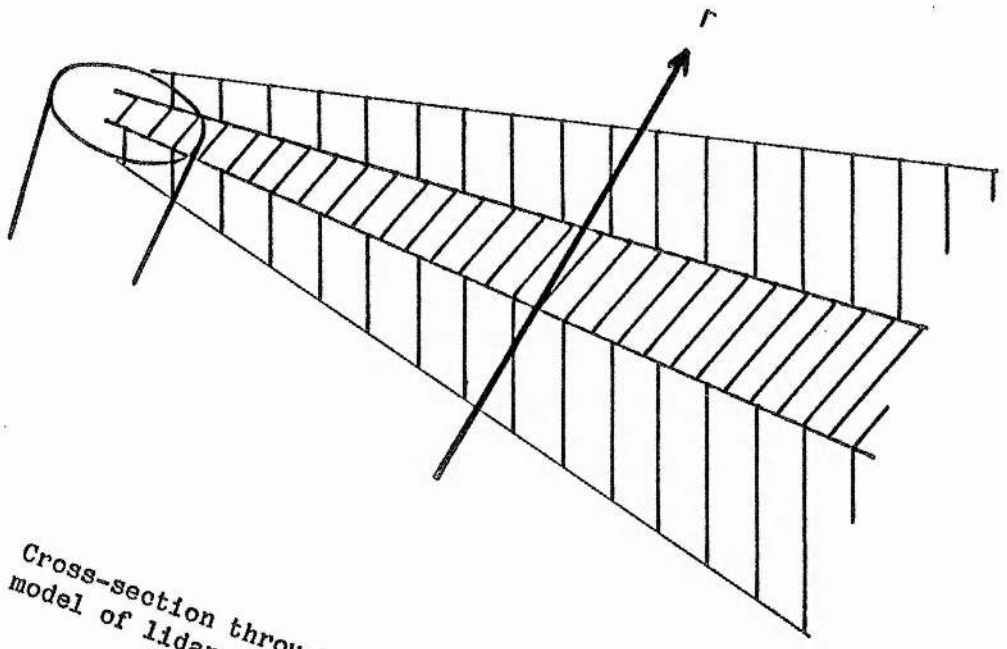

Figure 8.4.3 Cross-section through a simulated smoke plume in a model of lidar returns

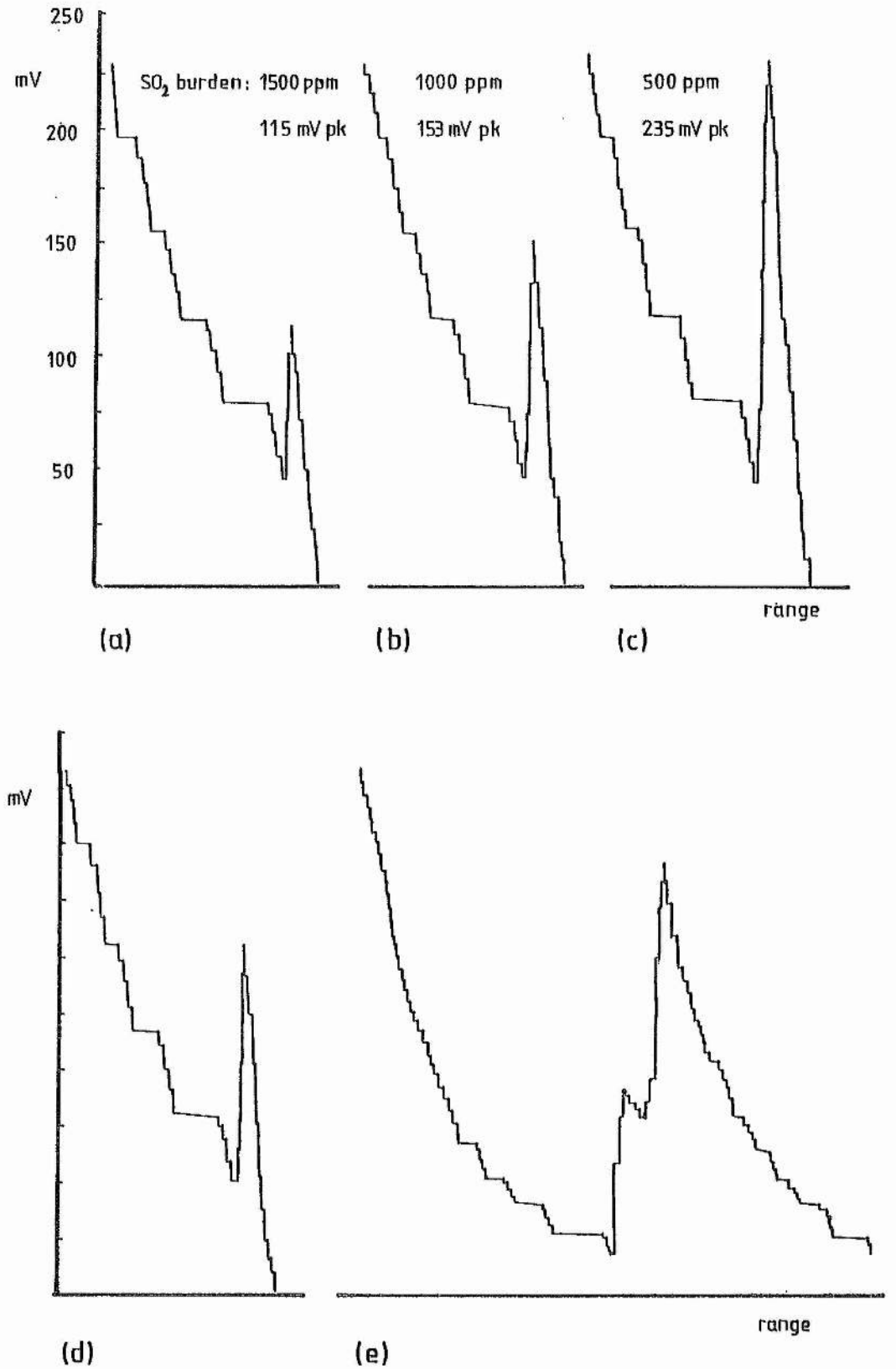

Figure 8.4.4(a) to (e) Modelled single pulse lidar returns

Table 8.4.1 Program Parameters for Modelled Lidar Return

Parameter Type	Program Symbol	Analytical Variable	Description
Constants	%C	c	speed of light
	%H	h	Planck's constant
	%G	e	electronic charge
Enter: System Parameters	%T	τ	laser pulse fwhm
	%E	E_o	laser pulse energy
	%W	λ	laser wavelength
	%O	t_T	laser pulse transmission efficiency
	%A	A	telescope mirror area
	%S	$\mathcal{R}$	mirror reflectivity
	%F	T_F	detector filter transmissivity
	%K	η	photomultiplier quantum efficiency
	G	G	photomultiplier gain
	R	R_L	photomultiplier load resistance
	P	P	atmospheric pressure
	T	T	temperature
	%X	σ	SO_2 gas absorption cross-section
Enter: Model Atmosphere Parameters	VV(255)		visibility in range element defined by array components
	NN(255)		SO_2 concentration in range element defined by array component
Program Variables	V	V(km)	visibility (km)
	%N	N'	SO_2 concentration (ppm)
	%J	α_R	Rayleigh scatter coefficient
	%M	α_M	Mie scatter coefficient
	%Q	q	power in Mie calculation
	%U	$e^{-2\int_o^r \alpha\, dr}$	scatter attenuation
	%P	$e^{-2\int_o^r \beta N dr}$	absorption attenuation
	%B	β'	backscatter coefficient
	%Z		scatter attenuation accumulation
	%Y		absorption attenuation accumulation
	%W	λ	wavelength (308nm to 0.55)
	%L	n_o	number of laser pulse photons
	%I	$n^9(r)$	received photon current from range r
	%D	t_R	reception efficiency
	%R	r	range
	%V	V	photomultiplier output voltage
	J		program counter and range increment
	S	j	number of range elements

Table 8.4.2 System Parameter Values for the Lidar Model

Description	Symbol	Value
Laser pulse, fwhm	τ	32 ns (3%)
Laser pulse energy	E_o	5 mJ (10%)
Laser wavelength	λ	308 nm
Laser pulse transmission efficiency	t_T	1
Telescope mirror area	A	0.0507 m^2
Mirror reflectivity	$\mathcal{R}$	0.8
Detector filter transmissivity	T_F	0.2 (7%)
Photomultiplier quantum efficiency	η	0.01 (10%)
Photomultiplier gain	G	10^6
Photomultiplier load resistance	R_L	100 Ω
Atmospheric pressure	P	1013 mbar (1%)
Temperature	T	283 ^oK (2%)
SO_2 gas absorption cross-section	σ	23 X 10^{-24} m^2
Range element	$c\tau/2$	4.5 m (3%)

Table 8.4.3 Parameter Values of a Model Atmosphere

Visibility and SO_2 concentration

Total plume extent of 45m; major plume density across 9m range.

Range element length of 4.5m.

Range element :0		45	49	51	55	90
Range (metres):0		203	221	230	248	405
Model						
(a)	Visibility(km)	20	3	1	3	20
	SO_2 conc(ppm)	0	150	1500	150	0
(b)		20	3	1	3	20
		0	100	1000	100	0
(c)		20	3	1	3	20
		0	50	500	50	0
(d)		20	3	1	1	1
		0	100	1000	1000	1000
(e)		20	3	1	1	1
		0	0	0	0	0

8.5 Single Pulse Experiments at Methil Power Station

Experiments, involving single pulses, were carried out at Methil power station.

The oscilloscope traces of figure 8.5.2 were taken from the different target positions along and in the centre of the smoke plume, illustrated in figure 8.5.1. Irregularity of the pulse is due to the impedance mis-match of 100Ω/1MΩ between the photomultiplier load resistor and the oscilloscope input. Peak voltages and approximate signal pulse widths are tabulated in table 8.5.1. The measured scattering range element is given. The ranging feature of lidar, by time of flight measurement, was not attempted.

A large signal was obtained by direct scatter from the chimney stack itself. This, shown in figure 8.5.2(e), is the single range response from scatter from a surface. The expected return pulse width would be that of the transmitted laser pulse, as shown in the space-time diagram of figure 8.5.3. However, the width appears to be about one half of that expected, without considering the effect of instrument response. Figure 8.5.4 shows the reduction in peak voltage from returns in figures 8.5.2(a) to (d) as they are taken from the plume, further along from the chimney. A reduction is expected since backscatter is reduced as the smoke becomes more diffuse. However, the effect is partially offset by the reduction in SO_2 absorption as it too becomes less concentrated along the plume. Thus, the peak voltage does not appear to drop as much in this relation as might be expected.

The return pulse temporal widths in figures 8.5.2(a) to (d) are interpreted to give the approximate spatial extent of the plume via the identity of equation (8.2.11). However, in table 8.5.1, a correction is made to the

direct translation of the temporal widths by subtracting the single range response, in spatial terms, as obtained from the chimney stack return of figure 8.5.2(e). Corrected spatial widths are given for the fwhm of the return, describing the extent of the bulk of the plume, and for the base width of the return, describing the full measureable extent of the plume. These values are plotted in figure 8.5.5 to show the relation with distance along the plume; ie. the dispersion. A more practical interpretation of the values is in figure 8.5.6, which is of the measured smoke plume extent in section. The chimney top diameter of 5.6 m, superimposed on figure 8.5.6, is very close to the plume diameter measured just above, providing a useful check on the width results. A similar profile was produced by Hamilton from an investigation of the Northfleet power station plume (P.M.Hamilton, 1969). The spatial interpretation of the plume diameter further from the chimney is probably the lower limit due to attenuation by the plume material itself, creating a diminished return from the far side of the plume.

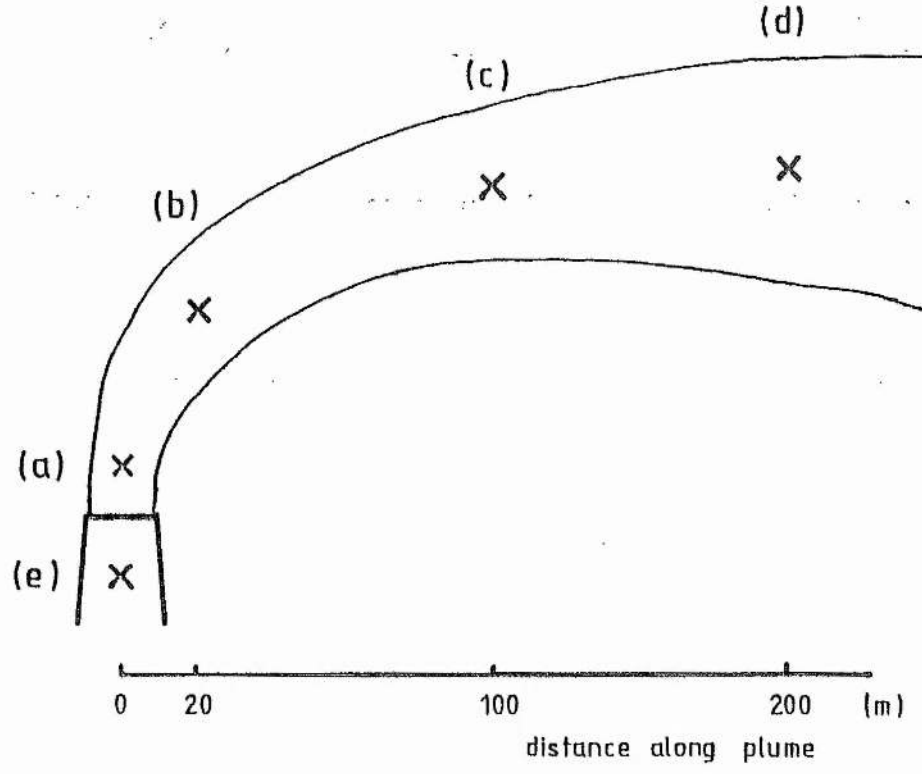

Figure 8.5.1 Schematic representation of the smoke plume from the chimney at Methil power station during lidar experiments, showing the sample points (a) to (e)

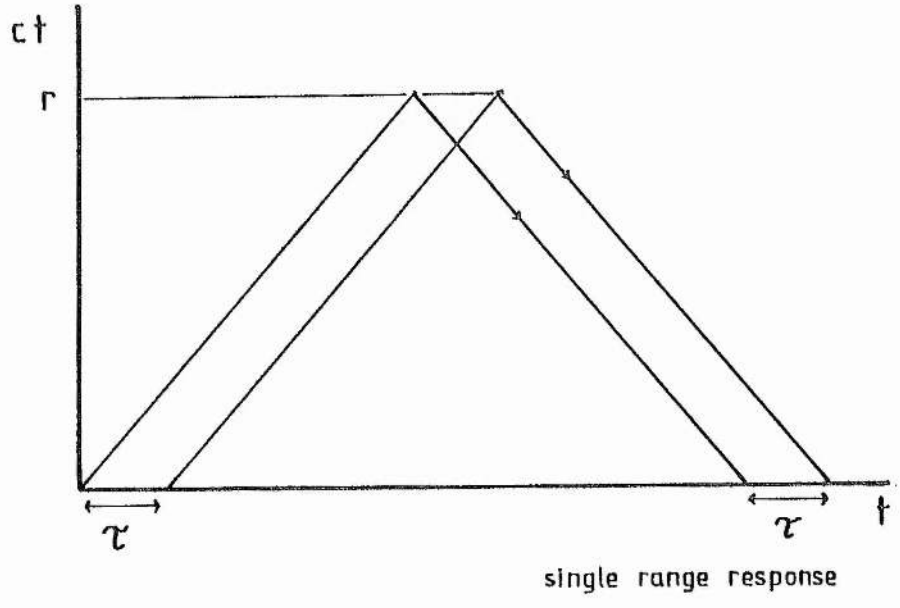

Figure 8.5.3 Space-time diagram showing expected single range response

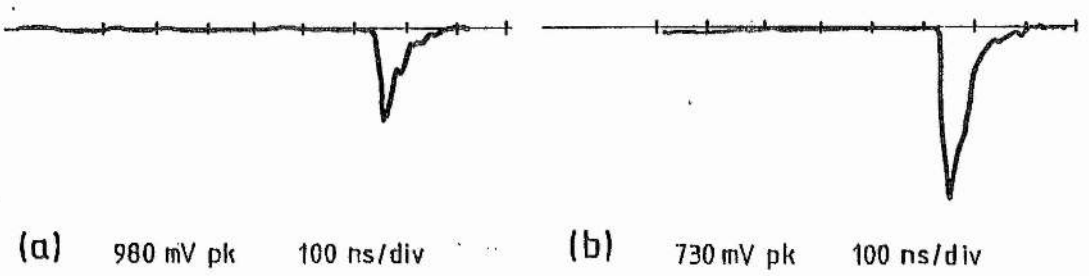

(a) 980 mV pk 100 ns/div (b) 730 mV pk 100 ns/div

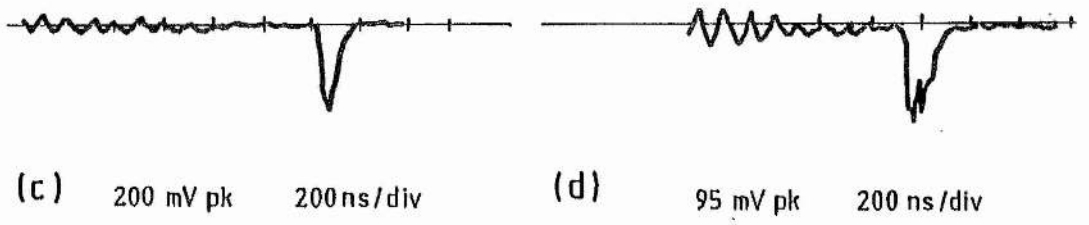

(c) 200 mV pk 200 ns/div (d) 95 mV pk 200 ns/div

(e) 2150 mV pk 100 ns/div chimney return

Figure 8.5.2(a) to (e) Oscillograph traces of lidar return pulses from the Methil power station plume

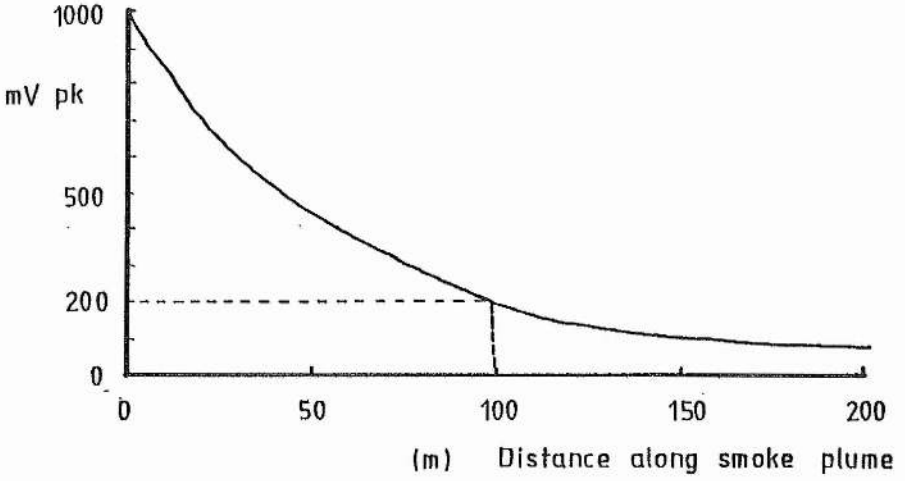

Figure 8.5.4 Variation of peak voltage in returns from positions along the smoke plume at Methil power station

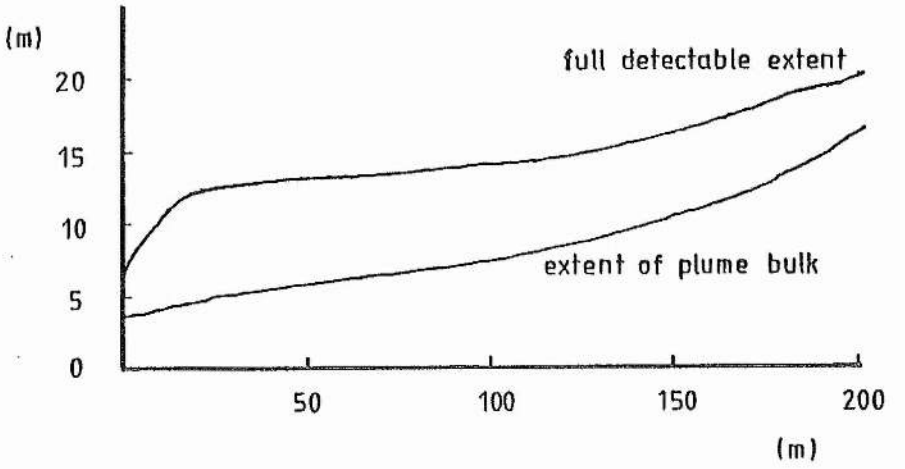

Figure 8.5.5 Variation of the sectional extent of the Methil plume along its length

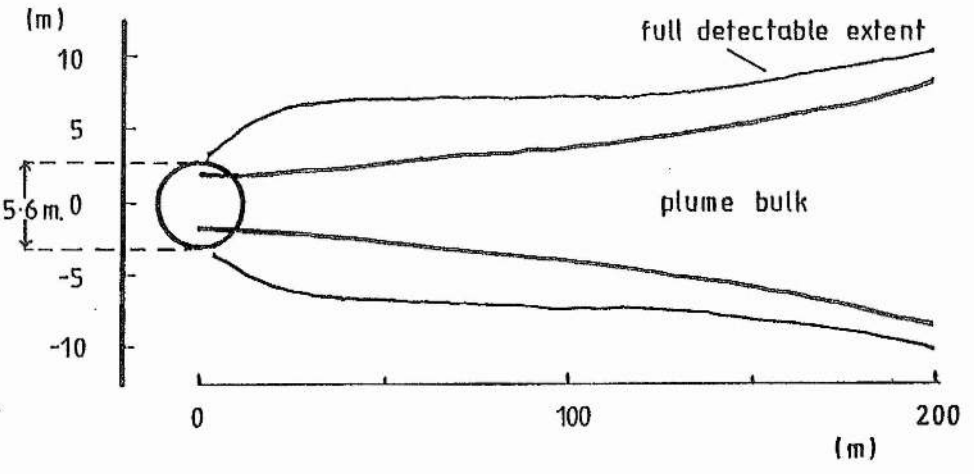

Figure 8.5.6 Sectional extent of the Methil plume as revealed by the results of the lidar experiment

Table 8.5.1 Lidar Return Pulses from Methil Power Station Plume

Peak Voltages and Pulse Widths

Target label	Peak voltage (mV)	Pulse widths (ns)		Scattering range element (m)			
				uncorrected		corrected	
		fwhm	base	bulk	total	bulk	total
(a)	980	40	75	6.00	11.3	3.45	6.05
(b)	730	50	115	7.50	17.3	4.95	12.05
(c)	200	66	130	9.90	19.5	7.35	14.25
(d)	95	130	170	19.5	25.5	16.95	20.25
(e)	2150	17	35	2.55	5.26	--	--

8.6 Comparison Between Experimental and Modelled Single Pulse Lidar Return

A comparison between the experimental returns of section 8.5 and the modelled returns of section 8.4 serves to check the validity of the lidar and photomultiplier output equations and to test the lidar signal acquisition system.

The modelled returns of figures 8.4.4(a), (b) and (c) are compared with the experimental returns of figures 8.5.2(a), (b), (c) and (d). An immediate difference is the apparent lack of near field ($1/r^2$) scatter on the experimental returns. It is suspected that this is due to poor laser and telescope field overlap at shorter range although the alignment was accurate enough for good smoke plume returns. The laser and telescope full fields are approximately 8 mrads and 10 mrads respectively, close enough for alignment inaccuracies to cause near field signal loss.

In the comparison, the model and experiment are matched by smoke plume width and peak voltages. The model plumes have a bulk smoke width of 9m. This dimension is matched to the experimental results to find the appropriate part of the empirically measured Methil plume by using figure 8.5.5, which shows that the Methil plume has a 9m bulk width at 130m along from the chimney. Figure 8.5.4 shows that the expected (measured) peak voltage return, from 130m along, is about 150mV. This, in turn, is related back to the model in figure 8.4.4(b), where a peak return voltage of 153mV represents the return from a smoke plume carrying a bulk burden of 1000 ppm. A burden of 1000 ppm would not be expected in a real plume as far away from the chimney as 130m. However, the model does not allow for absorption by SO_2 in the range intervening between the lidar system and the plume; ie. the ambient SO_2 concentration is taken as zero. Thus, the modelled plume

burden is considered as an upper limit if a real situation is envisaged. Another reason for mis-match between the model and the real situation would be if the telescope/laser field alignment was inaccurate, causing the experimental peak voltages to be lower than a model situation would predict. In this case, for example, higher peak voltage would correspond to a modelled plume carrying a lower SO_2 burden, as shown in figure 8.4.4(c), where the SO_2 burden is 500ppm.

Apart from the experimental absence of the short range scatter and the hit or miss inclusion of SO_2 levels, the model seems to give a reasonably close correlation with the experimental evidence on pulse width, although experimental peaks are still slightly on the low side of the predictions if realistic SO_2 burdens are considered. On the whole the agreement would indicate that the prototype lidar signal acquisition equipment is functioning as designed. The algorithm for describing the lidar return signal appears to be adequate.

8.7 Sample Time and Range Resolution

The instantaneous received signal is obtained by backscatter of radiation from over a spatial length, Δr, defined by the laser pulse duration, τ, in equation (8.2.4) and shown in the space-time diagram of figure 8.2.2. Signal handling equipment will sample the return signal over a finite sample time, τ_s. The effective spatial resolution is thus increased from its minimum of $c\tau/2$ to that which depends on the sample time of the equipment, as shown in the space-time diagram of figure 8.7.1. The range resolution is given by

$$\Delta r = c(\tau + \tau_s)/2. \qquad (8.7.1)$$

The processing equipment effectively integrates over the time period τ_s. This sample time and the signal processing bandwidth are related in equation (9.3.5). A quantitative analysis of the whole lidar receiver allows definition of system bandwidth and therefore of the range resolution.

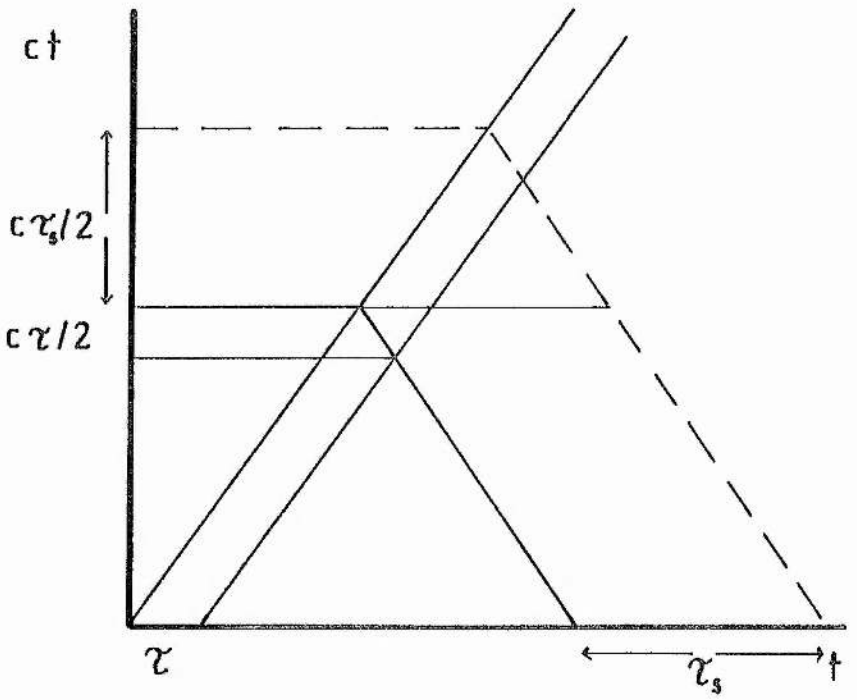

Figure 8.7.1 Sample time and its relation to range resolution shown on a space-time diagram of the laser pulse

References for Chapter 8

Bennett; Introduction to Signal Transmission. McGraw-Hill, (1970)

Bullrich; Advances in Geophysics, vol.10, pp.105-260, (1948)

Campbell and Foster; Fourier Integrals for Practical Applications, (1948)

Duntley S.Q; The reduction of apparent contrast by the atmosphere. Opt.Soc.Am., 38, 179, (1948)

Eltermann L; Atmospheric attenuation model, 1964, in the U.V, visible and I.R region for altitude to 50 km. Environmental Research Papers, N46, AFCRL, Cambridge, Mass., (1964)

Fleagle and Businger; An Introduction to Atmospheric Physics (1963)

Frolich and Shaw; Appl.Opt., 19, 11, (1980)

Hamilton P.M; The application of a pulsed light rangefinder (lidar) to the study of chimney plumes. Philos.Trans.R.Soc.London A, 265, 153-172, (1969)

Hinkley E.D (Ed.); Laser Monitoring of the Atmosphere, Topics in Applied Physics, 1976

Junge C.E; J.Meteorol., 12, 13-25, (1955)

Kondratyev; Radiation in the Atmosphere. Academic Press, (1969)

Koschmeider H; Theorie der horizontalen Sichtweite. Beitr.Phys.Atmos., 12, 33, 171, (1926)

Kruse P.W, McQuistan R.B and McGlaughlin L.D; Elements of I.R Technology, Wiley, New York, (1962)

Methil power station, Assistant Chemist, private communication.

Mie G; Ann.Phys.(Germany), 30, 57, (1909)

Penndorf R; J.Opt.Soc.Am., vol.47, pp.176-182, (1957)

Uchino et al; Applications of excimer lasers to laser-radar observations of the upper atmosphere. IEEE J.Quantum Electron., QE-15, 10, October (1979)

Chapter 9 Excimer Laser Differential Absorption Lidar (DIAL) Theory

Chapter 8 discusses the collection of photons from over the scattering range described by the variable r. The lidar equation (8.2.10) as derived is applied to single pulse, single wavelength transmission and describes the modifications to the collected signal which are imposed by scatter and absorption. The latter feature is a property which is a function of the amount of the absorbing gas. If it were possible to define exactly the scatter coefficients, leaving, as the only unknown, the absorption attenuation term, then a measurement of return power with respect to the output power would allow calculation of the absorption depth and, with knowledge of the gas absorption cross-section, the gas concentration would be obtained. However, scattering, especially by aerosols, is too complicated and variable a phenomenon to asign sufficiently accurate values to coefficients. In addition, it is not necessarily just one gas which absorbs the radiation. A practical solution is to eliminate the scatter and superfluous absorption terms in differential absorption lidar, which involves two pulses, each of a different wavelength. It is convenient to consider the lidar equation applied for each pulse. The wavelengths are close enough for the scatter terms to be equivalent. Target gas selection is obtained by matching an absorption cross-section difference to the respective wavelengths so long as all other gases exhibit a flat absorption spectrum in that region. Thus, in DIAL theory a ratio of two lidar equations gives the return power ratio as a function of gas concentration. Methods by which DIAL has been applied to SO_2 monitoring have been

discussed in chapter 1. In this work the SO_2 spectrum is matched to the $XeCl^*$ dual wavelength output, also introduced in chapter 1.

Conventional dual wavelength DIAL, using the $XeCl^*$ output, is analysed in this chapter to give the expression for target gas concentration in terms of return signal ratio. This, distinct wavelength DIAL, is considered and evaluated specifically for detecting SO_2 with regard to detection limits arising from measurement innacuracies. Later sections repeat the procedure for a novel form of SO_2 DIAL, a feature of this work, where each DIAL pulse is of mixed wavelength content but relative levels within a pulse are different. The latter form, mixed wavelength DIAL, was developed as a relatively simple but robust way of applying the dual wavelength nature of the $XeCl^*$ laser output to a field instrument for monitoring SO_2 whilst avoiding the expensive and fragile methods for selecting one line at a time (discussion of laser tuning is in chapter 5). An absorption cell, placed within the optical cavity of the laser, merely modifies the relative intensities of the two lines for one of the DIAL pulses. The second pulse is transmitted unaltered.

A substantial section on noise, 9.3, in defining error sources in the system, is included to allow definition of DIAL accuracies in SO_2 measurement.

9.1 Dual Pulse, Distinct Wavelength DIAL Theory

A DIAL system requires an algorithm to translate the return signal levels into a value for the target gas concentration. This section takes the lidar equation of chapter 8 and repeats it for two wavelengths. The ratio is taken to eliminate scattering terms from the required function.

Equation (8.2.10) with (8.2.7) is applied for wavelength λ_1 to give the return photon current received from range r as

$$n'(r) = n_1 \beta'(cA/8\pi r^2)t_T t_R.\exp[-2\int_o^r(\alpha_M + \alpha_R)dr].\exp[-2\int_o^r \sigma_1 N dr], \quad (9.1.1)$$

where n_1 is the number of photons per pulse at λ_1 and σ_1 is the absorption cross-section of a target gas at λ_1, assuming a single absorber. Similarly, the return photon current at wavelength λ_2 is given by

$$n''(r) = n_2 \beta'(cA/8\pi r^2)t_T t_R.\exp[-2\int_o^r(\alpha_M + \alpha_R)dr].\exp[-2\int_o^r \sigma_2 N dr], \quad (9.1.2)$$

where n_2 is the number of photons per pulse at λ_2 and σ_2 is the absorption cross-section of a target gas at λ_2. In order to provide a range resolveable result, consideration is given to signals received from over the integrated range r and from the integrated range plus the target element $r + \Delta r$. The pollutant gas number concentration is taken as an average, $\bar{N}_r$, over the range r and, likewise, $\bar{N}$, over the range $r + \Delta r$, so that the exponential absorption attenuation arguments for wavelength λ_1 are given by the approximations

$$-2\int_o^r \sigma_1 N(r)dr \triangleq -2\sigma_1 \bar{N}_r dr \quad (9.1.3)$$

and

$$-2\int_{o}^{r+\Delta r}\sigma_1 N(r)dr \triangleq -2\,\sigma_1\bar{N}_r r - 2\,\sigma_1\bar{N}\;\; r. \qquad (9.1.4)$$

Similarly, the absorption at λ_2 is given by the approximations

$$-2\int_{o}^{r}\sigma_2 N(r)dr \triangleq -2\,\sigma_2 N_r r \qquad (9.1.5)$$

and

$$-2\int_{o}^{r+\Delta r}\sigma_2 N(r)dr \triangleq -2\,\sigma_2\bar{N}_r r - 2\sigma_2\bar{N}\;\; r. \qquad (9.1.6)$$

Equations (9.1.1) and (9.1.2), applying to range r, with the use of (9.1.3) and (9.1.5), are ratioed and the natural logarithm is taken to give the integrated concentration over range r, as $\bar{N}_r$ in the expression

$$\ln[(n'(r)/n''(r)).(n_2/n_1)] = -2(\sigma_1 - \sigma_2)N_r r. \qquad (9.1.7)$$

The same is done for application to the range $(r + \Delta r)$, using (9.1.4) and (9.1.6), to give

$$\ln[(n'(r+\Delta r)/n''(r+\Delta r)).(n_2/n_1)] = -2(\sigma_1 - \sigma_2)(\bar{N}_r r + \bar{N}\,\Delta r). \qquad (9.1.8)$$

The logarithm ratio differences of (9.1.7) and (9.1.8) is taken to allow solution of the expression for average target concentration, over the range-resolved element Δr, giving

$$\bar{N} = (-1/2\,\Delta r(\sigma_1 - \sigma_2)).(\ln[n'(r+\Delta r)/n''(r+\Delta r)] - \ln[n'(r)/n''(r)]) \quad m^{-3}. \qquad (9.1.9)$$

In ratioing the single wavelength returns, the like terms cancel. This is one of the principal features of DIAL, eliminating unpredictable atmospheric and systematic variables.

Appendix A9.1, equation (A9.1.5), outlines a conversion for concentration from units of m^{-3} to units of parts per million, ppm. Equation (9.1.9) becomes

$$\bar{N}' = (-T_r/1.45X10^{19}.\Delta r(\sigma_1 - \sigma_2).P_r).(\ln[n'(r+\Delta r)/n''(r+\Delta r)] - \ln[n'(r)/n''(r)] \text{ ppm.} \quad (9.1.10)$$

The conversion can be applied to (9.1.7) and (9.1.8). Application of the DIAL equations in different forms, as the basis for an algorithm in DIAL signal interpretation, or as the basis for a model, is discussed in section 9.9.

9.1.1 Effects of Pressure and Temperature Variation

Pressure and temperature variations, if no correction is made, will have a direct effect on the accuracy of the concentration calculation as given by equation (9.1.10). The variation of pressure with height, h is expressed in appendix A9.2 giving

$$P_r(h) = P_g.\exp[-0.034h/T), \quad (9.1.11)$$

where P_g is the pressure at ground level. The variation of pressure from that assumed at the ground (or an arbitrary height) is given by

$$\Delta P_r(h)\ \% = 100(1 - \exp[-0.034h/T]), \qquad (9.1.12)$$

which is plotted for a temperature of 283°K in figure 9.1.1. The pressure variation can be 2.5% at a height of 200m (T=283°K) rising to about 11% at 1 km. For measurements obtained at heights above about 750m it may be desirable to correct for the variation from ground level pressure by applying the ranging aspect of lidar and the angle of laser/telescope elevation, θ_h in the expression

$$h = r.\sin\theta_h. \qquad (9.1.13)$$

Thus, a pressure compensated DIAL equation is equation (9.1.10) modified by equations (9.1.11) and (9.1.13) to give the concentration at range r as

$$\bar{N}' = (-T_r/1.45X10^{19}\Delta r(\sigma_1-\sigma_2)P_g.\exp[-0.034r.\sin\theta_h/T_r])$$
$$X\ (\ln[n'(r+\Delta r)/n''(r+\Delta r)] - \ln[n'(r)/n''(r)] \quad \text{ppm}. \qquad (9.1.14)$$

In equations (9.1.11), (9.1.12) and (9.1.14) the temperature T(°K) is assumed to be constant over the lidar range. Likely temperature variations and their effect are discussed in these two paragraphs with regard to ambient temperature and localised extremes. A variation in ambient temperature from the assumed value of 283°K will be within ±10%, giving a maximum variation, or error, of 3.5% in the concentration result. Since the ambient temperature will be more closely defined than ±10%, the error arising from this source will be insignificant in comparison with that arising from pressure and localised temperature variations. In other words, the direct consequence of temperature uncertainty as an error in concentration evaluation is negligible as long as the ambient temperature is measured or estimated for inclusion in equation (9.1.10) or (9.1.14).

A temperature problem arises when measuring target gas concentration within a smoke plume near to the chimney, where temperatures are elevated to above ambient. When this is the case, the temperature value inserted into the DIAL equation should be estimated at a higher level. Chimney top plume temperature at Methil power station, Fife can be 440 ± 20 ^{o}K (SSEB, 1982). For applying this information to plume measurements near to the chimney top, the temperature parameter in equations (9.1.10) and (9.1.14) would have a value mid-way between the maximum at 460 ^{o}K and the ambient. In this way the accuracy of concentration measurements across the steep temperature gradient from maximum to ambient would be within about 25%. This is considered to be acceptable in the present form of the system although there is room for improvement with regard to the definition of temperature.

If necessary in a precise application, the data required for compensation of pressure and temperature variation, as defined above, would be obtained by sensors linked to micro-processor control, using lidar ranging information, of the DIAL data handling system. In applying an equation of the form of (9.1.10) to a theoretical or experimental situation, within the scope of this work, temperature parameters are set according to an average value between ambient and localised maximum. The pressure is set by the ambient atmospheric pressure.

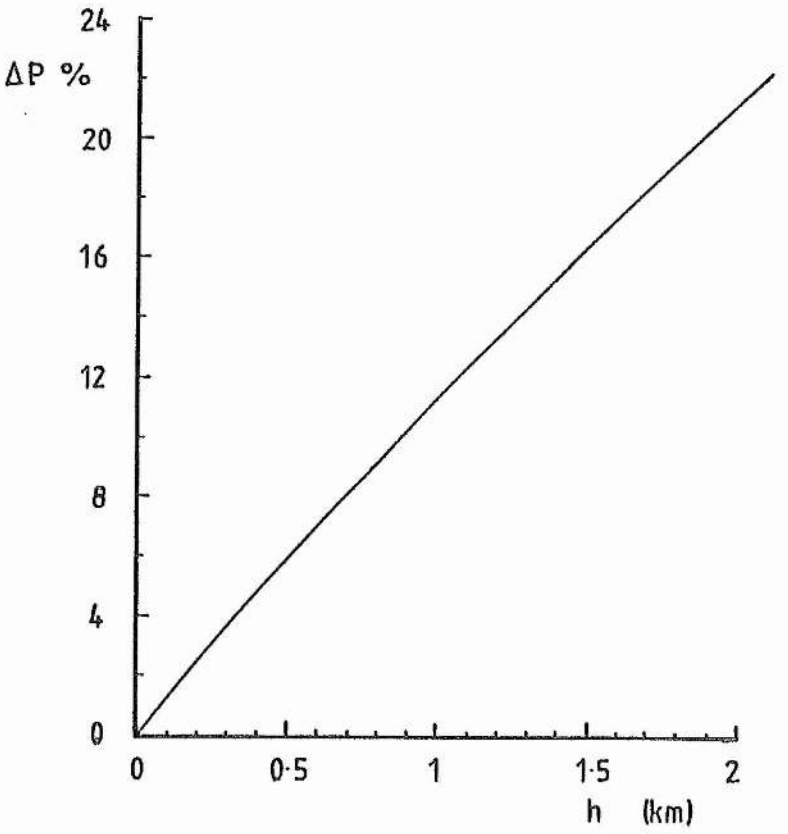

Figure 9.1.1 Variation of atmospheric pressure with height

9.2 Theoretical Signal Ratios from Distinct Wavelength DIAL SO_2 Returns

Equation (9.1.8) and the units conversion of (A9.1.5) are used in a model situation to relate the return signal ratio $n'(r+\Delta r)/n''(r+\Delta r)$ to the corresponding measured SO_2 concentration, $\bar{N}'$ (ppm), assuming a target of length Δr at range r and an average ambient SO_2 level, $\bar{N}_r'$ (ppm), measured over the integrated range. Equations (9.1.8) and (A9.1.5) are combined to give

$$n'(r+\Delta r)/n''(r+\Delta r) = (n_1/n_2).\exp[-1.45X10^{19}(\sigma_1 - \sigma_2)P_r(mb)(\bar{N}_r'r + \bar{N}'\Delta r)/T_r]. \quad (9.2.1)$$

The minimum resolveable range element Δr is given (from(8.2.11)) by the laser spatial pulse width, c2/2. The equation parameter values inserted for the purpose of this analysis are listed in table 9.2.1. The laser temporal pulse width was measured (see table 4.9.1). The ratio of the intensities of the two $XeCl^*$ emission peaks, n_1/n_2, was given the best statistical value, obtained as the average of 17 selected readings (see sub-section 4.9.5(b)). This ratio is defined per pulse pair in the DIAL system according to a normalization procedure which is described later. A temperature of 370^oK is set as the average between the chimney top plume temperature and a minimum ambient of 0^oC. The work of D.J.Brassington at C.E.R.L (Lab. note No. RD/L/2055N81, June 1981 and D.J.Brassington, 1981) provided an SO_2 absorption spectrum to give the cross-section difference between the $XeCl^*$ excimer wavelengths at 308.17 nm and 307.92 nm (Sze and Scott, 1978). The wavelengths and cross-sections are related in chapter 1. Figure 9.2.1 is of plots of the return ratios, $n'(r+\Delta r)/n''(r+\Delta r)$, given by equation (9.2.1), which are expected to arise from DIAL detection of SO_2 concentration, $\bar{N}'$ ppm over four ranges assuming the target range and integrated range SO_2

level, $\bar{N}_r$'. The program listing for these calculations is in appendix A9.3. The $(r+\Delta r)$ qualification on n' and n" is ignored in the rest of this thesis, $n'(r+\Delta r)/n''(r+\Delta r)$ being expressed, simply, as n'/n".

Figure 9.2.1 shows, roughly, the corresponding accuracy required in the measured ratio, n'/n", for a desired accuracy in measuring the SO_2 concentration. The concentration accuracy, defined by $\pm\Delta N'$, suggests a desired accuracy in the ratio n'/n" which in turn requires a certain accuracy in measuring each of n' and n". Precision of SO_2 concentration measurement is defined and examples are evaluated for this case in section 9.4, after the introduction to error sources in section 9.3 from which an estimation is made of the likely error in single pulse measurement.

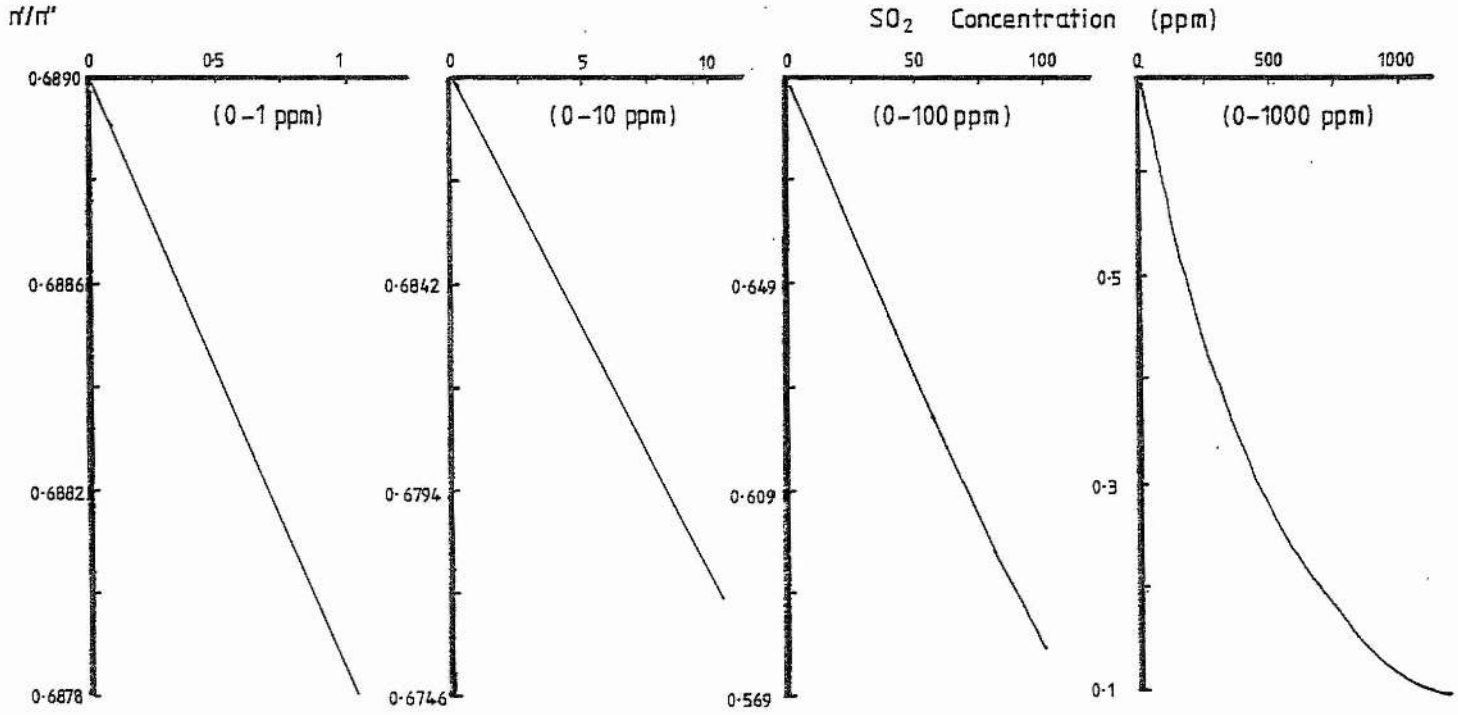

Figure 9.2.1 Distinct wavelength DIAL theory: Signal return ratio, n'/n'' vs. SO_2 concentration, $\overline{N}'$ (ppm)

Table 9.2.1 Model DIAL Equation Parameters

Description	Symbol	Value
Average temperature (smoke at top of chimney	T_r	370°K
fwhm of laser pulse (table 4.9.1)	τ	32 ns
SO_2 absorption cross-sections (D.J.Brassington, 1981)	σ_1	27.5×10^{-24} m^2
	σ_2	18.5×10^{-24} m^2
Average ambient SO_2 level over range r	$\overline{N}_r'$	0.05 ppm
Range of target element	r	200 m
Atmospheric pressure (standard)	P_r	1013 mbar
$XeCl^*$ laser peak intensity ratios between 307.92 and 308.17 nm (accurate values, table 4.9.3, due to Sze and Scott)	n_1/n_2	0.6915
SO_2 absorption cell active length	x	0.01 m
Absorption cell temperature	T	283 °K
Number of single passes of the absorption cell (correction factor)	N_c	2.36
Cell material absorption factor (by experiment)	K	0.8

9.3 Error Sources in the Excimer Laser DIAL System

Any errors which arise in handling the DIAL signals will have a subsequent effect on the measurement accuracy of the target gas concentration. This section introduces each predictable error source and develops it quantitatively as it appears in this application. An expression is derived for the total noise appearing in the peak voltage measured across the anode of the detecting photomultiplier, allowing the formation of a further expression for signal-to-noise ratio, which can be interpreted as a system error. This is considered later in the chapter in evaluating the theoretical concentration measurement accuracy in distinct wavelength and mixed wavelength DIAL. Signal-to-noise ratio can also be used to define the maximum range of the system if atmospheric visibility and target backscatter coefficients can be evaluated. This was not done because of the absence of an empirical comparison.

One defineable source of error in the system is the electronic measurement accuracy of the analogue-to-digital conversion which, at 12 bit, is 0.024%. Major noise contributions come from the various types of noise which are characteristic of a photomultiplier and output signal channel, including the statistical components of the signal itself. Undefineable errors arise in parts of the system. These are discovered when the equipment is operated and are removed or reduced during the first stages of the operational period.

The lower limit for SO_2 concentration detection may be imposed by the statistical fluctuations (shot noise) in the photomultiplier dark current, the signal arising from atmospheric background radiation, or in the signal itself. The background level, effectively biasing the signal, may also be a

problem. The extent of the limitation is dependent on the system bandwidth and the signal-to-noise ratio requirement. Signal averaging, described below, can be used to improve signal-to-noise ratio whilst maintaining a high bandwidth.

9.3.1 Background Radiation

Background radiation may obscure a weak return signal within its random fluctuation or shot noise. All shot noise components and their effect within the system are dealt with in sub-section 9.3.3. That analysis requires that the level of background radiation , affecting the DIAL signal channel, be estimated. The level of solar radiation at ground level varies according to the time of day and atmospheric conditions, ie. whether the sky is cloudy or clear. A qualitative solar spectrum of scattered radiation at ground level in St.Andrews is given in chapter 3 as part of the work on the detector and the reduction of background interference.

A useful value for sky radiance at the filter peak transmission wavelength of 307 nm is estimated from the irradiance spectra of Knestrick and Curcio (1970)(5 $mWm^{-2}sr^{-1}nm^{-1}$), Kondratyev (Radiation in the Atmosphere, p.876, 1969)(1 $mWm^{-2}sr^{-1}nm^{-1}$) supported by other wavelength reference values of Byer and Garbuny (1973)(@ 400 nm) and Adrain et al (1979, Kondratyev-derived)(@ 300 nm). A maximum adopted value of 5 $mWm^{-2}sr^{-1}nm^{-1}$ is applied to the system with a filter of a certain bandwidth and a telescope of a certain field of view and mirror area to give the collected power which can be eventually expressed as an average cathode current. Generally, the cathode current arising from a sky radiance, F, is given by

$$i_{kb} = \mathcal{R}^2 T_F \eta e \lambda_F \pi A \theta^2 (\text{rads}) B_{f\lambda} (\text{nm}) F / 4hc, \qquad (9.3.1)$$

where T_F is the filter peak transmission at wavelength λ_F, η is the photomultiplier quantum efficiency, A is the area of the telescope mirror of reflectivity ρ, θ is the telescope planar full field of view and $B_{f\lambda}$ is the filter bandwidth. Equation (9.3.1), evaluated for the system, with parameters in table 9.3.1, gives a maximum background cathode current as

$$i_{kb\ max} = 6.3 \times 10^{-11} \text{ amps.} \qquad (9.3.2)$$

Background is avoided to a great extent by operating in a region of the spectrum where ground level solar radiation is at a minimum (chapter 3), a useful feature of the $XeCl^*$ excimer laser lidar. A narrow band filter reduces detected radiation to that at the region of interest. Further reduction is by using an adjustable iris to confine the field of view of the receiver to that of the laser field of divergence. The main feature of the detection system in this work is the use of a nearly solar blind photomultiplier, sensitive only to ultra-violet radiation (chapter 3). The d.c component of the background which does exist can be compensated for in the DIAL analysis. However, the randomly generated shot noise, calculated below, is more of a problem as the d.c. level increases.

9.3.2 Photomultiplier Dark Current

The EMI G26H314LF photomultiplier ,described in chapter 3, was selected for its very low photocathode dark current, or thermal emission of electrons. The maximum dark current is expressed in the EMI catalogue as an anode maximum of

$$i_{ad\ max} = 0.2 \text{ nA} \qquad (9.3.3)$$

which, assuming a gain of 10^6, gives a cathode maximum of

$$i_{kd\ max} = 2 \times 10^{-16}\ A. \qquad (9.3.4)$$

The anode dark current quoted for the particular tube used was 4×10^{-12} amps.

9.3.3 Overall Shot Noise and Bandwidth

Shot noise in the photon signal arises from the random arrival of quanta at the photocathode. It is analysed as "the statistical fluctuation in the emission rate of photo-electrons resulting from both signal and background radiation incident upon the detector" (Northend et al, 1966). The effect worsens if the sample, or integration, time, Δt_s, is reduced so that, during the interval Δt_s, any fluctuation in the rate of photon or electron arrival is more noticeable. System response characteristics are expressed as the measurement bandwidth, B, related to Δt_s according to the equation

$$B = 1/2\,\Delta t_s, \qquad (9.3.5)$$

(Monte Ross, Laser Receivers, 1966). A brief discussion of bandwidth is necessary before defining shot noise. Following from equation (9.3.5), a higher bandwidth system is desirable where fast time resolution is required. Thus, in lidar, the bandwidth defines the range resolution according to equation (8.7.1) where $\tau_s \equiv \Delta t_s$.

The measurement bandwidth of the system is limited to that of the component with the slowest response. This requires a definition and evaluation of component bandwidths. If the detector has a response time of Δt_r, then it has a bandwidth given by

$$B_d = 1/2\pi\ \Delta t_r \qquad (9.3.6)$$

(Monte Ross, Laser Receivers, 1966, p.30) and determined from the rise time specification. The photomultiplier output circuit response time is determined by the load resistance, R_L and the parallel load capacitance, C_L giving the output bandwidth as

$$B_{RC} = 1/2\pi R_L C_L. \qquad (9.3.7)$$

Any further signal handling equipment, be it a digital processor or simply an oscilloscope, possesses a bandwidth called B_p. The system bandwidth, B,given in equation (9.3.5), is given by the lowest of B_d, B_{RC} or B_p.

Shot noise is defined in a current, $\bar{i}$, averaged over a sample time Δt_s, by the rms. value given by (Rice, 1945; Grum and Becherer, Optical Radiation Measurement, vol.1, Radiometry, p.182, 1979)

$$(\bar{i}^2)^{1/2} = (2eiB)^{1/2}, \qquad (9.3.8)$$

due to Schottky in 1918 (Ott, Noise Reduction Techniques in Electronic Systems, p.208, 1976). Cathode shot noise has three components. That of the signal current, i_k, is accompanied by that of the background current, i_{kb}, and that of the cathode dark current, i_{kd}. The latter two currents are quantified for this excimer laser lidar system in (9.3.2) and (9.3.4). The cathode current shot noise is given by the root of the sum of the squares in

$$(\bar{i}_{ks}^{\,2})^{1/2} = (2ei_kB + 2ei_{kb}B + 2ei_{kd}B)^{1/2}. \qquad (9.3.9)$$

At the anode, the cathode shot noise has been increased by the overall gain of the photomultiplier. In addition, the statistical variation of the dynode secondary emission coefficients, δ_i, is taken into account. The major contribution to dynode noise is from the first stage, where any fluctuation is amplified by the greatest part of the multiplier chain. Contributions from later stages decrease towards the anode (EMI, Photoelectric Cells and Photomultipliers, 1961; RCA, Electro-Optics Handbook, 1974). The anode shot noise is given by

$$(\bar{i}_{as}^{\,2})^{1/2} = [(2G^2 ei_k B + 2G^2 ei_{kb} B + 2G^2 ei_{kd} B)(1+1/\delta_1+1/\delta_2 \cdots {}_n)]^{1/2}. \qquad (9.3.10)$$

The dynode shot noise factor can be approximated, assuming equal secondary emission coefficients, to give the useful anode shot noise expression

$$(\bar{i}_{as}^{\,2})^{1/2} = [(2G^2 ei_k B + 2G^2 ei_{kb} B + 2G^2 ei_{kd} B)(1/(1-1/\delta_1))]^{1/2}, \qquad (9.3.11)$$

where the secondary emission coefficient, δ_1, is given by that at the vital first stage in equation (3.1.1) expressed as

$$\delta_1 = A(V_1)^B, \qquad (9.3.12)$$

where the constants are defined for the EMI G26314LF tube ,in section 3.4, with the values $A = 0.098$ and $B = 0.737$. The voltage V_1, depends on the overall operating voltage V_o. An overall voltage of 1600V gives V_1 as 130V, allowing the secondary emission coefficient to be given by (9.3.12) as

$$\delta_1 = 3.5. \qquad (9.3.13)$$

The effect of shot noise is only reduced if the bandwidth is lowered, at the cost of temporal resolution, or if signal strengths are increased.

9.3.4 Thermal (Johnson) Noise

Thermal noise generated in the photomultiplier output load resistor is given as an effective anode noise component by the expression

$$(\bar{i}_{aR}^2)^{1/2} = (4kT_R B/R_L)^{1/2}. \qquad (9.3.14)$$

In estimating the level of this noise source a value for temperature is assumed at 293°K. A maximum value for thermal noise would be given by a load resistance of 50 Ω. Assuming a bandwidth which is limited by the output circuit constant, $R_L C_L$, then, by equation (9.3.7), for a load capacitance, C_L, of 335 pF (measured on the photomultiplier output cable to the signal processing unit), the maximum bandwidth is given as

$$B_{max} = 10^7 \text{ Hz}. \qquad (9.3.15)$$

This gives

$$(\bar{i}_{aR}^2)^{1/2}_{max} = 5.7 \times 10^{-8} \text{ A}. \qquad (9.3.16)$$

9.3.5 Total Anode Noise

Total noise at the anode is obtained from the combination of equations (9.3.11) and (9.3.14), which gives

$$(\bar{i}_{an}^2)^{1/2} = [(2G^2 ei_k B + 2G^2 ei_{kb} B + 2G^2 ei_{kd} B)(1/(1-1/\delta_1)) + 4kT_R B/R_L]^{1/2}. \qquad (9.3.17)$$

A maximum anode noise current would be given by the maximum component values, given in (9.3.2), (9.3.4), (9.3.14) and (9.3.16). Maximum bandwidth in the present system would be 10^7 Hz, according to (9.3.15). Equation (9.3.17), using δ_1 from (9.3.13), is evaluated to give

$$(\bar{i}_{an}^2)^{1/2}_{max} = [4.5i_k + 2.8 \times 10^{-10}]^{1/2}. \qquad (9.3.18)$$

From the evaluation in equation (9.3.18), it appears that the signal independent part of the noise problem in this maximum case is due primarily to background, with some slight contribution from multiplier chain noise. Even when a lower background radiance is considered, at a level of 1 $mWm^{-2}sr^{-1}nm^{-1}$ (Kondratyev, Radiation in the Atmosphere, 1969) instead of the adopted maximum at 5 $mWm^{-2}sr^{-1}nm^{-1}$ (Knestrick and Curcio, 1970), then the background induced noise is still a magnitude of roughly 100 times higher than the maxima likely to originate as thermal or as dark current shot noise (factor of 10^4 as equivalent currents). On these grounds the dark current and the thermal components are ignored and are discounted in further noise analysis. Thus the anode current noise expressed in equation (9.3.17) is approximated by

$$(\bar{i}_{an}^2)^{1/2} = G[2.8eB(i_k + i_{kb})]^{1/2}, \qquad (9.3.19)$$

where the secondary emission noise contribution has been calculated according to evaluation (9.3.11).

At this stage the consideration of dark current limitation has been removed, leaving background or signal shot noise as the possible limitation on system accuracy, expressed in the S/N ratio below.

9.3.6 Signal-to-Noise-Ratio (S/N)

The signal-to-noise ratio at the anode is the ratio of the anode current to the rms anode noise current given in general by equation (9.3.17). In particular, however, the S/N ratio in measuring the peak voltage response expressed as the peak cathode current is given by using equation (9.3.19) in

$$S/N \leqslant i_{k\ pk}/[2.8eB(i_{k\ pk} + i_{kb})]^{1/2}, \qquad (9.3.20)$$

where the inequality is introduced to realistically apply (9.3.20) to the S/N ratio of the peak voltage detected in the first stage sample-and-hold circuit of the lidar signal processor (chapter 6).

The bandwidths of the present system are given as

$$B_d = 7 \times 10^7 \ \text{Hz} \qquad (9.3.21)$$

for the EMI G26H314LF photomultiplier and

$$B_{RC\ max} = 10^7 \ \text{Hz}, \qquad (9.3.22)$$

given in (9.3.15) for a minimum load resistance of 50Ω and the measured anode capacitance of 335pF (including the co-axial cable). The limiting bandwidth for substitution into (9.3.20), because it is lower, is based on that of the RC output circuit, given by equation (9.3.7) as

$$B_{RC} = 1/2\pi R_L C_L. \qquad (9.3.23)$$

9.3.6(a) S/N Ratio in DIAL

Equations (9.3.20) and (9.3.23) are applied to plotting the maximum S/N ratio for load resistance (and bandwidth) variation in figure 9.3.1, at different peak cathode signal currents, $i_{k\,pk}$. The program listing for the calculation is in appendix A9.5.

An additional guide to the load resistance which should be used in a particular DIAL application is given by the corresponding range resolution scale in figure 9.3.1 where the sample time, τ_s is determined by the load resistance according to equation (9.3.7) and equation (9.3.5). The minimum detectable voltage profile is included in figure 9.3.1 as the lower limit of a voltage corresponding to the peak cathode current, shown as i_k (As the $R_L C_L$ constant increases the voltage developed across the load R_L is actually greater than that given by the simple Ohm's law relation; see chapter 3).

The value of the background level is also marked on figure 9.3.1 as a guide to the expected minimum signal levels.

9.3.7 Signal Averaging and Measurement Error

If the error in a single measurement, M, is ΔE and m measurements are taken and averaged, then the error in the sum of the measurements is given by the sum of the squares of the errors as

$$\Delta \sum_i M_i = (m \Delta E^2)^{1/2} \qquad (9.3.24)$$

with the result that the error in the average, $\bar{M}$, by dividing (9.3.24) by m, is given by

$$\Delta\bar{M} = \Delta E/m^{1/2}. \qquad (9.3.25)$$

Thus, signal averaging of m pulse measurements will reduce the error per average by a factor $m^{1/2}$.

The percentage error in a single measurement is obtained from the reciprocal of the signal-to-noise ratio in

$$\Delta E/M = 1/(S/N). \qquad (9.3.26)$$

The resulting error in m averages is linked to the single measurement signal-to-noise ratio by equations (9.3.25) and (9.3.26) in

$$\Delta\bar{M}/\bar{M} = 1/(S/N)m^{1/2}. \qquad (9.3.27)$$

The error expressed by the signal-to-noise ratio is effectively reduced by signal averaging. However, if a certain error $(\Delta\bar{M}/\bar{M})_{max}$ is the maximum allowed, then the tolerated single measurement S/N ratio can be reduced as more signals are averaged. In this case, (9.3.27) is specifically expressed as

$$(S/N)_{tol} = 100/(\Delta\bar{M}/\bar{M}\%)_{max} \cdot m^{1/2}. \qquad (9.3.28)$$

The measurement error of equation (9.3.26) is included in figure 9.3.1 as a percentage, showing the necessity for higher signal current and/or higher load resistance (lower bandwidth) if higher accuracy (lower error) is required. Equation (9.3.28) is applied in figure 9.3.1 to show the tolerated single pulse S/N ratio after averaged pulses if a final accuracy of 1% ($\Delta\bar{M}/\bar{M}\%$) is required.

Error reduction is shown in figure 9.3.2 which shows the reduction to the final error, $\Delta\bar{M}/\bar{M}\%$ in comparison with the single pulse error, $\Delta E/M\%$ after m averaged pulses (by equation (9.3.25)). It is reasonable to expect no more than about 400 averages in this DIAL system.

In the DIAL equation (9.1.10) and the error equations arising from (9.3.20), developed in the next section, signal averaging has an equivalent effect on system precision whether the averaging is carried out with single pulse measurements, pulse pair ratios, or with the concentration measurements themselves.

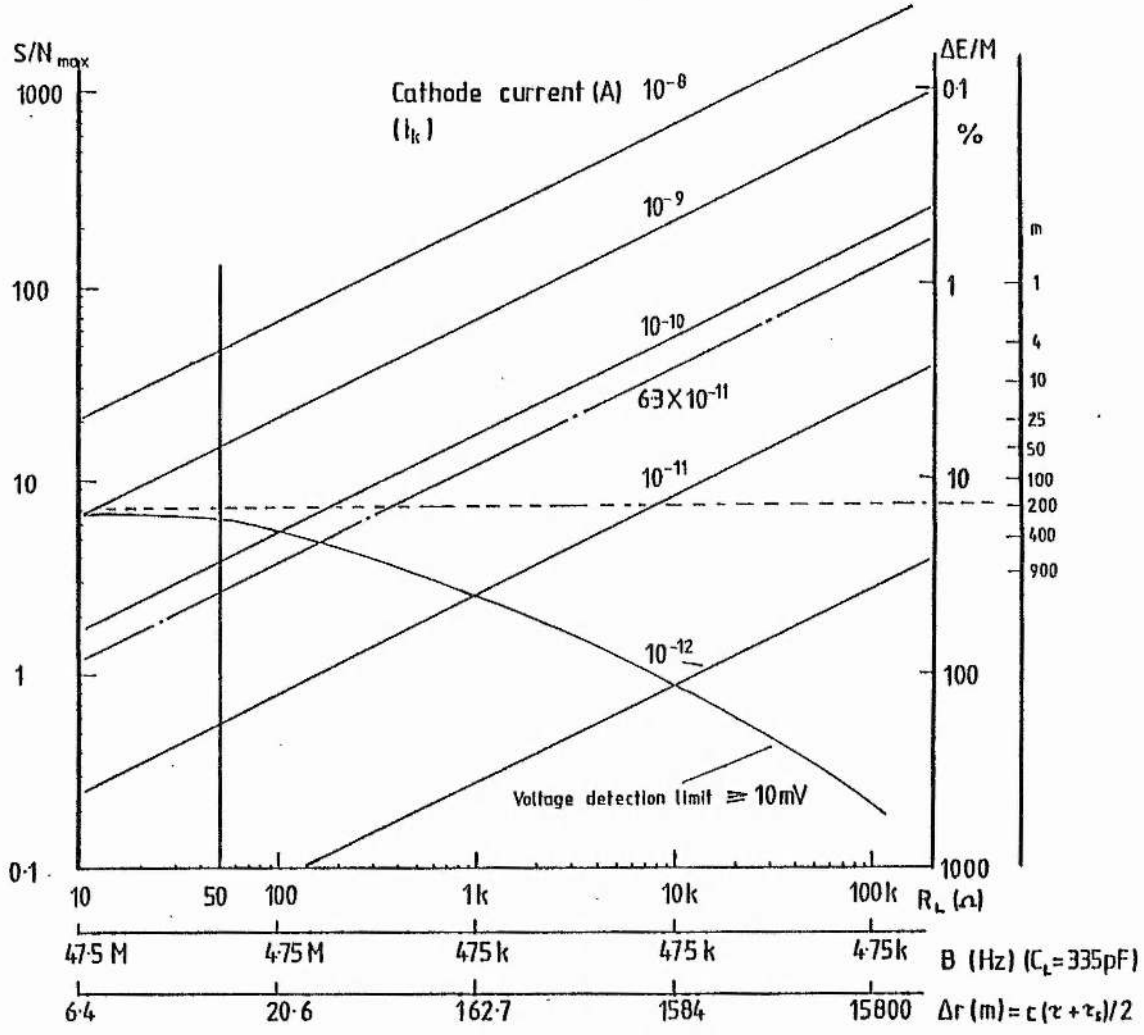

Figure 9.3.1 Signal to noise ratio and measurement error, $\Delta E/M$, of photomultiplier O/P signal with varying O/P load resistance, R_L, and different cathode current values, i_k. The load resistance defines measurement bandwidth in a particular case and hence lidar range resolution. The number of averaged pulses, m, on the right hand ordinate, is scaled to show the minimum tolerated ingle pulse S/N ratio if a final averaged accuracy of 1% is required.

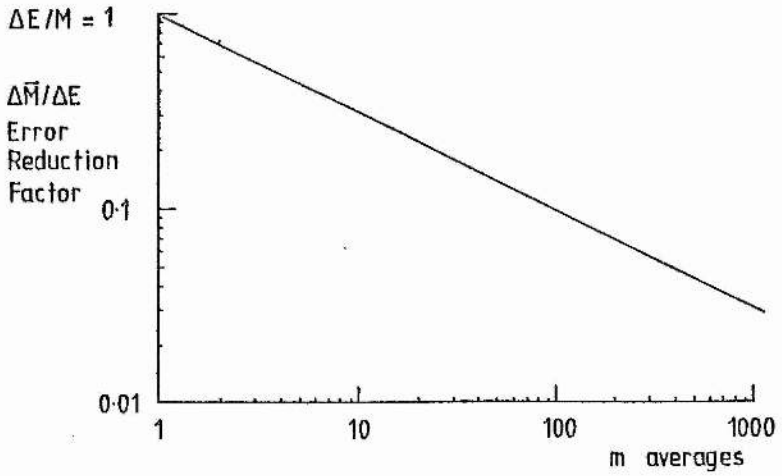

Figure 9.3.2 Error reduction by averaging m measurements

Table 9.3.1 Parameters in Determining Background Signal

Description	Symbol	Value
Narrow-band filter peak response	λ_F	307.1 nm
Narrow-band filter peak transmission	T_F	20%
Narrow-band filter bandwidth	B_f	10 nm
Telescope mirror reflectivity (primary and secondary)	$\mathcal{R}$	80%
Telescope mirror area	A	0.0507 m^2
Telescope full field of view	θ	10 mrads
Photomultiplier quantum efficiency	η	1%

9.4 Distinct Wavelength DIAL SO_2 Detection Limits

Figures 9.2.1 have already been introduced in section 9.2, relating the return signal ratios to the corresponding SO_2 concentration. The precision with which the concentration is evaluated depends upon the accuracy of single pulse measurements, defined by the measurement error $\Delta E(\%)$. This accuracy, applying to each of two pulses, is propagated through the algorithm in DIAL signal processing (equation (9.1.10)) to appear as an uncertainty in the value for SO_2 concentration, $\Delta\bar{N}'$. The link between $\Delta E(\%)$ and $\Delta\bar{N}'(\%)$ can be applied to define the necessary measurement error for a required precision in SO_2 concentration. Alternatively, in a prediction of the operational situation, the measurement error can be input to the form of the DIAL equation to estimate the accuracy of the result. The measurement error itself is the rms shot noise value which is determined by the signal level and the background.

A further error may arise from the variation in intensity from pulse to pulse. However, this can be countered by normalisation of each pulse by measuring laser output energy, in an on-line mode.

In this section the concentration error is related to the concentration being measured for the particular cathode signal current, given the specification for the DIAL model used earlier in the chapter, tabulated in table 9.2.1. A model is set up to evaluate the concentration error and the detection limits.

9.4.1 The Concentration Uncertainty Equations in Distinct Wavelength DIAL

The error is assumed to originate in determining the ratio, n'/n", of the measurements of signal returns. Equation (9.1.10) is

$$\bar{N}' = (C/\Delta r)(\ln[n'(r+\Delta r)/n''(r+\Delta r)] - \ln[n'(r)/n''(r)]), \qquad (9.4.1)$$

where C is the constant. The error arises in each ln term. The error arising in $\ln[n'(r)/n''(r)]$ is obtained by differentiation, leading to the percentage error

$$\Delta\ln[n'(r)/n''(r)]\% = \Delta(n'(r)/n''(r))\%/\ln[n'(r)/n''(r)]. \qquad (9.4.2)$$

Similarly, the percentage error in $\ln[n'(r+\Delta r)/n''(r+\Delta r)]$ is given by

$$\Delta\ln[n'(r+\Delta r)/n''(r+\Delta r)]\% = \Delta(n'(r+\Delta r)/n''(r+\Delta r))\%/\ln[n'(r+\Delta r)/n''(r+\Delta r)]. \qquad (9.4.3)$$

The measured concentration, $\bar{N}'$, in (9.4.1) carries an error, expressed by

$$\Delta\bar{N}'\% = (\Delta(n'/n'')\%^2 + \Delta(n'(r)/n''(r))\%^2)^{1/2}$$
$$\doteq (\ln[n'/n''] - \ln[n'(r)/n''(r)]) \qquad (9.4.4)$$

where $\Delta\bar{N}'$ is the average of the uncertainties about the value $\bar{N}'$, given as $\pm\Delta\bar{N}'$. The error in the ratios n'(r)/n"(r) and n'/n" (from r+Δr), occuring in (9.4.2) and (9.4.3), is given by the error in each measurement, according to the expressions

$$\Delta(n'(r)/n''(r))\% = 100[(\Delta n'(r)/n'(r))^2 + (\Delta n''(r)/n''(r))^2]^{1/2} \qquad (9.4.5)$$

and

$$\Delta(n'/n'')\% = 100[(\Delta n'/n')^2 + (\Delta n''/n'')^2]^{1/2}, \qquad (9.4.6)$$

respectively, where the quantities $\Delta n'(r)/n'(r)$, $\Delta n''(r)/n''(r)$, $\Delta n'/n'$ and $\Delta n''/n''$ are the inverse of the signal-to-noise ratio in measurements of the return signals.

A simplification is made with respect to equation (9.4.4) for the purpose of the model defining SO_2 detection limits. The error in the integrated path measurement, over the range r, is ignored. A justification applies in this case, where the integrated range measurements, providing the correction for any SO_2 present between the telescope and the range resolved sample, are obtained from a retro-reflector (eg. the chimney itself), giving high S/N ratio.

A further simplification is applied to the model in that the ambient SO_2 level itself, expressed as $\overline{N}_r'$ ppm over the intervening range, is assumed to be zero, so that equation (9.1.8) is applied for $\overline{N}_r' = 0$ and concentration units are converted by (A9.1.5) to give

$$\overline{N}' = (-T_r(^oK)/1.45X10^{19}(\alpha_1 - \alpha_2).P_r(mb)\Delta r).\ln[(n'/n'').(n_2/n_1)] \text{ ppm}. \qquad (9.4.7)$$

The lack of a considered integrated range burden will create an artificially low difference between n' and n'', causing the resulting % error to be at an upper limit. This, however, is partially or wholly offset by the artificial lowering of the error occuring by ignoring the integrated range measurement error. The inclusion of a long path SO_2 presence would

show a weaker signal over a certain range, which would have to be specified in a model. The signal strength, as cathode current i_{k1}, is accounted for anyway and the effect of its variation is shown in the results of the model in figure 9.4.1.

The error in $\bar{N}'$ is found by differentiation of (9.4.7), giving

$$d\bar{N}' = [d(n'/n'')/(n'/n'')][-T_r/1.45 \times 10^{19} \Delta r(\sigma_1 - \sigma_2) P_r(\text{mbar})] \qquad (9.4.8)$$

from which the errors are expressed as percentages to give

$$\Delta\bar{N}'\% = -\Delta(n'/n'')\%.T_r/1.45 \times 10^{19} \Delta r(\sigma_1-\sigma_2)P_r(\text{mbar})\bar{N}'. \qquad (9.4.9)$$

The uncertainty, $\Delta\bar{N}'$, is taken to be the average of the + uncertainties about $\bar{N}'$. In fact, the positive error, $+\Delta\bar{N}'$, increases in relation to the negative error, $-\Delta\bar{N}'$, significant above 25ppm. However, the average error contains the mean over the whole range of $\bar{N}'$.

The error in the ratio n'/n'' is given by the error in each measurement by the simple error expression

$$\Delta(n'/n'')\% = 100[(\Delta n'/n')^2 + (\Delta n''/n'')^2]^{1/2}, \qquad (9.4.10)$$

where the quantities $\Delta n'/n'$ and $\Delta n''/n''$ are the inverse of the signal-to-noise ratio in measurements of the photomultiplier anode voltage peak. Assuming signal shot noise limitation, the fractional error will be greater in the weakest signal which is, in this case, expressed as a return photon current n'. If the dominant noise is background induced, then the

errors will be the same in each signal n' and n". In general however, the signal-to-noise ratio given in (9.3.20) is introduced, using equation (9.3.27), as the error per pulse measurement but including error reduction by averaging of m single pulses to give each subsequent measurement error as

$$\Delta\bar{M}/\bar{M} \geqslant [2.8eB(i_{k\ pk} + i_{kb})]^{1/2}/m^{1/2}i_{k\ pk}. \qquad (9.4.11)$$

The peak cathode current in equation (9.4.11) is replaced by a term describing the return photon current (assuming peak measurement) according to the expression

$$i_{k1} = n'\eta\, e \qquad (9.4.12)$$

for wavelength λ_1, and a similar expression

$$i_{k2} = n''\eta\, e \qquad (9.4.13)$$

for wavelength λ_2. Equations (9.4.12) and (9.4.13) are used in equation (9.4.11) to replace the respective error of equation (9.4.10) so that it is expressed in terms of signal-to-noise ratio to give

$$\Delta(n'/n'')\% \geqslant [100(2.8eB)^{1/2}/\eta e n' m^{1/2}].[n'\eta e(1+n'/n'') + i_{kb}(1+(n'/n'')^2)]^{1/2}, \qquad (9.4.14)$$

where the weakest DIAL signal, n', is considered because it is the limiting signal. Equation (9.4.12) can be applied to re-introduce the corresponding cathode current so that (9.4.14) becomes

$$\Delta(n'/n'')\% \geq [100(2.8eB)^{1/2}/i_{k1}m^{1/2}].[i_{k1}(1+n'/n'') + i_{kb}(1+(n'/n'')^2)]^{1/2} \quad (9.4.15)$$

for 2m pulses, ie. m pulse pairs.

Equation (9.4.15) is applied in equation (9.4.9). The n'/n'' vs. $\bar{N}'$ relation is provided by equation (9.4.7). The effect of pulse averaging is equivalent at whatever stage of the signal processing it is applied, confirming a statement made in sub-section 9.3.7. The uncertainty equations are applied below.

9.4.2 Concentration Uncertainty Model in Distinct Wavelength DIAL

Equations (9.4.9), (9.4.15) and (9.4.7) are applied to DIAL error appraisal using the parameters given in table 9.2.1. The sample length, Δr, is taken to be the minimum resolveable range element of length $c\tau/2$. This definition of Δr is almost arbitrary since the ultimate sensitivity of the system is taken in units of ppm.m for evaluation of absolute sensitivity with any range resolution element.The particular form of equation (9.4.7) is

$$n'/n'' = 0.6915.\exp[-1.71 \times 10^{-3}\bar{N}'] \quad (9.4.16)$$

which defines n'/n'' within equation (9.4.15) which in turn defines $\Delta(n'/n'')\%$ within equation (9.4.9), expressed specifically as

$$\Delta\bar{N}'\% = -585.85\,\Delta(n'/n'')\%/\bar{N}'. \quad (9.4.17)$$

The bandwidth is defined for a worst case by setting its maximum by a

minimum load resistance, R_L, of 100Ω. The error $\Delta\bar{N}'\%$ is plotted over four ranges of concentration, $\bar{N}'$, at different cathode current values, in figure 9.4.1 for one pulse-pair and a range resolution of $c\tau/2 = 4.8m$. A cathode current variation represents the variation in signal strength over the scattering range. Signal averaging over m pulse-pairs reduces the effective error, $\Delta\bar{N}'$, by a factor $1/m^{1/2}$ as shown in figure 9.3.2. The program listing for the calculations to figure 9.4.1 is given in appendix A9.6. The error scale is extended to a full scale of 2000%. This would give a resultant error of 100% after averaging over a suggested maximum of 400 pulse-pairs.

9.4.2(a) Detection Limits

A detection limit is defined as the target concentration $\bar{N}_1'$ giving a resultant error, after averaging over m pulse-pairs, of $-\Delta\bar{N}'/m^{1/2}\% = 100\%$, applying to all the curves of figure 9.4.1. The scale at the right gives m, the number of pulse-pairs averaged, which reduces the original concentration error to -100%, following the effect of m in equation (9.4.15) applied to (9.4.17). The resulting detection limits are marked in brackets on each signal strength curve, giving useful results on the prediction of system sensitivity.

As would be expected, the % concentration error and detection limits are reduced as the signal level increases. However, the difference in the error between order of magnitude increments in cathode current, decreases towards stronger signals. This is due to the noise in the background, arising from atmospheric radiation having a more noticeable effect on weaker signals. This is noticeable where the detection limits are more closely grouped between cathode currents of 10^{-10}A to 10^{-8}A, the background level being set lower at 6.3×10^{-11}A. With this in mind, the region of interest of figure

9.4.1 is the area beneath the horizontal line corresponding to the considered number of pulse-pair averages, between the points of intersection on the curves for cathode currents of 10^{-10} and 10^{-8}A, giving the range of likely minimum measureable target concentrations with best range resolution. For example, if 25 pulse-pairs were averaged then the range of minimum measureable concentrations, depending on signal strength and for Δr = 4.8m, is from 2.2ppm to 28ppm. At worst, without signal averaging (m=1) then the range of minimum measureable concentrations in this case is from 11ppm to 120ppm.

The detection limits arising from figure 9.4.1 are plotted for signal level in figure 9.4.2, at different values of m, the number of pulse pairs averaged in noise reduction. The effect of averaging on the defined detection limits, seen in both figures 9.4.1 and 9.4.2, does not follow the $1/m^{1/2}$ proportionality unless higher signal levels are considered. The $1/m^{1/2}$ law does, however, apply to the reduction in the percentage error.

Figure 9.4.2 shows the detection limits for the minimum range resolution of $\Delta r = c\tau/2$ at 4.8m. It is more useful to express the detection limit as the product $\bar{N}_1' . \Delta r$ in units of ppm.m, for application to any spatial sample length, determined by bandwidth (hence sample time) according to equation (8.7.1). Figure 9.4.3 is derived from figure 9.4.2, replacing the ppm scale by one of ppm.m.

The detection limit and overall concentration accuracy is improved with more pulse-pairs averaged and with stronger signals, as would be obtained at shorter lidar ranges. The evaluation given here is a worst case as regards shot noise since the highest bandwidth has been used in equation (9.4.15). The detection limits obtained in practice, assuming no other

interference, may be improved by a factor of two to four times if lower bandwidth is employed at the expense of range resolution. Integration over greater range improves the detection limit though range is restricted by the $1/r^2$ relation and signal strength. The signal strength affects, directly, the signal-to-noise ratio.

9.4.3 Pulse Normalization

The previous error analysis has assumed no error source from pulse to pulse energy variation. In the simplified equation (9.4.7), used as an algorithm in converting the ratio n'/n'' to an SO_2 concentration, the value of the $XeCl^*$ laser dual wavelength intensity ratio is n_1/n_2, defined for the model used in this theoretical study. In a working system using a single pulse-pair algorithm (integrated path DIAL), however, the individual values of n_1 and n_2 may vary up to 10% (chapter 4), with a subsequent error in n_1/n_2 and eventually in the SO_2 concentration $\bar{N}'$. If the ratio can be determined per pulse-pair by measuring a sample per pulse from the back end of the laser cavity then n_1/n_2 serves as a normalization to correct for pulse-to-pulse variation. However, it would still be possible that the error in measuring n_1 and n_2 as well as n' and n'' would affect the overall accuracy.

In providing an expression for concentration uncertainty, equation (9.4.7) is differentiated with respect to n'/n''. Now the equation is differentiated with respect to $(n'.n_2/n''.n_1)$ to give

$$\Delta\bar{N}'\% = -\Delta(n'.n_2/n''.n_1)\%.T_r/1.45 \times 10^{19}\,\Delta r(\sigma_1-\sigma_2).P_r(\text{mbar})\bar{N}', \quad (9.4.18)$$

which is equivalent to equation (9.4.9). The error in the measurements is given per pulse-pair by

$$\Delta(n'.n_2/n''.n_1)\% = 100[(\Delta n'/n')^2 + (\Delta n''/n'')^2 + (\Delta n_1/n_1)^2 + (\Delta n_2/n_2)^2]^{1/2} \quad (9.4.19)$$

as distinct from equation (9.4.10). If no normalisation were carried out, then the errors $\Delta n_1/n_1$ and $\Delta n_2/n_2$ would represent the pulse-to-pulse variation, given in table 4.9.4, for the $XeCl^*$ laser, providing a significant source for uncertainty. The pulse return measurement errors are still given by the S/N ratio in equation (9.4.19) and subsequent application in equation (9.4.18).

When a normalizing procedure is undertaken, then two situations may arise. The measurements of n_1 and n_2 are made with a solid state detector on relatively strong optical pulses. Thus, in considering photodiode shot noise (p.160 RCA Electro-Optics Handbook) it would be expected that errors $\Delta n_1/n_1$ and $\Delta n_2/n_2$ are negligible in comparison to the shot noise errors in measuring the return signals, allowing, in the simplest case, an assumed reduction of (9.4.19) and (9.4.18) to the form of (9.4.10) and (9.4.9), respectively. In a second case the errors $\Delta n_1/n_1$ and $\Delta n_2/n_2$ would be derived from the measurement error arising from a source other than shot noise which may or may not be significant in comparison with $\Delta n'/n'$ and $\Delta n''/n''$. This latter point would be considered in the event of normalization signal noise problems.

In the range resolved DIAL situation, the effect of n_1/n_2 is removed from the DIAL algorithm (9.1.10). For the purpose of this work, the analytical predictions of sub-section 9.4.1 and equations used in the model are applied to error appraisal in the real situation, assuming no effect from pulse-to-pulse variation.

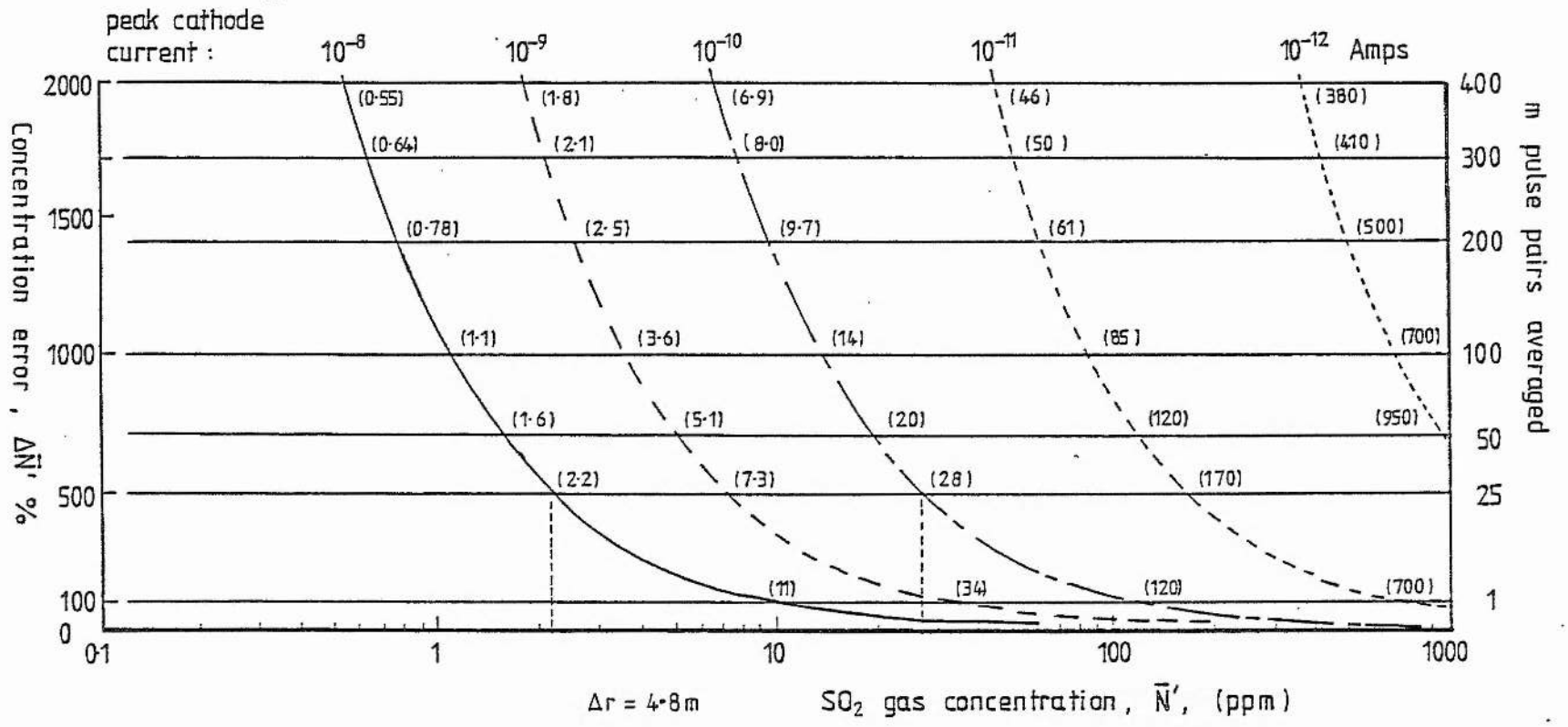

Figure9.4.1 Distinct wavelength $XeCl^*$ excimer laser DIAL:
Concentration error curves over four concentration ranges at different cathode peak current levels, covering the likely range of return signal intensities. Detection limits (bracketed) for different numbers of averaged pulse pairs, based on $\bar{N}'$ at $\Delta\bar{N}'/\sqrt{m} = 100\%$

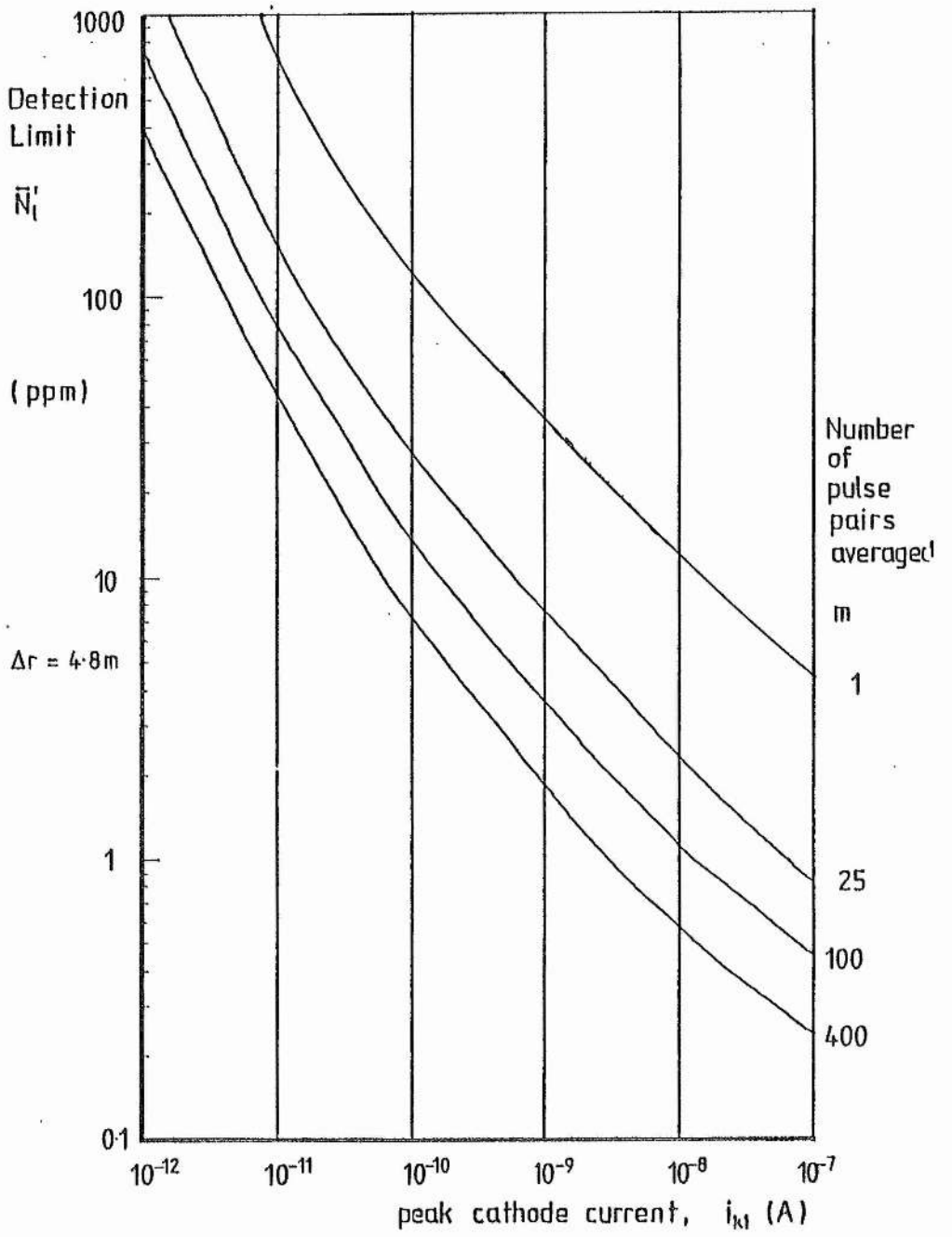

Figure 9.4.2 Detection limits defined by a resulting concentration error of 100%

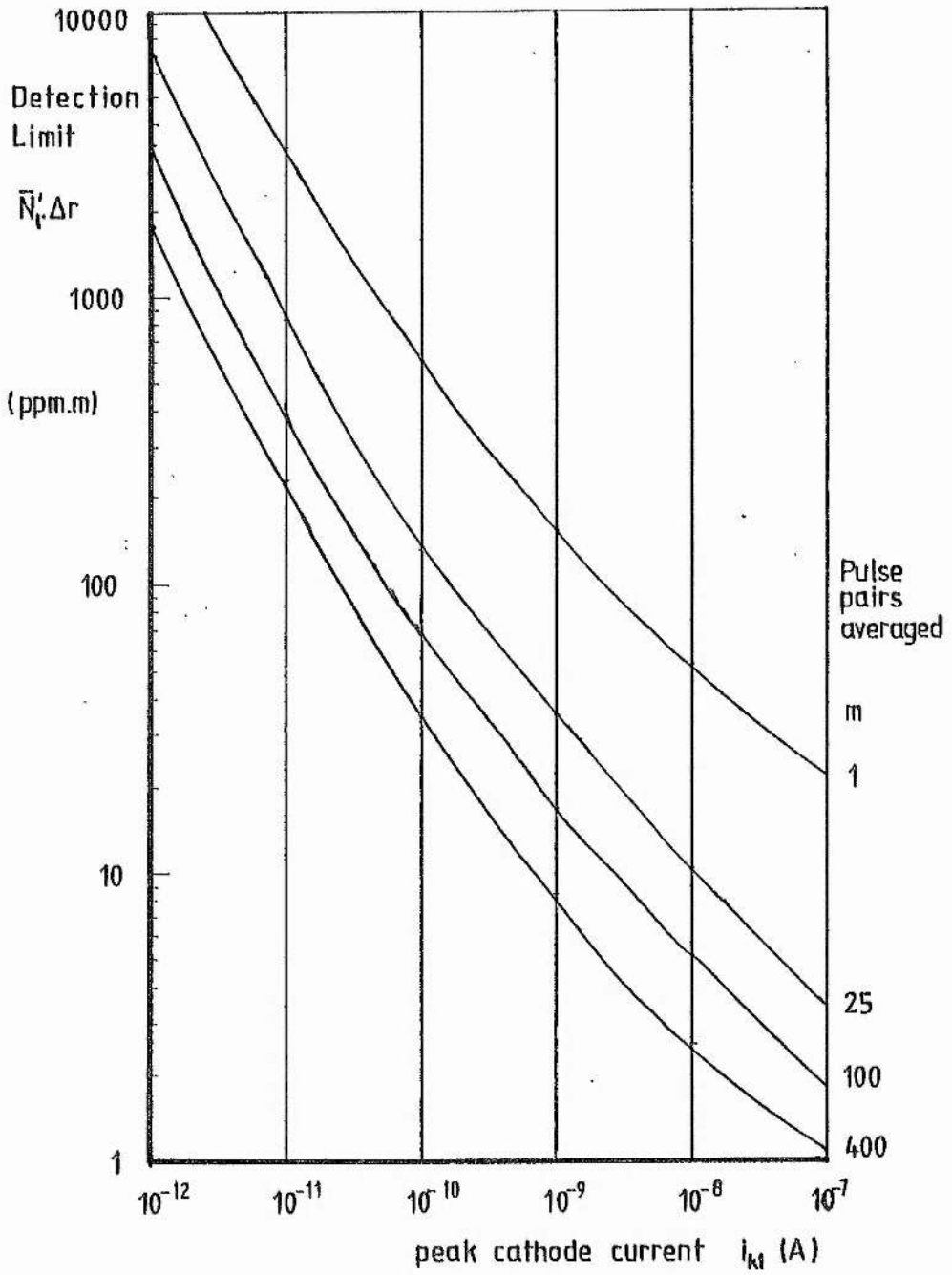

Figure 9.4.3 Detection limit/range element product defined by a resulting concentration error of 100%

9.5 Dual Pulse, Mixed Wavelength DIAL Theory

Section 9.1 outlines the DIAL equation for two return pulses, each of a single wavelength radiation. This is achieved in practice if the laser is tunable between two wavelengths, as in a dye laser or by using fine tuning apparatus on a multi line source. The $XeCl^*$ excimer laser source in the present system exhibits a dual wavelength lasing spectrum around 308.2 nm and 307.9 nm (see figure 4.9.4). A distinct, single wavelength, output requires selection of one or other of the lines. The options for a selection method have been discussed in chapter 5. A robust and relatively easy method of creating two pulses with different wavelength content was sought. The solution was (section 5.5) to place, within the laser optical cavity, a cell of gas which has different absorption cross-section between the wavelengths. The cell is inserted for one of the DIAL pulses, giving a dual wavelength output with relative intensities altered. The cell is removed for the second DIAL pulse, allowing emission of an unmodified $XeCl^*$ output. An immediate choice for the absorbing gas was low pressure SO_2 since its spectrum is known in sufficient detail as the target pollutant species.

The return photon current distribution is expressed for each of the two mixed wavelength DIAL pulses, the first being for the cell- modified laser output, described in section 5.5, the second being the signal obtained after transmission of a "raw" $XeCl^*$ spectrum.

Each wavelength component of the modified pulse is altered according to the spectral absorption coefficients a and b, given by equations (5.5.5) and (5.5.6), respectively. Lidar equation (8.2.10) with (8.2.7) is applied with equations (5.5.5) and (5.5.6) for the respective wavelength to give the

combined return photon current as

$$n'(r) = (an_1.\exp[-2\int_0^r \sigma_1 N(r)dr] + bn_2.\exp[-2\int_0^r \sigma_2 N(r)dr])$$
$$X \quad (\beta' cAt_T t_R/8\pi r^2).\exp[-2\int_0^r (\alpha_M(r) + \alpha_R(r))dr]. \qquad (9.5.1)$$

The unmodified pulse is a straight transmission of the dual wavelength spectrum (a=1, b=1) leading to a return photon current given as

$$n''(r) = (n_1.\exp[-2\int_0^r \sigma_1 N(r)dr] + n_2.\exp[-2\int_0^r \sigma_2 N(r)dr])$$
$$X \quad (\beta' cAt_T t_R/8\pi r^2).\exp[-2\int_0^r (\alpha_M(r) + \alpha_R(r))dr]. \qquad (9.5.2)$$

Both equations, (9.5.1) and (9.5.2), are considered under the assumption that the wavelength components have identical function shapes.

As for the distinct wavelength case, described in section 9.1, the range resolveable result is obtained by measuring the dual wavelength pulse ratio from range r and that from range $r+\Delta r$, considering the average SO_2 concentration, $\bar{N}_r$, over the range r and the target gas concentration, $\bar{N}$, within the range element Δr. The absorption attenuation term over the integrated range r is approximated for wavelengths λ_1 and λ_2 by equations (9.1.3) and (9.1.5), respectively, used in (9.5.1) and (9.5.2) to give

$$n'/n''(r) = (an_1\exp[-2\sigma_1\bar{N}_r r] + bn_2\exp[-2\sigma_2\bar{N}_r r])$$
$$\div \quad (n_1\exp[-2\sigma_1\bar{N}_r r] + n_2\exp[-2\sigma_2\bar{N}_r r]). \qquad (9.5.3)$$

Similarly for the integrated range $r+\Delta r$ the equations (9.1.4) and (9.1.5) are used with (9.5.1) and (9.5.2) to give

$$n'/n''(r+\Delta r) = (an_1\exp[-2\sigma_1\bar{N}_r r - 2\sigma_1\bar{N}\Delta r] + bn_2\exp[-2\sigma_2\bar{N}_r r - 2\sigma_2\bar{N}\Delta r]) \div (n_1\exp[-2\sigma_1\bar{N}_r r - 2\sigma_1\bar{N}\Delta r] + n_2\exp[-2\sigma_2\bar{N}_r r - 2\sigma_2\bar{N}\Delta r]). \quad (9.5.4)$$

Equation (9.5.3) is solved for concentration to give

$$\ln[(n_2/n_1)(b - n'(r)/n''(r))/(n'(r)/n''(r) - a)] = -2\bar{N}_r r(\sigma_1 - \sigma_2). \quad (9.5.5)$$

Likewise, (9.5.4) gives

$$\ln[(n_2/n_1)(b-n'(r+\Delta r)/n''(r+\Delta r))/(n'(r+\Delta r)/n''(r+\Delta r)-a)] = -2(\bar{N}_r r+\bar{N}\Delta r)(\sigma_1-\sigma_2) \quad (9.5.6)$$

The logarithmic difference is taken to allow solution of the expression for target concentration, over the element Δr, giving

$$\bar{N} = (-1/2\,\Delta r(\sigma_1 - \sigma_2)) \times (\ln[(b-n'/n'')/(n'/n''-a)] - \ln[(b-n'(r)/n''(r))/(n'(r)/n''(r)-a)])\ m^{-3}, \quad (9.5.7)$$

where $n'(r+\Delta r)/n''(r+\Delta r)$ is expressed, simply, as n'/n'' and the ratio n_1/n_2 is eliminated.

The concentration is more suitably given as ppm according to the conversion equation (A9.1.5) so that (9.5.7) becomes

$$\bar{N}' = (-T_r(^oK)/1.45 \times 10^{19} \Delta r(\sigma_1 - \sigma_2).P_r(mb)) \times (\ln[(b-n'/n'')/(n'/n''-a)] - \ln[(b-n'(r)/n''(r))/(n'(r)/n''(r)-a)]) \text{ ppm.} \quad (9.5.8)$$

This has its equivalent distinct wavelength expression in (9.1.10) and the measurement concentration is subject to the same effects of temperature and pressure variation as are described in sub-section 9.1.1. Equation (9.5.8) can be corrected for pressure variation with height by application of equation (9.1.11).

9.6 Theoretical Return Signal Ratios in Mixed Wavelength DIAL

Equation (9.5.4) and the concentration units conversion of (A9.1.5) are used in a model situation to relate the return signal ratio from a range $r+\Delta r$ to the corresponding average SO_2 concentration contained within Δr, assuming a zero ambient SO_2 level, setting $\bar{N}_r = 0$ (ppm). The equivalent distinct wavelength model is given in section 9.2 though an ambient SO_2 level was considered in that case. The minimum resolveable range element, adopted for Δr, is given by the laser spatial pulse width $c\tau/2$. Table 9.2.1 gives the parameters required for insertion into the model equation. The coefficients a and b, given by equations (5.5.5) and (5.5.6) are expressed as a function of cell pressure, allowing plots to be made, in figure 9.6.1, of return ratios as a function of concentrations for different cell pressures. The plot of figure 9.6.1, distinct from that of figure 9.2.1, is over only the range 0 to 1000 ppm to show the variation in ratio n'/n" for a greater range of cell pressures. The micro-computer program listing for the calculations is in appendix A9.4.

An immediately obvious difference between the mixed and distinct wavelength DIAL methods, as presented, is that the return signal ratios decrease in distinct wavelength DIAL but increase in the mixed wavelength case. This is due to the definition of the mixed wavelength DIAL output and return photon signals.

More significantly, in comparing figure 9.6.1 with figure 9.2.1(d), the potential accuracy of the mixed wavelength method appears to be worse than that of distinct wavelength DIAL as indicated by the relatively low range of mixed wavelength n'/n" values obtained over the concentration range 0 to 1000 ppm. Errors in concentration determination arise from single pulse

measurement errors which dictate the uncertainty in the ratio n'/n". Assuming constant single pulse measurement errors, then the subsequent constant uncertainty in n'/n leads to greater concentration error if the range of n'/n" values is low for a given ppm range. Figure 9.6.1 indicates, by the difference in gradients, that a greater absorption cell pressure gives a greater range of n'/n" values, and therefore, for a certain error in n'/n", a better accuracy. The effect of cell pressure on system accuracy is given in the analysis of mixed wavelength DIAL detection limits below.

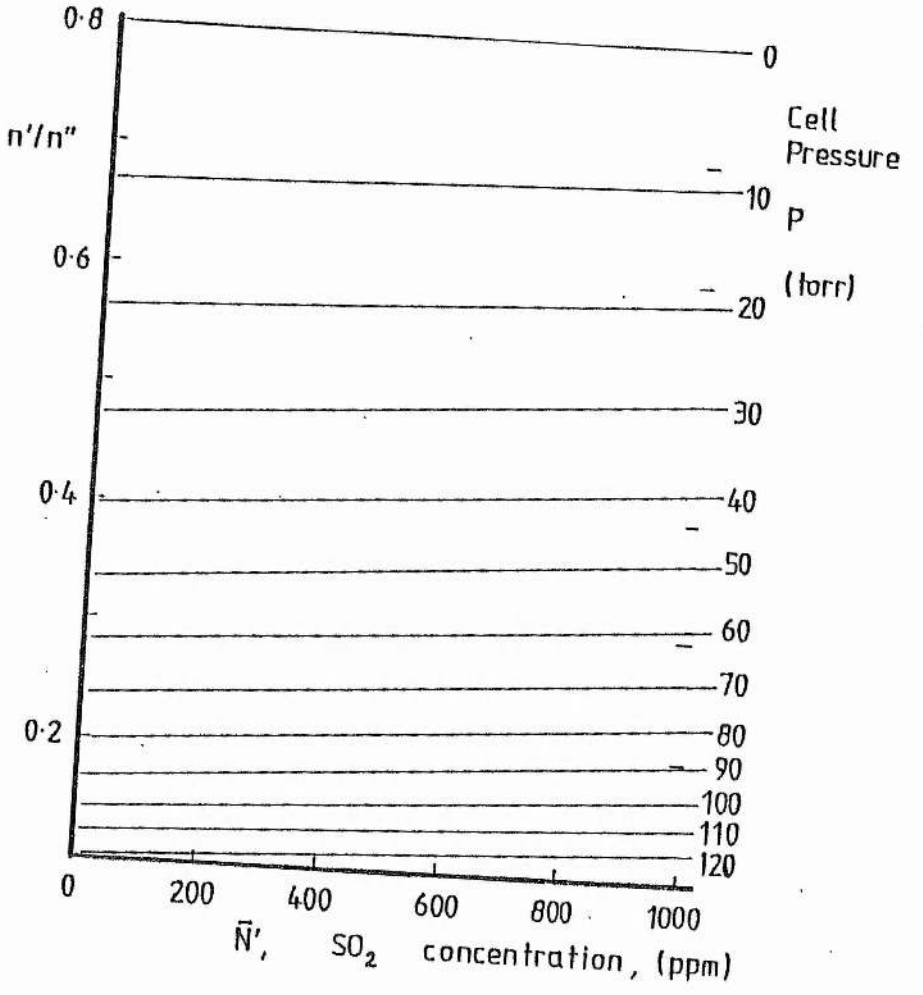

Figure 9.6.1 Mixed wavelength DIAL theory: Signal return ratio, n'/n'' vs. SO_2 concentration, $\bar{N}'$ (ppm)

9.7 Mixed Wavelength DIAL SO_2 Detection Limits

Section 9.6 relates the return signal ratios to the corresponding SO_2 concentration and indicates a lower accuracy in measuring target SO_2 concentration than the distinct wavelength DIAL method, assuming an equivalent single pulse measurement accuracy. A further complication is added by the variability of absorption cell pressure which must not be so high as to weaken, unduly, the output pulse but which must be high enough to provide a large dual wavelength intensity differential, greater ratio range, for adequate DIAL accuracy. This section predicts mixed wavelength DIAL accuracy as a function of the variables of target concentration, absorption cell pressure and photomultiplier peak cathode current, where the latter represents the return signal level.

9.7.1 The Concentration Uncertainty in Mixed Wavelength DIAL

The analysis given in this sub-section for the mixed wavelength DIAL is similar to that for the distinct wavelength case, given in section 9.4, in that the error in the target concentration is derived from the error in the return pulse ratio measurement, using a differentiation of the DIAL equation. Equation (9.5.8) is the expression for the range resolved concentration measurement. However, as for the distinct wavelength model, the sensitivity is evaluated by this particular method via the same simplification described in section 9.4. Equation (9.5.6) is applied for zero ambient SO_2 level, $\bar{N}_r = 0$, and the concentration units are converted to ppm by equation (A9.1.5) to give

$$\bar{N}' = (-T_r(^oK)/1.45 \times 10^{19}(\sigma_1-\sigma_2).P_r(mb)\,\Delta r).\ln[(n_2/n_1)(b-n'/n'')/(n'/n''-a)]$$

ppm. (9.7.1)

Equation (9.7.1) is differentiated with respect to the return signal ratio n'/n'' to give

$$d\bar{N}' = d(n'/n'')[T_r/1.45 \times 10^{19}\Delta r(\sigma_1 - \sigma_2)P_r(\text{mbar})](b-a)/(n'/n''-a)(b-n'/n''), \quad (9.7.2)$$

which is expressed as the percentage errors $\Delta\bar{N}'$ and $\Delta(n'/n'')$ in

$$\Delta\bar{N}'\% = \Delta(n'/n'')\%[T_r/1.45 \times 10^{19}\Delta r(\sigma_1-\sigma_2)P_r(\text{mbar})](n'/n'')(b-a) \div (n'/n''-a)(b-n'/n'')\bar{N}', \quad (9.7.3)$$

where $\Delta\bar{N}'\%$ is the average of the uncertainties about $\bar{N}'$. The measurement errors have already been defined in section 9.3 and applied in section 9.4 in equation (9.4.15). The signal ratio n'/n'' in equations (9.4.15) and (9.7.3) is given by equation (9.5.4) (including equation (A9.1.5)). The absorption cell coefficients a and b are given as a function of pressure in equations (5.5.5) and (5.5.6), respectively.

The equations are applied below, in a model for estimating the precision of this mixed wavelength SO_2 DIAL under different conditions of signal strength, cell pressure and signal averaging.

9.7.2 Concentration Uncertainty Model in Mixed Wavelength DIAL

The parameters applied in the model situation are given in table 9.2.1. The range element Δr is given by the spatial pulse width, $c\tau/2$. Equation (9.7.3) becomes

$$\Delta\bar{N}'\% = (585.85\ \Delta(n'/n'')\%/N')(n'/n'')(b-a)/(n'/n''-a)(b-n'/n''), \quad (9.7.4)$$

where the measurement error is given by (9.4.15) as

$$\triangle(n'/n'')\% \geq [100(2.8eB)^{1/2}/i_{k1}m^{1/2}][i_{k1}(1+n'/n'') + i_{kb}(1+(n'/n'')^2)]^{1/2} \qquad (9.7.5)$$

for a maximum bandwidth of B = 4.75 MHz, given by equation (9.3.7), with load parameters of R_L = 100Ω and C_L = 335 pF. The background, represented as i_{kb}, is set at the maximum given by equation (9.3.2) as 6.3 X 10^{-11}A. The signal ratio in (9.7.4) is given by a target concentration in equations (9.5.4) and (A9.1.5) which are combined to give

$$n'/n'' = (0.6915a.\exp[-0.00522\bar{N}'] + b.\exp[-0.00351\bar{N}']) \div (0.6915.\exp[-0.00522\bar{N}'] + \exp[-0.00351\bar{N}']). \qquad (9.7.6)$$

The cell coefficients a and b in these equations are given by equations (5.5.5) and (5.5.6) and modelled in terms of cell pressure as

$$a = 0.8 \exp[-0.02215\ P(torr)], \qquad (9.7.7)$$

$$b = 0.8 \exp[-0.01490\ P(torr)]. \qquad (9.7.8)$$

Equations (9.7.4) to (9.7.8) are applied by using a model program, outlined in appendix A9.7. The relation between variables $\Delta\bar{N}'\%$, $\bar{N}'$, i_{k1} and P are illustrated in figures 9.7.1 and 9.7.2. Figure 9.7.1 shows the variation in concentration error with cell pressure at certain target concentrations and signal levels, given by the cathode peak current. An addition to the

pressure scale is the corresponding total pulse energy reduction as a percentage of the output pulse intensity, calculated with respect to an unmodified pulse as the ratio given by

$$(an_1 + bn_2)/(n_1 + n_2). \qquad (9.7.9)$$

9.7.2(a) Absorption Cell Pressure

Figure 9.7.1 provides the upper and lower limits on the likely range of chosen absorption cell pressure. The dual wavelength pulse energy differential is increased as cell pressure is increased, giving greater accuracy (lower $\Delta\tilde{N}'\%$) in measuring SO_2 concentration. A lower limit on pressure is set by the accuracy requirement. An absolute pressure minimum, allowing strong signal measurements down to 100 ppm, with averaging over less than 25 pulse-pairs, would be 20 torr. More realistically, however, a minimum should be set at 40 torr to allow weaker signals to be utilised at low pulse-pair averaging and to permit analysis of strong signals, down to a burden of 10 ppm, with about 200 averaged pulse-pairs. The upper limit is set by the cell's absorption attenuation of the laser pulse energy, reducing maximum lidar range and/or the strength of the received signals. Figure 9.7.1 indicates a reduction in pulse output to about 15% of an unaltered pulse if 100 torr is used in the cell. This would represent a reduction in range, at the signal detection limit (power), by a factor of about 2.5 times, according to the $1/r^2$ law appearing in the lidar equation. For signals from a constant range, a reduction of 15% would be translated directly to an equivalent reduction in return signal level, suggesting the 100 torr limit. Thus the cell pressure is constrained, in practice, according to the limits

$$40 \text{ torr} < P < 100 \text{ torr}. \qquad (9.7.10)$$

9.7.2(b) Detection Limits

The cell pressure limits of (9.7.10), in defining the permitted pressure range, allow the concentration uncertainty to be plotted for concentration in figure 9.7.2, at cell pressures of 100 torr and 40 torr, respectively, and at different cathode currents, by following a similar procedure to that of figure 9.4.1 for the distinct wavelength case. The averaging of m pulse pairs is applied to show the detection limits (bracketed) in reducing the resulting concentration error to $\Delta\bar{N}' = 100\%$, according to the definition of detection limit given in sub-section 9.4.2(a).

In figure 9.7.2, just as for the distinct wavelength case, the background noise (from background level of $i_{kb} = 6.3 \times 10^{-11}$A) is significant in that the difference in the detection limits, between orders of magnitude increase in cathode current, decreases towards higher signal level, leaving the greatest difference between 10^{-10}A and 10^{-11}A. The region of interest therefore, if defined by likely signal levels, is bound by the 10^{-10}A and 10^{-8}A (or greater, if possible) curves, though these are smeared by the possible range of absorption cell pressure. Minimum measureable target concentration, in the modelled case, if optimised by a cell pressure of 100 torr, is, for example, from 11.5 ppm to 160 ppm when 25 pulse pairs are averaged. With no averaging, the range of values is undefined at the higher limit unless signal strengths give cathode currents better than about 5×10^{-9}A when the limit is still as high as several hundred ppm. In this case the best value for detection limit with the strongest signals (around 10^{-8} A) is likely to be around 60 ppm, whilst preserving best range resolution of 4.8m.

The detection limits arising from figure 9.7.2 are plotted in figure 9.7.3

to show their variation with signal level at different values of m averaged pulse-pairs and for the upper and lower limits of cell pressure (by (9.7.10)).

Figure 9.7.3 shows the detection limits if a minimum range element of 4.8m is applied. Figure 9.7.4 is a more useful expression of system sensitivity, giving it in units of ppm.m, allowing any range resolution element or long range, total path integration to be considered. This is more optimistic in that it shows how lower levels of SO_2 can be measured as an average over a suitably long sample length.

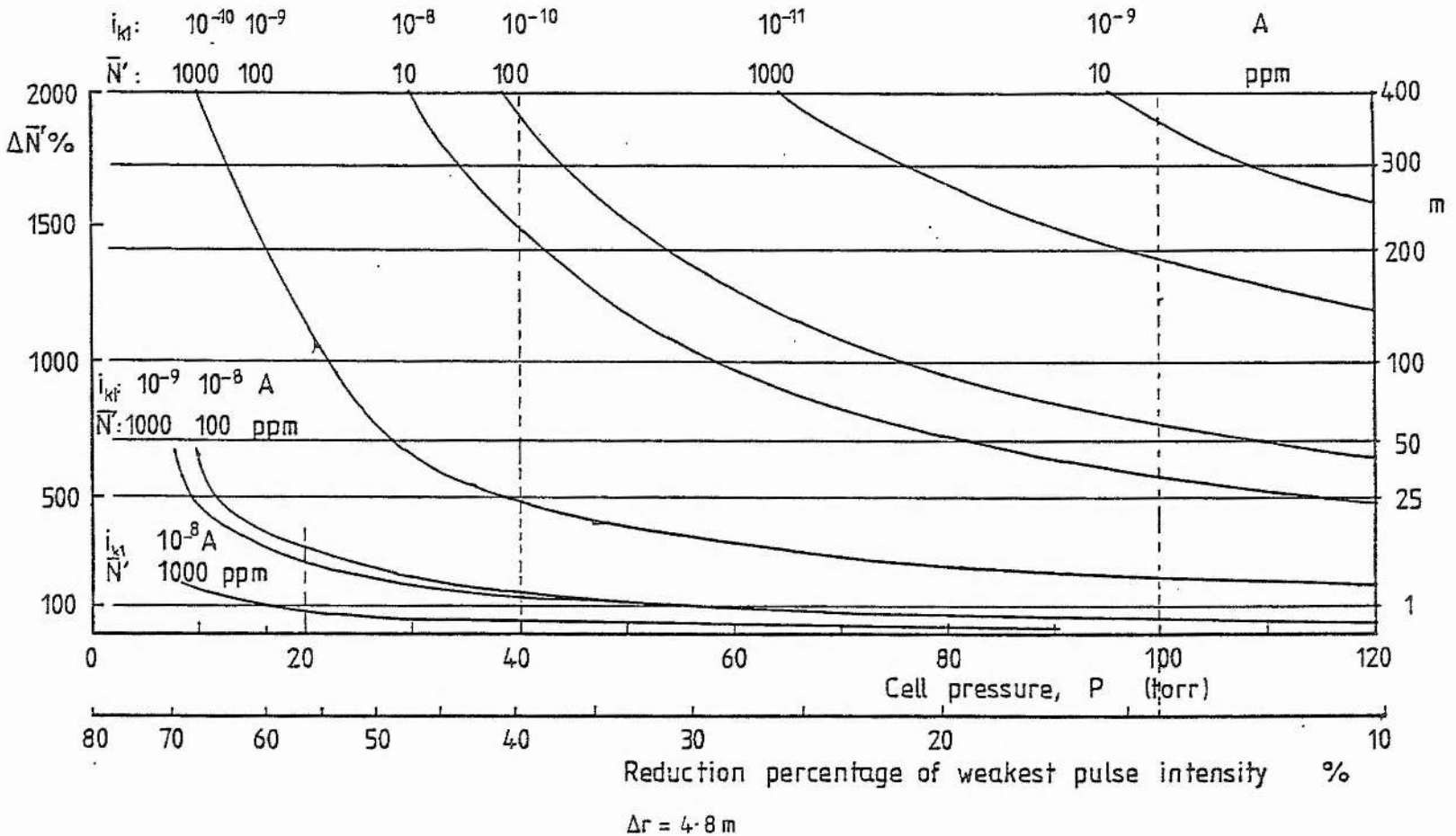

Figure9.7.1 Mixed wavelength $XeCl^*$ excimer laser DIAL: Concentration error curves over the range of absorption cell pressures, at certain target SO_2 concentrations and signal levels

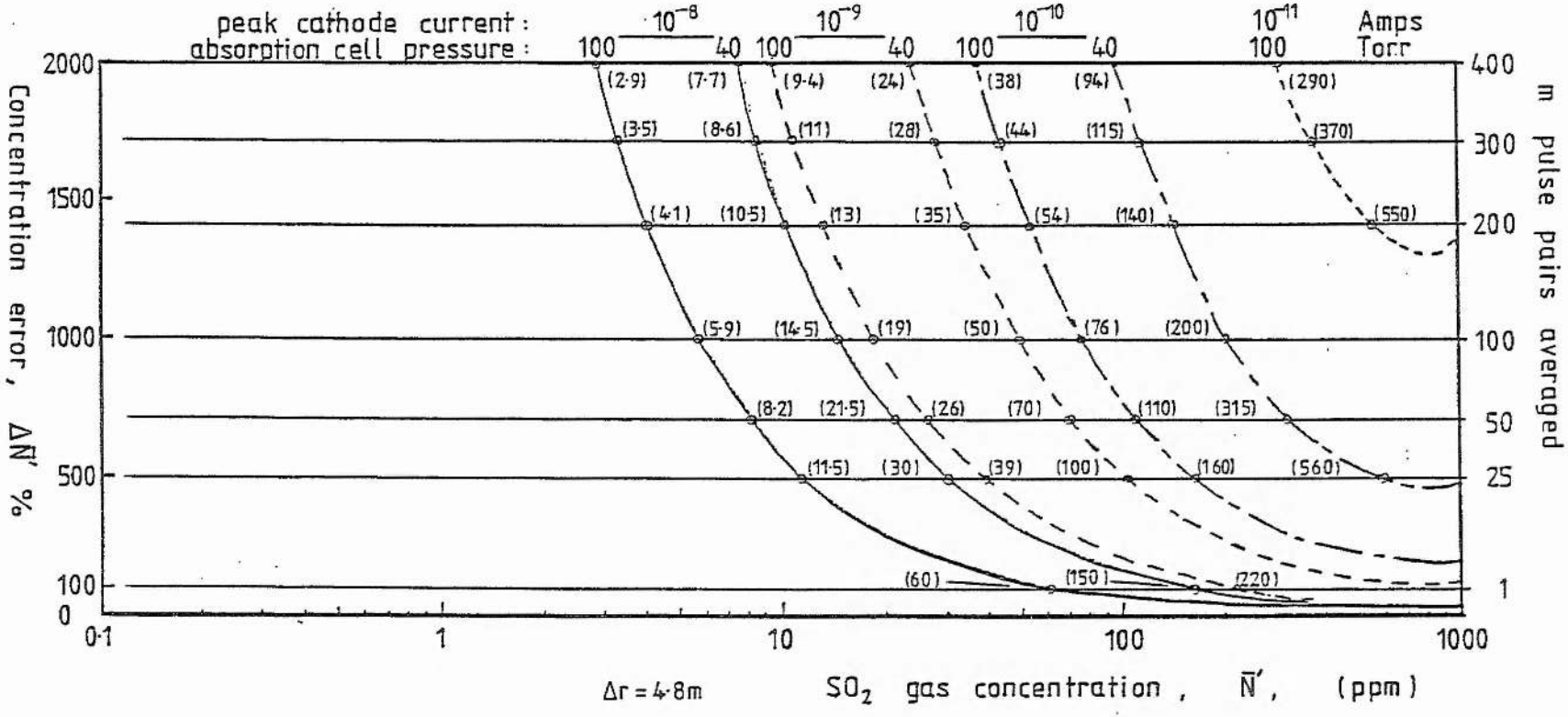

Figure 9.7.2 Mixed wavelength XeCl* excimer laser DIAL: Concentration error curves over four concentration ranges at different cathode peak current levels and absorption cell pressures at each extreme of the likely range. Detection limits (bracketed) for different number of pulse pair averages, based on $\bar{N}'$ at $\Delta\bar{N}'/\sqrt{m} = 100\%$

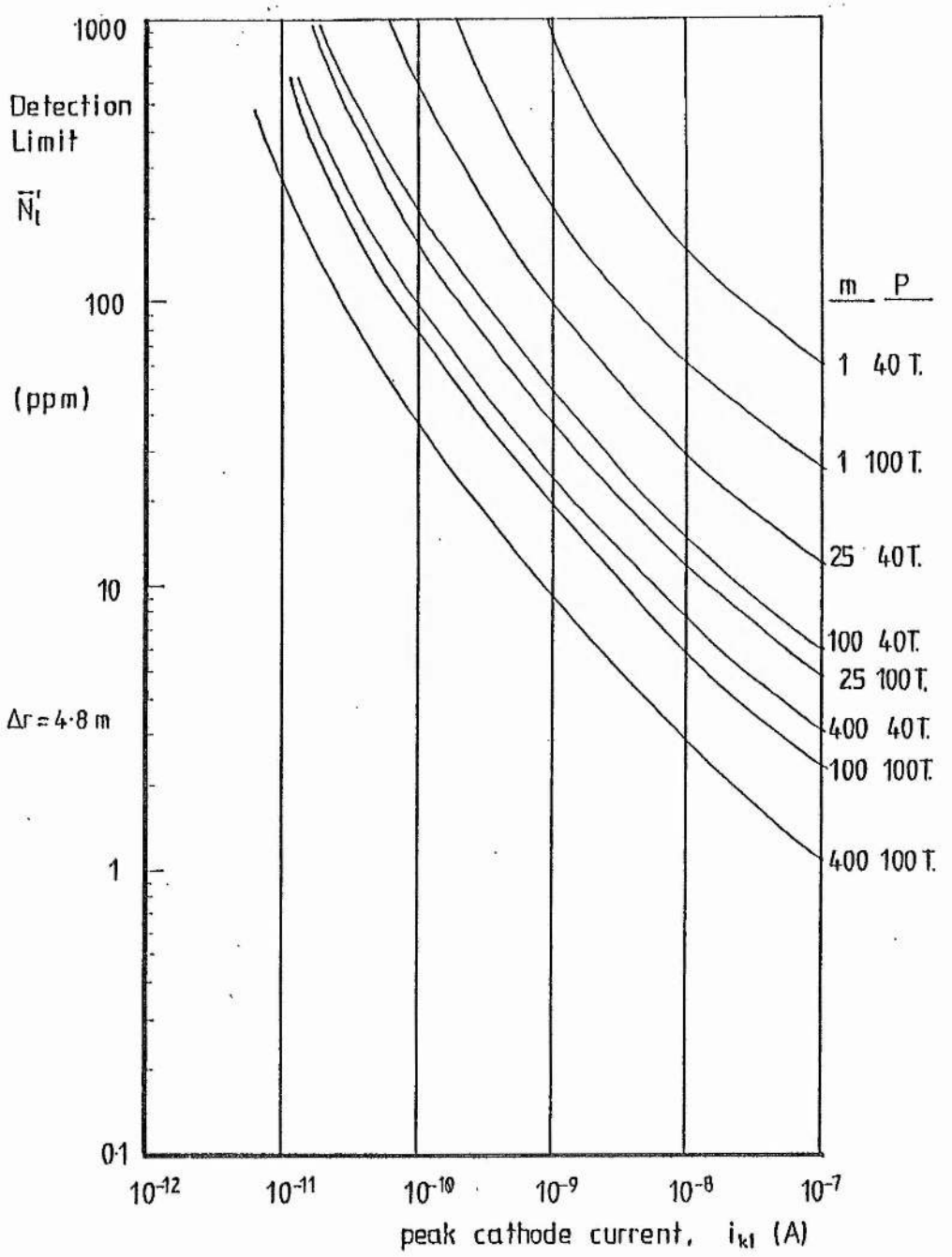

Figure 9.7.3 Detection limits defined by a resulting concentration error of 100%

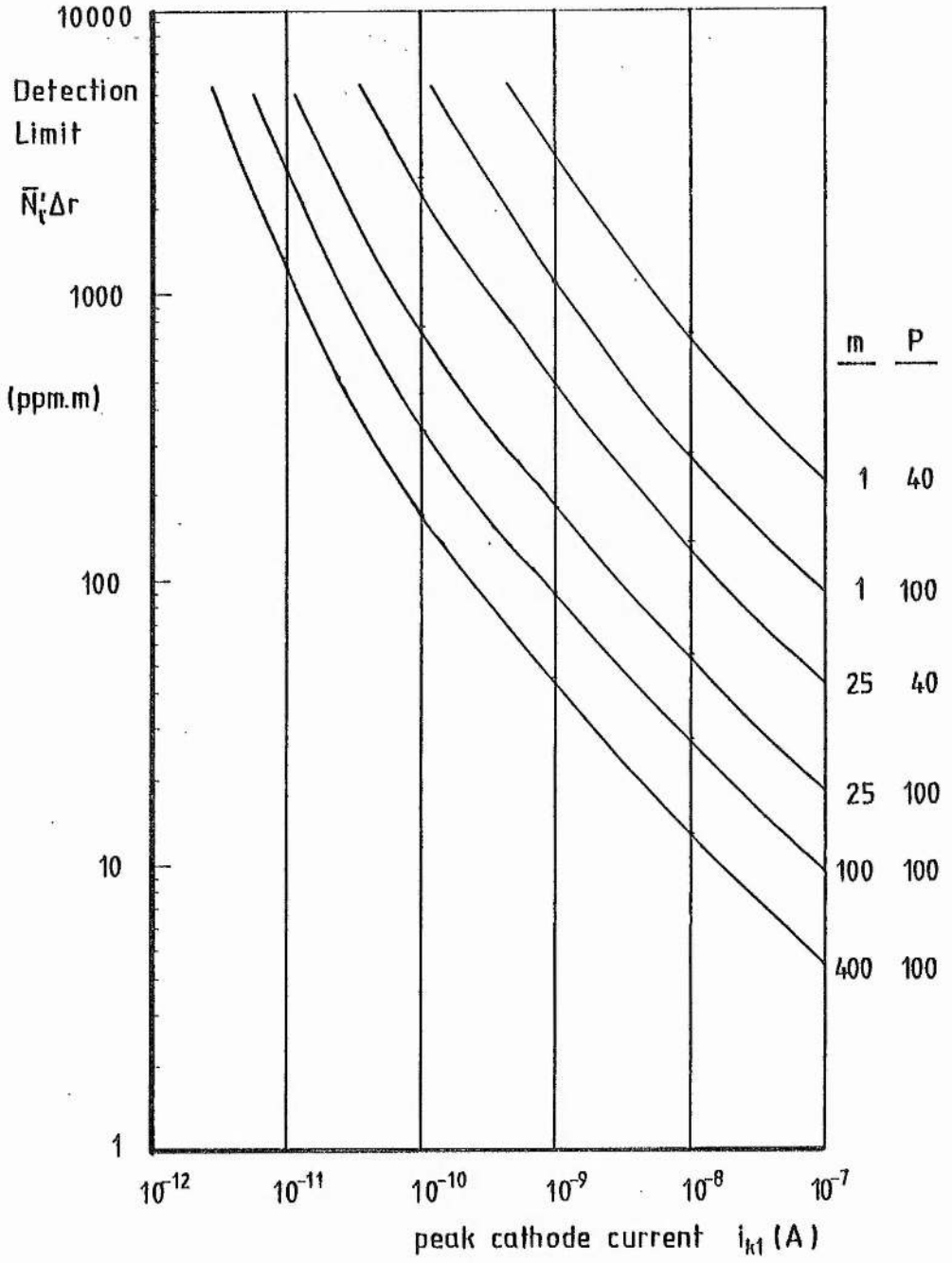

Figure 9.7.4 Detection limit/range element product defined by a resulting concentration error of 100%, in the mixed wavelength case.

9.8 Theoretical Comparison of Distinct and Mixed Wavelength DIAL

A comparison of the distinct and mixed wavelength DIAL methods is based on the errors in measuring SO_2 concentration over a sample length of 4.8m and on the detection limits as obtained in the modelled situations in sections 9.4 and 9.7, respectively.

The detection limits for each case are taken from figures 9.4.1 and 9.7.2 and are plotted for the number of pulse pairs averaged in figures 9.8.1 in comparison of the sensitivities. Figure 9.8.1(a) is for a weakest signal cathode current of 10^{-8}A and figure 9.8.1(b) is for a weakest signal cathode current of 10^{-9}A. The best mixed wavelength accuracy is set by a cell pressure of 100 torr, giving the lowest likely detection limit ratio, between the two methods, of a factor of about 5.5. The worst mixed wavelength accuracy, at a cell pressure of 40 torr, gives a factor of about 14 in the difference between the two methods.

This loss of accuracy in using the cell differential absorption technique is offset by the simple and robust nature of the method. In adopting the cell, the system experiments continued without delay and with minimal expense. A distinct wavelength tuning technique (birefringent filter; see chapter 5) is preferable if range resolved measurements of SO_2 levels below 1 ppm are required. However, the application of a suitable device required more time than was available within the limits of the project.

With both methods, but especially so with the mixed wavelength case, the sensitivity is increased at the expense of range resolution, by increasing the signal sample time, ie. reducing the bandwidth. An indicated distinct wavelength sensitivity of 4.8 ppm.m (figure 9.8.1(a), m=100) would mean

that the $XeCl^*$ system should be able to measure urban ambient SO_2 levels (say 0.02 ppm) but only by integrating return signals over the entire range of at least 200m. Equivalently, (figure 9.8.1(a)) a mixed wavelength sensitivity of 25 ppm.m at strong signal levels indicates a need for integration over 1 km for similar sensitivity to ambient SO_2. For such ambient measurments it would probably be necessary to employ a retro-reflector at the appropriate range to provide sufficient backscatter for the necessarily high S/N ratio (cathode peak current of $i_{k1} = 10^{-8}$A).

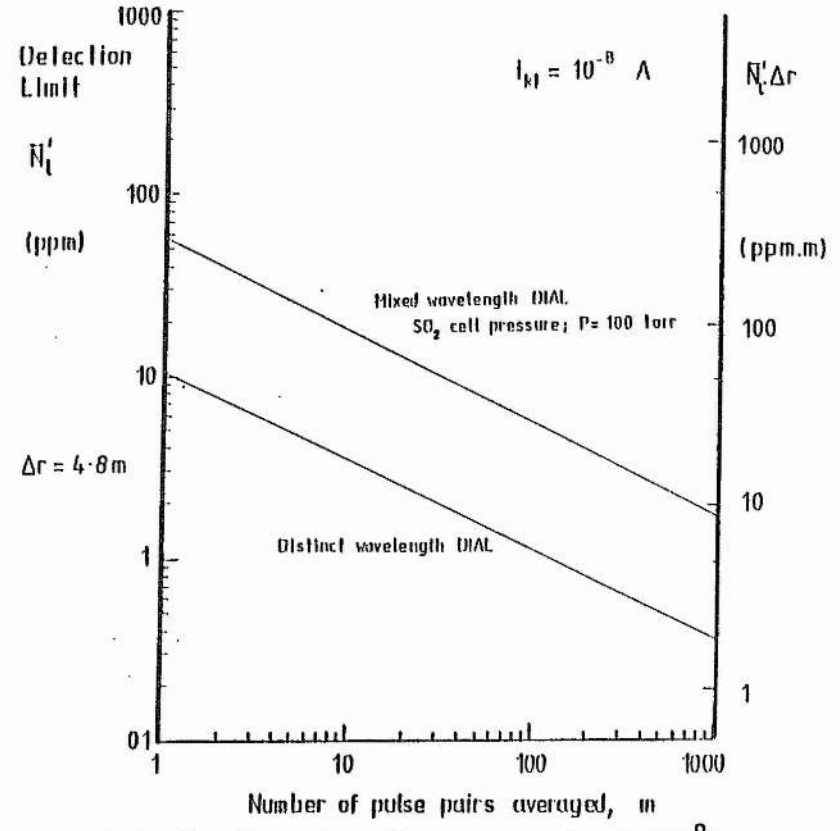

(a) signal peak cathode current of 10^{-8}A

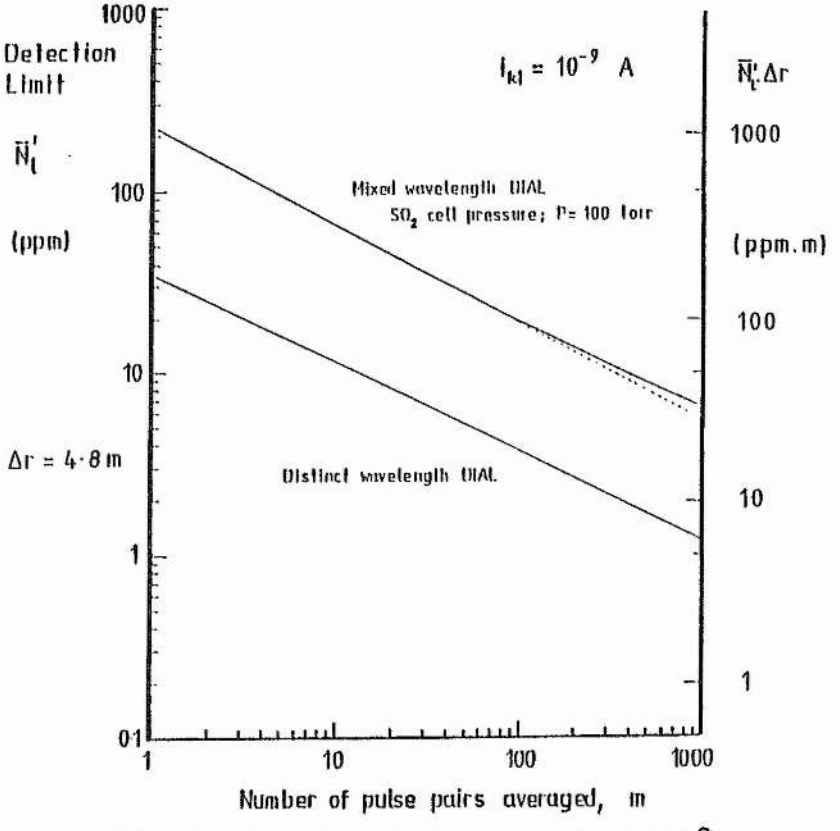

(b) signal peak cathode current of 10^{-9}A

Figure 9.8.1 Distinct/Mixed wavelength DIAL detection limits for number of averaged pulse pairs

9.9 Application of DIAL Algorithms

In distinct and mixed wavelength DIAL, respectively, equations (9.1.10) and (9.5.8) would provide the algorithm for a range resolved SO_2 measurement within an atmosphere containing SO_2 throughout the range.

For measurement of high SO_2 levels (compared with ambient level) contained within a smoke plume at low range ($\simeq$ 200m), equations (9.1.8) and (9.5.6) would be simplified by setting the ambient level to zero ($\bar{N}_r=0$) as negligible compared with $\bar{N}.\Delta r$. This provides the basis for SO_2 sensitivity models in sections 9.4 and 9.7.

If ambient levels are to be measured, then long path integrated returns would be considered and the algorithm for analysis would be derived from equations (9.1.7) and (9.5.5).

References for Chapter 9

Adrain R.S, Brassington D.J, Sutton S, Varey R.H; The measurement of SO_2 in power station plumes with differential lidar. Opt.and Quantum. Electron., 11, 253-264, (1979)

Brassington D.J; Sulphur dioxide absorption cross-section measurements from 290 to 317 nm. Appl.Opt.vol 20, 21, 3774-3779, (1 Nov. 1981)

Brassington D.J; Tunable dye laser measurements of the SO_2 absorption spectrum between 290 and 317 nm. CERL, Lab. note no.RD/L/2055N81, Job no. VC299, (June 1981)

Byer R.L and Garbuny M; Pollutant detection by absorption using Mie scattering and topographic targets as retroreflectors. Appl.Opt. 12, 7, 1496, (July 1973)

EMI, Photoelectric Cells and Photomultipliers, 1961

Fleagle and Businger, An Introduction to Atmospheric Physics

Grum and Becherer, Optical Radiation Measurement, vol.1, Radiometry, 1979

Knestrick G.L and Curcio J.A; Measurement of ultra-violet spectral radiance of the horizon sky. Appl.Opt. 9, 7, 1574-1576, (July 1970)

Kondratyev, Radiation in the Atmosphere, 876, 1969

Northend C.A, Honey R.C, Evans W.E; Laser radar (lidar) for meteorological observations. Rev.Sci.Instrum., 37, 4, (April 1966)

Ott, Noise Reduction Techniques in Electronic Systems, 1976

RCA, Electro-Optics Handbook, 1974

Rice, 1945

Ross Monte, Laser Receivers, 1966

Sze Robert C and Scott Peter B; Intense lasing in discharge excited noble-gas monochlorides. Appl.Phys.Lett., 33, 5, (September 1978)

Chapter 10 Excimer Laser DIAL Experiments

In order to prove the potential of the $XeCl^*$ laser in DIAL, the completed system has been used in experiments to measure atmospheric sulphur dioxide. The procedure and results, peculiar to this system, are described in this chapter.

10.1 Procedure for SO_2 Concentration Measurements

The procedure for measuring target SO_2 concentration, summarised in figure 10.1.1, is followed after the switch-on procedure, given in section 7.3, figure 7.3.2. This section is a list of the operational procedure.

10.1.1 Signal Handling System Test Sequence

After the DIAL system has been switched on (figure 7.3.2), the signal handling system test sequence is carried out to check for the correct operation of the VIA I/O ports, the computer keyboard, the printer, the circuit reset and on/off line functions, the cell position sensor and to test memory accessibility. The appropriate commands are listed in table 6.3.1, in the column headed "access (enter)". The correct responses during the test sequence are shown by the VDU display and/or appropriate LED illumination on the signal handling unit panel. These responses are summarised in table 6.3.2(a). Access to the signal handling sequences is by the initial command "LINK £A000" which produces the menu for the test procedures (numbered "1" to "5") and for the data acquisition and analysis sequence (numbered "6").

10.1.2 Target Ranging

Determination of the range of the target sample is by measurement of the time-of-flight of the laser pulse to the target and back to the receiver, displayed on the time-base of an oscilloscope (the Tektronix 7834 storage oscilloscope in this case). Range, r, is given by the time-of-flight, t, and the speed of light, c, in the expression

$$r = ct/2. \qquad (10.1.1)$$

The value is required for insertion into the DIAL algorithm, evaluated within the analytical routine.

The target ranging calibration method is given in appendix A10.2. For ranging purposes, the return pulse is sharpened by a higher bandwidth signal line ($\leqslant 500\Omega$ impedance) to the oscilloscope (a line impedance of 10k is used for signal measurements).

10.1.3 Equilibrium within the Sulphur Dioxide Cell

An experiment which is described in appendix A10.1 shows how an equilibrium must be achieved within the sulphur dioxide absorption cell before data acquisition.

After the trigger unit has been switched on, the laser is operated until the oscilloscope traces of return pulses and those showing laser output show no undue variation between adjacent pulses. This should establish the equilibrium in the cell but it is necessary to proceed immediately with initiation of the data collection system and data acquisition.

The pressure to temperature ratio (P/T), which describes the differential absorption property of the SO_2 cell, is defined by the laser energy measurement ratio, given as the program variable %P, after each data acquisition. The connection between %P and P/T, made in appendix A10.1, is shown in figure 10.1.2, which is applied manually during data analysis.

10.1.4 Initiation of the Data Collection System

Once SO_2 cell equilibrium has been reached, the system is set for data acquisition and storage by selecting "6" off the computer function menu (see table 6.3.1). The required number, m, of DIAL pulse pairs is entered and the "return" key is depressed. The graphic display appears on the VDU with a double apostrophe character at the top of the screen. The system is now ready for data acquisition, upon operation of the laser trigger unit.

10.1.5 Data Acquisition and Analysis

Once the data collection system has been initiated, the laser trigger unit is switched-on to operate the laser and to trigger the signal peak measurement circuits, A-D conversion and data storage.

The computer functions, during data acquisition and analysis, are summarised in the lower part of table 6.3.1. At the end of the procedure for initiation of the data collection system, the VDU displays a pattern with a double apostrophe character at the top of the screen. On switching-on the laser trigger, this character changes to an exclamation mark for the next pulse and back to the apostrophe for the next, etcetera, according to the responses which are listed in table 6.3.2(b), until data from m pulse pairs (2m pulses) has been collected. At this stage, the pattern disappears and data from each of the DIAL pairs is averaged and the result is displayed, giving the return signal average ratio %R and the laser energy

ratio, %P. Note that any deviation from alternate display of the apostrophe and exclamation mark characters is an indication of a malfunction in switching the SO_2 cell in and out of the laser cavity.

The display now shows a request for the analytical mode to be entered, giving a choice of analysing the measured values for a sulphur dioxide concentration as an average over the entire lidar range (range-integrated) or as the concentration in an element of range at the target (range-resolved). Figure 6.3.2 gives examples of two typical print-outs, expected from the range-integrated and the range-resolved routine respectively.

A range-integrated measurement of ambient SO_2 level should be made before re-directing the instrument at a suspected volume of localised SO_2. The ambient measurement (the data from it) is used to correct the data taken from the target element. In both analytical routines, the range of the target is entered (see 10.1.2) and the P/T ratio for the laser is taken from figure 10.1.2, using the %P value. Values for ambient temperature and pressure are inserted, unless parameters pertaining to the range-resolved target can be estimated (for example; a smoke plume near to the chimney and hence, at a higher temperature than ambient).

FIGURE 7.3.2

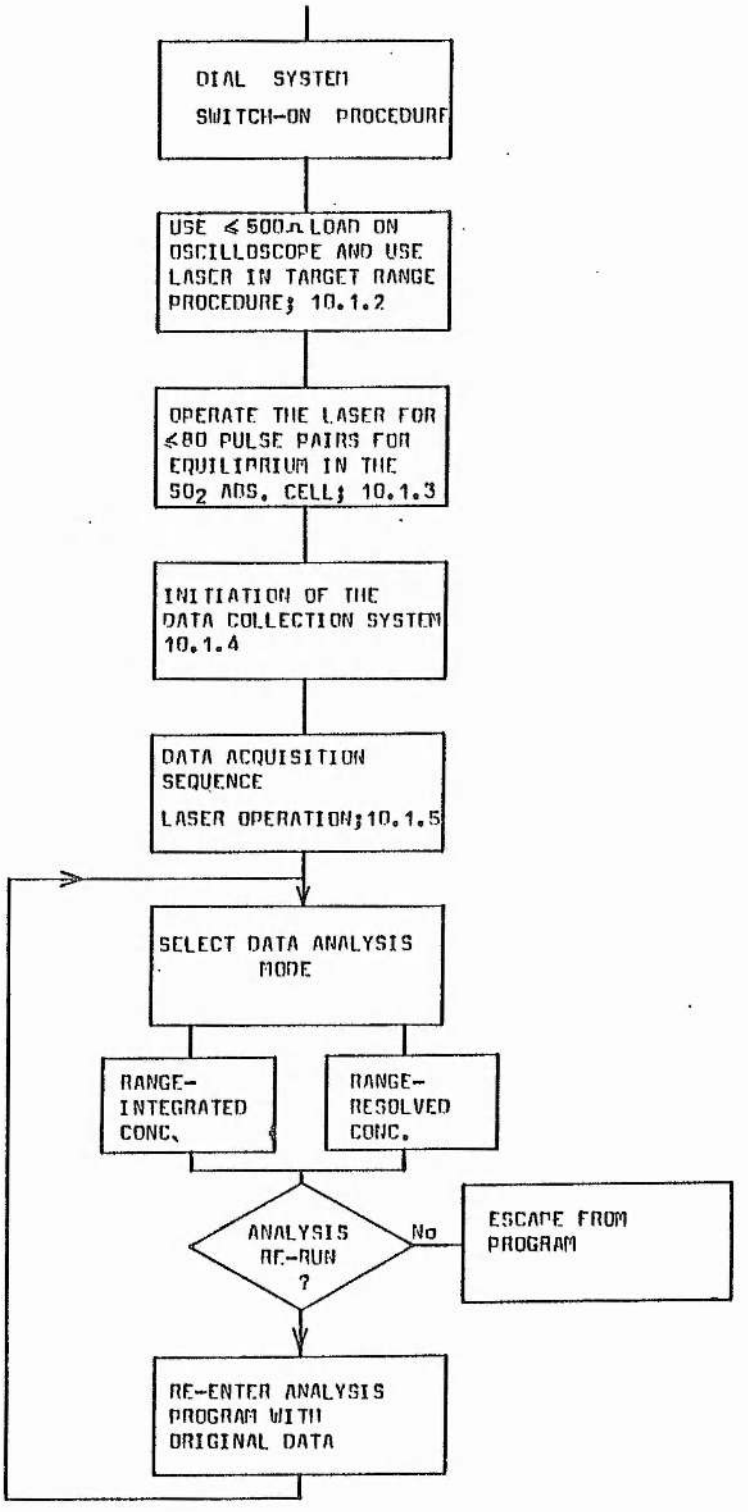

Figure 10.1.1 Procedure for SO_2 concentration measurements using the $XeCl^*$ laser DIAL system (used after figure 7.3.2)

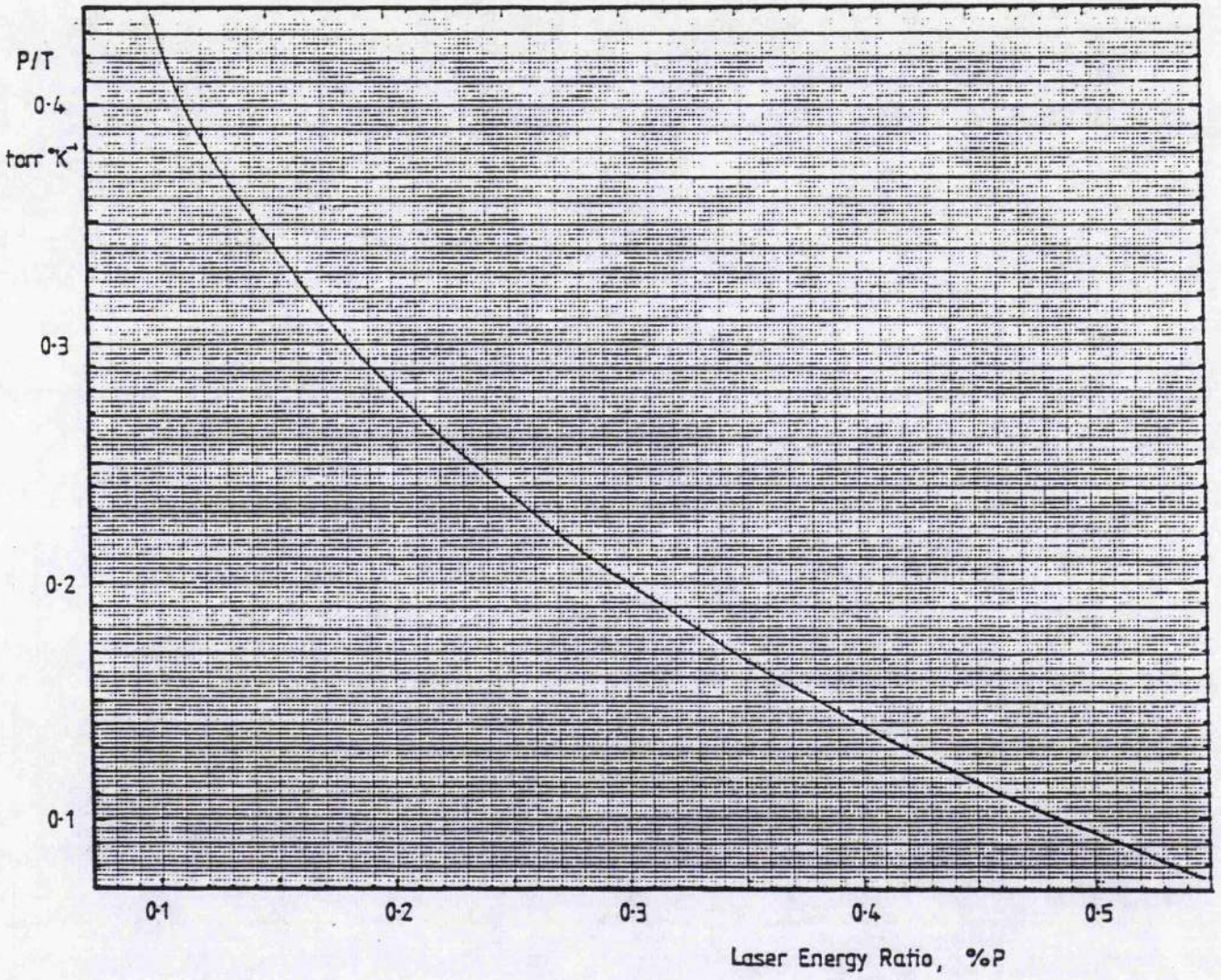

Figure 10.1.2 Calibration plot for the sulphur dioxide absorption cell P/T vs %P (laser output energy ratio)

10.2 Measurement of Atmospheric Sulphur Dioxide Concentration

The system is applied to give SO_2 concentration data (ppm) to show its viability as a detector of SO_2 and to allow experimental evaluation of measurement uncertainties, for comparison with theoretical accuracy, given in chapter 9.

10.2.1 Physical Situation

Figure 10.2.1 shows the experimental layout. The laser pulse is directed at a wall situated 40m from the lidar system. The outlet of a cylinder of sulphur dioxide is fitted with a perforated tube to disperse the gas in a sheet in the path of the laser pulse. Gas flow rate is measured to allow estimation of dispersal under the ambient conditions at the time of the measurements. Data is acquired and averaged to give a range-integrated measurement of SO_2 concentration, as an average over the entire lidar range between the laser and the wall. The acquisition and analysis routines are repeated to get measurements when no SO_2 is emitted, to give a calibration for zero ambient concentration.

10.2.2 Sulphur Dioxide Concentration Results

Each concentration result is plotted in figures 10.2.2, in four sequences, showing the occurrence of any external factors such as changes in local air movement and sulphur dioxide control. All the base line measurements of figures 10.2.2 have been set at zero ppm, even though actual 'zero' measurements were biased, due to a disparity between the laser energy ratio (%P) and the zero ppm return ratio (%R), per DIAL pulse pair.

The features of figure 10.2.2 are explained in table 10.2.1.

10.2.3 Comparison of Experimental Levels with Expected Results

The levels of sulphur dioxide and their persistence is dependent on the physical dimensions of the SO_2 'sheet', the flow rate and the effectiveness of dispersal by ambient air movements.

The proportion of SO_2 expected in the laser pulse path is estimated, very roughly, from figure 10.2.3, by proportions of volume, giving an expected maximum of $\triangleq$ 130 ppm by volume, assuming no dilution by dispersal. This compares with measured peak levels (shown in figure 10.2.2) of 122 and 115 ppm, obtained in still conditions.

The flow rate of 4.5 $cm^3 min^{-1}$ is interpreted to give the cross-sectional area (2 X 10^{-5} m^2) of the emitted gas an effective speed of 0.008 mph. This is overcome by even a very light breeze, accounting for apparently easy dispersal of the gas under such conditions, shown in figure 10.2.2.

10.2.4 Variation of Measurement Values

The predicted accuracy of measurements of SO_2 concentrations and the detection limits applying to the present system are given in chapter 9 and illustrated in figures 9.7.2 and 9.8.1.

The experimental measurements of finite SO_2 levels, shown in figure 10.2.2, show fluctuations about a mean. The respective average level is shown in parts (a) and (d) of figure 10.2.2. The theoretical limits of accuracy, calculated in appendix A10.4.1, are shown to give a good match to the spread of measurements about the mean.

The theoretical detection limits for the system, given in figure 9.8.1, are included on figure 10.2.2. The parameters involved in this evaluation are listed in appendix A10.4.2. The detection limits are close to the limits of experimental fluctuation above 0 ppm, as expected.

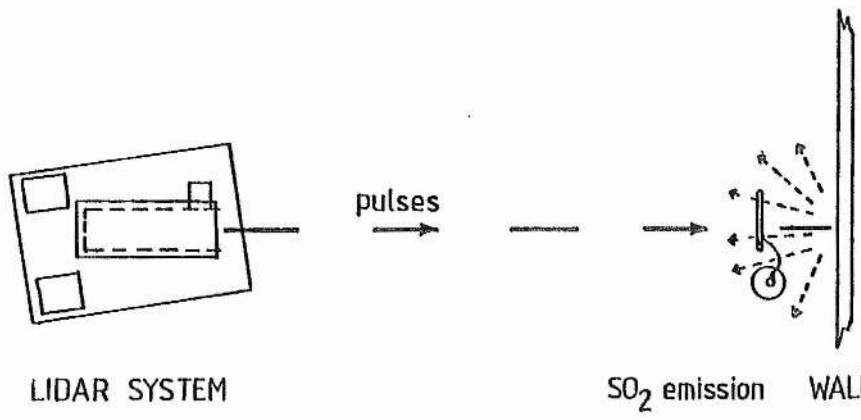

Figure 10.2.1 Physical layout of SO_2 measuring experiments

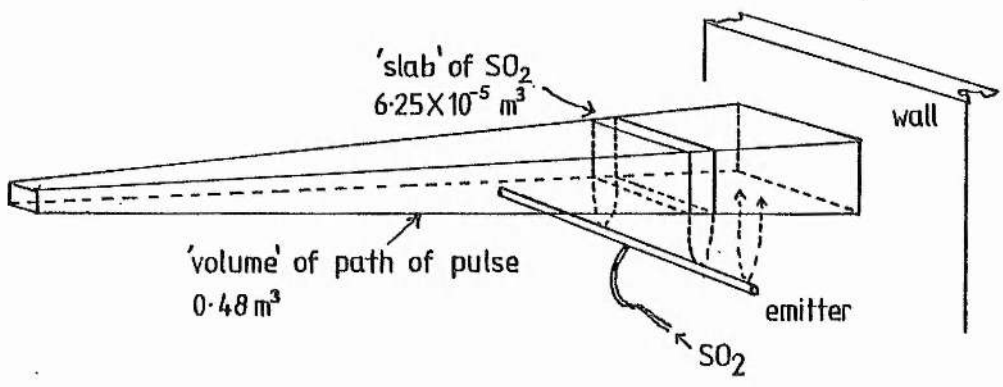

Figure 10.2.3 Estimation of sulphur dioxide concentration by volume proportion during DIAL experiments.

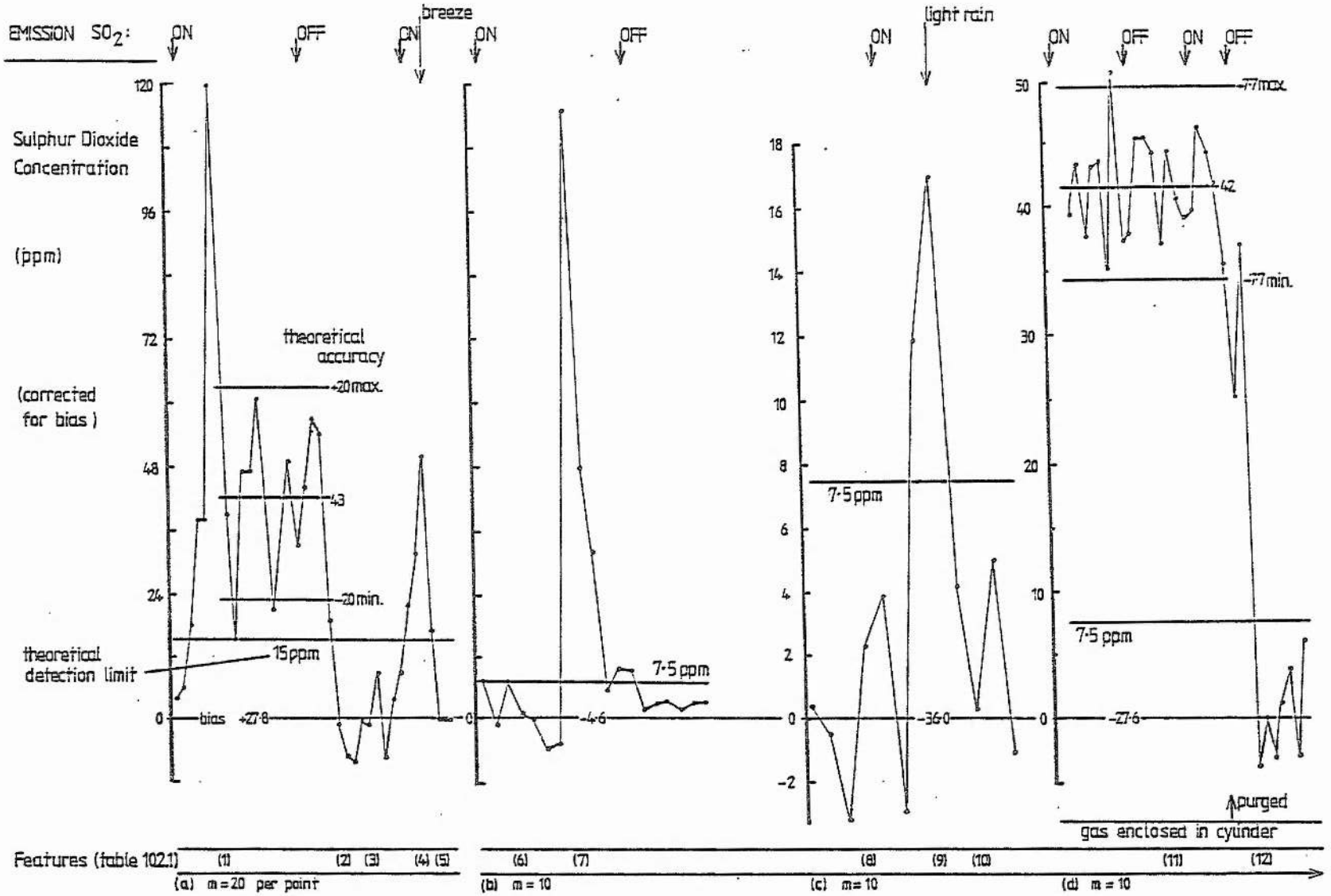

Figure 10.2.2 Measurements of sulphur dioxide concentrations; $\bar{N}'$ vs time
Each point represents the average result from m=10 pulse pairs, except for (a), where m=20 per point.
Each concentration is an average over a range of 40m.

Table 10.2.1 Description of Features on Figure 10.2.2, Measurements of Sulphur Dioxide with the XeCl* Laser DIAL System

Feature	Concentration	Comments
(1) Peak	120 ppm	Peak development is delayed after SO_2 is turned on, as it disperses into the path of the pulse
(2) Persistence then drop		High concentration continues after SO_2 is turned off, as gas disperses
(3) Base-line	about zero	Set to 0 ppm in contrast to emitted levels
(4) Peak	51 ppm	Peak develops in same way as peak (1)
(5) Level drop		SO_2 still turned on but a breeze develops and gas is carried away faster than emitted
(6) Base-line	about zero	as (3)
(7) Peak	115 ppm	Peak development delayed, as in (1) and (4). Dispersal is aided by local air movement at a faster rate than it is emitted
(8) Base-line	about zero	as (3)
(9) Peak	17 ppm	Peak development delayed, as (1) (4) and (7)
(10) Level drop		Start of a light shower aids dispersal, though not completely
(11) High level maintained	about 42 ppm	SO_2 contained within open-ended cylinder (modification on experimental arrangement), thus, it is not dispersed by air movement
(12) Level drop		Cylinder purged of SO_2 after gas turned off

Chapter 11 Conclusion

Development of the $XeCl^{*}$ DIAL system components has been described in chapters 2 to 7, inclusive. The successful operation of these components and the possibilities for their improvement are discussed in this chapter with particular attention being paid to possible, more flexible, signal processing schemes. The system is compared with other DIAL systems, reviewed in chapter 1, with special regard to detection limits in measuring SO_2 concentration. The detection limits have been evaluated on a theoretical basis in chapter 9, using the lidar equation, developed in chapter 8. Theoretical detection limits are summarised below, and compared with those of other systems. Successful application of the system to measuring SO_2, and subsequent measurement accuracy, have been described in chapter 10. Finally, in this chapter, experimental and theoretical accuracy of the system are compared.

11.1 Equipment Status and Possibilities for Improvement

11.1.1 Signal Acquisition System

Laser, telescope and detector performance as a lidar signal acquisition system was proven by lidar tests at Methil power station, when return signals were obtained from the smoke plume. Signal peak voltages in the range 95 mV to 980 mV were measured from the smoke returns and peaks around 2 V were measured from the chimney itself. This size of signal is large enough to give good signal-to-noise ratio when measured in the signal handling and interpretation system. A reasonably close correlation was obtained between the empirical peak voltages and return pulse widths and those predicted by a computer model. Thus, the laser, telescope and detector satisfy the system requirements.

There are possibilities for improvements. The "home-built" laser, as it stands, cannot be improved upon without destroying its relative simplicity and reliability. A requirement for higher laser pulse power, with a view to obtaining higher signal-to-noise ratio and/or greater lidar range, would be better met by a completely new laser design, involving adoption of an improved pre-ionization method, or even by purchasing a commercial $XeCl^{*}$ excimer laser. The latter, though expensive and bulky, would probably be packaged within a more effective r.f shield than the present device, thus reducing pick-up, one of the greatest problems in operating the signal handling system.

In the telescope, a primary mirror with a shorter focal length would allow construction of a more compact instrument. Even so, this would only be worth while if the rest of the system, including the laser, were to be correspondingly reduced in size. A more practical suggestion is the

purchase of a larger mirror for improved light collection efficiency. However, it has been shown (chapter 2) that the corresponding improvement in extended lidar range does not justify the expense of a larger mirror.

The adoption of an EMI solar-blind photomultiplier tube, narrow-band interference filter and the design and construction of a dedicated circuit cannot be faulted. However, with hindsight, it would have been quicker and easier to employ and modify an EMI photomultiplier housing, complete with electro-magnetic shielding.

11.1.2 Laser Tuning

Laser "tuning" is accomplished by the intra-cavity SO_2 absorption cell, which provides a modification to the relative spectral content of one of the DIAL pulses. This novel method is very simple, robust, and easily applied. However, further development of a laser tuning method has already been undertaken (section 5.4) in the design of a birefringent filter. This would allow a single wavelength to be selected per pulse of the DIAL pair, in contrast to the present system of "spectral modification". The theoretical evaluation of the system's sensitivity to SO_2 concentration (figure 9.8.1) shows that the present "mixed wavelength" DIAL detection limit is improved upon by, roughly, a factor of 5, in the envisaged and more conventional "distinct wavelength" DIAL situation.

Tuning by etalon was discounted on the basis of its susceptibility to shock and to temperature fluctuation. However, McDermid et al (1984) are employing three air-spaced etalons, contained within a pressure vessel, to tune a $XeCl^*$ oscillator-amplifier over 307.6 - 308.4 nm, used in a fluorescence lidar system.

11.1.3 Signal Processing

The signal handling equipment is sensitive to signals at the millivolt level, with linearity up to saturation (12 bits) at about one volt. This gives a good dynamic range to allow accurate detection of a DIAL return pulse pair, where one signal may be five times weaker than the other. In its present form, the signal processing method provides the minimum facility for taking measurements of return signals and, as such, is the weakest part of this DIAL system. The peak detection, sample-and-hold and A-to-D conversion circuit does not have the means for taking samples at intervals along the return distribution. This is a feature of more elaborate equipment, allowing the SO_2 distribution along the lidar range to be mapped from one data acquisition sequence. A summary of DIAL signal processors is given in table 11.1.1.

Two relatively simple schemes for sampling at intervals along the return have been described in the literature. Rothe et al (1974) supplied a series of n counters with the amplified signal from the photomultiplier, gating the operation of each counter to measure an interval of the return. Vanin et al (1976) reported a system where the analogue-to-digital converter is gated to select a particular interval of the return signal. The size of the signal, integrated over the interval, is given by the duration of a constant amplitude pulse at the converter output. The latter method, though it selects a range interval, does not provide information from a series of intervals over the lidar range from one acquisition sequence. More elaborate systems (Adrain et al, 1979; Altmann et al, 1980) have employed transient digitizers and storage rings (Grant et al, 1974; Murray et al, 1976; Hawley, 1981), allowing the entire return signal to be collected and digitised where necessary. Operating at up to 100 MHz, the sample interval can be as low as 10 ns. Information from the digitizer is passed to a mini-

computer. The computer in the DIAL system of Adrain et al is used to control the entire system, including laser triggering. The computer in each of the referred systems is used, just as the Acorn Atom micro-computer is used in the St.Andrews system, to average the data for noise reduction and to present the results for SO_2 concentration.

There is room for providing a much more useful signal processing system for the $XeCl^*$ laser DIAL without detracting from the inherent simplicity and robustness of the complete system. It may be possible to supersede the present peak detection circuit with an improved, faster, version. However, a scheme for providing a measurement from any interval along the return pulse could be provided by adopting the method of Rothe et al or of Vanin et al, described above. The ideal solution, though it is expensive, is to use a transient digitiser and appropriate computer back-up, as described by other DIAL workers, whilst keeping size small and operation simple.

Adrain et al have reported deconvolution of the laser pulse shape from the return pulse, to allow better spatial definition of backscattering media and SO_2 concentrations. The technique is not deemed necessary for the present $XeCl^*$ laser DIAL system, where the spatial resolution does not need to be so precisely defined and where the laser pulse width (32ns) is about thirty times smaller than the original pulse width (1μs) of Adrain et al at C.E.R.L (The uprated system at C.E.R.L uses a laser with smaller pulse length).

11.1.4 General Improvements

In view of the required reliability and serviceability in field equipment, all electronic and electrical circuits should be re-built on "slot-in" boards in a rack configuration, permitting rapid replacement in the event of failure.

Re-accommodation of the DIAL system in an aluminium trailer, of the type used by small retailers and exhibitors, in preference to the present, open, trailer, would give all-weather protection, security and would permit faster travel between operating sites. The use of pneumatic mounts under the laser/telescope head would, preferably, be extended to all the equipment units.

11.2 Summary and Conclusion of Theoretical and Experimental Results

11.2.1 Lidar Equation and its Components

The derivation of lidar equations, given in section 8.2, was necessary to provide the algorithm for the lidar model of section 8.4. Comparison, in section 8.6, of the model with results of lidar signal acquisition experiments (section 8.5) has proved, within limits, the validity of the lidar equation. Its application to DIAL, given in chapter 9, produced the algorithms for signal interpretation and the equations necessary for defining SO_2 concentration limits. Appendices A8.1 and A8.2 show the derivation of expressions for Rayleigh and Mie atmospheric scattering coefficients for inclusion in the lidar equation when applied to lidar reception of radiation, around 308nm, from a model atmosphere. The Mie scattering term is interpreted in this work to include the Rayleigh coefficient at 0.55μ, as a modification to the definition based on atmospheric visibility at that wavelength. The form of all derived expressions is in agreement with those given in the literature of other workers.

11.2.2 DIAL Equations

Chapter 9 gives the derivation of expressions for the ratio of signals received as a DIAL pair, so that the measured concentration of atmsopheric SO_2 is obtained as a function of that return ratio. The novel method of modifying the spectral output of one of the DIAL pulses, using an SO_2 absorption cell, gives an unusual expression for SO_2 concentration as a function of return signal ratio. The "mixed wavelength" DIAL equation is analysed alongside the conventional "distinct wavelength" DIAL case which would be applied if an alternative tuning method was used.

The DIAL equation, applying to the use of the SO_2 absorption cell in "tuning" the laser, gives the atmospheric SO_2 concentration averaged over a target range element. This expression is used as the algorithm for the DIAL signal interpretation programs (chapter 6), for a range-resolved result. In addition, the range element can be taken as the entire lidar range, to give a range-integrated result. This is implemented before a range-resolved measurement is taken, to give the correction for any SO_2 present in the range intervening between the lidar system and the target element.

In evaluating the performance of the system in measuring SO_2 concentrations, the DIAL equations are simplified to evaluate return signal ratios versus the corresponding SO_2 concentration (figure 9.2.1). In the "mixed wavelength" case, the SO_2 absorption cell pressure is shown as another variable (figure 9.6.1).

11.2.3 Sulphur Dioxide Detection Limits

The crux of any DIAL system is its sensitivity to target gas concentration. The theoretical detection limits of the $XeCl^*$ laser DIAL system have been evaluated and displayed graphically in sections 9.4, 9.7 and 9.8. The system is evaluated as being shot noise limited and an analysis of worst case shot noise and thermal noise at the photomultiplier anode is given in section 9.3. Shot noise components arise from the background radiation (around 308nm) signal, the photomultiplier dark current (negligible) and the lidar return signal itself. Thermal (Johnson) noise is generated in the photomultiplier load resistor.

The theoretical detection limits of the $XeCl^*$ laser system are compared with those of other SO_2 DIAL systems (from table 1.5.1) in table 11.2.1. Accuracy is also dependent (equations (9.4.8) and (9.7.3)) on the

absorption cross-section difference between the two DIAL wavelengths and on the number of pulse-pairs averaged. These parameters are included in table 11.2.1. The tabulated detection sensitivity, obtained in this work, is from figure 9.8.1(b), where the signal strength is estimated to be in the middle of the likely range. Comparison between the systems is made by standardising the effect of pulse-pair averaging by multiplying the detection limit, in units of ppm.m, by the square root of the number of averaged pulse-pairs, to give (ppm.m)$\sqrt{m}$.

The excimer laser system, if it is operated with an SO_2 "tuning" cell at 100torr partial pressure, appears to be less sensitive than that of Adrain by a factor of over 20, while the system tuned in the "distinct wavelength" mode is less sensitive by a factor of about 4. A factor of 10 would be expected between these two systems, due to that order of magnitude difference in absorption cross-section difference (table 11.2.1).

The "mixed wavelength" DIAL sensitivity is variable by altering the SO_2 cell pressure, as shown in figure 9.2.3. The practical range of cell SO_2 partial pressures is limited, by detection limit and signal strength considerations, to between 40torr and 100torr. The best sensitivity to atmospheric SO_2 is obtained at the upper limit of cell pressure, at the expense of signal strength so the absorption cell is usually filled to a pressure of about 100 torr.

Average excimer laser DIAL sensitivity is 100ppm.m for "mixed wavelength" DIAL and 18ppm.m for "distinct wavelength" DIAL, when 100 pulse-pairs are averaged. In this case, therefore, the "mixed wavelength" system will have to measure the average SO_2 concentration over at least 5km (range-integrated) to detect ambient levels down to 0.02ppm. The "distinct

wavelength" system will have to measure average SO_2 concentration over a minimum range of 900m for sensitivity to 0.02ppm.

11.2.4 Theoretical and Experimental Measurement Uncertainties Compared

Experiments were succesfully carried-out to detect and to measure sulphur dioxide, introduced into the path of the laser pulse, proving the viability of the system. The results are summarised in figure 10.2.2. Uncertainties in the experimental results are shown by fluctuation of repeated results about a mean concentration value. The extent of these fluctuations compares closely with uncertainties and detection limits which have been predicted by theory.

Table 11.1.1 DIAL Systems Signal Processing

Investigator	Sample Interval	Signal Processing Scheme
Grant et al, 1974	≥100ns (≥16m)	P-M ⟶ A-D, 9.6MHz, 8-bit ⟶ storage ring ⟶ HP2115 mini-computer
Rothe et al, 1974	≥3.3μs (≥500m)	P-M ⟶ amplifier ⟶ fan-out ⟶ counter 1, counter 2, ⋮, counter n ⟵ each counter activated by variable-width gate
Murray et al, 1976	≥400ns (slow detector) (≥60m)	detector ⟶ amplifier ⟶ filter, 2.5MHz ⟶ A-D, 4.8MHz, 10-bit ⟶ storage ring ↓ HP2115 mini-computer
Vanin et al, 1976	200ns - 10μs (30 - 1500m)	P-M ⟶ emitter follower ⟶ A-D, 5MHz ⟶ constant-amplitude pulse of width proportional to charge interval; ↑ gating unit selects range interval to be digitised
Adrain et al, 1979	≥10ns (≥1.5m)	P-M ⟶ pre-amplifier ⟶ Biomation 8100 transient digitiser, 100MHz, 8-bit ↓ Interdata 7-16 mini-computer
Altmann et al, 1980	≥40ns (≥6m)	detector array ⟶ amplifier ⟶ Biomation 8100 transient digitiser, 25MHz, 8-bit ↓ PDP 11/34 mini-computer
Hawley, 1981 EPRI, 1979	≥100ns (≥16m)	P-M ⟶ A-D, 10-bit ⟶ storage ring ⟶ HP21 MX/E mini-computer

Table 11.2.1 Comparison of SO_2 DIAL System Detection Limits

Investigator	Absorption X-section Difference $(\sigma_1 - \sigma_2)$ $(X10^{-24}m^2)$	Pulse Pairs Averaged m	Theoretical Detection Sensitivity (ppm.m)	Comparison Figure (ppm.m)$\sqrt{m}$
Grant and Hake	46.5	8	10	28.3
Adrain et al	91	200	3	42.4
Hawley	97	100	10	100
SSEB/St. Andrews University				
"mixed" wavelength	9	100	100	1000
"distinct" "			18	180

References for Chapter 11

Adrain R.S, Brassington D.J, Sutton S, Varey R.H; The measurement of SO_2 in power station plumes with differential lidar, Opt. and Quantum Electron. 11, 253-264, (1979)

Altmann J, Lahmann W, Weitkamp C; Remote measurement of atmospheric N_2O with DF laser lidar, Appl. Opt., 19, 20, 3453, 15 October (1980)

Grant W.B, Hake R.D Jnr., Robbins R.C, Liston E.M, Proctor E.K Jnr.; Calibrated remote measurement of NO_2 using the differential absorption backscatter technique, Appl. Phys. Lett., 24, 11, 550, 1 June (1974)

Hawley J.G; Dual wavelength laser radar probes for air pollutants, Laser Focus, p.60, March (1981)

Characterization of the EPRI differential absorption lidar (DIAL) system, Final Report, EA-1267, Project 862-14, December (1979)

McDermid I.S, Laudenslager J.B, Pacala T.J; Design of a narrow-bandwidth lidar system for tropospheric hydroxyl measurements, Proc. 12th International Laser Radar Conference, Aix-en-Provence, France, 13-17 August (1984)

Murray E.R, Hake R.D Jnr., van der Laan J.E, Hawley J.G; Atmospheric water vapour measurements with an infra-red (10μm) differential absorption lidar system, Appl. Phys. Lett., 28, 9, 542, 1 May (1976)

Rothe K.W, Brinkmann U, Walther H; Application of tunable dye lasers to air pollution detection: Measurement of the atmospheric NO_2 concentrations by differential absorption, Appl. Phys.B, 3, 115-119, (1974)

Vanin N.V, Migulin A.V, Rybakov S.Yu; Lidar for atmospheric investigations by various methods, Sov. J. Quantum Electron., 6, 9, September (1976)

Appendix for Chapter 2

A2.1 Reflecting Telescope Image Sizes as a Function of Mirror Separation

A2.1.1 Image Size: Method 1

Figure A2.1 is a ray diagram indicating the maximum primary image size, of diameter d_I, which is formed by the extreme rays at the edge of the field. An intermediate parameter, g, is introduced to define the point where a parallel light ray passes through the secondary mirror. This allows equation (A2.1.1) to be written and equation (A2.1.2) to be formed from similar triangles. These relations are

$$d_I = D_s - 2g \qquad \text{(A2.1.1)}$$

and

$$g/(f - d) = (D_p - D_s)/2d, \qquad \text{(A2.1.2)}$$

which are combined in the simultaneous equation to give the maximum primary image size in the expression

$$d_I = (dD_p + fD_s - fD_p)/d. \qquad \text{(A2.1.3)}$$

The magnification of the primary image diameter by the action of a convex Cassegrain type secondary is given by parameters shown in figure A2.1 in the relation

$$m = (b + d)/(f - d), \qquad \text{(A2.1.4)}$$

which is applied with equation (A2.1.3) via the simple expression

$$d_i = m d_I \qquad \text{(A2.1.5)}$$

so that the final image diameter is given by

$$d_i = (b + d)(dD_p + fD_s - fD_p)/d(f - d). \qquad \text{(A2.1.6)}$$

A2.1.2 Image Size: Method 2

Final system image size for the full field of view can be derived directly from the trigonometrical study shown in the ray diagram of figure A2.2 The diagram shows the angles β, ω and γ, introduced for the purpose of analysis. The distance y relates the image radius to the secondary radius, expressed below. The angle between the secondary radius of curvature and the optical axis is given by

$$\tan\beta = D_s/4f'. \qquad \text{(A2.1.7)}$$

The edge ray of the field reaches the focal plane at an angle γ to the optical axis, given by

$$\tan\gamma = y/(b + d). \qquad \text{(A2.1.8)}$$

The same ray reaches the edge of the secondary mirror at an angle ω to the optical axis, giving the relation

$$\tan\omega = (D_p - D_s)/2d. \qquad \text{(A2.1.9)}$$

Image diameter at the system focal plane is introduced by

$$d_i = D_s - 2y. \qquad \text{(A2.1.10)}$$

The introduced angles are related by the symmetry about the secondary radius of curvature in the expression

$$\beta + \gamma = \omega - \beta \ . \qquad \text{(A2.1.11)}$$

Combination of equations (A2.1.7), (A2.1.8), (A2.1.9), (A2.1.10) and (A2.1.11) gives the system image diameter in the expression

$$d_i = D_s - 2(b + d).\tan[\tan^{-1}((D_p-D_s)/2d) - 2\tan^{-1}(D_s/4f')]. \qquad \text{(A2.1.12)}$$

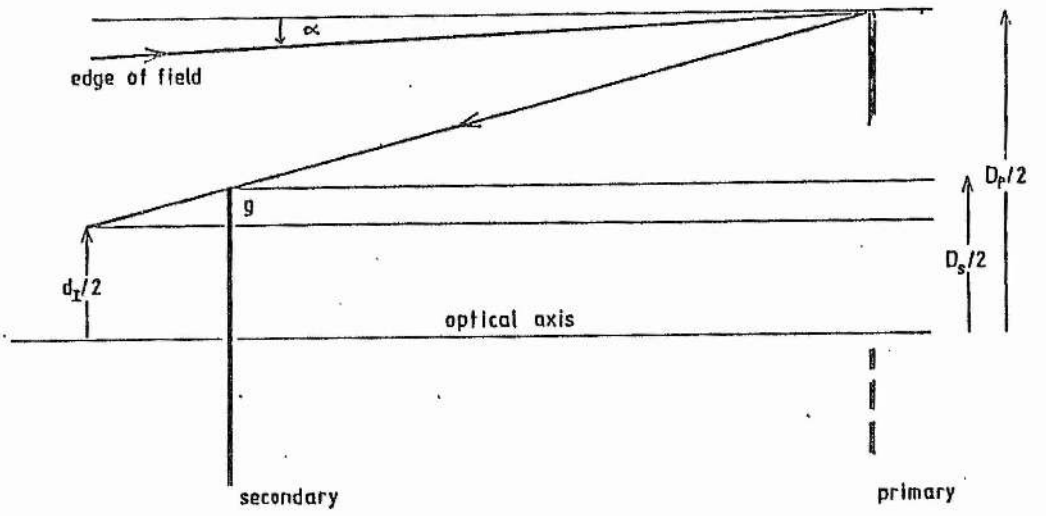

Figure A2.1 Primary Image Size Produced by the Edge Ray

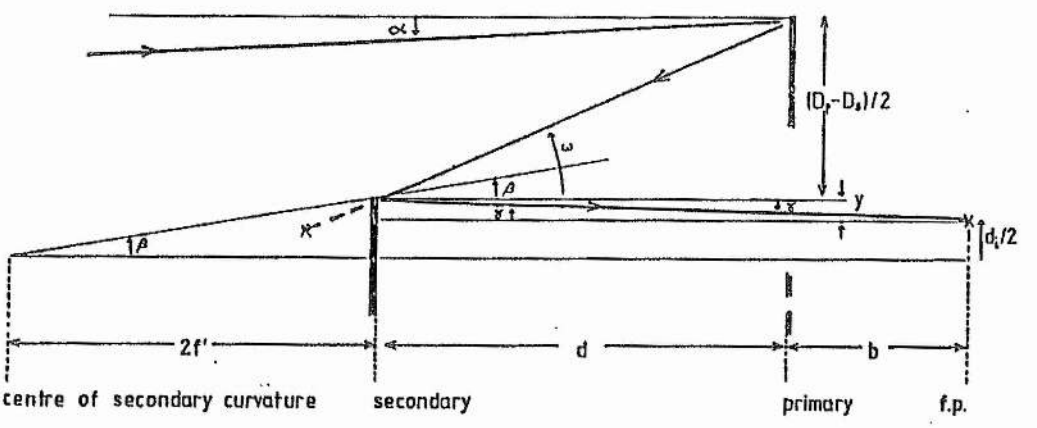

Figure A2.2 Primary and System Image Sizes Produced by the Edge Ray

Appendix for Chapter 3

A3.1 Gain Equation 1

The secondary emission coefficient at each stage is a function of the accelerating voltage V_s across the stage (figure A3.1.4) so that it is expressed as

$$\delta = A(V_s)^B; \qquad \text{(A3.1.1)}$$

A and B are constants which can be found from the gain and voltage specification for a particular tube. An example is given in sub-section 3.4.2. Examples of equation (A3.1.1) for two materials are

$$\delta = 0.2\ V_s^{0.7} \qquad \text{(A3.1.1a)}$$

and

$$\delta = 0.025\ V_s \qquad \text{(A3.1.1b)}$$

for CsSb and caesiated AgMgO dynodes, respectively (Photoelectronic Devices, Dance). The overall gain G of a multiplier chain of n dynodes is given by

$$G = f.g_1\delta_1.g_2\delta_2.....g_n\delta_n, \qquad \text{(A3.1.2)}$$

where f is the collection efficiency between the cathode and the first dynode and g_n are the collection efficiencies between each stage. In modern dynode design the latter have value near unity (100%)(EMI catalogue, 1979) allowing g_n to be set. The quantity f must not be ignored and is therefore

evaluated with the constant A when the equations are applied to a tube. Equation (A3.1.2) is re-expressed, setting g=1, to give

$$G = f.\prod_{i=1,n} \delta_i \qquad \text{(A3.1.2a)}$$

Equation (A3.1.1) gives the secondary emission coefficient so that (A3.1.2a) becomes

$$G = f.A^n[\prod_{i=1,n} V_{si}]^B. \qquad \text{(A3.1.3)}$$

The voltage across each stage is defined by a zener diode or by the interstage resistances as parts of a divider chain. If the total chain resistance is R_T and the voltage across it is V_R then the voltage across a stage resistance R_S is given by

$$V_s = V_R.R_S/R_T. \qquad \text{(A3.1.4)}$$

If the overall applied voltage, including V_Z across any zeners, is V_o then the chain voltage is given by

$$V_R = V_o - V_Z. \qquad \text{(A3.1.5)}$$

Equations (A3.1.3), (A3.1.4) and (A3.1.5) are applied more particularly to two likely examples of divider chains.

Figure 3.1.4 is the circuit diagram of the first example, a resistive divider chain with only the cathode to first dynode voltage set by a zener diode. The final resistor in the chain is between the anode and earth and does not enter the gain expression except as part of the total resistance

R_T. Equation (A3.1.4) is applied to denote the voltage across each of n-1 resistive stages so that equation (A3.1.3) becomes the series expression

$$G = f.A^n[V_{Zk}.V_R{}^{n-1}.R_2.R_3.....R_n/R_T{}^{n-1}]^B, \qquad (A3.1.6)$$

defining the gain of a tube for a known applied voltage. The cathode-to-first-dynode zener voltage is more clearly defined as V_{Zk}. Equation (A3.1.6) is re-arranged to give

$$V_R = [(G/f.A^n)^{1/B}.R_T{}^{n-1}/V_{Zk}.R_2.R_3....R_n]^{1/n-1}, \qquad (A3.1.7)$$

which, when used in conjunction with equation (A3.1.5) defines the overall voltage to be set for a desired gain.

A3.2 Gain Equation 2

The second divider circuit example, shown in figure 3.1.5, uses zener diodes to set final stage voltages, thus allowing variation of gain at high signal pulse currents without losing linearity of response. Response linearity is explained in section 3.2. The final zener voltage does not enter the gain expression except as a contributor to V_Z in equation (A3.1.5). If there are m+1 final stage zeners, with m of these active in providing gain, then equation (A3.1.3) becomes

$$G = f.A^n[V_{Zk}.V_{Z1}.....V_{Zm}.V_R{}^{n-m-1}.R_2.R_3....R_{n-m}/R_T{}^{n-m-1}]^B. \qquad (A3.2.1)$$

In the example in figure 3.1.5 there are three final stage zeners (m=2). Equation (A3.1.5) is applied to give

$$V_R = V_o - (V_{Zk} + V_{Z1} + V_{Z2} + V_{Z3}). \qquad (A3.2.2)$$

The voltage V_o, for a gain G, is given by equation (A3.2.2) in conjunction with equation (A3.2.1) which is re-arranged to give

$$V_R = [(G/f.A^n)^{1/B} R_T^{n-m-1}/V_{Zk}.V_{Z1}.....V_{Zm}.R_2.R_3.....R_{n-m}]^{1/n-m-1}. \qquad (A3.2.3)$$

A3.3 Prediction of the Transfer Function

If the cathode current function is i_k, the anode current function is i_a and the transfer function is H, then a convolution by the product of Fourier transforms gives

$$\mathcal{F} i_a = \mathcal{F} i_k . \mathcal{F} H \qquad (A3.3.1)$$

For the sake of analysis the anode current is predicted to have the form of a Gaussian function if the cathode current is nearly instantaneous (EMI, Photoelectric Cells and Photomultipliers, 1961). In fact an instantaneous optical pulse at the photocathode produces a cathode emission with the form of an exponential decay. However, the time constant, τ, of this is less than the time spread in transfer through the photomultiplier structure. Furthermore, the anode current, in fact, will rise more rapidly and fall more slowly than a Gaussian. An approximation is made to a delta function by assuming a pulse duration of Δt with a finite ordinate, shown in figure A3.2. If N electrons are emitted over the interval Δt then the cathode current is given by

$$i_k = Ne/\Delta t \qquad (A3.3.2)$$

A delta function is expressed by

$$\int_{-\infty}^{\infty} \delta(t)dt = 1. \qquad \text{(A3.3.3)}$$

Approximating this to the form of figure A3.2 gives

$$\delta(t)\,\Delta t \;\underset{t\to 0}{=}\; 1. \qquad \text{(A3.3.4)}$$

Application of equation (A3.3.4) to equation (A3.3.2) gives

$$\mathcal{F} i_k = Ne\,(0). \qquad \text{(A3.3.5)}$$

The Fourier transform of equation (A3.3.5) is given by

$$\mathcal{F}\, i_k = Ne. \qquad \text{(A3.3.6)}$$

The Gaussian anode current results from the cathode pulse after a gain of G. The anode current is predicted to be given by

$$i_a(t)_{\delta t} = (NeG/\sqrt{2\pi}\,\tau_2).\exp(-t^2/2\tau_2^2), \qquad \text{(A3.3.7)}$$

where τ_2, the standard deviation of the Gaussian, is given by

$$\tau_2 = fwhm/2.36. \qquad \text{(A3.3.8)}$$

The fwhm value is given by the photomultiplier manufacturer to denote time response. The Fourier transform of a Gaussian is another Gaussian, so that the anode current of equation (A3.3.7) becomes

$$\mathcal{F} i_a(t)_{\delta t} = NeG.\exp(-\omega^2\tau_2^2/2). \qquad (A3.3.9)$$

Convolution of equations (A3.3.5) and (A3.3.7) according to (A3.3.1), using equations (A3.3.6) and (A3.3.9) gives the pulse transfer function in frequency space as

$$\mathcal{F} H = G.\exp(-\omega^2\tau_2^2/2). \qquad (A3.3.10)$$

This is deconvolved to give

$$H = (G/\sqrt{2\pi}\,\tau_2).\exp(-t^2/2\tau_2^2), \qquad (A3.3.11)$$

which describes the time response and gain of the photomultiplier tube.

A3.4 Application of the Transfer Function to a Gaussian Optical Function

The transfer function of equation (A3.3.11) is applied in the transform of equation (A3.3.10) to the passage of an incident optical pulse function which has been approximated to a photon current of Gaussian form given by

$$n'(t) = (n_i/\sqrt{2\pi}\,\tau_o).\exp(-t^2/2\tau_o^2), \qquad (A3.4.1)$$

where n_i is the total number of photons in the pulse, given by

$$n_i = \int_{-\infty}^{\infty} n'dt; \qquad (A3.4.2)$$

τ_o is the standard deviation of the optical pulse, related to the fwhm of the

pulse by

$$\tau_o = \text{fwhm}/2.36. \qquad \text{(A3.4.3)}$$

The cathode response, denoted by an exponential decay time constant τ_1 shown in figure A3.3, is negligibly small compared with the response of the tube or the duration of the optical pulse so that the following limits apply.

$$\tau_1 \ll \tau_o, \qquad \text{(A3.4.4)}$$

$$\tau_1 \ll \tau_2. \qquad \text{(A3.4.5)}$$

The cathode current arises directly by equation (A3.4.1) with the electronic charge, e, and the quantum efficiency, η, to give

$$i_k = (\eta e n_i / \sqrt{2\pi}\ \tau_o).\exp(-t^2/2\tau_o^2). \qquad \text{(A3.4.6)}$$

This is used in convolution with the transfer function, resulting in the anode current function given by

$$i_a = [\eta e n_i G/\sqrt{2\pi}\ (\tau_o^2 + \tau_2^2)^{1/2}].\exp[-t^2/2(\tau_o^2 + \tau_2^2)]. \qquad \text{(A3.4.7)}$$

This shows the time spread effect imposed by a photomultiplier of time response given by equation (A3.3.8) on an optical pulse of duration given by equation (A3.4.3). That is, the standard deviation of the optical pulse, τ_o becomes $(\tau_2^2 + \tau_o^2)^{1/2}$ at the anode. This is more realistically expressed as

$$\text{fwhm}_{\text{pulse}} = (\text{fwhm}^2_{\text{pulse}} + \text{fwhm}^2_{\text{photomultiplier}})^{1/2}. \qquad \text{(A3.4.8)}$$

A3.5 Applying the Tube Transfer Function to Any Incident Distribution

The final time dependent anode current function is desired in an analysis of a detected optical pulse. The transfer function, H is applied in convolution via equation (A3.3.1) with the cathode current function, i_k, as in the prediction of A3.3 and the application to a Gaussian in A3.4. It is useful, especially when theorising on the lidar return distribution, to consider the optical function as the photon distribution n'(t), applying directly to the lidar equation of chapter 8. This is easily expressed as the cathode current output, given the conditions of (A3.4.4) and (A3.4.5), by the equality

$$i_k = n'(t)\eta e \qquad (A3.5.1)$$

The transfer equation is given, strictly, using (A3.3.1) as

$$\mathcal{F} i_a = \eta e \mathcal{F} n'(t) . \mathcal{F} H. \qquad (A3.5.2)$$

A3.6 Cathode Current Limitation; Fatigue and Heating

An excessive cathode current can cause heating, to the detriment of the cathode material. The cathode resistivity may limit the current to a level which is lower than intended. A manufacturer will state the maximum average cathode current, the maximum average cathode current density or just the maximum average anode current for a particular tube or tube type. The latter is more useful since the maximum cathode current, after a gain of perhaps 10^5 or 10^6 times, becomes a current which far exceeds the maximum anode current. In section 3.4 it is seen that the maximum average anode current does impose a stricter limit on incident photon energy than does the cathode restriction. It is necessary to be aware that restrictions are

usually expressed as the maximum average current, expressed for the cathode as $\bar{i}_{k\ max}$. In application to pulse detection the pulse current i_k', repetition rate S, and pulse duration (fwhm) are related to the average current $\bar{i}_k$ by

$$\bar{i}_k = i_k'.S.fwhm_{cathode} \qquad (A3.6.1)$$

where the pulse current can be given by the charge, Q, emitted from the cathode in the expression

$$i_k' = Q_k/fwhm_{cathode}. \qquad (A3.6.2)$$

This enables apparently large pulsed currents to pass without fear of cathode degradation, although it may be limited in some other way.

A3.7 Anode Current Limitation; Fatigue, Heating, Gain and Noise

An excessive current through the anode can cause deterioration. The anode is able to dissipate a power which, according to equation (A3.7.1) determines the maximum average anode current.

$$W_{max} = R_{anode}\bar{i}^2_{max}. \qquad (3.7.1)$$

In a worse case a very high anode current may heat the last few dynodes, resulting in loss of the active dynode material and it's deposit on the anode. In tubes which can take high anode current pulses the voltages on the last dynodes are set high to improve electron transfer, thus avoiding space-charge effects which would lower tube gain and increase the noise level.

The average anode current is given for a current pulse by the expression

$$\bar{i}_a = i_a' . S . fwhm_{anode}, \qquad (A3.7.2)$$

where i_a' is the anode pulse current, S is the repetition rate and $fwhm_{anode}$ is the pulse duration. The anode pulse current is given by

$$i_a' = Q_a / fwhm_{anode}. \qquad (A3.7.3)$$

A3.8 Interdynode Voltages; Feedback, Afterpulses and Saturation

The interdynode voltages set by the divider chain of resistors are limited to avoid ionization of residual gases within the tube. This limitation is as much a protection against insulation breakdown between stages. If the overall voltage is too high the anode leakage current to the cathode and dynodes may enhance the noise characteristic of the tube. Ionization may lead to optical and ionic feedback when the photons and ions produced strike the cathode, causing it to emit electrons. The signal pulse itself may stimulate this sort of feedback, leading to spurious after pulses, occurring in two categories. Those occurring a few microseconds later have their origin in stimulated ionic feedback which produces electrons from the cathode or dynodes. Those arising a few nanoseconds later are due to optical feedback where photons from the anode region strike the cathode. The degree of ionization creating these problems is reduced by cooling the tube to lower the vapour pressures of the residual gases, allowing higher voltages to be employed.

Adequate voltages must be applied between stages to ensure that there is no

loss of gain due to space charge effects. The voltage applied between the cathode and the first dynode is the most critical since it is the collection efficiency of the first dynode which most influences tube gain. For best results the cathode-to-first-dynode voltage is higher than the interdynode voltages, apart from the possibilty of higher final stage voltages for pulse applications. Efficiency is further improved by setting the first-to-second-dynode voltage higher than those of the intermediate stages. It is wise to stabilise the first stage voltage by zener diodes, enabling alteration of overall voltage without changing the original gain.

The cathode-to-first-dynode and the interdynode voltages are fixed by the voltage divider circuit which is designed with consideration of manufacturers stated maxima and recommended values for stage and overall voltages. These given values may vary between tubes for different detection purposes. For example, a fast linear focused tube uses higher cathode to first dynode and interdynode voltages than does a slower response tube with a venetian blind structure and the same diameter. Smaller diameter tubes use lower voltages, sufficient to maintain collection efficiencies in smaller area cathode and dynode structures. Recommended voltages and a standard circuit are usually used by the manufacturer in testing a photomultiplier and in detailing the specification of a particular device. Application of these parameters can be used to define the specification of a tube operated under modified conditions.

A3.9 Final Dynode Voltages in Pulsed Applications; Response Linearity

The ideal photomultiplier would maintain a constant gain over the whole range of detected optical intensities. However, a large current pulse at the anode and at the last few dynode stages is apt to produce space charge

saturation between these stages unless higher voltages are applied to transfer all the electrons and thus maintain constant gain. Greater resistances in the divider circuit supply the necessary final stage voltages. If the centre stage resistances are each of the value R then EMI recommend (EMI catalogue, 1979) final stage resistors of 1.25R, 1.5R, 1.75R and 3R in high current pulse detector circuits. The last four components of such a circuit are illustrated in figure 3.2.4 with parallel decoupling capacitors to further preserve linearity. This other effect of high current pulses on linearity is explained in appendix A3.12.

A3.10 Divider Chain: Response Linearity (Voltage and Current Consideration)

The linearity of response with respect to the d.c parameters of the divider circuit involves the average anode current, i_a and the divider circuit current, i_d. The anode current reduces the electron collecting potential by lowering the divider current at the final stages, especially the last stage, where more electrons are handled. The resistive stages and conventional currents shown in figure A3.4 are considered for the analysis below. Considering the n^{th} dynode and applying Kirchoff's rule for currents at a node ($\Sigma i = 0$) then the current from the dynode to the chain is given by

$$i_{dn}=\bar{i}_a- i_{n-1}, \qquad \text{(A3.10.1)}$$

where $\bar{i}_a$ is the average anode signal current between the last dynode and earth. i_{n-1} is the signal current to the previous stage. The divider chain current is i_d when the anode current is zero but it is reduced by i_{dn}, given in equation (A3.10.1) when an electron signal passes down the tube. Other dynode currents are present but the signal currents at those places

are insignificant when compared with that of the final stage. The final amplification is determined by the final resistor, R_n, which, for zero anode current, sets the final voltage given by

$$V_a = i_d R_n. \qquad \text{(A3.10.2)}$$

When an anode current is drawn, however, this final voltage is reduced by (3.10.1) to give

$$V_n = (i_d - \bar{i}_a + i_{n+1})R_n. \qquad \text{(A3.10.3)}$$

The current gain at the last dynode is given by the secondary emission coefficient, δ in the expression

$$\delta i_{n-1} = \bar{i}_a, \qquad \text{(A3.10.4)}$$

allowing equation (A3.10.3) to be re-expressed as

$$V_n = [i_d - \bar{i}_a(1 - 1/\delta)]R_n. \qquad \text{(A3.10.5)}$$

The preservation of gain linearity is considered to be a function of the final stage voltages and therefore of the currents involved. The prime factors in gain are the secondary emission coefficients as a function of the inter-stage voltages as, for example, in equation (A3.1.1a) for CsSb dynodes. If the linearity is defined by a change in voltage, ΔV, as a percentage or fraction of a voltage, V, then consider the change expressed by $\Delta V/V = 1\%$. Equation (A3.1.1a) gives $\delta = 5.024$ @ $V = 100$ volts and $\delta = 5.059$ @ $V = 101$ volts. The secondary emission coefficient changes by 0.7%, which is less than the corresponding voltage change, as is typical

where the voltage is raised to a power less than unity. Therefore, in using $\Delta V/V$ as a definition of linearity for design purposes then the limits are set for the worst case, a function of voltage. Departure from linearity is expressed by

$$\Delta V/V = (V_a - V_n)/V_a \qquad \text{(A3.10.6)}$$

which becomes, with equations (A3.10.2) and (A3.10.5)

$$\Delta V/V = \bar{i}_a(1 - 1/\delta)/i_d. \qquad \text{(A3.10.7)}$$

The extreme upper limit is applied at infinite secondary emission coefficient to give the departure from linearity, given by (A3.10.7) as

$$L = \bar{i}_a/i_d. \qquad \text{(A3.10.8)}$$

The maximum allowed departure from linearity is given when equation (A3.10.8) is expressed as the inequality

$$i_d \geqslant \bar{i}_a/L_{max}. \qquad \text{(A3.10.8a)}$$

Equation (A3.10.8a) is applied to a pulsed signal using equations (A3.7.2) and (A3.7.3) to define the average anode current in terms of the charge, Q_a at a repetition rate of S pps. The divider current is given by

$$i_d = V_R/R_T, \qquad \text{(A3.10.9)}$$

which is used in (A3.10.8a) to give the limit

$$L_{max} > (Q_a S)_{max} R_{T\ max} / V_{R\ min}. \qquad \text{(A3.10.10)}$$

To keep within the linearity requirement the divider current is maximised when large anode currents are expected. To this end, a divider chain of low resistance would be used but for circuit heating. Minimum circuit resistance can be set using expression (A3.10.11), which imposes a lower limit on divider chain resistance, the upper limit being imposed by linearity in (A3.10.10). Total chain resistance is set by the dissipative ability of the resistors according to

$$W > 2V_{R\ max}^2 / n_R R_T, \qquad \text{(A3.10.11)}$$

where W is the maximum average power rating per resistor, V_R is the maximum voltage likely across the chain of n_R resistors with total resistance R_T. The factor of two ensures that maximum power ratings are not exceeded. Equations (A3.10.10) and (A3.10.11) are combined to define the allowable range of divider chain resistances by

$$2V_{R\ max}^2 / n_R W < R_T < L V_{R\ min} / (Q_a S)_{max}. \qquad \text{(A3.10.12)}$$

The power ratings for individual resistors should not be exceeded. The value of $(Q_a S)_{max}$ may be given by the anode fatigue limitation, thereby defining the upper limit of R_T for a required linearity.

For the detection of high current pulses the introduction of decoupling capacitors (figure 3.2.4) means that the linearity requirement is preserved whilst the peak pulse current exceeds the dynode current. The average anode current must conform to the limit

$$\bar{i}_a << i_d, \qquad \text{(A3.10.13)}$$

whilst allowing the peak of pulse current i_a' to exist in the limit

$$i_{a'peak} >> i_d \qquad \text{(A3.10.14)}$$

at low pulse rate and short pulse width. The average current, $\bar{i}_a$ is connected to the pulse current by equation (A3.7.2).

Another way of maintaining the correct potential across the final stages is to use zener diodes on those stages in conjunction with the decoupling capacitors, as illustrated in figure A3.5. In this configuration it is possible to alter the overall tube gain by varying the overall voltage and therefore the intermediate stage voltages. The use of zener diodes eliminates the need for a very high divider chain current. Less stringent conditions apply to this case. The limits are

$$\bar{i}_a < i_d \qquad \text{(A3.10.15)}$$

under the conditions of

$$i_{a'peak} >> i_d \qquad \text{(A3.10.16)}$$

at low pulse rate and short pulse width.

A3.11 Effect of Load Resistance on Linearity

An upper limit must be imposed upon the load resistance because the potential developed across the load resistor, between the anode and the

earth, reduces the voltage between the anode and the last dynode. The final section of figure A3.4 is drawn in its equivalent form in figure A3.5. The current between the final dynode and the anode is assumed to form the circuit which satisfies Kirchoff's rule, giving the sum of potentials in

$$V = \Sigma iR. \qquad \text{(A3.11.1)}$$

This is applied to figure A3.5 to give the effective potential across the final stage as

$$V_n = R_n(i_d - \bar{i}_a - i_{n-1}) - R_L i_a. \qquad \text{(A3.11.2)}$$

This is different from that given in equation (A3.10.3), which was formed to consider a more critical limit on linearity and could ignore this effect as negligible in comparison. When no load resistance is present, then V_n is given by equation (A3.10.3). The change in the voltage in comparing equations (A3.11.2) and (A3.10.3) is $R_L i_a$. Thus the linearity, by constraint of load potential, is given by

$$L = i_a R_L / V_n. \qquad \text{(A3.11.3)}$$

A3.12 Divider Chain; Response Linearity in Pulse Detection

It has been mentioned that final stage capacitors can be included to preserve linearity when handling high current pulses. The limits on the divider chain specification and on the anode currents applying to such configurations were given in equations (A3.10.13) and (A3.10.14). This appendix explains why capacitors are used for this purpose and it derives expressions to be used in defining capacitor values in a specific

application.

A high current pulse at a final dynode or the anode will produce a significant positive potential with respect to earth, tending to reduce the existing accelerating negative potential (with respect to earth) between stages, thereby altering the gain of the device. This occurs because the electron flow towards the anode behaves as a current opposing the divider chain current, shown in figure A3.6. The result is appreciable at the final stages where charge pulses have been amplified. An immediately obvious way around this problem appears to be to increase the divider current so as to be far greater than any peak pulse current. However, the much lower resistances involved would lead to excessive circuit heating, a source of noise and fatigue even if the resistors could dissipate the power. The solution is to provide a capacitor across each of the final stages, as shown in figure 3.2.4, to compensate for fast rising changes in interstage potential. The d.c chain current charges the capacitor which is then partially discharged by the opposing charge pulse. The final stage to the anode is the most critical in this respect and is considered here (figure 3.2.4). If the signal pulse, of charge Q_a, would change the interstage voltage, V, by ΔV then the capacitor must have a value given by

$$C_d = Q_a / \Delta V. \qquad \text{(A3.12.1)}$$

The required linearity, as a fraction, is expressed as

$$L = \Delta V / V_n. \qquad \text{(A3.12.2)}$$

Equations (A3.12.1) and (A3.12.2) are combined to give

$$C_d = Q_a/V_n L, \qquad (A3.12.3)$$

where, more usefully, the lower limit is set by

$$C_d > Q_{a\ max}/V_{n\ min} L, \qquad (A3.12.4)$$

where $Q_{a\ max}$ is the maximum likely anode charge and $V_{n\ min}$ is the minimum likely final dynode to earth voltage. If V_n is maximised then the linearity is preserved for larger charge pulses. This is why higher value resistors are used to provide higher voltages on the final stages of high current pulse tubes. The upper limit on these capacitors is set by the charging time of the capacitor in relation to the signal pulse repetition rate. A capacitor is re-charged via the divider chain resistors, value R_c, linking it to the supply (figure 3.2.3). The re-charging time-constant must be less than the temporal pulse separation so that, if pulse repetition rate is given by S then the limit is given by

$$C_d < 1/R_c S. \qquad (A3.12.5)$$

In applying (A3.12.5) the upper limit on capacitance is quickly defined since R_c is fixed by the divider circuit configuration, decided upon by other considerations. The maximum likely value of S is taken. Equation (A3.12.4) is used after defining capacitance and minimum voltage to set the limit on $Q_{a\ max}$ and hence the signal intensity for a desired maximum linearity. The allowed signal level may or may not fall within the maximum set by the fatigue limitation, depending on the particular application.

Equations (A3.12.4) and (A3.12.5) apply to the final stage at the anode and they are used to set the final stage capacitor value first. The preceeding

stages can take lower capacitance values since the signal charge pulse is weaker. If the minimum s^{th} stage capacitance is $C_{ds\ min}$ and the minimum capacitance at the preceding stage is $C_{d(s-1)\ min}$, then they are related by their relative stage voltages and the $(s-1)^{th}$ secondary emission coefficient to give

$$C_{d(s-1)\ min} = C_{ds\ min} V_s / V_{s-1\ min}\ \delta_{s-1} \qquad \text{(A3.12.6)}$$

for the same L and $Q_{a\ max}$ as given in (A3.12.4) and for s in the range given by

$$2 \leqslant s \leqslant n. \qquad \text{(A3.12.7)}$$

The secondary emission coefficient δ_{s-1} is given by a form of equation (A3.1.1) as

$$\delta_{s-1} = A(V_{s-1})^B \qquad \text{(A3.12.8)}$$

where A and B are set by the particular tube in a method described in section 3.4.

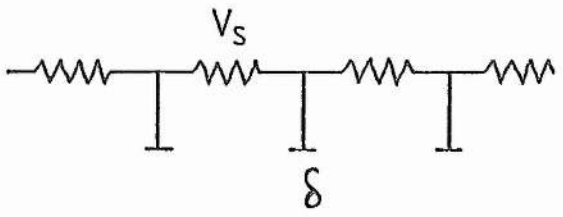

Figure A3.1 Secondary emission coefficient of a dynode after the accelerating voltage, V_s

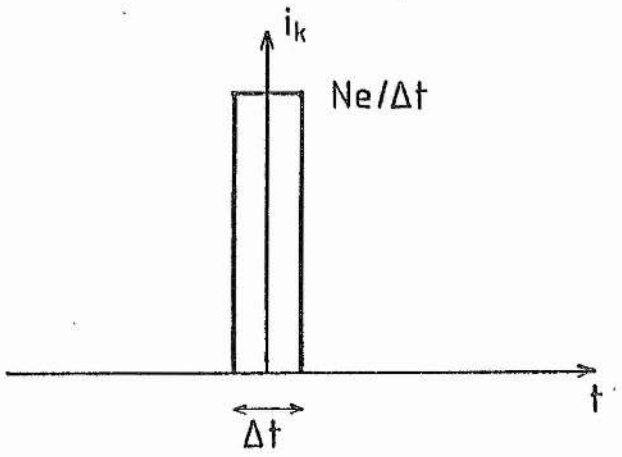

Figure A3.2 Cathode emission approximated to a delta function

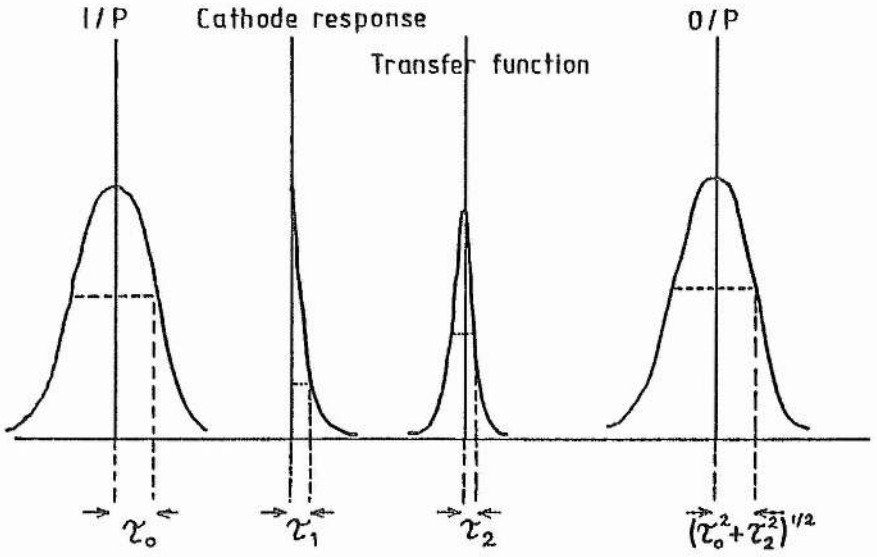

Figure A3.3 Time dependent functions involved in photomultiplier detection of a Gaussian pulse

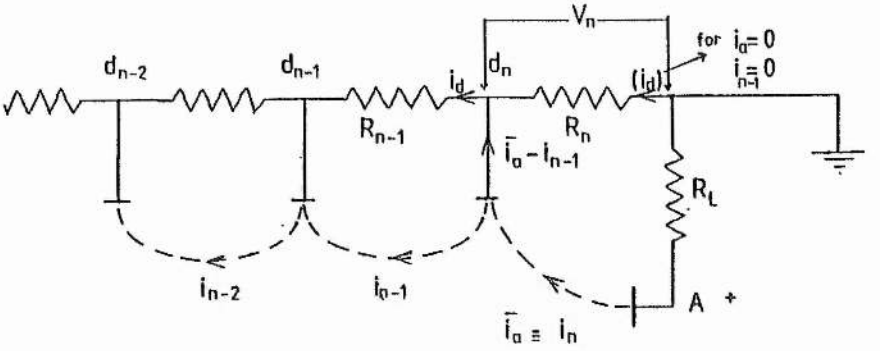

Figure A3.4 Effective currents in a circuit used in the analysis of photomultiplier resistive voltage divider circuit operation

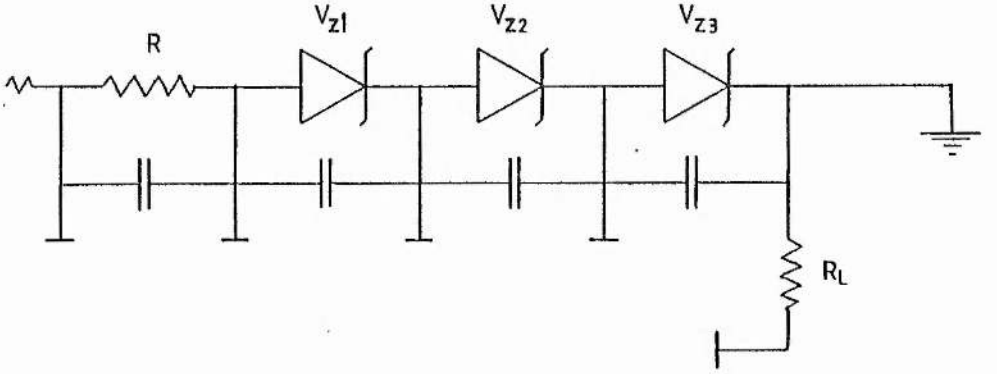

Figure A3.5 An example (EMI) of the final stage configuration of a photomultiplier divider circuit applied for high pulse current propagation and allowing variable gain

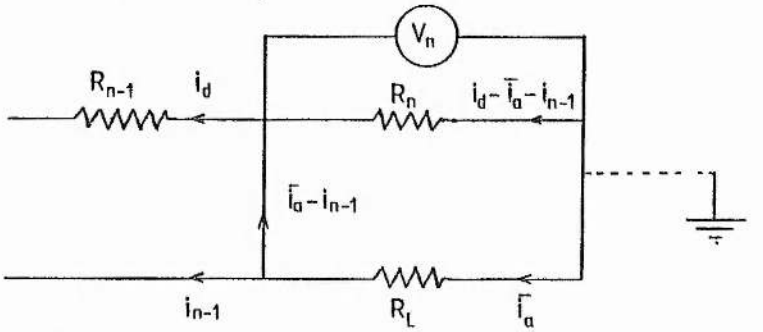

Figure A3.6 The equivalent O/P circuit of a photomultiplier

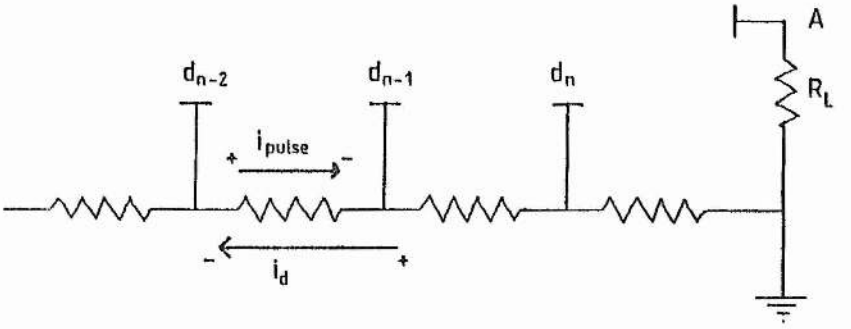

Figure A3.7 The negating effect of a detected pulse current on divider chain current, leading to voltage drop and gain and linearity reduction in a photomultiplier

Appendix for Chapter 5

A5.1 Theory of the Birefringent Filter

A birefringent crystal is optically anisotropic and exhibits two principal indices of refraction, n_f and n_s, along the fast (ordinary) and slow (extra-ordinary) axis, respectively. If polarized light of wavelength λ is transmitted through the crystal, its electric vector, E (see figure A5.1) is resolved into components along each axis so that the velocity along the fast axis is given by

$$v_f = c/n_f \qquad \text{(A5.1.1)}$$

and the velocity along the slow axis is given by

$$v_s = c/n_s. \qquad \text{(A5.1.2)}$$

The result of passage of radiation through the crystal is a phase difference between the two axis components, described by the difference in refractive indices, given as the relative retardation

$$n_1 = d_1 (n_f - n_s) / \lambda . \qquad \text{(A5.1.3)}$$

If the radiation now meets a polarizer, P_1, aligned with its axis parallel to the polarization of the original incident light (figure A5.2) the two components interfere. The spectral transmission of this birefringent filter, b_1 and polarizer, p_1 combination is given by

$$T_1 = \cos^2 \pi n_1 \qquad \text{(A5.1.4)}$$

and transmission peaks occur when n_1 is an integer, their separation increasing as crystal thickness is decreased. The spectrum is given in figure A5.3(a). The transmission minima reach zero if the angle between the incident E-vector and the fast axis is 45^o (figure A5.2), a criterion for good design. If a thicker birefringent element, b_2, is made with the next integer of relative retardation to the first, then the transmission through a polarizer, P_2 is given by

$$T_2 = \cos^2 2\pi n_1 \qquad \text{(A5.1.5)}$$

which is shown in figure A5.3(b). The resulting transmission of the pair is given in figure A5.3(c), showing the narrowing of each passband. A further, thicker element, b_3, to sharpen the peaks, would have a transmission through a polarizer, p_3, given by

$$T_3 = \cos^2 4\pi n_1 \qquad \text{(A5.1.6)}$$

and is shown in figure A5.3(d). The eventual transmission spectrum of the combination of $p_o b_1 p_1 b_2 p_2 b_3 p_3$ illustrated in figure A5.4 is given by equations (A5.1.4), (A5.1.5) and (A5.1.6) as

$$T = \cos^2 \pi n_1 . \cos^2 2\pi n_1 . \cos^2 4\pi n_1 \qquad \text{(A5.1.7)}$$

is shown in figure A5.3(e). Generally, if there are M b,p elements, the resultant transmission spectrum is given by

$$T = \cos^2(\pi n_1).\cos^2(2\pi n_1).....\cos^2(2^{M-1}\pi n_1), \qquad \text{(A5.1.8)}$$

where n_1 is given by (A5.1.3) and d_1 is the thickness of the thinnest element. The passband separation is determined by the thinnest element and the passband width by the thickest element. The thickness of the M^{th} element is given by

$$d_M = 2^{M-1}d_1 \qquad \text{(A5.1.9)}$$

Filter tunability can be achieved by inserting a quarter-wave retarder ($\lambda/4$) between the birefringent element and polarizer of each stage (figure A5.5) to change the relative retardation (Evans, 1949). Thus, the phase difference after each birefringent element is changed by angle, ρ_M, between the axis of the M^{th} quarter-wave plate and the axis of the immediately following polarizer. Each respective angle is given by

$$\rho_M = 2^{M-1}\rho_1, \qquad \text{(A5.1.10)}$$

where ρ_1 is the angle between the axes of p_1 and the preceeding quarter-wave plate. The general transmission spectrum of A5.1.8 now becomes

$$T = \cos^2(\pi n_1 - \rho_1).\cos^2(2\pi n_1 - 2\rho_1).....\cos^2(2^{M-1}\pi n_1 - 2^{M-1}\rho_1). \qquad \text{(A5.1.11)}$$

A5.2 Bandwidth and Separation of Birefringent Filter Transmission Peaks

The minimum pass bandwidth of the complete simple birefringent filter is given by the thickest birefringent element having a transmission function according to the final component of equation A5.1.10 and drawn in figure A5.3(d). The bandwidth is expressed as half the peak separation of the

characteristic shown in A5.3(d) giving the expression

$$B_\lambda = (\lambda_1 - \lambda_2)/2. \qquad \text{(A5.2.1)}$$

Using equation (A5.1.3) with the final component of equation (A5.1.11), the peaks occur when the transmission function satisfies the requirement

$$2^{M-1}\pi d_1(n_f - n_s)/\lambda - 2^{M-1}\rho_1 = 0, \pi, 2\pi, 3\pi, 4\pi \text{ etc.} \qquad \text{(A5.2.2)}$$

Equation (A5.2.2) is repeated for adjacent wavelength peaks at λ_1 and λ_2, separated in phase by π. Thus, the wavelength difference is given as

$$\lambda_1 - \lambda_2 = \lambda_1 \lambda_2/(2^{M-1}d_1(n_f - n_s)), \qquad \text{(A5.2.3)}$$

which is used with equation (A5.2.1) to give minimum bandwidth as

$$B_\lambda = \lambda_1^2/(2^M d_1(n_f - n_s) + 2\lambda_1), \qquad \text{(A5.2.4a)}$$

which can be re-expressed as

$$2^M = (\lambda_1^2/B_\lambda - 2\lambda_1)/d_1(n_f - n_s) \qquad \text{(A5.2.4b)}$$

to give the number of elements required for a given bandwidth.

Passband separation is given by the thinnest element of the filter, using the transmission characteristic of the first component of equation (A5.1.11). The characteristic is drawn in figure A5.3(a) showing peaks at wavelengths λ_a and λ_b. Thus the peak separation is given by

$$\Delta\lambda = \lambda_a - \lambda_b. \qquad \text{(A5.2.5)}$$

These passband peaks occur when the transmission function contained within equation (A5.1.11) satisfies the requirement

$$\pi d_1(n_f - n_s)/\lambda - \rho_1 = 0, \pi, 2\pi, 3\pi, 4\pi \text{ etc.} \qquad \text{(A5.2.6)}$$

When (A5.2.6) is applied for adjacent peaks at λ_a and λ_b, then equation (A5.2.5) becomes

$$\Delta\lambda = \lambda_a^2/(d_1(n_f - n_s) + \lambda_a), \qquad \text{(A5.2.7a)}$$

which can be re-expressed as

$$d_1 = (\lambda_a^2/\Delta\lambda - \lambda_a)/(n_f - n_s) \qquad \text{(A5.2.7b)}$$

to give the width requirement on the thinnest plate, given the passband separation.

A5.3 Tuning the Simple Birefringent Filter

The transmission spectrum of the filter is described by equation (A5.1.11). Tunability is obtained by varying the angle between the units. The relative angular rotation between each respective unit of elements is related to the corresponding wavelength shift in the following analysis.

A5.3(a) Tuning Between Wavelengths

The first term of equation (A5.1.11) defines the passband separation and the final term defines the passband width. Equation (A5.2.2) gives the

condition for transmission at wavelengths λ as the argument of the final $\cos^2$ term of equation (A5.1.11), given in the expression

$$2^{M-1}\pi d_1(n_f - n_s)/\lambda - 2^{M-1}\rho_1) = 0, \pi, 2\pi, 3\pi, \text{etc.} \qquad (A5.3.1)$$

The wavelengths of the passbands are to be shifted by changing the angle between the first two units from ρ_1 to $\rho_1+\Delta\rho$ or, more generally, by changing the angle between the M^{th} quarter-wave plate and the following polarizer to give the respective angles, ρ_M, given by

$$\rho_M = 2^{M-1}(\rho_a + \Delta\rho) \text{ radians}, \qquad (A5.3.2)$$

where ρ_a is the angle required to set a transmission peak at wavelength λ_a. The first unit remains fixed in relation to the optical axis. The wavelength changes are such that the argument of the $\cos^2$ term in (A5.1.11) (ie. the right-hand side of equation (A5.3.1)) remains constant. Thus, according to (A5.3.1), if the angle is increased, the wavelength peak values are decreased. An increase in angle ρ, according to equation (A5.3.2), will reduce a peak wavelength at λ_a to a peak at λ_ρ, expressed as a wavelength shift in

$$\Delta\lambda_\rho = \lambda_\rho - \lambda_a \qquad (A5.3.3)$$

with the inequality

$$\lambda_\rho < \lambda_a. \qquad (A5.3.4)$$

The condition for transmission maxima, equation (A5.3.1), is applied for an original wavelength peak at λ_a and is repeated for a new wavelength

peak, at λ_ρ. The expressions are equated to give

$$\pi d_1(n_f - n_s)/\lambda_a - \rho_a = \pi d_1(n_f - n_s)/\lambda_\rho - (\rho_a + \Delta\rho). \qquad (A5.3.5)$$

Equation (A5.3.5) becomes

$$\Delta\rho = \pi d_1(n_f - n_s)(\lambda_a - \lambda_\rho)/(\lambda_a\lambda_\rho), \qquad (A5.3.6)$$

allowing the angle change, $\Delta\rho$, to be determined for a desired wavelength shift, $\Delta\lambda_\rho$, independent of the original angle, ρ_a, set for tuning to λ_a. The analysis can be followed, equivalently, from the first term of the transmission equation. Equation (A5.3.6) can be expressed generally in terms of the wavelength shift and the original wavelength, for all angles, using (A5.3.2), as

$$\Delta\rho_M = 2^{M-1}\pi d_1(n_f - n_s)\Delta\lambda_\rho / \lambda_a^2. \qquad (A5.3.7)$$

The angular position about the instrument axis, for the M^{th} polarizer axis (see figure A5.5, p_M) is given by the sum of the relative rotations, up to and including the M^{th} units, in

$$\theta_M = \sum_M \rho_M = \sum_M 2^{M-1}(\rho_a + \Delta\rho), \qquad (A5.3.8)$$

defined by the angular setting, ρ_a, required to tune to wavelength λ_a and by the further rotation, $\Delta\rho$, desired to tune from λ_a to wavelength λ_ρ.

A5.3(b) Tuning to a Specific Wavelength

The angle ρ_1, allowing transmission of wavelength λ, is defined by the first term of equation (A5.1.11), where the argument satisfies the integer

condition given by (A5.2.6) as

$$n = d_1(n_f - n_s)/\lambda - \rho_1/\pi . \qquad (A5.3.9)$$

The integer, n, is calculated for the transmission peak nearest to the wavelength λ_a, allowing minimal angular shift to tune to λ_a. The value for λ_a is inserted into (A5.3.9), setting $\rho_1 = 0$, and the integer value is taken to give n. The angular setting required to tune to λ_a, maintaining the integer requirement, is given by equation (A5.3.9), applied at λ_a. Thus, the angle ρ_a, by (A5.3.9) ($\rho_1 \equiv \rho_a$), is used in equation (A5.3.2) (setting $\Delta\rho = 0$) to calculate the respective angles between the units of the birefringent filter, given as

$$\rho_M = 2^{M-1}(\pi d_1(n_f - n_s)/\lambda_a) - \pi . \text{integer value of } 2^{M-1}(d_1(n_f - n_s)/\lambda_a) \qquad (A5.3.10)$$

Equation (A5.3.10) can be used to define the angles between the quarter-wave plate and the respective following polarizers, necessary for tuning to a desired wavelength. This permits variation of the phase angle ($n\pi$). However, for tuning over a shorter wavelength period, from a set wavelength, it is more convenient to use the same transmission peak, maintaing a constant phase angle ($n\pi$). The calculations for constant phase wavelength shifting are given in A5.3(a).

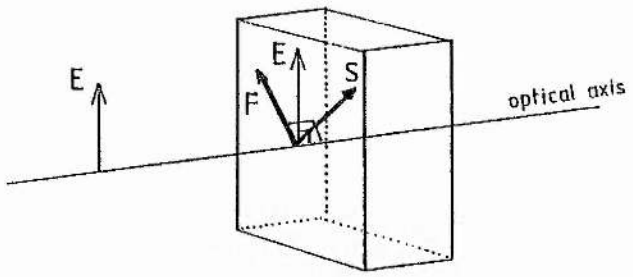

Figure A5.1 The fast (ordinary), F, and the slow (extra-ordinary), S, axes of a birefringent crystal, including the polarized light vector, E.

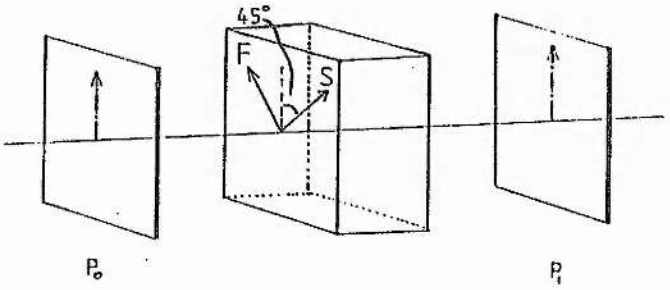

Figure A5.2 A birefringent plate and polarizers as the basic tuning element.

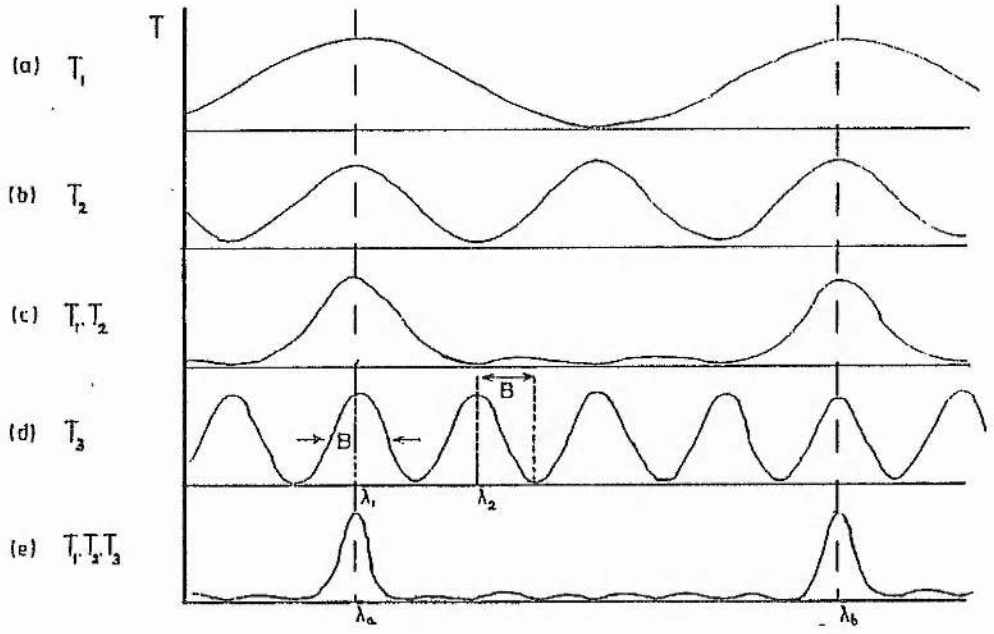

Figure A5.3 Transmission characteristics of the elements of a simple, 3 element, birefringent filter.

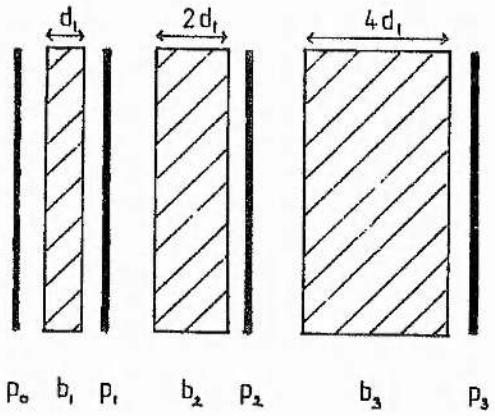

Figure A5.4 A simple, 3 unit, birefringent filter.

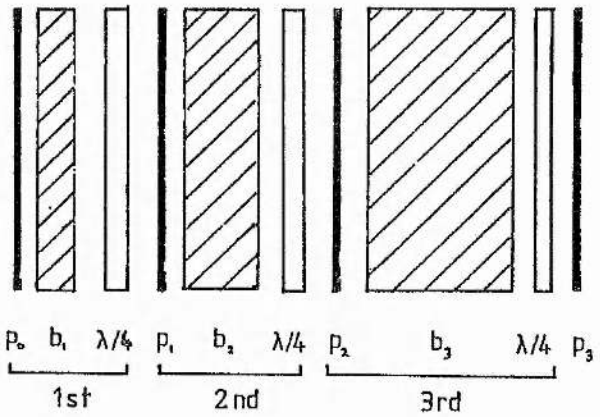

Figure A5.5 A simple, 3 unit, tunable birefringent filter.

A6.1(a) DIAL Test Program (in machine code)

```
A000  A2 00     LDX @£00      \
A002  BD 00 A6  LDA £A600,X    |
A005  20 F4 FF  JSR £FFF4      | print menu
A008  E8        INX            |
A009  C9 00     CMP @£00       |
A00B  D0 F5     BNE P-£09     /
A00D  20 E6 FF  JSR £FFE6     \
A010  C9 31     CMP @£31       |
A012  F0 3A     BEQ P+£3C      |
A014  C9 32     CMP @£32       |
A016  D0 03     BNE P+£05      |
A018  4C E0 A0  JMP P+£00C8    |
A01B  C9 33     CMP @£33       |
A01D  D0 03     BNE P+£05      |
A01F  4C 17 A1  JMP P+£00F8    | menu select
A022  C9 34     CMP @£34       |
A024  D0 03     BNE P+£05      |
A026  4C 2B A1  JMP P+£0105    |
A029  C9 35     CMP @£35       |
A02B  D0 03     BNE P+£05      |
A02D  4C C2 A2  JMP P+£0295    |
A030  C9 36     CMP @£36       |
A032  D0 03     BNE P+£05      |
A034  4C 90 A4  JMP P+£045C   /
A037  A2 00     LDX @£00      error key start
A039  BD 30 A4  LDA £A430,X    |
A03C  20 F4 FF  JSR £FFF4      |
A03F  E8        INX            |
A040  C9 00     CMP @£00       |
A042  D0 F5     BNE P-£09      |
A044  20 E6 FF  JSR £FFE6      |
A047  C9 0D     CMP @£0D       |
A049  D0 F9     BNE P-£05      |
A04B  4C 00 A0  JMP P-£004B   error key end
A04E  EA        NOP
A04F  EA        NOP
A050  EA        NOP
A051  EA        NOP
A052  EA        NOP
A053  EA        NOP
A054  EA        NOP
A055  EA        NOP
A056  EA        NOP
A057  A9 00     LDA @£00      port test start
A059  8D 0C B8  STA £B80C      |
A05C  A9 FF     LDA @£FF       |
A05E  8D 02 B8  STA £B802      |
A061  8D 03 B8  STA £B803      |
A064  A9 00     LDA @£00       |
A066  A2 00     LDX @£00       |
A068  38        SEC            |
A069  2A        ROL A          |
A06A  8D 01 B8  STA £B801      |
A06D  8D 00 B8  STA £B800      |
A070  85 80     STA £80        |
A072  A9 41     LDA @£41       |
A074  85 81     STA £81        |
A076  AD 01 B8  LDA £B801      |
A079  C5 80     CMP £80        |
A07B  D0 2A     BNE P+£2C      |
A07D  A9 42     LDA @£42       |
A07F  85 81     STA £81        |
A081  AD 00 B8  LDA £B800      |
A084  C5 80     CMP £80        |
A086  D0 1F     BNE P+£21      |
A088  A2 00     LDX @£00       |
A08A  BD 98 A0  LDA £A098,X    |
A08D  20 F4 FF  JSR £FFF4      |
A090  E8        INX            |
A091  C9 00     CMP @£00       |
A093  D0 F5     BNE P-£09      |
A095  4C 44 A0  JMP P-£0051
```

```
A098  0A        ASL A
A099  0D 50 4F  ORA £4F50
A09C  52        ???
A09D  54        ???
A09E  20 4F 4B  JSR £4B4F
A0A1  41 59     EOR (£59,X)
A0A3  0A        ASL A
A0A4  0D 00 00  ORA £0000
A0A7  A2 00     LDX @£00
A0A9  BD CE A0  LDA £A0CE,X
A0AC  20 F4 FF  JSR £FFF4
A0AF  E8        INX
A0B0  C9 00     CMP @£00
A0B2  D0 F5     BNE P-£09
A0B4  A5 B1     LDA £B1
A0B6  20 F4 FF  JSR £FFF4
A0B9  A5 B0     LDA £B0
A0BB  18        CLC
A0BC  69 30     ADC @£30
A0BE  20 F4 FF  JSR £FFF4
A0C1  A9 0D     LDA @£0D
A0C3  20 F4 FF  JSR £FFF4
A0C6  A9 0A     LDA @£0A
A0C8  20 F4 FF  JSR £FFF4
A0CB  4C 44 A0  JMP P-£00B7
A0CE  0D 0A 50  ORA £500A
A0D1  4F        ???
A0D2  52        ???
A0D3  54        ???
A0D4  20 46 41  JSR £4146
A0D7  49 4C     EOR @£4C
A0D9  20 41 54  JSR £5441
A0DC  20 00 00  JSR £0000
A0DF  00        BRK
A0E0  A2 00     LDX @£00
A0E2  BD F0 A0  LDA £A0F0,X
A0E5  20 F4 FF  JSR £FFF4
A0E8  E8        INX
A0E9  C9 00     CMP @£00
A0EB  D0 F5     BNE P-£09
A0ED  4C 44 A0  JMP P-£00A9
A0F0  0D 0A 57  ORA £570A
A0F3  48        PHA
A0F4  45 4E     EOR £4E
A0F6  20 54 45  JSR £4554
A0F9  53        ???
A0FA  54        ???
A0FB  20 43 4F  JSR £4F43
A0FE  4D 50 4C  EOR £4C50
A101  45 54     EOR £54
A103  45 20     EOR £20
A105  50 52     BVC P+£54
A107  45 53     EOR £53
A109  53        ???
A10A  20 52 45  JSR £4552
A10D  54        ???
A10E  55 52     EOR £52,X
A110  4E 0A 0D  LSR £0D0A
A113  00        BRK
A114  00        BRK
A115  00        BRK
A116  00        BRK
A117  A9 02     LDA @£02
A119  20 F4 FF  JSR £FFF4
A11C  A2 20     LDX @£20
A11E  8A        TXA
A11F  20 F4 FF  JSR £FFF4
A122  E8        INX
A123  8A        TXA
A124  C9 7B     CMP @£7B
A126  D0 F7     BNE P-£07
A128  4C 44 A0  JMP P-£00E4
A12B  A2 00     LDX @£00
A12D  BD 3B A1  LDA £A13B,X
A130  20 F4 FF  JSR £FFF4
A133  E8        INX
A134  C9 00     CMP @£00
A136  D0 F5     BNE P-£09
A138  F0 1B     BEQ P+£1D
A13A  FF        ???
```

data "port okay"

data "port fail at"

port test end
keyboard test start

data "when test complete
press return"

keyboard test end

printer test start

printer test end
memory test start

```
A13B  0A        ASL A
A13C  0D 45 4E  ORA £4E45
A13F  54        ???
A140  45 52     EOR £52
A142  20 53 54  JSR £5453
A145  41 52     EOR (£52,X)
A147  54        ???
A148  20 41 44  JSR £4441
A14B  44        ???
A14C  52        ???
A14D  45 53     EOR £53
A14F  53        ???
A150  20 23 00  JSR £0023
A153  00        BRK
A154  00        BRK
```

data "enter start address"

```
A155  A2 04     LDX @£04
A157  A0 00     LDY @£00
A159  20 E6 FF  JSR £FFE6
A15C  85 82     STA £82
A15E  38        SEC
A15F  E9 30     SBC @£30
A161  A8        TAY
A162  38        SEC
A163  E9 0A     SBC @£0A
A165  30 06     BMI P+£08
A167  A5 82     LDA £82
A169  38        SEC
A16A  E9 37     SBC @£37
A16C  A8        TAY
A16D  98        TYA
A16E  95 83     STA £83,X
A170  CA        DEX
A171  8A        TXA
A172  D0 E5     BNE P-£19
A174  A2 00     LDX @£00
A176  BD 83 A1  LDA £A183,X
A179  20 F4 FF  JSR £FFF4
A17C  E8        INX
A17D  C9 00     CMP @£00
A17F  D0 F5     BNE P-£09
A181  F0 10     BEQ P+£12
A183  0A        ASL A
A184  0D 45 4E  ORA £4E45
A187  44        ???
A188  20 41 44  JSR £4441
A18B  44        ???
A18C  52        ???
A18D  45 53     EOR £53
A18F  53        ???
A190  20 23 00  JSR £0023
```

data "enter end address"

```
A193  A2 04     LDX @£04
A195  A0 00     LDY @£00
A197  20 E6 FF  JSR £FFE6
A19A  85 82     STA £82
A19C  38        SEC
A19D  E9 30     SBC @£30
A19F  A8        TAY
A1A0  38        SEC
A1A1  E9 0A     SBC @£0A
A1A3  30 06     BMI P+£08
A1A5  A5 82     LDA £82
A1A7  38        SEC
A1A8  E9 37     SBC @£37
A1AA  A8        TAY
A1AB  98        TYA
A1AC  95 87     STA £87,X
A1AE  CA        DEX
A1AF  8A        TXA
A1B0  D0 E5     BNE P-£19
A1B2  A5 87     LDA £87
A1B4  0A        ASL A
A1B5  0A        ASL A
A1B6  0A        ASL A
A1B7  0A        ASL A
A1B8  18        CLC
A1B9  65 86     ADC £86
A1BB  85 86     STA £86
A1BD  A5 85     LDA £85
```

```
A1BF  0A        ASL A
A1C0  0A        ASL A
A1C1  0A        ASL A
A1C2  0A        ASL A
A1C3  18        CLC
A1C4  65 84     ADC £84
A1C6  85 85     STA £85
A1C8  A5 8B     LDA £8B
A1CA  0A        ASL A
A1CB  0A        ASL A
A1CC  0A        ASL A
A1CD  0A        ASL A
A1CE  18        CLC
A1CF  65 8A     ADC £8A
A1D1  85 8A     STA £8A
A1D3  A5 89     LDA £89
A1D5  0A        ASL A
A1D6  0A        ASL A
A1D7  0A        ASL A
A1D8  0A        ASL A
A1D9  18        CLC
A1DA  65 88     ADC £88
A1DC  85 89     STA £89
A1DE  A0 A0     LDY @£A0
A1E0  B1 85     LDA (£85),Y
A1E2  85 84     STA £84
A1E4  A7 AA     LDA @£AA
A1E6  91 85     STA (£85),Y
A1E8  B1 85     LDA (£85),Y
A1EA  C9 AA     CMP @£AA
A1EC  D0 26     BNE P+£28
A1EE  A9 55     LDA @£55
A1F0  91 85     STA (£85),Y
A1F2  B1 85     LDA (£85),Y
A1F4  C9 55     CMP @£55
A1F6  D0 1C     BNE P+£1E
A1F8  A5 84     LDA £84
A1FA  91 85     STA (£85),Y
A1FC  A5 85     LDA £85
A1FE  C5 89     CMP £89
A200  F0 05     BEQ P+£07
A202  E6 85     INC £85
A204  4C DE A1  JMP P-£0026
A207  A5 86     LDA £86
A209  C5 8A     CMP £8A
A20B  F0 7B     BEQ P+£7D
A20D  E6 86     INC £86
A20F  E6 85     INC £85
A211  4C DE A1  JMP P-£0033
A214  A2 00     LDX @£00
A216  BD 23 A2  LDA £A223,X
A219  20 F4 FF  JSR £FFF4
A21C  EB        INX
A21D  C9 00     CMP @£00
A21F  D0 F5     BNE P-£09
A221  F0 1E     BEQ P+£20
A223  0A        ASL A
A224  0D 4D 45  ORA £454D
A227  4D 4F 52  EOR £524F
A22A  59 20 46  EOR £4620,Y
A22D  41 49     EOR (£49,X)
A22F  4C 20 41  JMP £4120
A232  54        ???
A233  20 23 00  JSR £0023
A236  00        BRK
A237  FF        ???
A238  FF        ???
A239  FF        ???
A23A  FF        ???
A23B  FF        ???
A23C  FF        ???
A23D  FF        ???
A23E  FF        ???
A23F  FF        ???
A240  FF        ???
A241  A5 86     LDA £86
```

data "memory fail at £"

```
A243  4A        LSR A
A244  4A        LSR A
A245  4A        LSR A
A246  4A        LSR A
A247  AA        TAX
A248  18        CLC
A249  69 30     ADC @£30
A24B  A8        TAY
A24C  38        SEC
A24D  8A        TXA
A24E  E9 0A     SBC @£0A
A250  30 05     BMI P+£07
A252  8A        TXA
A253  18        CLC
A254  69 37     ADC @£37
A256  A8        TAY
A257  98        TYA
A258  20 F4 FF  JSR £FFF4
A25B  A5 86     LDA £86
A25D  29 0F     AND @£0F
A25F  AA        TAX
A260  18        CLC
A261  69 30     ADC @£30
A263  A8        TAY
A264  38        SEC
A265  8A        TXA
A266  E9 0A     SBC @£0A
A268  30 05     BMI P+£07
A26A  8A        TXA
A26B  18        CLC
A26C  69 37     ADC @£37
A26E  A8        TAY
A26F  98        TYA
A270  20 F4 FF  JSR £FFF4
A273  A9 30     LDA @£30
A275  20 F4 FF  JSR £FFF4
A278  20 F4 FF  JSR £FFF4
A27B  A9 0D     LDA @£0D
A27D  20 F4 FF  JSR £FFF4
A280  A9 0A     LDA @£0A
A282  20 F4 FF  JSR £FFF4
A285  4C 44 A0  JMP P-£0241
A288  A2 00     LDX @£00
A28A  BD 98 A2  LDA £A298,X
A28D  20 F4 FF  JSR £FFF4
A290  E8        INX
A291  C9 00     CMP @£00
A293  D0 F5     BNE P-£09
A295  4C 44 A0  JMP P-£0251
A298  0A        ASL A
A299  0D 4D 45  ORA £454D
A29C  4D 4F 52  EOR £524F
A29F  59 20 4F  EOR £4F20,Y
A2A2  4B        ???
A2A3  41 59     EOR (£59,X)
A2A5  0A        ASL A
A2A6  0D 00 00  ORA £0000
A2A9  00        BRK
A2AA  00        BRK
A2AB  00        BRK
A2AC  FF        ???
A2AD  FF        ???
A2AE  FF        ???
A2AF  FF        ???
A2B0  FF        ???
A2B1  FF        ???
A2B2  FF        ???
A2B3  FF        ???
A2B4  FF        ???
A2B5  FF        ???
A2B6  FF        ???
A2B7  FF        ???
A2B8  FF        ???
A2B9  FF        ???
A2BA  FF        ???
A2BB  FF        ???
A2BC  FF        ???
A2BD  FF        ???
A2BE  FF        ???
A2BF  FF        ???
A2C0  68        PLA
A2C1  40        RTI
```

data "memory okay"

memory test end ↑

```
A2C2  A9 A2     LDA @£A2          interface test start
A2C4  8D 05 02  STA £0205                  ↓
A2C7  A9 C0     LDA @£C0
A2C9  8D 04 02  STA £0204
A2CC  A9 7F     LDA @£7F
A2CE  8D 02 B8  STA £B802
A2D1  AD 0B 02  LDA £020B
A2D4  85 80     STA £80
A2D6  18        CLC
A2D7  69 03     ADC @£03
A2D9  8D 08 02  STA £0208
A2DC  A2 00     LDX @£00
A2DE  BD EB A2  LDA £A2EB,X
A2E1  20 F4 FF  JSR £FFF4
A2E4  E8        INX
A2E5  C9 00     CMP @£00
A2E7  D0 F5     BNE P-£09
A2E9  F0 2A     BEQ P+£2C
A2EB  0A        ASL A
A2EC  0D 72 65  ORA £6572
A2EF  73        ???
A2F0  65 74     ADC £74
A2F2  20 50 52  JSR £5250
A2F5  45 53     EOR £53          data "RESET press any key"
A2F7  53        ???
A2F8  20 41 4E  JSR £4E41
A2FB  59 20 4B  EOR £4B20,Y
A2FE  45 59     EOR £59
A300  0A        ASL A
A301  0D 00 00  ORA £0000
A304  00        BRK
A305  00        BRK
A306  00        BRK
A307  00        BRK
A308  00        BRK
A309  00        BRK
A30A  00        BRK
A30B  00        BRK
A30C  00        BRK
A30D  00        BRK
A30E  00        BRK
A30F  00        BRK
A310  00        BRK
A311  00        BRK
A312  00        BRK
A313  00        BRK
A314  00        BRK
A315  20 E6 FF  JSR £FFE6
A318  C9 0D     CMP @£0D
A31A  F0 12     BEQ P+£14
A31C  A9 00     LDA @£00
A31E  8D 00 B8  STA £B800
A321  A9 20     LDA @£20
A323  8D 00 B8  STA £B800
A326  A9 00     LDA @£00
A328  8D 00 B8  STA £B800
A32B  4C 15 A3  JMP P-£0016
A32E  A2 00     LDX @£00
A330  BD 3D A3  LDA £A33D,X
A333  20 F4 FF  JSR £FFF4
A336  E8        INX
A337  C9 00     CMP @£00
A339  D0 F5     BNE P-£09
A33B  F0 2A     BEQ P+£2C
A33D  0A        ASL A
A33E  0D 6F 6E  ORA £6E6F
A341  20 6C 69  JSR £696C
A344  6E 65 20  ROR £2065
A347  50 52     BVC P+£54
A349  45 53     EOR £53          data "ON LINE press any key"
A34B  53        ???
A34C  20 41 4E  JSR £4E41
A34F  59 20 4B  EOR £4B20,Y
A352  45 59     EOR £59
A354  0A        ASL A
A355  0D 00 00  ORA £0000
A358  00        BRK
A359  00        BRK
A35A  00        BRK
A35B  00        BRK
```

```
A35C  00        BRK
A35D  00        BRK
A35E  00        BRK
A35F  00        BRK
A360  00        BRK
A361  00        BRK
A362  00        BRK
A363  00        BRK
A364  00        BRK
A365  00        BRK
A366  00        BRK
A367  20 E6 FF  JSR £FFE6
A36A  C9 0D     CMP @£0D
A36C  F0 12     BEQ R+£14
A36E  A9 00     LDA @£00
A370  8D 00 B8  STA £B800
A373  A9 10     LDA @£10
A375  8D 00 B8  STA £B800
A378  A9 00     LDA @£00
A37A  8D 00 B8  STA £B800
A37D  4C 67 A3  JMP P-£0016
A380  A2 00     LDX @£00
A382  BD BF A3  LDA £A3BF,X
A385  20 F4 FF  JSR £FFF4
A388  E8        INX
A389  C9 00     CMP @£00
A38B  D0 F5     BNE R-£09
A38D  F0 2A     BEQ R+£2C
A38F  0A        ASL A
A390  0D 66 69  ORA £6966
A393  6C 74 65  JMP (£6574)
A396  72        ???
A397  20 54 4F  JSR £4F54
A39A  20 45 4E  JSR £4E45
A39D  44        ???
A39E  20 50 52  JSR £5250
A3A1  45 53     EOR £53
A3A3  53        ???
A3A4  20 53 48  JSR £4853
A3A7  49 46     EOR @£46
A3A9  54        ???
A3AA  0A        ASL A
A3AB  0D 00 00  ORA £0000
A3AE  00        BRK
A3AF  00        BRK
A3B0  00        BRK
A3B1  00        BRK
A3B2  00        BRK
A3B3  00        BRK
A3B4  00        BRK
A3B5  00        BRK
A3B6  00        BRK
A3B7  00        BRK
A3B8  00        BRK
A3B9  AD 01 B0  LDA £B001
A3BC  C9 7F     CMP @£7F
A3BE  F0 51     BEQ R+£53
A3C0  AD 00 B8  LDA £B800
A3C3  29 80     AND @£80
A3C5  D0 25     BNE R+£27
A3C7  A9 20     LDA @£20
A3C9  20 F4 FF  JSR £FFF4
A3CC  A9 49     LDA @£49
A3CE  20 F4 FF  JSR £FFF4
A3D1  A9 4E     LDA @£4E
A3D3  20 F4 FF  JSR £FFF4
A3D6  A9 20     LDA @£20
A3D8  20 F4 FF  JSR £FFF4
A3DB  A9 08     LDA @£08
A3DD  20 F4 FF  JSR £FFF4
A3E0  20 F4 FF  JSR £FFF4
A3E3  20 F4 FF  JSR £FFF4
A3E6  20 F4 FF  JSR £FFF4
A3E9  4C B9 A3  JMP P-£0030
A3EC  A9 20     LDA @£20
A3EE  20 F4 FF  JSR £FFF4
A3F1  A9 4F     LDA @£4F
A3F3  20 F4 FF  JSR £FFF4
A3F6  A9 55     LDA @£55
A3F8  20 F4 FF  JSR £FFF4
A3FB  A9 54     LDA @£54
A3FD  20 F4 FF  JSR £FFF4
A400  A9 08     LDA @£08
```

data "FILTER to end press shift"

```
A402  20 F4 FF  JSR £FFF4
A405  20 F4 FF  JSR £FFF4
A408  20 F4 FF  JSR £FFF4
A40B  20 F4 FF  JSR £FFF4
A40E  4C B9 A3  JMP P-£0055
A411  A5 80     LDA £80
A413  8D 0B 02  STA £020B
A416  A9 00     LDA @£00
A418  8D 00 B8  STA £B800
A41B  A9 20     LDA @£20
A41D  8D 00 B8  STA £B800
A420  4C 00 A0  JMP P-£0420      interface test end
A423  FF        ???
A424  FF        ???
A425  FF        ???
A426  FF        ???
A427  FF        ???
A428  FF        ???
A429  FF        ???
A42A  FF        ???
A42B  FF        ???
A42C  FF        ???
A42D  FF        ???
A42E  FF        ???
A42F  FF        ???
A430  0C        ???
A431  0A        ASL A
A432  0A        ASL A
A433  0A        ASL A
A434  0A        ASL A
A435  50 48     BVC P+£4A
A437  59 53 49  EOR £4953,Y
A43A  43        ???
A43B  53        ???
A43C  20 44 45  JSR £4544
A43F  50 41     BVC P+£43
A441  52        ???
A442  54        ???
A443  4D 45 4E  EOR £4E45
A446  54        ???
A447  20 0A 0D  JSR £0D0A
A44A  55 4E     EOR £4E,X
A44C  49 56     EOR @£56
A44E  45 52     EOR £52
A450  53        ???
A451  49 54     EOR @£54
A453  59 20 4F  EOR £4F20,Y
A456  46 20     LSR £20
A458  53        ???
A459  54        ???
A45A  2E 41 4E  ROL £4E41
A45D  44        ???
A45E  52        ???
A45F  45 57     EOR £57          error key data
A461  53        ???
A462  20 0A 0D  JSR £0D0A
A465  45 4C     EOR £4C
A467  45 43     EOR £43
A469  54        ???
A46A  52        ???
A46B  4F        ???
A46C  4E 49 43  LSR £4349
A46F  53        ???
A470  20 57 4F  JSR £4F57
A473  52        ???
A474  4B        ???
A475  53        ???
A476  48        PHA
A477  4F        ???
A478  50 0A     BVC P+£0C
A47A  0D 20 20  ORA £2020
A47D  20 20 20  JSR £2020
A480  28        PLP
A481  43        ???
A482  29 20     AND @£20
A484  31 39     AND (£39),Y
A486  38        SEC
A487  33        ???
A488  0A        ASL A
A489  0A        ASL A
A48A  0D 00 FF  ORA £FF00
A48D  FF        ???
A48E  FF        ???
A48F  FF        ???
```

A6.1(b) DIAL Data Acquisition Program (in machine code)

```
A490  18        CLC          m single runs start
A491  AD 08 02  LDA £0208    printer mark
A494  85 82     STA £82      printer on mark  £80
A496  69 03     ADC @£03     printer off mark £84
A498  85 84     STA £84
A49A  EA        NOP
A49B  A9 00     LDA @£00  }  set up VIA port DDR-A
A49D  8D 03 B8  STA £B803 }
A4A0  A9 70     LDA @£70  }  set up VIA port DDR-B
A4A2  8D 02 B8  STA £B802 }
A4A5  A9 20     LDA @£20  }  reset interface
A4A7  8D 00 B8  STA £B800 }
A4AA  A9 10     LDA @£10  )
A4AC  8D 04 02  STA £0204 {  set up interface routine start address
A4AF  A9 A5     LDA @£A5  {  (A510)
A4B1  8D 05 02  STA £0205 )
A4B4  A2 00     LDX @£00  )
A4B6  BD C6 A4  LDA £A4C6,X{  output message "type run"
A4B9  20 F4 FF  JSR £FFF4 {
A4BC  E8        INX       {
A4BD  C9 00     CMP @£00  )
A4BF  D0 F5     BNE £-£09
A4C1  A9 A7     LDA @£A7     select ROM BASIC program start address
A4C3  85 12     STA £12      (A700)
A4C5  60        RTS          return to BASIC
A4C6  08        PHP       )
A4C7  54        ???       {
A4C8  59 50 45  EOR £4550,Y{  data characters
A4CB  20 52 55  JSR £5552 {
A4CE  4E 20 00  LSR £0020 )
A4D1  FF        ???
A4D2  FF        ???
A4D3  FF        ???
A4D4  FF        ???
A4D5  FF        ???
A4D6  FF        ???
A4D7  FF        ???
A4D8  FF        ???
A4D9  FF        ???
A4DA  A9 00     LDA @£00  }  re-program DDR-A as outputs (printer
A4DC  8D 03 B8  STA £B803 }  and interface ports)
A4DF  A5 84     LDA £84   }  remove printer
A4E1  8D 08 02  STA £0208 }
A4E4  A9 00     LDA @£00  }  clear run count
A4E6  85 81     STA £81   }
A4E8  A9 10     LDA @£10  }  turn interface ON LINE
A4EA  8D 00 B8  STA £B800 }
A4ED  A9 A1     LDA @£A1  }  reset screen cursor character
A4EF  85 83     STA £83   }
A4F1  18        CLC
A4F2  A5 83     LDA £83   }  update cursor
A4F4  8D 0C 80  STA £800C }
A4F7  A5 81     LDA £81   }  test for completed sample runs
A4F9  C5 80     CMP £80   }
A4FB  D0 F5     BNE £-£09    branch to A4F2
A4FD  A5 82     LDA £82   }
A4FF  8D 08 02  STA £0208 }  connect printer
A502  A9 10     LDA @£10  }
A504  8D 00 B8  STA £B800 }  turn interface OFF LINE
A507  A9 00     LDA @£00  }  set port B to zero
A509  8D 00 B8  STA £B800 }
A50C  60        RTS          return to BASIC
A50D  FF        ???
A50E  FF        ???
A50F  FF        ???
A510  08        PHP       }  initialise and turn off interrupts
A511  78        SEI       }
A512  A9 80     LDA @£80  }  test if filter is in or out
A514  2D 00 B8  AND £B800 }  if it is out go to A560
A517  D0 47     BNE £+£49
A519  E6 83     INC £83      increment cursor character
A51B  E6 81     INC £81      increment run count
A51D  A6 81     LDX £81                    data pointer
A51F  AD 01 B8  LDA £B801 }  store upper eight data bits (12 bit)) }
A522  9D 00 90  STA £9000,X)                                        } %I return
A525  A9 0F     LDA @£0F     mark                                   }
A527  2D 00 B8  AND £B800 }  store lower four data bits             }
A52A  9D 00 91  STA £9100,X)
A52D  A9 40     LDA @£40  }  change sample and convert new data
A52F  8D 00 B8  STA £B800 }
```

```
A532  EA        NOP
A533  EA        NOP
A534  EA        NOP
A535  EA        NOP
A536  EA        NOP
A537  EA        NOP
A538  EA        NOP
A539  EA        NOP
A53A  EA        NOP
A53B  EA        NOP        36 µs delay @ ϕ2 = 1 MHz
A53C  EA        NOP
A53D  EA        NOP
A53E  EA        NOP
A53F  EA        NOP
A540  EA        NOP
A541  EA        NOP
A542  EA        NOP
A543  EA        NOP
A544  A9 20     LDA @£20   }   reset interface
A546  8D 00 B8  STA £B800  }
A549  AD 01 B8  LDA £B801  }   store upper eight data bits (12 bit))
A54C  9D 00 92  STA £9200,X}                                        }%I laser
A54F  A9 0F     LDA @£0F       mark                                 }
A551  2D 00 B8  AND £B800  }   store lower four data bits           }
A554  9D 00 93  STA £9300,X}
A557  A9 00     LDA @£00   }   set port to zero
A559  8D 00 B8  STA £B800  }
A55C  28        PLP        }   return from interrupt (switch on interrupts,
A55D  68        PLA        }   load old value of accumulator and load old
A55E  40        RTI            value of status register)
A55F  FF        ???
A560  A6 81     LDX £81    }   test runs to synchronise start (if zero, RTI (A59E)
A562  F0 3A     BEQ £+£3C  }
A564  C6 83     DEC £83        decrement cursor character
A566  AD 01 B8  LDA £B801  }   store upper eight data bits (12 bit))
A569  9D 00 94  STA £9400,X}                                        }%J return
A56C  A9 0F     LDA @£0F       mark                                 }
A56E  2D 00 B8  AND £B800  }   store lower four data bits           }
A571  9D 00 95  STA £9500,X}
A574  A9 40     LDA @£40   }   change sample and convert new data
A576  8D 00 B8  STA £B800  }
A579  EA        NOP
A57A  EA        NOP
A57B  EA        NOP
A57C  EA        NOP
A57D  EA        NOP
A57E  EA        NOP
A57F  EA        NOP
A580  EA        NOP
A581  EA        NOP        36 µs delay @ ϕ2 = 1 MHz
A582  EA        NOP
A583  EA        NOP
A584  EA        NOP
A585  EA        NOP
A586  EA        NOP
A587  EA        NOP
A588  EA        NOP
A589  EA        NOP
A58A  EA        NOP
A58B  A9 20     LDA @£20   }   reset interface
A58D  8D 00 B8  STA £B800  }
A590  AD 01 B8  LDA £B801  }   store upper eight data bits (12 bit))
A593  9D 00 96  STA £9600,X}                                        }%J laser
A596  A9 0F     LDA @£0F       mark                                 }
A598  2D 00 B8  AND £B800  }   store lower four data bits           }
A59B  9D 00 97  STA £9700,X}
A59E  A9 20     LDA @£20   }   reset interface
A5A0  8D 00 B8  STA £B800  }
A5A3  A9 00     LDA @£00   }   set port to zero
A5A5  8D 00 B8  STA £B800  }
A5A8  28        PLP        }   return from interrupt (as at A55C)
A5A9  6B        PLA        }
A5AA  40        RTI            
A5AB  FF        ???
A5AC  FF        ???
  .
  .     "       "
  .
A5FF  FF        ???
A600  03        ???
```

```
A601  06 0C     ASL £0C
A603  4C 49 44  JMP £4449
A606  41 52     EOR (£52,X)
A608  20 4F 53  JSR £534F
A60B  2E 20 56  ROL £5620
A60E  32        ???
A60F  2E 39 0D  ROL £0D39
A612  0A        ASL A
A613  0A        ASL A
A614  0A        ASL A
A615  31 20     AND (£20),Y
A617  50 4F     BVC P+£51
A619  52        ???
A61A  54        ???
A61B  20 54 45  JSR £4554
A61E  53        ???
A61F  54        ???
A620  20 0D 0A  JSR £0A0D
A623  32        ???
A624  20 4B 45  JSR £454B
A627  59 42 4F  EOR £4F42,Y
A62A  41 52     EOR (£52,X)
A62C  44        ???
A62D  20 54 45  JSR £4554
A630  53        ???
A631  54        ???
A632  20 0D 0A  JSR £0A0D
A635  33        ???
A636  20 50 52  JSR £5250
A639  49 4E     EOR @£4E
A63B  54        ???
A63C  45 52     EOR £52
A63E  20 54 45  JSR £4554
A641  53        ???
A642  54        ???
A643  20 0D 0A  JSR £0A0D
A646  34        ???
A647  20 4D 45  JSR £454D
A64A  4D 4F 52  EOR £524F
A64D  59 20 54  EOR £5420,Y
A650  45 53     EOR £53
A652  54        ???
A653  20 0D 0A  JSR £0A0D
A656  35 20     AND £20,X
A658  49 4E     EOR @£4E
A65A  54        ???
A65B  45 52     EOR £52
A65D  46 41     LSR £41
A65F  43        ???
A660  45 20     EOR £20
A662  54        ???
A663  45 53     EOR £53
A665  54        ???
A666  20 0D 0A  JSR £0A0D
A669  36 20     ROL £20,X
A668  4D 20 53  EOR £5320
A66E  41 4D     EOR (£4D,X)
A670  50 4C     BVC P+£4E
A672  45 20     EOR £20
A674  52        ???
A675  55 4E     EOR £4E,X
A677  53        ???
A678  20 0D 0A  JSR £0A0D
A67B  45 4E     EOR £4E
A67D  54        ???
A67E  45 52     EOR £52
A680  20 31 20  JSR £2031
A683  54        ???
A684  4F        ???
A685  20 36 0D  JSR £0D36
A688  0A        ASL A
A689  00        BRK
A68A  FF        ???
A68B  FF        ???
 .
 :    "          "
 :
 .
A6E7  FF        ???
A6E8  FF        ???
```

menu data

A6.2 DIAL Analysis Program (in BASIC)

```
>L.
    2P.$2''"XeCl Laser DIAL"';GOS.m
    4%X=.01;%O=27.5*10^-24;%W=18.5*10^-24;%K=.8;%L=2.36;%S=.35
    6%T=32*10^-9;%F=335*10^-12;%C=2.99*10^8;R=100
    8%Y=7.24*10^18;%Z=9.657*10^24;%V=1.45*10^19;%U=.034
   10T=283;P=1013;G.14
   12P."Analysis Re-run"''
   14P."SELECT REQUIRED MODE"'
   16P."0 Integrated Conc."'"1 Range Resolved Conc."';IN.X
   18IFX>1THENG.14
   20IFX=0THENGOS.i
   22IFX=1THENGOS.r
   26iP."Integrated Conc."';IN."ENTER LIDAR RANGE (m)"'D
   28GOS.c;GOS.e;GOS.p;GOS.j;%B=%R
   30%H=(-T/(%V*(%O-%W)*P*D))*LOGABS((%B-%R)/((%R-%A)*%E))
   32FP."Sulphur dioxide conc. of"'%H" ppm"'
   34P."averaged over range"'D" metres"'';G.12
   38rP."Range Resolved Conc."';GOS.c;GOS.p;Y=0;N=1;Z=2
   40IN."IS THE AMBIENT CONC. RATIO KNOWN? Y or N"Z
   42IFZ=0THENG.46
   44FIN."ENTER THE AMBIENT CONC."%H;GOS.a
   46FP."Ambient return ratio is"'%B';GOS.s;GOS.j
   48%M=LOGABS((%B-%R)/(%R-%A))-LOGABS((%B-%B)/(%B-%A))
   50%N=(-T/(%Y*P*%C*(%T+PI*R*%F)*(%O-%W)))*%M
   52FP."Sulphur dioxide conc. of"'%N" ppm"'
   54FP."in minimum range element "'%D" metres"'
   56P."at a range of"'D" metres"'';G.12
   60aIN."ENTER TARGET RANGE (m) "D;%M=-%V*P*%H*D/T
   62%B=(%A*%E*EXP(%M*%O)+%B*EXP(%M*%W))
   64%B=%B/(%E*EXP(%M*%O)+EXP(%M*%W));R.
   68cFP."Cell P/T ratio"'%9';FIN."ENTER CELL P/T RATIO"%9
   70FP."No. of single passes"'%L'
   72FP."Cell attenuation factor"'%K'
   74%A=%K*EXP(-%Z*%L*%O*%X*%S);%B=%K*EXP(-%Z*%L*%W*%X*%S);R.
   80pP."Pressure"P" mbar"';P."Temperature"T" oK"'
   82IN."ENTER PRESSURE"P;IN."ENTER TEMPERATURE"T;Y=0;N=1;Z=2
   84IN."Is pressure/height compensation  required? Y or N"Z
   86IFZ=1THENG.90
   88IN."ENTER THE LIDAR ANGLE"A;%M=P
   89%M=%M*EXP(-%U*D*(SIN(A*PI/180))/T);P=%M
   90R.
   94sP."Output circuit R and C"'R';FP.%F'
   96IN."ENTER LOAD RESISTANCE"R
   98%D=%C*(%T+PI*R*%F)/2;R.
  102j          FP."Return signal ratio"'%R'';R.
  106e%E=.6915;FP."Laser peak ratio"'%E';Y=0;N=1;Z=2
  108IN."IS NORMALIZATION REQUIRED? Y or N"Z
  110IFZ=1THENG.116
  112%E=(%P-%B)/(%A-%P)
  114FP."Normalizing laser peak ratio"'%E'
  116R.
  120mCLEAR0
  122P.$30'';IN."ENTER M (1-253)="M;?£80=(M+1);CLEAR4;CLEAR0
  124LINK£A4DA;%I=0;%J=0;%P=0;%R=0;F.I=1TO M
  126%I=    (?(I+£9000)*16)+?(£9100+1)
  128%J=    (?(I+£9400)*16)+?(£9500+I);%R=%R+%I/%J
  130%I=(?(I+£9200)*16)+?(£9300+I)
  132%J=(?(I+£9600)*16)+?(£9700+I);%P=%P+%I/%J;N.;%R=%R/M
  134%P=%P/M;P.$2"%R  ";FP.%R ';P."%P  ";FP.%P ';R.
>
```

A6.3 Impedance Matching in Signal Transmission Lines

Impedance matching between the photomultiplier and the signal handling circuit, and between the photomultiplier and the oscilloscope, is necessary to avoid severe ringing of the return pulse. Pulse degradation of this sort, seen in a mis-match situation, creates innaccuracies during measurement. Matching must take into account the source load impedance, Z_L, the characteristic cable impedance, Z_c, an added series impedance, Z_m, and the input impedance at the measuring system, Z_i, shown in the circuit of figure A6.1. Matching is achieved when the combination of impedances satisfies the equation

$$Z_L = (Z_c + Z_m)^2/Z_i. \qquad (A6.5.1)$$

Equation (A6.5.1) is applied to a standard co-axial cable impedance of $Z_c = 50\Omega$ and a variety of load resistances and input resistances of values 50Ω, 100Ω, 500Ω, $1k\Omega$ and $10k\Omega$, where $Z_L = Z_i$, to allow several input impedance matching circuits to be made for insertion in-line, near to the signal handling system. The in-line resistance, Z_m, is added to 50Ω to bring the series resistance value to that of Z_L or Z_i (only applicable when $Z_L = Z_i$).

Lower load and input resistances are used if, for example, target range is to be more closely defined.

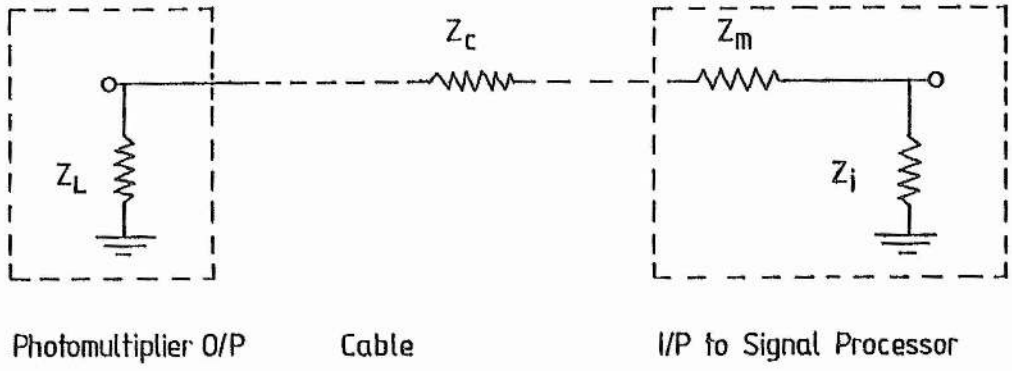

Figure A6.1 Circuit for impedance matching between detector and signal handling system.

Appendix for Chapter 8

A8.1 Rayleigh Scattering Coefficients

A8.1(a) Rayleigh Scattering

In Rayleigh scattering incident radiation is considered to excite the molecules, which then re-emit at the same wavelength. A linear scattering coefficient, $\alpha_{R,\theta}$, describes the portion of incident radiation scattered by a unit volume into an elemental solid angle $d\omega$ in direction θ, illustrated in figure A8.1. Thus the coefficient is given by

$$dF = \alpha_{R,\theta} E.d\omega , \qquad (A8.1.1)$$

where dF is the elemental energy scattered into solid angle $d\omega$ from a total incident energy E. Scattering is described by a planar geometric scattering function $y(\theta)$ and a term x_R which is peculiar to the optical molecular properties and their interaction with the dipole radiation field. The coefficient is made of these components to give

$$\alpha_{R,\theta} = x_R y(\theta) \quad m^{-1}sr^{-1}. \qquad (A8.1.2)$$

Equations (A8.1.1) and (A8.1.2) combine to give

$$dF = x_R y(\theta).E.d\omega. \qquad (A8.1.3)$$

If scatter is considered in a two dimensional plane, assuming symmetry in the third dimension, then the solid angle element can be replaced by a function of the directional angle θ in the expression

$$d\omega = 2\pi \sin\theta.d\theta \quad sr. \qquad (A8.1.4)$$

Equation (A8.1.4) is inserted into (A8.1.3) which is then integrated to give the total energy scattered over the whole solid angle, expressed as

$$F = 2\pi x_R E \int_o^{\pi} y(\theta) \sin\theta . d\theta \quad m^{-1}. \qquad (A8.1.5)$$

Just as the coefficient $\alpha_{R,\theta}$ decribes the proportion of energy scattered into an element of space in planar direction θ, then a coefficient α_R describes the proportion scattered into all space to give

$$F = \alpha_R E \quad m^{-1} \qquad (A8.1.6)$$

which is compared with (A8.1.5) using (A8.1.2) to give

$$\alpha_R = 2\pi \int_o^{\pi} \alpha_{R,\theta} \sin\theta . d\theta \quad m^{-1}. \qquad (A8.1.7)$$

Since α_R describes the removal of radiation from the direction of incidence in single scattering, it is known as the extinction coefficient.

The optical interaction is given by

$$x_R = \pi^2 (n_r^2 - 1)^2 / 2N_a \lambda^{4.09} \quad m^{-1} \qquad (A8.1.8)$$

(Kondratyev, 1969), where n_r is the refractive index at the scattering site at range r and N_a is the atmospheric molecular number density. The power to which the wavelength parameter is raised gives a correction for dispersion although the refractive index itself can be corrected through a suitable expression (R.Penndorf; Kondratyev, 1969).

The distribution of scattered radiation is given by the geometric

scattering function, which is

$$y(\theta) = (1 + \cos^2\theta) \quad sr^{-1}. \tag{A8.1.9}$$

Thus, by (A8.1.2), with (A8.1.8) and (A8.1.9) the coefficient for scattering through angle θ is expressed as

$$\alpha_{R,\theta} = \pi^2(n_r^2 - 1)^2(1 + \cos^2\theta)/2N_a \lambda^{4.09} \quad m^{-1}sr^{-1}. \tag{A8.1.10}$$

The total Rayleigh scatter coefficient in (A8.1.7) is now expressed using (A8.1.10) after integration as

$$\alpha_R = 8\pi^3(n_r^2 - 1)^2/3N_a \lambda^{4.09} \quad m^{-1}. \tag{A8.1.11}$$

The optically anisotropic scattering behaviour of the molecules tends to increase scattering efficiency and necessitates the inclusion of a depolarizing term in the expression for the Rayleigh scattering coefficients (Penndorf; Frolich and Shaw, 1980; Uchino et al, 1979). Thus equation (A8.1.10) becomes

$$\alpha_{R,\theta} = (\pi^2(n_r^2-1)^2/2N_a \lambda^{4.09})(1+\cos^2\theta)(6+3\delta)/(6-7\delta) \quad m^{-1}s^{-1} \tag{A8.1.12}$$

and equation (A8.1.11) becomes

$$\alpha_R = (8\pi^3(n_r^2-1)^2/3N_a \lambda^{4.09})(6+3\delta)/(6-7\delta) \quad m^{-1}. \tag{A8.1.13}$$

The value of the depolarizing factor, δ, is taken as 0.035 according to experimental observations (L.Eltermann, 1964; E.D.Hinkley; Uchino et al, 1979).

A8.1(b) Rayleigh Backscatter

Backscatter (ie. scatter through an angle of 180^{o}) is important as the prime mechanism for obtaining lidar signals. A Rayleigh backscatter coefficient is obtained from the angular scattering coefficient, $\alpha_{R,\theta}$, given in equation (A8.1.10), applied for $\theta = 180^{o}$. The backscatter coefficient is given as

$$\beta_R = \alpha_{R,\pi} \qquad m^{-1}sr^{-1} \qquad \text{(A8.1.14)}$$

or, by using (A8.1.12),

$$\beta_R = (\pi^2(n_r^2-1)^2/N_a\,\lambda^{4.09})(6+3\delta)/(6-7\delta) \qquad m^{-1}sr^{-1}. \qquad \text{(A8.1.15)}$$

Comparison of equation (A8.1.15) with (A8.1.13) gives

$$\beta_R = 3\,\alpha_R/8\pi \qquad m^{-1}sr^{-1} \qquad \text{(A8.1.16)}$$

which allows the backscatter to be evaluated from the scatter extinction coefficient.

Two final steps in providing a useful term for α_R expresses the molecular concentration, N_a, in terms of atmospheric pressure (mbar) and temperature (^{o}K) and replaces the refractive index term (n_r^2-1) by one which is also a function of temperature and pressure.

A8.1(c) Atmospheric Number Density

The atmospheric number density, N_a, is given by the relation

$$N_a = N/V \qquad m^{-3}. \tag{A8.1.17}$$

This is applied in the ideal gas equation

$$PV = NkT, \tag{A8.1.18}$$

where N is the number of molecules in volume, V, to give

$$N_a = P/kT. \tag{A8.1.19}$$

Pressure is converted from units of Nm^{-2} to mbar by the identity

$$1 \text{ mbar} = 100 \ Nm^{-2} \tag{A8.1.20}$$

to give

$$N_a = 7.243 \times 10^{24} \ P_r(\text{mbar})/T_r. \tag{A8.1.21}$$

A8.1(d) Refractive Index Transformation

The refractive index term in equation (A8.1.13) is replaced by a function of ambient pressure and temperature. Refractive indices under different conditions are related by the different gas densities. Thus, the refractive index of a gas at lidar range, r, is given by (Kondratyev, 1969)

$$n_r^2 = 1 + 2(n_{STP} - 1) \rho_r / \rho_{STP}, \tag{A8.1.22}$$

where ρ_r is the gas density at range r, ρ_{STP} is the gas density at standard temperature and pressure and n_{STP} is the refractive index at STP. An ideal gas equation is assumed as

$$PV \propto NT, \qquad \text{(A8.1.23)}$$

where pressure, P, and volume, V, are related to temperature, T, and the number of molecules, N. The equation is re-expressed as

$$P \propto \rho T, \qquad \text{(A8.1.24)}$$

where ρ is the gas density. Using (A8.1.24) in simultaneous equations for a target gas at range r or for a gas at STP gives

$$\rho_r / \rho_{STP} = P_r T_{STP} / P_{STP} T_r \qquad \text{(A8.1.25)}$$

which is replaced in equation (A8.1.22) to give

$$n_r^2 = 1 + 2(n_{STP} - 1) P_r T_{STP} / P_{STP} T_r. \qquad \text{(A8.1.26)}$$

Upon insertion of the STP values $P_{STP} = 1013.25$ mbar, $T_{STP} = 273\ ^0K$, and $n_{STP}-1 = 292 \times 10^{-6}$ this becomes

$$n_r^2 - 1 = 1.573 \times 10^{-4} . P_r / T_r. \qquad \text{(A8.1.27)}$$

A8.1(e) Active Equations for Rayleigh Coefficients

Upon substitution of (A8.1.21), (A8.1.27) and depolarization into equation (A8.1.13) the Rayleigh extinction coefficient becomes

$$\alpha_R = 9.951 \times 10^{-7} P_r / \lambda(\mu m)^{4.09} T_r \quad m^{-1}, \qquad (A8.1.28)$$

where the wavelength is in μm. Similarly, equation (A8.1.12) becomes

$$\alpha_{R,\theta} = (5.939 \times 10^{-8} / \lambda(\mu m)^{4.09})(P_r/T_r)(1 + \cos^2\theta) \quad m^{-1}sr^{-1}. \qquad (A8.1.29)$$

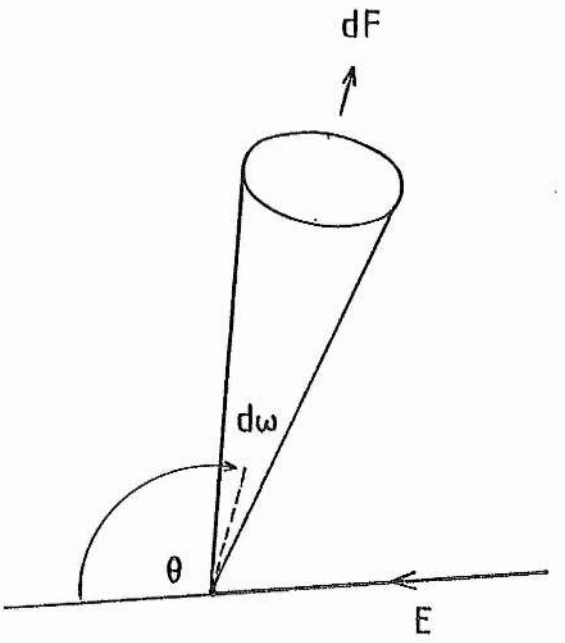

Figure A8.1 Rayleigh scattering of energy dF, through angle θ, into solid elemental angle dω, from incidence of energy E, in Rayleigh scattering analysis

A8.2 Mie Scattering Coefficients

A8.2(a) Mie Scattering

The extremely complicated nature of atmospheric Mie scattering has not allowed a rigorous derivation of the Mie scattering coefficient. A useful expression for the coefficient has been obtained empirically in other works (Kruse et al, 1962). Its form is partly justified by the analysis below, allied to the method of Bullrich (Bullrich, 1948). The final coefficient arises from the distribution of aerosol sizes and is expressed for the scatter into all space.

The starting point for the analysis is a Mie coefficient, $\alpha_{M,a,\theta}$, which describes scatter through angle θ, assuming spherical particles of a single radius, a. Scatter into all space by aerosols of radius a is given by the coefficient in the expression

$$\alpha_{M,a} = 2\pi \int_{o}^{\pi} \alpha_{M,\theta,a} \sin\theta . d\theta \qquad m^{-1}. \qquad (A8.2.1)$$

similar to equation (A8.1.7) for Rayleigh scattering. The extinction coefficient arising from scatter by aerosols within the size distribution from radius a_1 to radius a_2 is given by

$$\alpha_{M} = \int_{a_1}^{a_2} \alpha_{M,a} dN \qquad m^{-1}, \qquad (A8.2.2)$$

where dN is the number of particles in the size range a to a+da, contained within a unit volume. This latter quantity defines the size distribution in terms of a according to an analysis taken after Junge (C.E.Junge, 1955) given below.

A8.2(b) Aerosol Size Distribution

The distribution relating particle concentration to particle radius, assuming spheres in a Mie model, can be applied between naturally occurring limits of radius. A lower limit is maintained by the loss of small particles ($<0.1\mu$) as they coagulate into larger ones as a result of Brownian motion collisions. Giant particles ($>10\mu$) are lost in gravitational fallout. The complete range of sizes, from radii of 0.005μ to 20μ cover three particle classes; the smaller Aitken nuclei, the large particles and the giant particles. Figure A8.2, taken from Junge (C.E.Junge, 1955), illustrates the distribution and the aforementioned cut-offs, according to measurements by five methods. As the particle size range is spread over several orders of magnitude, the distribution is defined on a logarithmic (base ten) scale of radius. Total particle concentration, N, over a given size range is expressed as

$$N=\int_{a_1}^{a_2} n(a).d(\log a), \qquad (A8.2.3)$$

where n(a) is the concentration of particles with a radius a. Equation (A8.2.3) becomes

$$dN = n(a).d(\log a), \qquad (A8.2.4)$$

giving the concentration of particles in a size range imposed by the element d(loga). This is the form of the distribution in figure A8.2. The linear parts of figure A8.2, over two magnitudes of size, can be described by asigning a power law to concentration of particles with a general radius a to give

$$n(a) = \text{constant}/a^{\gamma} \qquad (A8.2.5)$$

Junge (C.E.Junge, 1955) has confirmed this for the optical behaviour of atmospheric haze, giving a value for γ in the range 2.5 to 3.5. The model considers particles in the size range 0.08μ to 10μ. Applying equation (A8.2.5) to (A8.2.4) gives

$$dN = Ca^{-\gamma}d(\log a). \qquad \text{(A8.2.6)}$$

The interval d(loga) is re-written as

$$d(\ln a)/d(\log a) = \ln 10 \qquad \text{(A8.2.7)}$$

which is combined with the differential

$$d(\ln a)/da = 1/a \qquad \text{(A8.2.8)}$$

to give the final expression

$$dN = (C/\ln 10)a^{-(\gamma+1)}da \qquad m^{-3} \qquad \text{(A8.2.9)}$$

for the number concentration of particles in the size range a to a+da.

A8.2(c) Mie Coefficient with Size Distribution and Spectral Dependence

Equations (A8.2.9) and (A8.2.2) are combined to give the Mie coefficient as

$$\alpha_M = (C/\ln 10) \int_{a_1}^{a_2} \alpha_{M,a}/a^{\gamma+1}\, da. \qquad \text{(A8.2.10)}$$

A scatter cross-section is defined as a function of the single radius coefficient, $\alpha_{M,a}$, as

$$K(x) = \alpha_{M,a}/\pi a^2. \qquad \text{(A8.2.11)}$$

Mie assumed the cross-section to be a function of only the size parameter, $K(x)$ (also known as the Mie parameter), which introduces the spectral dependence in the form

$$x = 2\pi a/\lambda . \qquad \text{(A8.2.12)}$$

Using (A8.2.11) and (A8.2.12) to eliminate the radius a, the coefficient in (A8.2.10) becomes

$$\alpha_M(\lambda) = (C\pi/\ln 10)(2\pi/\lambda)^{\gamma-2}\int_{x_1}^{x_2} K(x)/x^{\gamma-1}dx. \qquad \text{(A8.2.13)}$$

These final steps have only replaced the integral containing unknown terms by another, also containing unknown terms. However, the spectral dependence is now evident. For convenience, equation (A8.2.13) is re-written as

$$\alpha_M(\lambda) = (C\pi/\ln 10)(2\pi/\lambda)^{\gamma-2}K(\lambda). \qquad \text{(A8.2.14)}$$

A8.2(d) Theoretical Mie Coefficient with respect to Visible Range

Equation (A8.2.15) can still be taken to a more useful form by referencing the scatter coefficient to one based on atmospheric visibility, based in turn on the Koschmeider relation (H.Koschmeider, 1926) at the wavelength of peak eye response at 0.55μ. The visual range is the distance at which the target contrast equals the threshold contrast of the eye (Bullrich, 1948; S.Q.Duntley,1948) and is expressed in terms of the sum of Rayleigh and Mie coefficients in

$$\alpha_M(0.55\mu) + \alpha_R(0.55\mu) = 3.912/V. \qquad \text{(A8.2.15)}$$

Equation (A8.2.14) is expressed as it stands and is repeated for a wavelength of 0.55μ and the two expressions are taken in ratio, followed by substitution of equation (A8.2.15) for $\alpha_M(0.55\mu)$ to give

$$\alpha_M(\lambda) = [3.912/V - \alpha_R(0.55\mu)][0.55/\lambda(\mu m)]^{\gamma-2}[K(\lambda)/K(0.55\mu)]. \qquad \text{(A8.2.16)}$$

This expression still carries the unknown quantities $K(\lambda)$ and γ, preventing its direct application, although γ has been predicted empirically. The explanation and result (equation A8.2.16) in the above analysis, serve to justify the often quoted empirical relation (Kruse at al, 1962) in a form which is given below.

A8.2(e) Empirical Relation for the Mie Coefficient

The relation accepted for the coefficient is given as

$$\alpha_M(\lambda) = [3.912/V(m)][0.55/\lambda(\mu m)]^q \quad m^{-1}, \qquad \text{(A8.2.17)}$$

where $q = 0.585.V(km)^{1/3}$ for $V < 6$ km and $q = 1.3$ for average seeing conditions. The value of q in equation (A8.2.17) would be in agreement within the range of values for γ of 2.5 to 3.5 (C.E.Junge, 1955) in comparing equations (A8.2.16) and (A8.2.17). However, the extreme value of 3.5 for γ suggests a maximum range of about 16km for the empirical relation. The empirical relation, equation (A8.2.17), appears to neglect Rayleigh scattering. Rayleigh scattering affects visibility (as shown in equation (A8.2.15)) and should therefore be included in equation (A8.2.17) for a more realistic application of α_M. The unknown quantity $K(\lambda)/K(0.55\mu)$ is assumed to be unity. This is possibly corrected by the adopted value

of q. Thus the useful expression for the Mie coefficient is

$$\alpha_M(\lambda) = [3.912/V(m) - \alpha_R(0.55\mu)][0.55/\lambda(\mu m)]^q \quad m^{-1}, \qquad (A8.2.18)$$

where $q = 0.585.V(km)^{1/3}$ for $V<10km$ (compromise) or $q = 1.3$ under average seeing conditions.

A8.2(f) Mie Backscatter Coefficient

The backscatter coefficient is a complex function of size distribution, wavelength and angle. Mie scatter shows an increase in forward scattering and a relatively low backscatter in comparison with Rayleigh scatter. The Rayleigh backscatter coefficient was expressed in terms of the linear coefficient by an analysis which gave agreement with a reference of Hamilton (1969). The same reference states a similar relation for Mie backscattering, one which falls within a range given by other works and measurements (Hinkley, 1976). The relation is given as

$$\beta_M = \alpha_M/8\pi \quad m^{-1}sr^{-1}. \qquad (A8.2.19)$$

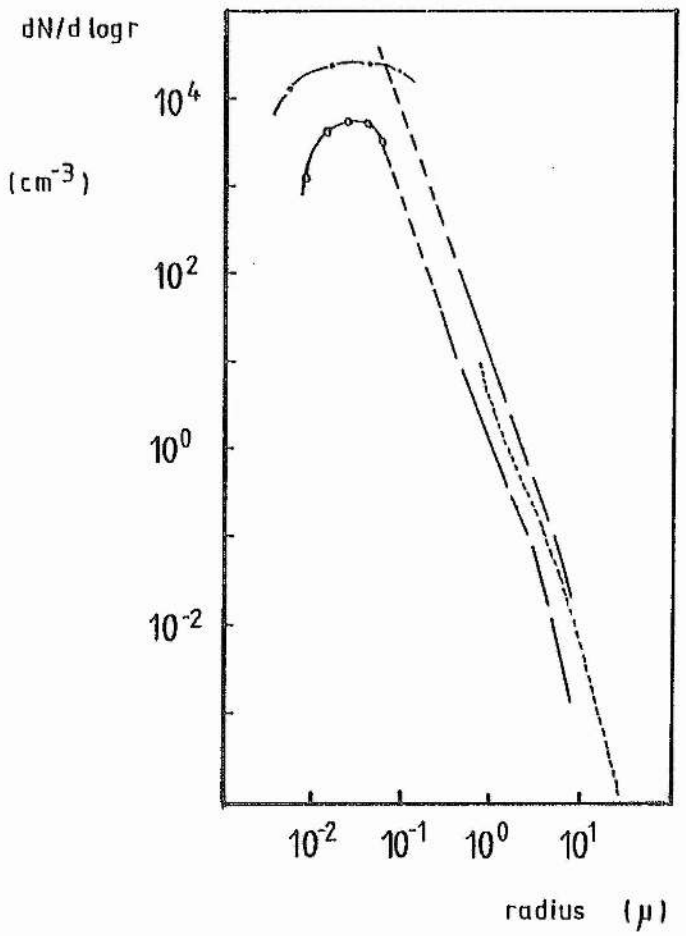

Figure A8.2 Complete size distribution of natural aerosols, (after Junge, 1958)

A8.3 Approximating a Gaussian Pulse to a Square Function

Figure A8.3 illustrates the approximation of a Gaussian laser pulse function to a rectangular function of the same width, τ. The Gaussian photon current is expressed as

$$n_o' = (n_o/\sqrt{2\pi}\ \tau')\exp[-t^2/2\ \tau'^2] \qquad s^{-1}, \qquad (A8.3.1)$$

where n_o is the total number of photons in the pulse. The fwhm (full width at half maximum) of the pulse is given by

$$\tau = 2.36\ \tau' \qquad s, \qquad (A8.3.2)$$

where τ' is the standard deviation in the Gaussian. From equation (A8.3.1), when $t=0$, the peak photon current is

$$n_p' = n_o/\sqrt{2\pi}\ \tau' \qquad s^{-1} \qquad (A8.3.3)$$

which becomes, using (A8.3.2)

$$n_p' = n_o/1.06\tau \qquad s^{-1}. \qquad (A8.3.4)$$

Thus, the peak photon current is approximated to the function of the rectangular pulse by equating n_o' with n_p' using (A8.3.4) to give

$$n_o' \simeq n_o/\tau \qquad s^{-1} \qquad (A8.3.5)$$

between the limits of $-\tau/2 < t < +\tau/2$. The error in this approximation is 6%.

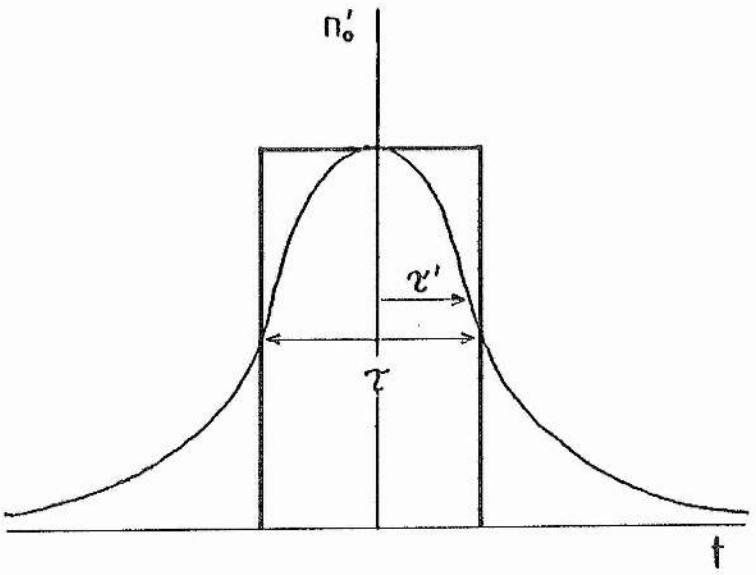

Figure A8.3 Approximation of a Gaussian pulse of fwhm τ to a square pulse of width τ ns.

A8.4 Convolution Applied to Function Transfer

The response r(t) of a system to the transfer of an original function s(t) is expressed as the integral, in frequency space, of function products by (Bennett, 1970) the expression

$$r(t) = \int_{-\infty}^{\infty} H(\omega).S(\omega)\exp[j\omega t]d\omega \ , \qquad \text{(A8.4.1)}$$

where $S(\omega)$ is the Fourier transform of s(t), denoted by

$$S(\omega) = \mathcal{F}\, s(t), \qquad \text{(A8.4.2a)}$$

which is, in turn, given by

$$S(\omega) = \int_{-\infty}^{\infty} s(t)\exp[-j\omega t]dt. \qquad \text{(A8.4.2b)}$$

The inverse transform is expressed as

$$s(t) = \mathcal{F}\, S(\omega), \qquad \text{(A8.4.3a)}$$

given by

$$s(t) = \int_{-\infty}^{\infty} S(\omega)\exp[j\omega t]d\omega \ . \qquad \text{(A8.4.3b)}$$

The response of the system in the time domain is related to itself in the frequency domain via the inverse Fourier transform of the same form as (A8.4.3b) to give

$$r(t) = \int_{-\infty}^{\infty} R(\omega)\exp[j\omega t]d\omega \,. \qquad \text{(A8.4.4)}$$

In comparing (A8.4.4) with (A8.4.1) the three functions $R(\omega)$, $H(\omega)$ and $S(\omega)$ are related by

$$R(\omega) = H(\omega).S(\omega). \qquad \text{(A8.4.5)}$$

This is expressed, using the form of (A8.4.2a), as

$$\mathcal{F}\, r(t) = \mathcal{F}\, H(t).\mathcal{F}\, s(t) \qquad \text{(A8.4.6)}$$

which is a convolution of the transmitted function s(t) with the transfer function H(t) to give the final function, r(t).

A8.5 Fourier Transform of a Delta Function

The delta function is given by the integral (Bennett, 1970)

$$\delta(t) = \int_{-\infty}^{\infty} \exp[j\omega t] d\omega \,. \qquad \text{(A8.5.1)}$$

The Fourier transform of the delta function is sought by applying the rule outlined in appendix A8.4, equations (A8.4.2), giving

$$\mathcal{F}\,\delta(t) = \int_{-\infty}^{\infty}\int_{-\infty}^{\infty} \exp[j\omega t].\exp[-j\omega t] d\omega\, dt \qquad \text{(A8.5.2a)}$$

with the result

$$\mathcal{F}\,\delta(t) = 1. \qquad \text{(A8.5.2b)}$$

A8.6 BASIC Program Listing for the Modelled Lidar Return

```
    5  REM CONSTANTS
   10 %C= 2.998*10^8
   15 %H= 6.626*10^-34
   20 %Q= 1.602*10^-19
  150 REM INPUTS
  160FINPUT"PULSE FWHM "%T
  170FINPUT"PULSE ENERGY "%E
  175FINPUT"WAVELENGTH(MI)"%W
  180FINPUT"TRANS. EFF. "%O
  190FINPUT"MIRROR AREA "%A
  200FINPUT"MIRROR REFL. "%S
  210FINPUT"FILTER TRANS. "%F
  220FINPUT"P-M Q.E "%K
  230INPUT"P-M GAIN "G
  240INPUT"P-M LOAD RESISTOR "R
  250INPUT"ATMOS. PRESSURE "P
  260INPUT"AMBIENT TEMP "T
  270FINPUT"ABS X-SECTION,GAS"%X
  280 DIM VV(255): DIM NN(255)
  300 REM VIS AND CONC
  310 B=0
  320 P."ENTER RANGE ELEMENTS WITHIN"B" TO 255"'
  330 P."STARTING AT"B:A=B:P.'
  335 INPUT"ENDING AT "B
  340 INPUT"VIS IN THIS RANGE "V
  350FINPUT"CON IN THE RANGE "%N
  360 FOR S=A TO B
  370 VV(S)=V : NN(S)=%N
  380 NEXT S
  390 IF S<255 THEN G.320
 1000 CLEAR4
 1010 MOVE 0,10 : DRAW 256,10
 1020 MOVE 10,0 : DRAW 10,192
 1030 MOVE 10,10
 1500 %R=0
 1510 %Z=0
 1520 %Y=0
 2000 FOR J=0 TO 100
 2100 GOSUBj
 2110 GOSUBr
 2120 GOSUBm
 2130 GOSUBb
 2140 GOSUBd
 2150 GOSUBe
 2160 GOSUBn
 2170 GOSUBu
 2180 GOSUBp
 2190 GOSUBl
 2200 GOSUBv
 3000 DRAW (J+10),(10+%V*30)
 3500 NEXT J
 4000                        END
```

```
4500j REM RANGE ACCUMALATION
4510 %R=1+(0.5*%C*%T*J)
4520  RETURN
5000r REM RAYLEIGH COEFF.  (/M)
5010 %J=(9.95i*10^-7)*(P/T)/(%W^4.09)
5020 RETURN
5050m REM MIE COEFFICIENT  (/M)
5060 %N=0.55; GOSUBr
5065  V=VV(J)
5070 %Q=(V^.3333)*.585
5075 %N=.308
5080 %M=((3.912/(1000*V))-%J)*((.55/%W)^%Q)
5090 RETURN
5100b REM BACKSCATTER COEF(/M)
5110  GOSUBr ;GOSUBm
5120  %B = 1.5*%J + 0.5*%M
5130  RETURN
5150d REM DETECTION EFFICIENCY
5160  %D=2*%S*%F
5170  RETURN
5200e REM LASER ENERGY(MILLIJ)
5210 %L=(%W*%E)/((10^6)*%H*%C)
5220  RETURN
5300n REM POLLUTANT CONC
5305  %N=NN(J)
5310 %N=(7.24307*10^18)*%N*P/T
5320 RETURN
5400u REM ATTENUATION,SCATTER
5410%Z=%Z+(%J+%M)*(.5*%T*%C)
5420  %U=EXP(-2*%Z)
5430  RETURN
5500p REM ATTENUATION,ABSORP.
5510  %Y=%Y+(%N*(.5*%C*%T))
5520  %P=EXP(-2*%X*%Y)
5530  RETURN
6000i REM PHOTON CURRENT
6010  %I=(%L*%B*%C*%A*%O*%D*%U*%P)/(8*PI*(%R^2))
6020  RETURN
6050v REM O/P VOLTAGE, APPROX
6060  %V=%K*%G*G*R*%I
6070  RETURN
```

Appendix for Chapter 9

A9.1 Gas Concentration as a Function of Pressure

A target gas concentration in S.I units is a number density (m^{-3}). It is usual to express the concentration of a trace gas in the atmosphere as the number of parts per million of air (ppm). The macroscopic properties of air at 1 atmosphere and typical tropospheric temperatures are reasonably described by the ideal gas equation, given as

$$PV = NTk \qquad \text{(A9.1.1)}$$

where N is the number of air molecules in volume V, at temperature T and pressure P. The air molecular number density at a position in the atmosphere given by range r is thus described from equation (A9.1.1) as

$$N/V = P_r/kT_r \quad m^{-3}. \qquad \text{(A9.1.2)}$$

If $\bar{N}(m^{-3})$ is the target gas average density at range r, then the density in ppm is given by

$$\bar{N}' = (\bar{N} \times 10^6)/(N/V) \quad \text{ppm}, \qquad \text{(A9.1.3)}$$

which becomes, on substitution of (A9.1.2),

$$\bar{N}' = \bar{N}kT_r \times 10^6/P_r \quad \text{ppm}. \qquad \text{(A9.1.4)}$$

In this equation, P_r is given in units of Nm^{-2} but it is usual to express atmospheric pressure in units of mbar (where 1 standard atmosphere = 1013.25 mbar) using the conversion 1 mbar = 100 Nm^{-2}. In converting

equation (A9.1.4) and substituting the value of the Boltzmann constant k, it becomes

$$\bar{N}' = \bar{N}(m^{-3})T_r(^oK)/7.24307 \times 10^{18}P_r(mbar) \quad ppm. \qquad (A9.1.5)$$

In some cases it is convenient to express pressure in units of torr. For pressure entered in mbar, equation (A9.1.2) is evaluated as the number density

$$N/V = 7.24307 \times 10^{24} P(mbar)/T(^oK) \quad m^{-3}. \qquad (A9.1.6)$$

The equivalent for pressure in torr is

$$N/V = 9.6566 \times 10^{24} P(torr)/T(^oK) \quad m^{-3}. \qquad (A9.1.7)$$

A9.2 Variation of Pressure with Height

The variation of atmospheric pressure with height follows the barometric equation

$$P(h) = P_g.\exp[-Mgh/RT], \qquad (A9.2.1)$$

where M is the weight of one mole of air, given by

$$M = \rho_{STP}V_{m\ STP} \quad kg, \qquad (A9.2.2)$$

where ρ_{STP} is the air density at STP. In general the density itself decreases with pressure. The volume of the one mole of air at STP is V_m

$_{STP}$; ie. 22.4 l. Equation (A9.2.1) is evaluated (using the values ρ_{STP} = 1.293 kg.m^{-3}, R = 8.314 J/mole.deg, g = 9.8 ms^{-2}) to give

$$P(h) = P_g.\exp[-0.034\ h/T). \qquad (A9.2.3)$$

Figure A9.2.1 shows variation of pressure with height for a temperature of 283^{o}K and a P_g value at ground level of 1013 mbar, the average world sea-level pressure. The sea level pressure has a world variation of about 980 to 1040 mbar (Fleagle and Businger, An Introduction to Atmospheric Physics). The percentage variation from the assumed average is deduced from equation (A9.2.3) to give

$$\Delta P\% = 100(1 - \exp[-0.034\ h/T]) \qquad (A9.2.4)$$

and it is plotted for a specific temperature in the text.

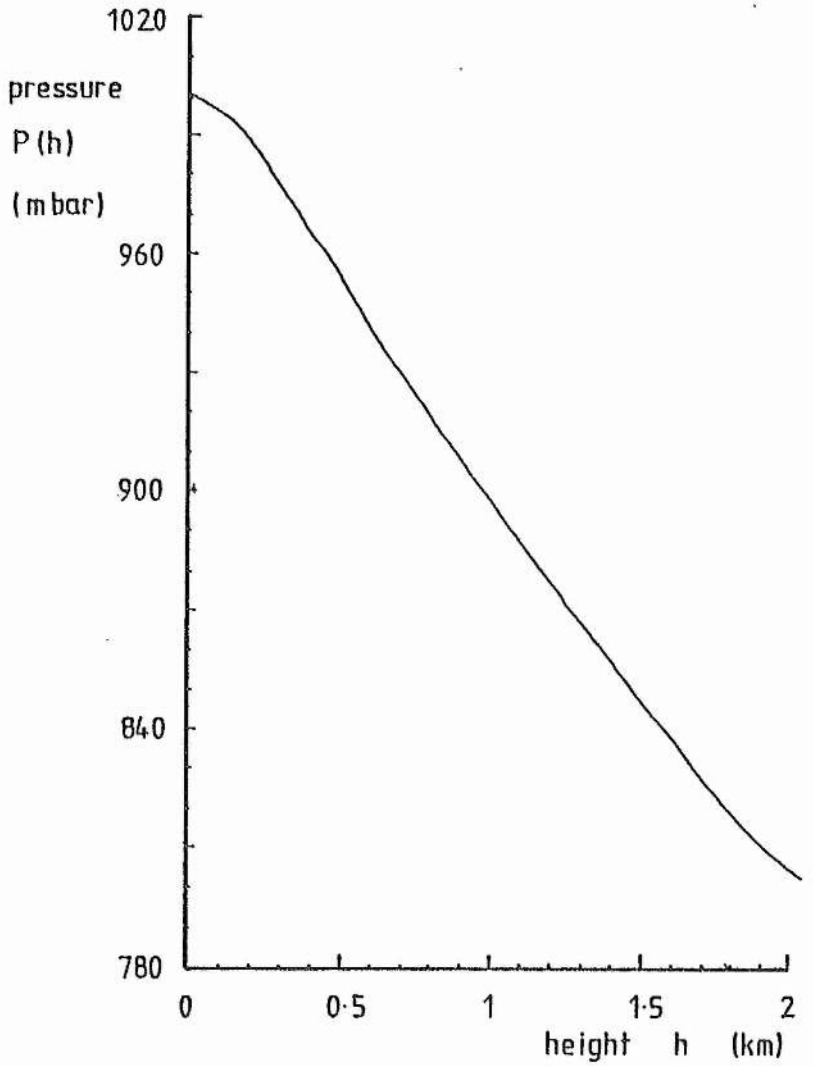

Figure A9.1 Variation of atmospheric pressure with height

A9.3 Program Listing (BASIC) Distinct Wavelength n'/n" vs N'

```
  1 REM DISTINCT WAVELENGTH
  2 REM  CONC VS RATIO
  5 P.''
 10 P."RETURN RATIOS IN 902"'
 20 P."CONCENTRATION RANGES"''
 30 P."**********************"''
 40 P."ENTER THE START "
 50 P."AND END POINT "
 60 P."CONCENTRATIONS FOR "
 70 P."THE DESIRED RANGE."'
 80 FINPUT %S; P.'
 90 FINPUT %E; P.'
100 P."ENTER THE CONCENTRATION INCREMENT"'
110 FINPUT %H; P.'
120 P."**********************************"''
200 REM  CONSTANTS
210 %C= 2.99*10^8
220 %A= 9*10^-24
230 %T= 370
240 %K=-7.24*10^18
250 %F= 32*10^-9
260 %P= 1013
270 %L= 0.6915
300 REM  HEADING
310 P."CONC(PPM)       RATIO"''
350 REM CALCULATION LOOP
360 %N=%S ; GOS.r
370 DO %N=%N+%H
380 GOS.r
390 UNTIL %N>=%E
400 END
500r %R= %L*EXP(%K*%C*%F*%A*%P*%N/%T)
550 FP.%N," ",%R'
600 RETURN
```

A9.4 Program Listing (BASIC) Mixed Wavelength n'/n" vs N'

```
>L.
    1 REM MIXED    WAVELENGTH
    2 REM CONC.VS.RATIO VS.P
    5 P.'''
   10 P."RETURN RATIOS IN %02"'
   20 P."CONCENTRATION RANGES"'
   25 P."AT DIFFERENT CELL P."''
   30 P."**********************"''
   40 P."ENTER THE START "
   50 P."AND END POINT "
   60 P."VALUES FOR "
   70 P."THE DESIRED RANGE."'
   75 P."CONCENTRATION:"'
   80 FINPUT %S
   90 FINPUT %E
   92 P."CELL PRESSURE:"'
   94 INPUT X
   96 INPUT  Y
  100 P."ENTER THE INCREMENTS:"'
  105 P."CONCENTRATION:"'
  110 FINPUT %H
  112 P."CELL PRESSURE:"'
  115 INPUT J; P.'
  120 P."**************************************"''
  200 REM  CONSTANTS
  210 %C= 2.99*10^8
  220 %I= 27.5*10^-24
  225 %J= 18.5*10^-24
  230 %T= 370
  240 %X= 7.24*10^18
  245 %Y=-9.657*10^24
  250 %F= 32*10^-9
  260 %P= 1013
  265 %K= 0.8
  270 %L= 0.6915
  275 %Z= 0.01
  280 %M= 2.36
  285  T= 283
  300 REM  HEADING
  310 P."CELL P(TORR)      CONC(PPM)       RATIO"''
  350 REM CALCULATION LOOP
  360 P=X-J
  370 DO P=P+J
  380 P.'P
  385 %N=%S-%H
  390 DO %N=%N+%H
  400 GOS.p
  410 GOS.r
  420 UNTIL %N>=%E
  430 UNTIL P>=Y
  450 END
  500p %A=%K*EXP(%Y*%M*%I*%Z*P/T)
  510  %B=%K*EXP(%Y*%M*%J*%Z*P/T)
  520 RETURN
  600r %O=%X*%P*%N/%T
  610 %R=(%A*%L*EXP(-%I*%O*%C*%F))+(%B*EXP(-%J*%O*%C*%F))
  620 %R=%R/((%L*EXP(-%I*%O*%C*%F))+EXP(-%J*%O*%C*%F))
  630 FP."                    "%N"      "%R'
  640 RETURN
```

A9.5 Program Listing (BASIC) S/N ratio vs Cathode Current at Bandwidth

```
>L.
   10 P."S/N VS CATHODE & BANDWIDTH"'
   20 P."::::::::::::::::::::::::::::"''
   30 P."ENTER THE RANGE OF LOAD RESISTANCE VALUES"'
   40 FINPUT "START(>0)"%S
   50 FINPUT "END       "%E
   60 P."ENTER INCREMENT OF R"'
   70 FINPUT %H
   75 P."ENTER RANGE OF CATHODE CURRENT"'
   80 FINPUT "START"%X
   82 FINPUT"END   "%Y
   85 %Y=%Y*10^18
   90 P."ENTER X FACTOR OF CATHODE CURRENT"'
   95 FINPUT %J; P.'
  100 REM CONSTANTS
  110 %Q=  1.6*10^-19
  120 %B= 10^6
  130 %I= 6.3*10^-11
  150 %C= 335*10^-12
  190 P."BANDWIDTH(HZ)   LOAD R          S/N RATIO      CATHODE I"''
  200 REM CALCULATIONS
  210 %R=%S-%H
  220 DO %R=%R+%H
  222 FP.%B"      ",%R'
  223 %K=%X/%J
  225 DO %K=%K*%J
  230 GOS.k
  232 %A=%K; %A=%A*10^18
  235 UNTIL %A>=%Y
  237 P.'
  240 UNTIL %R>=%E
  250 END
  300k %B=1/(2*PI*%R*%C)
  310 %S= %K/SQR%(2.8*%Q*%B*(%K+%I))
  320 FP."                                    "%S,"    "%K'
  330 RETURN
```

A9.6 Program Listing (BASIC) Distinct Wavelength DIAL Errors

```
>L.
   10P."DISTINCT WAVELENGTH"
   15P." DIAL ERROR"'
   20P."**********************************"''
   30P."ENTER RANGE OF CATHODE CURRENT"'
   40 FINPUT"START"%X
   50 FINPUT"END   "%Y
   60 %Y=%Y*10^18
   70 P."ENTER X FACTOR OF CATHODE CURRENT"'
   80 FINPUT %J;P.'
   90 P."ENTER RANGE OF CONCENTRATION"'
  100 FINPUT"START(>0)"%S
  110 FINPUT"END       "%F
  120 P."ENTER  INCREMENT OF CONC."'
  130 FINPUT%H
  200 REM CONSTANTS
  210 %Q=   1.6*10^-19
  220 %C=   335*10^-12
  230  R=   100
  240 %I=   6.3*10^-11
  250 %M=   1
  270  REM HEADINGS
  275  P."CATHODE I        CONC.(PPM)       CONC.ERROR(PPM)"''
  310 %K=%X/%J
  320 DO %K=%K*%J
  330 FP.''%K
  340 %N=%S-%H
  350 DO %N=%N+%H
  360 GOS.r
  370 GOS.p
  380 GOS.e
  385 GOS.d
  390 UNTIL %N>=%F
  400 %A=%K*10^18
  410 UNTIL %A>=%Y
  430                END
  450d FP."                    "%N"    "%E'
  455 RETURN
  500r %R=0.6915*EXP((-1.71*10^-3)*%N)
  505 RETURN
  510p %P=SQR(%K*(1+%R)+%I*(1+(%R^2)))
  520 %B=1/(2*PI*R*%C)
  530 %P=%P*((100*SQR(2.8*%Q*%B))/((SQR%M)*%K))
  535 RETURN
  540e %E=-585.85*%P/%N
```

A9.7 Program Listing (BASIC) Mixed Wavelength DIAL Errors

NB. Lines 340 and 350 are altered for the desired data increment.

```
>L.
   10 P."MIXED WAVELENGTH  DIAL ERROR"'
   20 P."**********************************"'
   30 P."ENTER RANGE OF CATHODE CURRENT"'
   40 FINPUT"START"%F
   50 FINPUT"END  "%0
   60 %0=%0*10^18
   70 P."ENTER X FACTOR OF CATHODE CURRENT"'
   80 FINPUT%J;P.'
   90 P."ENTER RANGE OF CONCENTRATION"'
  100 FINPUT"START(>0)"%D
  110 FINPUT"END      "%0
  120 P."ENTER CONC. INCREMENT"'
  130 FINPUT%H;P.'
  140 P."ENTER RANGE OF ABSORPTION CELL PRESSURES"'
  150 FINPUT"START"%X
  160 FINPUT"END  "%Y
  170 P."ENTER INCREMENT OF CELL PRESSURE"'
  180 FINPUT%Z
  200 REM CONSTANTS
  210 %Q= 1.6*10^-19
  220 %S= 4.75*10^6
  230 %M= 1
  240 %I= 6.3*10^-11
  270 REM HEADINGS
  280 P."CATHODE I       CONC(PPM)       CELL PRESSURE  CONC.ERR"''
  300 %K=%F/%J
  310 DO %K=%K*%J
  320 FP.''%K
  340 %N=%D/%H
  350 DO %N=%N*%H
  360 FP."                    "%N'
  370 %P=%X-%Z
  380 DO %P=%P+%Z
  400 GOS.a
  410 GOS.r
  420 GOS.u
  430 GOS.e
  435 GOS.p
  440 UNTIL %P>=%Y
  450 UNTIL %N>=%0
  460 %L=%K*10^18
  470 UNTIL %L>=%0
  500                 END
 600a REM CELL COEFFICIENTS
  610  %A= 0.8*EXP(-0.02215*%P)
  620  %B= 0.8*EXP(-0.01490*%P)
  630  RETURN
 640r REM SIGNAL RATIO FROM CONC. MEASUREMENT
  650  %R= (0.6915*%A*EXP(-0.00522*%N))+(%B*EXP(-0.00351*%N))
  660  %R=%R/((0.6915*EXP(-0.00522*%N))+(EXP(-0.00351*%N)))
  670  RETURN
 700u  REM RATIO ERROR
  710  %U=SQR(%K*(1+%R)+%I*(1+(%R^2)))
  720   %U=%U*((100*SQR(2.8*%Q*%S))/((SQR%M)*%K))
  730   RETURN
 750e  %E=(%B-%A)*%R/((%R-%A)*(%B-%R))
  760   %E=%E*%U*585.85/%N
  770   RETURN
 800pFP."                                    "%P"    "%E'
 810 RETURN
```

Appendix for Chapter 10

A10.1 Calibration of the SO_2 Absorption Cell

A10.1(a) Non-automatic Calibration

The SO_2 absorption cell, within the laser cavity (described in section 5.5), is filled with SO_2 to a partial pressure of P(torr) at a temperature of T(^oK). The value of the ratio, P/T, is entered into the analytical routine of the signal processing program. The P/T value at the time of filling of the cell may not apply at a later time due, possibly, to any reaction which may remove or add gaseous SO_2 to the contents. An apparent increase in the degree of absorption of the radiation, in the course of a run of laser pulses, suggests a photolytically enhanced reaction which may promote production of gaseous SO_2. The increase in absorption with number of pulses is shown in figure A10.1 which shows the reduction in pulse-pair ratio, n'/n'', until about 80 pulses have passed through the cell. It is necessary, therefore, to operate the laser through the cell for at least 80 pulse pairs, immediately before any measurements are taken.

To account for any variation in effective P/T ratio, a calibration procedure is carried out to set P/T by measuring the DIAL signal ratio, n'/n'', at zero ambient SO_2 concentration or, more conveniently, taking the laser output energy ratio (DIAL pair), %P. The algorithm which is employed to give P/T is derived from the cell absorption coefficients, a and b, applying at the $XeCl^*$ laser wavelengths λ_1 and λ_2 respectively. Assuming no absorption by SO_2 over the lidar range (to a target and back to the receiver over very short range), the received ratio is given by

$$n'/n'' = (an_1 + bn_2)/(n_1 + n_2). \qquad (A10.1.1)$$

Equation (A10.1.1) is also obtained by setting the average SO_2 concentration, N_r, to zero in equation (9.5.3), which comes from a ratio of lidar equations for two pulses in DIAL. Equations (5.5.3) and (5.5.4) express a and b so that equation (A10.1.1) becomes

$$n'/n'' = K\exp(-9.657X10^{24}\,\sigma_1\,N_c xP/T)(n_1/n_2) + K\exp(-9.657X10^{24}\,\sigma_2\,N_c xP/T) \div (n_1/n_2 + 1). \qquad (A10.1.2)$$

Table 9.2.1 gives the values of constants and absorption coefficients so that equation (A10.1.2) becomes

$$n'/n'' = 0.473\,[0.6915\exp(-6.2675P/T) + \exp(-4.2162P/T)]. \qquad (A10.1.3)$$

Equation (A10.1.3) allows figure A10.2 to be plotted to show the P/T value to be set for a measured return signal ratio n'/n" (equivalent to %P) in the absence of any ambient SO_2 (ie. to give a zero correction). Figure A10.2 is used outwith the micro-computer-programmed analytical routine to select the P/T value. The unmodified laser spectrum peak wavelength ratio, n_1/n_2, is set at 0.6915 (given in table 4.9.3), for the purpose of the calibration. This value of n_1/n_2 is used in the target SO_2 concentration algorithms in the DIAL analytical program given in appendix A6.2. For further improvement in accuracy, the constant K, accounting for losses by the cell windows would be eliminated if an empty cell (no SO_2) is used at the laser output, in the "cell out" position.

A10.1(b) Automatic Calibration (Proposed)

The calibration procedure cannot be automated unless an iterative method is applied to solve equation (A10.1.2) for P/T, for which there is no

analytical method. In this case, therefore, the cell would be calibrated, per data acquisition sequence, by using the laser output energy measurements used for pulse energy normalization, in the data analysis routine (appendix A6.2, variable %P).

A10.2 Target Ranging Calibration Method

Triggering of the oscillograph trace must be calibrated to coincide with the time at which the laser pulse is emitted, compensating for the temporal discrepancy introduced between this event and the occurrence of the "time 0" synchronisation pulse of the laser trigger unit. To this end, the "time 0" pulse is used to trigger time-base A of the oscilloscope, where timebase B starts after A via an adjustable delay (B starts at Δt after A). The lidar return signal is displayed on channel B and can therefore be calibrated for range.

Calibration is done by "bouncing" a laser pulse off a target which is at a known distance, so that the time-of-flight, t_p, can be predicted. The signal is displayed on channel A (ie. uncalibrated) and the time between the trace initiation and the pulse, t_u, is measured. The delay time, Δt, between timebases A and B is set according to the difference given by

$$\Delta t = t_u - t_p. \qquad \text{(A10.2.1)}$$

The lidar signal is now displayed on channel B.

Alternatively, a delay line is inserted in the path of the synchronising pulse which is used to trigger the oscilloscope, so that it triggers at the time at which the laser pulse leaves.

A10.3 Relation between Photomultiplier Cathode Peak Current and Measured Voltage Peak: for the purpose of calculations

The photomultiplier cathode peak current, i_{k1}, of a pulse of fwhm = τ_k, and charge Q, is given by

$$i_{k1} \simeq Q/\tau_k. \qquad \text{(A10.3.1)}$$

The maximum voltage peak of a signal at the end of a signal cable from the photomultiplier output is given by

$$V_{pk} < R_i Q.G/t, \qquad \text{(A10.3.2)}$$

where R_i is the load impedance, G is the photomultiplier gain and t is the fwhm of the measured pulse. Combining (A10.3.1) and (A10.3.2) gives the lowest peak cathode current as

$$i_{k1\ min} = V_{pk}t/R_iG.\ \tau_k. \qquad \text{(A10.3.3)}$$

Values are, typically; $G = 10^6$, τ_k = 100ns, t = 3μs. The load resistance is variable but a load of R_i = 10kΩ has been employed in the DIAL experiments. Thus, for a weak DIAL signal, giving a peak voltage of about 10mV, the peak cathode current is of the order of 10^{-10}A. A stronger signal of around 100mV arises from a peak photocathode current of about 10^{-9}A.

A10.4 Theoretical DIAL Accuracy Applied to Experiments

A10.4.1 Calculation of Errors in DIAL Measurement, using Figure 9.7.2

The calculation is specific to sub-section 10.2.4 and figure 10.2.2. The accuracy is based upon the accuracy of the weaker of the two DIAL signals. Figure 10.2.2(a) is plotted from data obtained with relatively weak pulses so a photocathode current of 10^{-10}A peak is considered. Other relevant parameters are m = 20, range r = 40 and a concentration mean of $\bar{N}'$ = 43 ppm. Figure 9.7.2, predicting measurement error, gives $\Delta\bar{N}'$ = 380% for a 4.8m range interval. Applying this to figure 10.2.2(a) gives an uncertainty of $\Delta\bar{N}' = \pm 20$ ppm.

A similar calculation is made for the concentration mean of 42 ppm in figure 10.2.2(d), but for m =10 and based on a stronger signal at 10^{-9}A peak, to give $\Delta\bar{N}' = \pm 7.7$ ppm.

A10.4.2 Calculation of Detection Limits, using Figure 9.8.1

Figure 9.8.1 gives detection limits, applied to measurements of SO_2 shown in figures 10.2.2(b) to (d), of 300 ppm.m, giving 7.5 ppm when r = 40m. Figure 9.7.2 is used for the weaker signal applying to measurements shown in figure 10.2.2(a) to give 600 ppm.m, resulting in 15 ppm detection limit.

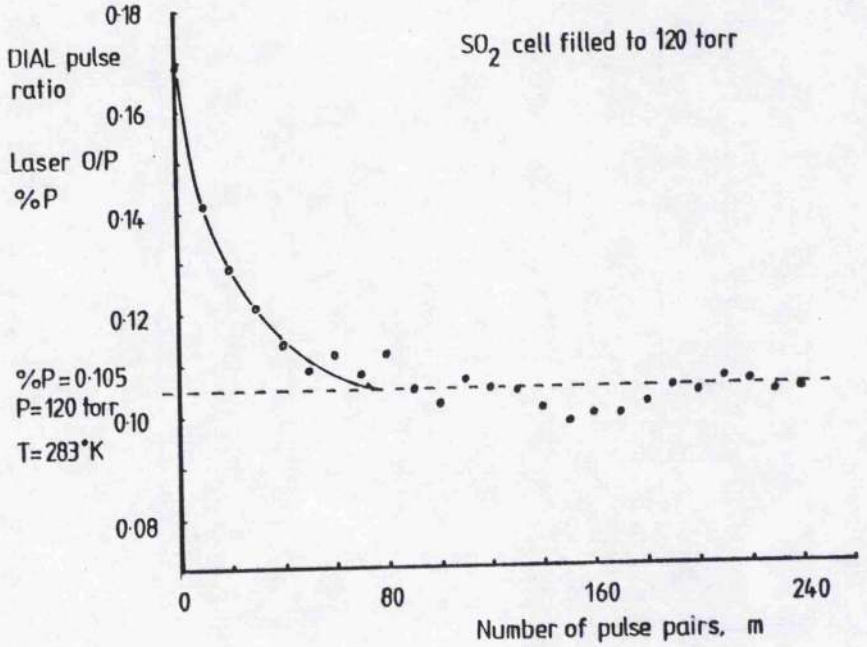

Figure A10.1 Attainment of equilibrium in the SO_2 absorption cell

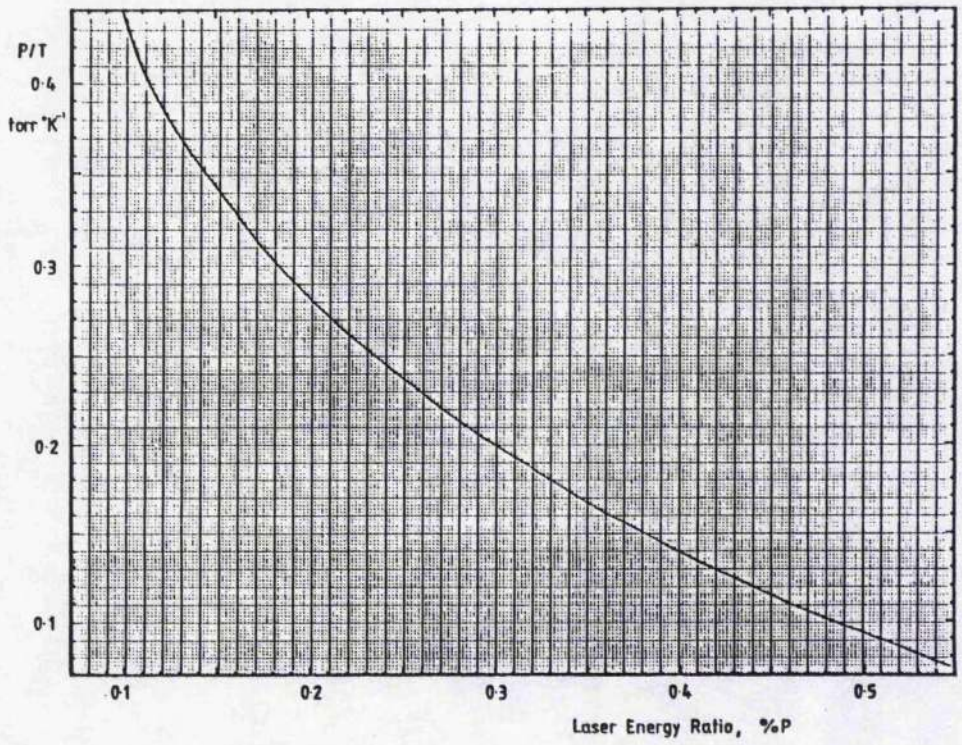

Figure A10.2 Calibration plot for the sulphur dioxide absorption cell P/T vs %P (laser output energy ratio)